



AFRL-AFOSR-VA-TR-2016-0313

Theory, computation and experiment on criticality and stability of vortices separating from edges

Ashok Gopalarathnam
North Carolina State University at Raleigh
NC State University, Campus Box 7001
Raleigh, NC 27695-0001

09/07/2016
Final Report

DISTRIBUTION A: Distribution approved for public release.

Air Force Research Laboratory
AF Office Of Scientific Research (AFOSR)/RTA1

REPORT DOCUMENTATION PAGE

*Form Approved
OMB No. 0704-0188*

The public reporting burden for this collection of information is estimated to average 1 hour per response, including the time for reviewing instructions, searching existing data sources, gathering and maintaining the data needed, and completing and reviewing the collection of information. Send comments regarding this burden estimate or any other aspect of this collection of information, including suggestions for reducing the burden, to the Department of Defense, Executive Service Directorate (0704-0188). Respondents should be aware that notwithstanding any other provision of law, no person shall be subject to any penalty for failing to comply with a collection of information if it does not display a currently valid OMB control number.

PLEASE DO NOT RETURN YOUR FORM TO THE ABOVE ORGANIZATION.

| | | | | | |
|--|-------------------------|---------------------------------------|---|--|--|
| 1. REPORT DATE (DD-MM-YYYY) 15-08-2016 | | 2. REPORT TYPE Final report | | 3. DATES COVERED (From - To) 15 April 2013 - 15 April 2016 | |
| 4. TITLE AND SUBTITLE Theory, computation and experiment on criticality and stability of vortices separating from edges | | | | 5a. CONTRACT NUMBER - | |
| | | | | 5b. GRANT NUMBER FA9550-13-1-0179 | |
| | | | | 5c. PROGRAM ELEMENT NUMBER - | |
| 6. AUTHOR(S) Gopalarathnam, Ashok; Hirato, Yoshikazu; Shen, Minao; Ramesh, Kiran; Suresh Babu, Arun Vishnu; Ol, Michael V., Granlund, Kenneth, and Edwards, Jack R. | | | | 5d. PROJECT NUMBER - | |
| | | | | 5e. TASK NUMBER - | |
| | | | | 5f. WORK UNIT NUMBER - | |
| 7. PERFORMING ORGANIZATION NAME(S) AND ADDRESS(ES) North Carolina State University, Department of Mechanical and Aerospace Engineering, 911 Oval Drive, Box 7910, Raleigh, NC 27695-7910. | | | | 8. PERFORMING ORGANIZATION REPORT NUMBER - | |
| 9. SPONSORING/MONITORING AGENCY NAME(S) AND ADDRESS(ES) Dr. Douglas R. Smith Flow Interactions & Control, Program Officer Air Force Office of Scientific Research (AFOSR), 875 N. Randolph St, Ste 325 Rm 3112 Arlington, VA 22203. | | | | 10. SPONSOR/MONITOR'S ACRONYM(S) - | |
| | | | | 11. SPONSOR/MONITOR'S REPORT NUMBER(S) - | |
| 12. DISTRIBUTION/AVAILABILITY STATEMENT DISTRIBUTION A: Distribution approved for public release. | | | | | |
| 13. SUPPLEMENTARY NOTES None | | | | | |
| 14. ABSTRACT The aim of this research effort was to extend earlier work airfoil leading-edge vortex (LEV) shedding to finite-wing flows. The current research shows that leading-edge suction, which was shown in the earlier work to govern LEV formation in airfoils with rounded leading edges, also governs LEV formation on finite wings. It is shown that when the maximum value of the spanwise distribution of leading-edge suction on a finite wing reaches a critical value, LEV initiation takes place. The critical value is the same as that for the corresponding airfoil section, allowing it to be determined from 2D experiments or computations. Further, the critical value is independent of motion kinematics so long as LEV formation is not preceded by significant trailing-edge flow reversal. This insight was used to augment an inviscid unsteady vortex lattice method (UVLM) to handle LEV shedding from finite wings by using a vortex sheet to model the LEV shedding along the span. By convecting the LEV sheet using local velocity, the UVLM was able to predict vortex-sheet roll up, which agreed well with high-order computations. The current research has brought to light important insights in the initiation of LEV shedding on finite wings, which can be used in low-order modeling and flow control. | | | | | |
| 15. SUBJECT TERMS unsteady aerodynamics; leading edge vortex; finite wing; tip vortex; dynamic stall | | | | | |
| 16. SECURITY CLASSIFICATION OF: | | | 17. LIMITATION OF ABSTRACT UU | 18. NUMBER OF PAGES 123 | 19a. NAME OF RESPONSIBLE PERSON Ashok Gopalarathnam |
| a. REPORT U | b. ABSTRACT U | c. THIS PAGE U | | | 19b. TELEPHONE NUMBER (Include area code) 919-515-5669 |

Reset

Standard Form 298 (Rev. 8/98)
Prescribed by ANSI Std. Z39.18
Adobe Professional 7.0

INSTRUCTIONS FOR COMPLETING SF 298

1. REPORT DATE. Full publication date, including day, month, if available. Must cite at least the year and be Year 2000 compliant, e.g. 30-06-1998; xx-06-1998; xx-xx-1998.

2. REPORT TYPE. State the type of report, such as final, technical, interim, memorandum, master's thesis, progress, quarterly, research, special, group study, etc.

3. DATES COVERED. Indicate the time during which the work was performed and the report was written, e.g., Jun 1997 - Jun 1998; 1-10 Jun 1996; May - Nov 1998; Nov 1998.

4. TITLE. Enter title and subtitle with volume number and part number, if applicable. On classified documents, enter the title classification in parentheses.

5a. CONTRACT NUMBER. Enter all contract numbers as they appear in the report, e.g. F33615-86-C-5169.

5b. GRANT NUMBER. Enter all grant numbers as they appear in the report, e.g. AFOSR-82-1234.

5c. PROGRAM ELEMENT NUMBER. Enter all program element numbers as they appear in the report, e.g. 61101A.

5d. PROJECT NUMBER. Enter all project numbers as they appear in the report, e.g. 1F665702D1257; ILIR.

5e. TASK NUMBER. Enter all task numbers as they appear in the report, e.g. 05; RF0330201; T4112.

5f. WORK UNIT NUMBER. Enter all work unit numbers as they appear in the report, e.g. 001; AFAPL30480105.

6. AUTHOR(S). Enter name(s) of person(s) responsible for writing the report, performing the research, or credited with the content of the report. The form of entry is the last name, first name, middle initial, and additional qualifiers separated by commas, e.g. Smith, Richard, J, Jr.

7. PERFORMING ORGANIZATION NAME(S) AND ADDRESS(ES). Self-explanatory.

8. PERFORMING ORGANIZATION REPORT NUMBER. Enter all unique alphanumeric report numbers assigned by the performing organization, e.g. BRL-1234; AFWL-TR-85-4017-Vol-21-PT-2.

9. SPONSORING/MONITORING AGENCY NAME(S) AND ADDRESS(ES). Enter the name and address of the organization(s) financially responsible for and monitoring the work.

10. SPONSOR/MONITOR'S ACRONYM(S). Enter, if available, e.g. BRL, ARDEC, NADC.

11. SPONSOR/MONITOR'S REPORT NUMBER(S). Enter report number as assigned by the sponsoring/monitoring agency, if available, e.g. BRL-TR-829; -215.

12. DISTRIBUTION/AVAILABILITY STATEMENT. Use agency-mandated availability statements to indicate the public availability or distribution limitations of the report. If additional limitations/ restrictions or special markings are indicated, follow agency authorization procedures, e.g. RD/FRD, PROPIN, ITAR, etc. Include copyright information.

13. SUPPLEMENTARY NOTES. Enter information not included elsewhere such as: prepared in cooperation with; translation of; report supersedes; old edition number, etc.

14. ABSTRACT. A brief (approximately 200 words) factual summary of the most significant information.

15. SUBJECT TERMS. Key words or phrases identifying major concepts in the report.

16. SECURITY CLASSIFICATION. Enter security classification in accordance with security classification regulations, e.g. U, C, S, etc. If this form contains classified information, stamp classification level on the top and bottom of this page.

17. LIMITATION OF ABSTRACT. This block must be completed to assign a distribution limitation to the abstract. Enter UU (Unclassified Unlimited) or SAR (Same as Report). An entry in this block is necessary if the abstract is to be limited.

Final Report prepared for
Air Force Office of Scientific Research
on AFOSR Grant # FA9550-13-1-0179

Project Title:

**Theory, Computation, and Experiment on Criticality and
Stability of Vortices Separating from Edges**

Principal Investigators:

Ashok Gopalarathnam, Jack R. Edwards

Department of Mechanical and Aerospace Engineering
North Carolina State University
Raleigh, NC 27695.

and Michael V. Ol

U.S. Air Force Research Laboratory, Air Vehicles Directorate,
AFRL/RBAA, Bldg. 45, 2130 8th St., WPAFB, OH 45433-7542.

Collaborators:

Yoshikazu Hirato, Minao Shen, Arun Vishnu Suresh Babu

Ph.D. students in the Department of Mechanical and Aerospace Engineering
North Carolina State University
Raleigh, NC 27695.

Kiran Ramesh Lecturer in Aerospace Engineering,
University of Glasgow, UK.

and Kenneth Granlund Assistant Professor,
Department of Mechanical and Aerospace Engineering
North Carolina State University
Raleigh, NC 27695.

Period of Performance:

15 April 2013 – 15 April 2016

Program Manager:

Dr. Douglas Smith

U.S. Air Force Office of Scientific Research

15 August 2016

Contents

| | | |
|----------|---|-----------|
| 1 | Executive Summary | 1 |
| 2 | Introduction | 3 |
| 2.1 | LEV-dominated airfoil flows | 3 |
| 2.2 | LEV-dominated finite-wing flows | 5 |
| 2.3 | Layout of this report | 6 |
| 3 | Computational Fluid Dynamics Methods | 7 |
| 3.1 | RANS CFD for supporting the development of the low-order methods | 8 |
| 3.2 | Identification of LEV formation from CFD | 8 |
| 3.3 | RANS analysis of LEV formation on finite wings and comparison to experiment . . . | 9 |
| 3.4 | LES/RANS Modeling Activities | 10 |
| 3.4.1 | Model Formulation | 10 |
| 3.4.2 | Aérospatiale A-Airfoil | 14 |
| 3.5 | Interim Conclusions | 17 |
| 4 | Experimental Facility and Techniques | 18 |
| 4.1 | Facility and Motion Mechanism | 18 |
| 4.2 | Force Measurement | 19 |
| 4.3 | Flow Visualization | 20 |
| 4.4 | Interim Conclusions | 20 |
| 5 | Factors Affecting LEV Initiation in Unsteady Airfoil Flows | 21 |
| 5.1 | Theoretical approach | 21 |
| 5.1.1 | Large-angle unsteady thin-airfoil theory | 21 |
| 5.1.2 | Leading Edge Suction Parameter (LESP) | 23 |
| 5.2 | Study of LEV initiation in low Reynolds-number flows | 25 |

| | | |
|----------|---|-----------|
| 5.2.1 | Definition of motion kinematics | 25 |
| 5.3 | Results of parametric studies of LEV initiation | 26 |
| 5.3.1 | Case study 1: kinematics with varying pivot locations | 26 |
| 5.3.2 | Case study 2: kinematics with varying pitch rates | 28 |
| 5.3.3 | Case study 3: kinematics with varying initial pitch angles | 30 |
| 5.3.4 | Case study 4: kinematics with pitch-plunge combination | 33 |
| 5.3.5 | Compilation of all test cases | 36 |
| 5.3.6 | Trigger/Suppress LEV formation using $LESP_{crit}$ | 38 |
| 5.4 | Interim conclusions | 40 |
| 6 | Model Reduction in Discrete-Vortex Methods for Unsteady Airfoil Flows | 43 |
| 6.1 | Background: The LESP-modulated Discrete Vortex Method (LDVM) | 43 |
| 6.1.1 | LESP criterion for initiation, shedding, and termination of LEV | 44 |
| 6.2 | The reduced order model | 44 |
| 6.2.1 | Initial rollup | 45 |
| 6.2.2 | Merging algorithm | 45 |
| 6.2.3 | Location of the combined DV | 46 |
| 6.2.4 | Identifying pinch-off | 47 |
| 6.2.5 | Intermittent LEV shedding | 47 |
| 6.3 | Results | 47 |
| 6.3.1 | Case 1: Flat plate undergoing 0-90 pitching motion about LE | 47 |
| 6.3.2 | Case 2: SD7003 airfoil undergoing 0-90-0 pitching motion about trailing edge | 49 |
| 6.3.3 | Case 3: Flat plate undergoing 0-45 pitch up-hold motion about leading edge . | 51 |
| 6.4 | Interim Conclusions | 55 |
| 7 | Unsteady Vortex Lattice Method with Modifications for Prediction of LEV For- | 56 |
| | mation on Finite Wings | |
| 7.1 | UVLM for prediction of LEV initiation | 56 |
| 7.1.1 | $LESP$ evaluation for finite wing | 56 |
| 7.1.2 | Optional tip-vortex model | 58 |
| 7.2 | Modified UVLM for prediction of LEV formation | 59 |
| 7.2.1 | Leading edge vortex | 59 |
| 7.2.2 | Solution of linear system | 62 |
| 7.2.3 | Calculation of aerodynamic load | 63 |

| | | |
|----------|--|-----------|
| 7.2.4 | Vortex sheet roll up | 63 |
| 7.2.4.1 | Numerical process of vortex roll up | 63 |
| 7.2.4.2 | Desingularized vortex model | 64 |
| 7.2.4.3 | Impingement of vortex sheets | 66 |
| 7.2.5 | Amalgamation of vortex sheets | 67 |
| 7.3 | Summary of Modified UVLM | 71 |
| 8 | Low-Order Prediction of LEV Initiation on Finite Wings | 73 |
| 8.1 | Methodology and Case Studies | 73 |
| 8.1.1 | Motion parameters | 76 |
| 8.1.2 | Determination of LEV initiation and $LESP_{max}$ from CFD and UVLM | 76 |
| 8.2 | Results and Discussion | 80 |
| 8.2.1 | Two-dimensional cases 2D1 and 2D2 | 80 |
| 8.2.2 | Baseline: case 1 | 80 |
| 8.2.3 | Case Study A: Effect of pivot location | 82 |
| 8.2.4 | Case Study B: Effect of pitch rate | 84 |
| 8.2.5 | Case Study C: Effect of taper ratio | 84 |
| 8.2.6 | Case Study D: Effect of tip twist | 87 |
| 8.2.7 | Case Study E: Effect of aspect ratio | 87 |
| 8.2.8 | Case Study F: Effect of sweep angle | 91 |
| 8.2.9 | Case Study G: Effect of leading-edge curvature | 91 |
| 8.2.10 | Case Study H: Effect of abrupt change in incidence | 94 |
| 8.2.11 | Case Study I: Partially sharpened wing | 94 |
| 8.2.12 | Summary | 97 |
| 8.3 | Interim Conclusions | 98 |
| 9 | Low-Order Prediction of LEV Formation on Finite Wings | 99 |
| 9.1 | Development of LEV structure | 99 |
| 9.2 | Prediction of aerodynamic loads with LEV | 103 |
| 9.3 | Computation time | 108 |
| 9.4 | Demonstration of three-dimensional amalgamation method | 110 |
| 9.5 | Known problems | 110 |
| 9.5.1 | Geometric restrictions | 110 |
| 9.5.2 | Management of numeric instability | 111 |

List of Figures

| | | |
|------|---|----|
| 3.1 | Body-fitted mesh used in computations. | 7 |
| 3.2 | Vorticity scale for all CFD vorticity plots in this report. | 8 |
| 3.3 | Vorticity and skin friction coefficient plots from CFD during the LEV formation process. Appearance of positive vorticity region is circled. | 9 |
| 3.4 | Representative mesh distribution for CFD analysis. | 10 |
| 3.5 | Volumes of iso-Q as a function of angle of attack. Left: PIV experiment. Right: CFD simulation. | 11 |
| 3.6 | Side views of three-dimensional streamline patterns as a function of angle of attack. Left: PIV experiment. Right: CFD simulation. | 12 |
| 3.7 | X-Y centerplane mesh for A-airfoil. | 14 |
| 3.8 | Iso-surfaces of swirl strength (2000 s^{-1}) illustrating development of eddy structures in airfoil boundary layer. | 14 |
| 3.9 | Mean pressure coefficient (left) and skin friction coefficient (right) distribution along the airfoil obtained by hybrid LES/RANS computation compared with experimental measurement. | 15 |
| 3.10 | Mean streamwise velocity profile as a function of normalized wall-normal distance obtained by hybrid LES/RANS computation; individual profiles are separated by a horizontal profile of 1.4. | 15 |
| 3.11 | Profile of the rms streamwise velocity fluctuations obtained by a hybrid LES/RANS computation; individual profiles are separated by a horizontal profile of 0.3 (left) and 0.2 (right). | 16 |
| 3.12 | Profile of the rms wall-normal velocity fluctuations obtained by a hybrid LES/RANS computation; individual profiles are separated by a horizontal profile of 0.3. | 16 |
| 3.13 | Profile of the Reynolds-averaged shear stress obtained by hybrid LES/RANS computation; individual profiles are separated by a horizontal profile of 0.014. | 17 |
| 4.1 | Test section and portion of motion rig mounted above test section of the AFRL Horizontal Free-surface Water Tunnel (left). $c = 3''$ flat plate with force balance mounted between steel coupler piece and plastic foot connecting to the plate (right). Dye injection is from a 0.5 mm diameter slot at the plate leading and trailing edges, $\frac{3}{4}$ spanwise location. | 18 |

| | | |
|------|---|----|
| 5.1 | Illustration of the time-stepping method in large-angle unsteady thin-airfoil theory. | 22 |
| 5.2 | Airfoil velocities (positive as shown) and pivot location. | 23 |
| 5.3 | Depiction of flow around a thin airfoil's leading edge. | 23 |
| 5.4 | Case study 1: pitch-angle variation with time, and pitch-angles at which LEV formation is initiated (kinematics with different pivot locations). | 27 |
| 5.5 | Case study 1: LESP variation with time, and LESP values at which LEV formation is initiated (kinematics with different pivot locations). | 27 |
| 5.6 | Case study 1: left to right - flow visualization from experiment, vorticity plots from CFD, C_p (upper and lower surfaces) and C_f (upper surface) distributions from CFD at the instants of LEV initiation. Top to bottom - pivot location at leading edge, quarter chord and three-quarter chord. | 28 |
| 5.7 | Case study 1: left to right - flow visualization from experiment, vorticity plots from CFD, C_p (upper and lower surfaces) and C_f (upper surface) distributions from CFD at $\Delta LESP = 0.1$ after the instants of LEV initiation. Top to bottom - pivot location at leading edge, quarter chord and three-quarter chord. | 29 |
| 5.8 | Case study 2: pitch-angle variation with time, and pitch-angles at which LEV formation is initiated (kinematics with different pitch rates). | 30 |
| 5.9 | Case study 2: LESP variation with time, and LESP values at which LEV formation is initiated (kinematics with different pitch-rates). | 30 |
| 5.10 | Case study 2: left to right - flow visualization from experiment, vorticity plots from CFD, C_p (upper and lower surfaces) and C_f (upper surface) distributions from CFD at the instants of LEV initiation. Top to bottom - pitch rate of 0.01, 0.03, 0.05, 0.1, 0.2 and 0.4). | 31 |
| 5.11 | Case study 2: left to right - flow visualization from experiment, vorticity plots from CFD, C_p (upper and lower surfaces) and C_f (upper surface) distributions from CFD at $\Delta LESP = 0.1$ after the instants of LEV initiation. Top to bottom - pitch rate of 0.01, 0.03, 0.05, 0.1, 0.2 and 0.4). | 32 |
| 5.12 | Case study 3: pitch-angle variation with time, and pitch-angles at which LEV formation is initiated (kinematics with different start angles). | 33 |
| 5.13 | Case study 3: LESP variation with time, and LESP values at which LEV formation is initiated (kinematics with different start angles). | 33 |
| 5.14 | Case study 3: left to right - flow visualization from experiment, vorticity plots from CFD, C_p (upper and lower surfaces) and C_f (upper surface) distributions from CFD at the instants of LEV initiation. Top to bottom - starting pitch angles of 10, 5, 0, -5, -10 and -15 deg). | 34 |
| 5.15 | Case study 3: left to right - flow visualization from experiment, vorticity plots from CFD, C_p (upper and lower surfaces) and C_f (upper surface) distributions from CFD at $\Delta LESP = 0.1$ after the instants of LEV initiation. Top to bottom - starting pitch angles of 10, 5, 0, -5, -10 and -15 deg). | 35 |
| 5.16 | Case study 4: pitch angle/plunge amplitude variation with time, and pitch angles at which LEV formation is initiated (baseline case and pitch-plunge combination). | 36 |

| | | |
|------|---|----|
| 5.17 | Case study 4: <i>LESP</i> variation with time, and <i>LESP</i> values at which LEV formation is initiated (baseline case and pitch-plunge combination). | 36 |
| 5.18 | Flow visualization from experiment, vorticity plots from CFD, C_p (upper and lower surfaces) and C_f (upper surface) distributions from CFD at the instant of LEV initiation for cases 1 and 15. | 37 |
| 5.19 | Flow visualization from experiment, vorticity plots from CFD, C_p (upper and lower surfaces) and C_f (upper surface) distributions from CFD at some $\Delta LESP$ after the initiation of LEV formation for cases 1 and 15. | 37 |
| 5.20 | Comparison of angle of attack for LEV initiation from low-order and high-order methods. | 38 |
| 5.21 | <i>LESP</i> values at the instant of LEV initiation (as determined from CFD), compiled for all cases considered. | 39 |
| 5.22 | Pitch amplitude variation with time for the baseline case, and plunge amplitude variations which are used in combination with baseline pitch to generate the two design cases. | 40 |
| 5.23 | <i>LESP</i> variation with time for the baseline case and the two design cases. As required by the design criteria, the intersection of instantaneous <i>LESP</i> with critical <i>LESP</i> is at $t^* - t_1^* = 0.5$ and 1.5 respectively. | 40 |
| 6.1 | Case 1: Comparison of predictions of the reduced order method and LDVM. Variation with $t^* = tU/c$ of: (a) <i>LESP</i> , (b) lift coefficient, (c) drag coefficient, and (d) pitching moment coefficient about the mid chord. | 48 |
| 6.2 | Case 1: Streamline patterns predicted by LDVM (left) and the reduced order method (right) at five time instants. | 50 |
| 6.3 | Case 2: Comparison of predictions of the reduced order method and LDVM. Variation with $t^* = tU/c$ of: (a) <i>LESP</i> , (b) lift coefficient, (c) drag coefficient, and (d) pitching moment coefficient about the quarter chord. | 51 |
| 6.4 | Case 2: Streamline patterns predicted by LDVM (left) and the reduced order method (right) at five time instants. | 52 |
| 6.5 | Case 3: Comparison of predictions of the reduced order method and LDVM. Variation with $t^* = tU/c$ of: (a) <i>LESP</i> , (b) lift coefficient, (c) drag coefficient, and (d) pitching moment coefficient about the quarter chord. | 53 |
| 6.6 | Case 3: Streamline patterns predicted by LDVM (left) and the reduced order method (right) at five time instants. | 54 |
| 7.1 | Illustration of vortex-lattice discretization of an example wing-tail geometry. | 57 |
| 7.2 | Snapshots of TEV shedding in vortex ring representation. | 57 |
| 7.3 | Schematic description of separated tip flow model. | 58 |
| 7.4 | Comparison of distribution of vortex lattices. | 59 |
| 7.5 | Placement of LEV ring vortex. | 61 |

| | | |
|------|---|----|
| 7.6 | Schematic description of pseudo vortex ring. | 61 |
| 7.7 | Comparison of tangential velocity distribution of Rankine and Lamb-Oseen model (Assuming $\Gamma = 1, r_c = 2\sqrt{\nu t} = 0.5$). | 65 |
| 7.8 | Range of application (colored by gray). | 67 |
| 7.9 | Schematic description of vortex sheet structure to be amalgamated. | 69 |
| 7.10 | Schematic description of implementation of amalgamation. | 69 |
| 7.11 | Schematic description of procedure of amalgamation. | 70 |
| 7.12 | Schematic flowchart of UVLM. | 72 |
| 8.1 | Comparison of SD 7003 (solid line) and sharpened SD 7003 (dashed line) | 74 |
| 8.2 | Geometries of the ten wings used in the 13 cases. | 75 |
| 8.3 | Pitch-up motions used in this study. | 76 |
| 8.4 | Sequence of events associated with LEV initiation and growth on an airfoil. Stream- lines and C_f at different angles of attack. | 78 |
| 8.5 | Upper-surface skin-friction lines for case 1. Right half of wing shown. In each snapshot, leading edge is on the top, wing tip is on the right, trailing edge is on the bottom, wing root is on the left. | 79 |
| 8.6 | Spanwise variation of $LESP$ and determination of $LESP_{max}$ for case 1. | 79 |
| 8.7 | Result of baseline (case 1) | 81 |
| 8.8 | Case study A: Effect of pivot location. Comparison of cases 1 and 2 at CFD frames just after LEV onset. | 83 |
| 8.9 | Case study B: Effect of pitch rate. Comparison of cases 1, 3, and 4 at CFD frames just after LEV onset. | 85 |
| 8.10 | Case study C: Effect of taper ratio. Comparison of cases 1 and 5 at CFD frames just after LEV onset. | 86 |
| 8.11 | Case study D: Effect of tip twist. Comparison of cases 1 and 6 at CFD frames just after LEV onset. | 88 |
| 8.12 | Case study E: Effect of aspect ratio. Comparison of cases 1, 7, 8, and 9 at CFD frames just after LEV onset. | 89 |
| 8.13 | Comparison of separated tip flow model and attached tip flow model for case 1 and 7. | 90 |
| 8.14 | Case study F: Effect of sweep angle. Comparison of cases 1 and 10 at CFD frames just after LEV onset. | 92 |
| 8.15 | Case study G: Effect of leading edge curvature. Comparison of cases 1 and 11 at CFD frames just after LEV onset. | 93 |
| 8.16 | Case study H: Partially deflected wing. Comparison of cases 1 and 12 at CFD frames just after LEV onset. | 95 |
| 8.17 | Case study I: Partially sharpened wing. Comparison of cases 1 and 13 at CFD frames just after LEV onset. | 96 |

| | | |
|------|---|-----|
| 8.18 | Comparison of low-order (UVLM) predictions with high-order (CFD) results for all the finite-wing cases. | 97 |
| 9.1 | Comparison of LEV structure of CFD (left) and UVLM (right) for case 1. | 100 |
| 9.2 | Comparison of LEV structure of CFD (left) and UVLM (right) for case 6. | 102 |
| 9.3 | LEV structure at $t^* = 3.300$, $\alpha = 45.00$ deg, predicted by UVLM | 103 |
| 9.4 | Comparison of LEV structure of CFD (left) and UVLM (right) for case 10. | 104 |
| 9.5 | Interaction of LEV and tip vortex, $t^* = 2.145$, $\alpha = 39.10$ deg. | 105 |
| 9.6 | Time variation of development of LEV structure (case 1). | 106 |
| 9.7 | Result of aerodynamic loads for case 1 (baseline) | 107 |
| 9.8 | Comparison of $LESP_{max}(t)$ for case 1. | 107 |
| 9.9 | Comparison of circulation strength for case Ex 1. | 108 |
| 9.10 | Snapshots of three-dimensional amalgamation method | 109 |

Chapter 1

Executive Summary

The aim of this research effort was to extend earlier work on two-dimensional airfoils undergoing high-intensity unsteady motions dominated by leading-edge vortex (LEV) shedding to finite-wing geometries. In the earlier work (supported by AFOSR grant FA9550-10-1-0120, PIs: Gopalaram, Edwards, and Ol, PM: Dr. Douglas Smith), an integrated theoretical, computational, and experimental research effort was used, in which experiments and higher-order computations were used to develop a low-order method for unsteady aerodynamic analysis of airfoils and plates undergoing large-amplitude, high-rate motions. Owing to the fact that such flows are dominated by LEV shedding and flow separation, they are well outside the validity of classical theoretical methods.

The major contribution from the earlier research effort was in identifying the importance of leading-edge suction in governing the initiation, formation, and termination of vortex shedding from rounded leading edges of unsteady airfoils in two-dimensional flow. It was shown that the value of this leading-edge suction at any time instant in unsteady flow could be tracked in an unsteady thin airfoil theory using an inviscid parameter which was named the Leading-Edge Suction Parameter, or LESP. When the instantaneous LESP exceeds a critical value, LEV shedding occurs. One of the major insights from that research effort was that the critical LESP is dependent only on the airfoil and Reynolds number, and is largely independent of motion kinematics so long as the LEV formation is not preceded by significant trailing-edge separation. Typically, LEV formation without accompanying trailing-edge separation occurs in high-rate and high-reduced-frequency motions. Thus, for this class of motions, the critical LESP for a given airfoil and Reynolds number can be determined from CFD or experiment for one prototypical motion, and can then be used for *any* other high-rate motion, including arbitrary combinations of pitch, plunge, and surge. This insight was used to augment an inviscid unsteady thin airfoil theory¹ with the addition of a discrete-vortex method to handle intermittent LEV shedding. The resulting method, named the LESP-modulated discrete vortex method, or LDVM, is described in detail in Ramesh *et al.*² The results from LDVM show remarkably good agreement in forces and flow fields with computational fluid dynamics (CFD) and experiments. The advantage of the rapid computational capability offered by a low-order method like the LDVM was illustrated in the prediction of non-linear aeroelastic behavior of airfoils having LEV shedding. As described in Ramesh *et al.*,³ such aeroelastic analysis requires computation for at least 1,000 convective times to establish the long-time aeroelastic behavior, which would be prohibitive with any high-order CFD-like method.

Motivated by the success of the two-dimensional-flow work, the research in the current effort was aimed at extending a three-dimensional inviscid analysis method to handle vortex shedding from

rounded leading edges of finite wings. Systematic studies of finite wings with LEV shedding were analyzed using an incompressible Reynolds-Averaged Navier Stokes (RANS) CFD method, the results of which were used for the development of the low-order method. At the foundation of the low-order finite-wing analysis method is a traditional unsteady vortex lattice method (UVLM). In the first part of the current work, the objective was to assess the applicability of the LESP concept to prediction of the time instant and spanwise location of LEV *initiation* on a finite wing undergoing unsteady motion. The UVLM was used to calculate the spanwise variation of *LESP* at every time step. LEV initiation, from low-order prediction, is assumed to occur at the time instant and spanwise location when the local value of *LESP* equals the two-dimensional value of critical *LESP*. Comparison of the low-order prediction of LEV initiation for a large number of wing planforms with CFD predictions is excellent, confirming that the flow physics governing LEV initiation in finite wings is the same as that for airfoils. Further, the critical value of LESP obtained for two-dimensional airfoil flow for one “high-rate” motion can be used for prediction of LEV initiation on any finite-wing geometry undergoing any other “high-rate” motion. Discrepancies between the low- and high-order prediction of LEV initiation were seen in very low-aspect-ratio wing ($AR = 2$), for which the rolled-up shed vorticity from the wing tip has a significant influence on the wing flow. Since the UVLM does not model the tip-vortex roll up, there is a noticeable discrepancy for the $AR = 2$ geometry.

The second part of the research focused on modifying the UVLM to handle LEV *formation*. In this modified UVLM, a vortex sheet from the leading edge is modeled, and its geometry is calculated in each time step by assuming that the corner points of the panels forming the sheet convect with the local velocity. The resulting self-induced roll up of the sheet is simulated, with the geometry agreeing reasonably well with CFD results. While the low-order prediction of LEV formation shows promise, significant challenges remain in the modeling of the sheet roll up and its intersection with the wing geometry. Discrete-vortex amalgamation techniques, studied as part of the current effort for 2D flows, shows some promise for reducing the number of vortex lattices in LEV sheets from finite wings. It is likely that some adaption of vortex amalgamation applied to vortex sheets from leading edges will allow for robust modeling for LEV shedding on finite wings.

Suggested future work includes (i) augmentation of the current UVLM formulation to include better modeling of tip-vortex shedding, (ii) development of a hybrid vortex-sheet / vortex-filament model for LEV shedding from finite wings, and (iii) extensions to the UVLM to handle LEV formation, growth, and detachment, allowing for modeling of intermittent LEV shedding.

Chapter 2

Introduction

Unsteady aerodynamic phenomena are prevalent in a large number of problems in modern aerospace engineering research. These include dynamic stall in wind turbines and helicopter rotors, and flapping-wing vehicle (micro-air vehicle) design. These problems are characterised by apparent-mass effects, flow separation and leading-edge vortex (LEV) formation and shedding. Unsteady flows with intermittent LEV formation are the focus of the current research. The LEV influences the flowfield tremendously, and is responsible for an enhancement in lift while it is present above the wing and also large nose-down pitching moments and flow separation over the entire airfoil when it convects either off the trailing edge or away from the airfoil.^{1,4} In examining past work to provide context to the current research, we first examine in Section 2.1 LEV-dominated two-dimensional airfoil flows first with special attention to low-order modeling using discrete-vortex approaches. Subsequently, in Section 2.2, we examine relevant literature for LEV-dominated finite-wing unsteady aerodynamics.

2.1 LEV-dominated airfoil flows

Methods of simulating the physics and effects of unsteady aerodynamic phenomena date back to Wagner⁵ and Theodorsen.⁶ The application of these theoretical methods is however limited by their assumptions such as attached flow, small amplitude motion and planar wake structure. For unsteady flows with vortex shedding such as those considered in the present study, experiments and high-fidelity computations have facilitated fundamental studies of the underlying phenomena. McGowan et al.,⁷ Ol et al.,⁸ Garmann & Visbal⁹ and Granlund et al.¹⁰ have analysed the forces and flowfields for such unsteady motions over a broad parameter space using both experimental and computational methods. Pitt Ford & Babinsky,¹¹ Baik et al.¹² and Rival et al.¹³ have studied leading edge vortices using experimental techniques. These methods are not suitable for the initial phases of aerodynamic/control design because of cost and time considerations. This has been the motivation of many researchers to construct low-order models for unsteady simulation of wings and airfoils.

Discrete-vortex methods have been successfully used in past decades to model unsteady separated flows. These methods are usually based on potential-flow theory, and the shear layers depicting separated flow are shed from the surface in the form of discrete vortices. Clements & Maull¹⁴ and Saffman & Baker¹⁵ have written detailed reviews on the historical development of the discrete-

vortex method. A review on more recent applications of vortex methods for flow simulation is given by Leonard.¹⁶ Sarpkaya,¹⁷ Clements,¹⁸ Kiya & Arie,¹⁹ amongst other researchers, have applied this category of methods successfully to model flow past inclined plates and bluff bodies. Katz²⁰ has developed a discrete-vortex method for separated flow past an airfoil, where the location of separation on the airfoil has to be prescribed using information from experiments or other means. More recently, low-order methods based on discrete vortices have been developed by Ansari et al.,²¹ Wang & Eldredge,²² Ramesh et al.² to model leading edge vortices in unsteady flows, with applications toward insect flight and MAV aerodynamics. Though these methods are based on potential theory, they capture the essential physics in flows of interest by combining inviscid theory with discrete-vortex shedding. Apart from providing a means to calculate the force coefficients on the airfoil, these methods also enable the study of flow features. These are significant advantages of this class of methods over semi-empirical methods, which only allow determination of the force coefficients through empirical fitting.

Many of the methods cited above assume some *ad-hoc* start and stop criteria for discrete-vortex shedding, such as continuous shedding from a given location (valid only for sharp edges) or shedding that starts and stops depending on whether the local angle of attack exceeds a critical value (valid only for a small range of motions). A more general vortex shedding criterion is required to make discrete-vortex methods broadly applicable to a wide range of geometries (including airfoils with rounded leading edges) and arbitrary unsteady motions. Ramesh et al.² have developed a discrete-vortex aerodynamic method to model unsteady flows with intermittent LEV shedding using a leading-edge suction parameter (LESP). The unique aspect of this method (LESP-modulated discrete vortex method, or, LDVM) is that vortex shedding is turned on or off at the leading edge using a criticality condition. This method is, therefore, ideally suited to modeling oscillatory airfoil flows in which intermittent LEV shedding is a key feature. In comparison with semi-empirical methods in which several parameters are typically used, for a given airfoil and a given Reynolds number, this model uses only a single empirical constant, the critical LESP, and is a highly physics-based approach.

LDVM has been shown to be successful in predicting forces and moments on the airfoil, as well as flow field around the airfoil for high-frequency unsteady maneuvers. However, it is necessary to track a significant number of discrete vortices in order to obtain the instantaneous forces and moments on the airfoil. The computational complexity increases as $\mathcal{O}(n^2)$ (when fast summation methods are not used), where n is the number of vortices in the flowfield, resulting in possibly large computing times. The computational time of any discrete vortex model can be significantly decreased by reducing the number of discrete vortices. The current study focuses on obtaining a model with a reduced number of leading edge vortices, thus improving the computation time.

The popular Brown-Michael model²³ was one of the earliest efforts towards modeling the leading edge vorticity using reduced number of vortices. Specifically, the Brown-Michael model used a single vortex with time-varying strength to represent the vorticity shed from a delta wing. Wang and Eldredge²² recently improved on this model to derive analytic expressions for the evolution of single vortices using impulse matching for a flat plate. Howe²⁴ has presented a generalized correction for the Brown-Michael model, and uses the model to study the effect of the translating vortex of time-varying strength on a rigid half-plane. One vortex with time-varying strength models the leading edge vorticity, while another similar vortex is used to represent the trailing edge vorticity. Cortelezzi and Leonard²⁵ used a single vortex with time-dependent strength to model the shear-layer roll up of a semi-infinite plate. This model was further revised to accommodate a shear layer feeding vorticity into a growing vortex.²⁶ Some of these models use an unsteady Kutta condition

at the leading edge to find the strength of the single vortex that models the LEV.

Several experimental studies have been conducted by various researchers to understand the evolution of the leading-edge-vortex structure. The shear layer emanating from the leading edge starts rolling up into a concentrated vortex. Vorticity is fed into this concentrated vortex structure by the shear layer, and it grows in strength. In case of prolonged vorticity shedding, the leading edge vortex pinches off from the shear layer, and is convected downstream. Meanwhile, a new vortex roll-up is initiated near the leading edge.^{13,27,28} Antonini et al.²⁹ use semi-empirical data to model the expanse of the time-varying vortex core.

Several articles can be found in the literature that address the merging of discrete vortices to reduce the count of discrete vortices in the flow field.^{17,30,31} For example, Nair and Taira³² give a network theoretic approach to identify important vortex-vortex interactions, and obtain a sparsified model that accurately predicts the dynamics of the original system based on these interactions. The conditions used for merging are based on closeness, relative velocity etc. between vortex pairs.

2.2 LEV-dominated finite-wing flows

Vortex shedding from the leading edges of wings and rotor blades have been observed in nature—on swimming and flying animals and seeds,^{33–36} and in engineering—on rotorcraft,³⁷ wind turbines,³⁸ swept and delta wings,^{39,40} and micro-air vehicles⁴¹ and flapping-wing energy-harvesting devices.^{42,43} Extensive investigation of leading-edge vortex (LEV) formation and shedding from airfoils in two-dimensional flow have revealed the connection between the onset of LEV formation and flow separation at the leading edge or leading-edge stall, and their dependence on leading-edge radius,^{37,44} Reynolds number,^{37,44,45} and unsteady motion kinematics of the airfoil.^{10,46,47} Numerous computational and experimental studies have shown the effects of the LEV growth, position, and detachment on the forces and moments experienced by the airfoil.^{47–49} The restriction to two-dimensional flow also enables the use of low-order discrete-vortex methods for modelling the airfoil LEV formation and its effects.^{50,51} In contrast, LEV formation, shedding, growth, and their effects on finite wings are considerably more complicated by the presence of spanwise velocities and pressure gradients, interaction with root and tip vortex structures, and the interplay between vorticity production and spanwise/chordwise advection.^{52,53} On some geometries like the highly-swept leading edges of delta wings, vorticity production at the leading edges is balanced by spanwise vorticity transport, leading to body-relative stable or stationary vortex structures, which can be harnessed for lift enhancement at high angles of attack and extra maneuverability.⁵⁴ The effects of these LEV flows are also amenable to simple and elegant theories such as the Polhamus leading-edge suction analogy.^{55,56}

On other configurations like unswept wings, the absence of mechanisms for spanwise transport of shed leading-edge vorticity appears to be the cause for non-uniform shedding and chordwise advection, leading to interesting and important flow structures like the omega-shaped (or horse-shoe-shaped) vortical structures that have been observed in experiments and computations.^{57–59} Further complicating the three-dimensional situation are the rotational effects on these phenomena on rotor blades and flapping wings.⁶⁰ It may be argued that the first step in unravelling the flow physics of finite-wing LEVs is the *initiation* of LEV formation: for any given wing and motion kinematic, at what time or angle of attack (AoA) and where along the span does the LEV start forming? The initial portion of this research was focussed on answering this specific question. Building on an earlier work on initiation of LEV formation on rounded-leading-edge airfoils,² and

using results from three-dimensional CFD computations for a large number of finite wings, it is shown that criticality of leading-edge suction, which governs LEV formation on airfoils, can also be reliably used to predict the initiation of LEV formation on finite wings in low-Mach number flows.

2.3 Layout of this report

Computational (CFD) and experimental studies have been used to guide the development of the low-order methods developed in the current research. Chapter 3 presents the CFD methods and Chapter 4 provides a description of the experimental facility and techniques. In Chapter 5, we present a detailed study of LEV initiation in airfoil flows, with emphasis on determining the range of validity of the LESP concept. It is shown that, so long as LEV formation is not preceded by significant trailing-edge flow reversal, the LESP concept holds. This condition is satisfied for high-rate motions. Chapter 6 presents research into amalgamation of discrete vortices in 2D airfoil flows in an attempt to reduce computational time. Ideas learned from this study were subsequently used in amalgamation of vortex lattices in finite-wing LEV sheets (Chapter 9). The main focus of the current effort is on low-order prediction of LEV-dominated finite-wing flows. Chapter 7 presents the unsteady vortex lattice method (UVLM), which forms the foundation for the finite-wing research. Also discussed are the modifications to the UVLM for modeling LEV vortex sheets.

The criterion to identify rollup in the model presented in the current work is based on angular velocity between vortex pairs at the tip of the shear layer. Additionally, a discrete vortex is merged with the growing vortex based on its closeness, relative and angular velocities with respect to the growing LEV. Chapter 8 presents the results on LEV initiation on finite wings, including comparison between low-order and CFD predictions. Chapter 9 presents results from the modified UVLM on prediction of LEV formation on finite wings. The report then wraps up with conclusions and suggestions for future work in Chapter 10.

Chapter 3

Computational Fluid Dynamics Methods

In this effort, the computational fluid dynamics (CFD) portion of the research had two objectives. The first objective was to provide high-order results from CFD simulations using “state-of-the-practise” Reynolds-Averaged Navier-Stokes (RANS) simulations and Spalart-Allmaras (SA) turbulence model to guide the development of the low-order method and provide validation data. Section 3.1 provides a brief description of this portion of the CFD effort. The second objective of the CFD effort was to develop improved capability via the development of a hybrid large-eddy simulation / Reynolds-averaged Navier-Stokes method suitable for 3D simulations on moving meshes. Progress on this portion of the CFD effort is described in Section 3.4. A version of this method includes the Menter-Langtry transition model. This new capability is expected to be useful for exploring the effects of transitional boundary layers on the formation of LEVs and improved predictions of LEV-dominated flows.

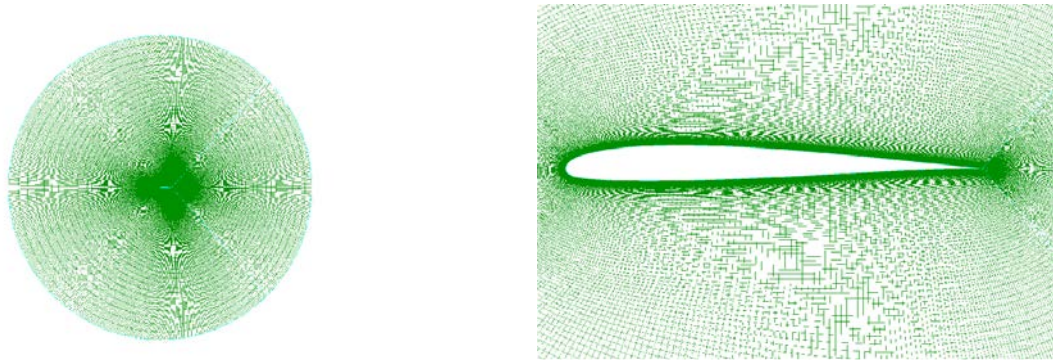


Figure 3.1: Body-fitted mesh used in computations.

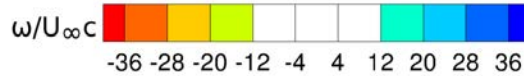


Figure 3.2: Vorticity scale for all CFD vorticity plots in this report.

3.1 RANS CFD for supporting the development of the low-order methods

CFD calculations using a body fitted grid were performed using NCSU’s REACTMB-INS code, which solves the time-dependent incompressible Navier-Stokes equations using a finite-volume method. The governing equations are written in arbitrary Lagrangian / Eulerian (ALE) form, which enables simulations of the flow’s response to the motion of a body-fitted computational mesh in accord with prescribed rate laws. Spatial discretization of the inviscid fluxes uses a low-diffusion flux-splitting method valid in the incompressible limit.⁶¹ This method is extended to higher-order spatial accuracy using TVD interpolations of the primitive variables $[p, u, v, w, \tilde{v}]^T$. Viscous terms are discretized using second-order central differences. A dual-time stepping method is used to integrate the equations in time. An artificial compressibility technique, discretized in a fully implicit fashion and solved approximately using ILU decomposition, is used to advance the solution in pseudo-time. Typically, eight sub-iterations per physical time step were need to reduce the residual errors two orders of magnitude. The Spalart-Allmaras model⁶² as implemented by Edwards and Chandra,⁶³ is used for turbulence closure. The computations were performed on a 2-D body-fitted mesh containing 92400 cells (Figure 3.1).

3.2 Identification of LEV formation from CFD

The surface skin friction (C_f) distributions from CFD provide a quantitative method of identifying the onset of LEV formation. Formation of LEV is preceded by the formation of a small region of reversed flow with negative, or counter-clockwise, vorticity at the surface near the leading edge of the airfoil. Onset of LEV shedding is subsequently initiated by the formation of a shear layer at the leading edge and this is accompanied by the development of a small region of positive, or clockwise, surface vorticity within the region of negative vorticity described earlier. Thus the formation of alternating negative and positive vorticity near the leading edge is a useful signature which we will use to determine the exact instant when LEV formation begins. Since the process of identifying onset of LEV formation visually using the vorticity plots is qualitative, we translate the same criterion to the skin friction coefficient. The formation of a negative vorticity region at the surface near the leading edge is indicated by a negative skin-friction coefficient near the leading edge. The formation of the positive vorticity region at the surface, which accompanies the development of the shear layer, can be identified by alternating positive and negative spikes in the skin-friction coefficient. Using the vorticity scale shown in Fig. 3.2, Fig. 3.3 shows a series of vorticity and skin-friction coefficient plots for an airfoil experiencing LEV formation.

In Figure 3.3, the vorticity and the skin-friction coefficient plots at the leading edge (from $x/c = 0$ to $x/c = 2\%$) are shown during four instants for an airfoil undergoing LEV formation. The flow behavior at instants (a) through (d) in the figure is described as follows:

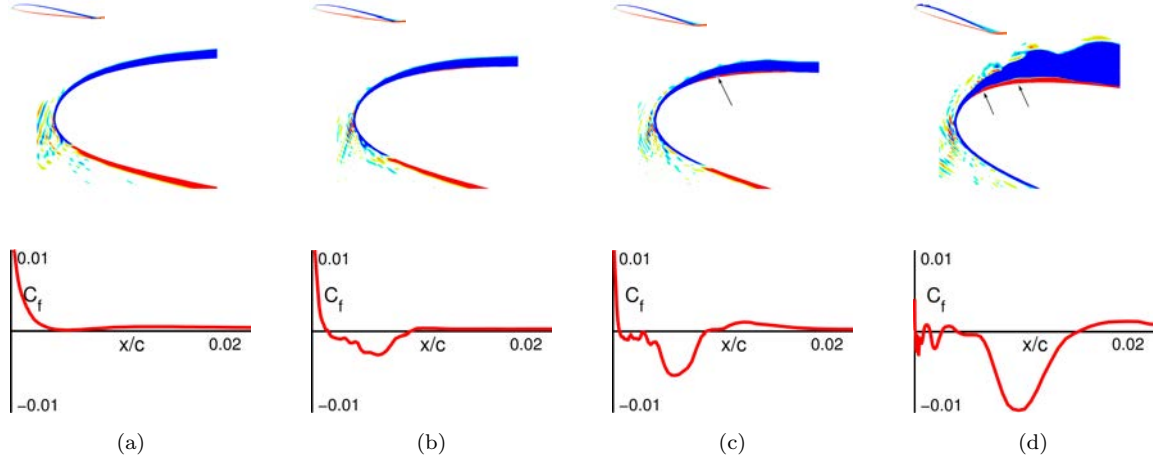


Figure 3.3: Vorticity and skin friction coefficient plots from CFD during the LEV formation process. Appearance of positive vorticity region is circled.

- (a) The flow is attached at the leading edge.
- (b) The boundary layer is still attached. However, there is a region of reversed flow near the leading edge, reflected in both the vorticity and the skin-friction coefficient plots.
- (c) Start of formation of the shear layer: A small region of positive vorticity starts developing at the surface within the negative vorticity region at the leading edge. This behavior also corresponds to the first occurrence of a small region of positive C_f within the region of negative C_f . In the C_f plot, the formation of spikes reaching up to zero and positive values in the region of negative C_f near the leading edge is seen. We use this signature in the C_f to quantitatively identify the time instant corresponding to the start of LEV formation in all results from CFD. This identification is done by post-processing the CFD results.
- (d) Shear layer is well established and LEV shedding is in progress.

3.3 RANS analysis of LEV formation on finite wings and comparison to experiment

NCSU’s REACTMB-INS solver is used for the computational fluid dynamics (CFD) calculations performed in this study. This finite-volume solver formulates the time-dependent incompressible Navier-Stokes equations in an arbitrary Lagrangian/Eulerian (ALE) fashion. The ALE form enables moving-mesh flow simulations on the 3-D body-fitted computational mesh. An incompressible version of Edwards’ Low-Diffusion Flux Splitting Scheme (LDFSS)⁶¹ is used for discretizing inviscid fluxes in space. Discretization of viscous terms is performed using a second-order central difference method. The LDFSS method is extended to higher order of accuracy in space using the Piecewise-Parabolic Method (PPM).⁶⁴ For time integration, second-order temporal accuracy is achieved by using an implicit artificial compressibility method⁶¹ with subiterations at each physical time step for continuity equation convergence. A version of Spalart-Allmaras one equation eddy viscosity model, modified by Edwards and Chandra,⁶³ is used for turbulence closure.

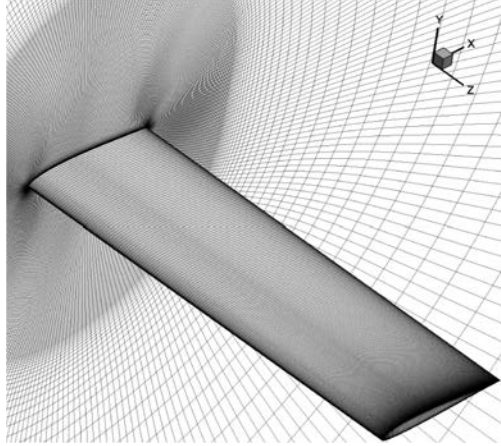


Figure 3.4: Representative mesh distribution for CFD analysis.

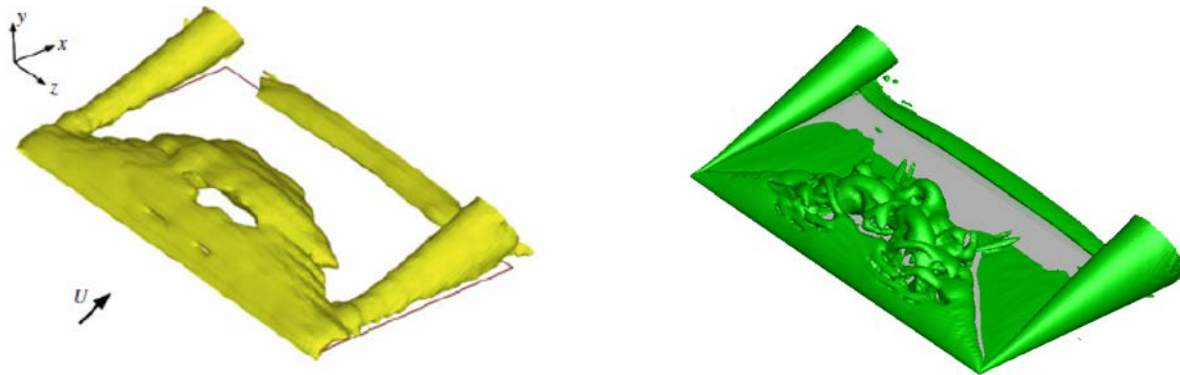
Figure 3.4 shows the mesh distribution of a rectangular half-wing used for the finite-wing calculations in the current work. The chord length is 0.1 meters. The O-type mesh has 164 cells chord-wise, with finer resolution near the leading edge and trailing edge. The span-wise average spacing on the airfoil is chord/100, with finer resolution near the tip of the wing. The span-wise calculation domain extends 2 chord lengths beyond the tip of the wing, with an average spacing of chord/40 in this region. In the wall-normal direction, cell spacing starts as 5×10^{-5} meters next to the wall, and has a growth factor of 1.15 moving away from the surface until the spacing reaches chord/100. From there, cell spacing is kept nearly uniform of chord/100 up to 1.3 chord from the surface. Then coarser meshes with a growth factor of 1.15 extend to 12 chord lengths away from the wing surface. Only the rectangular wing with an aspect ratio of 6 is shown here, but the general guidelines above are applied to meshes of all other wing geometries considered in this study.

The CFD model is validated by comparing the flow solution with the PIV results from the experimental study of Yilmaz and Rockwell⁵⁹ for a rectangular flat plate with an aspect ratio of 2 undergoing a 0-to-45-degree pitch-up motion. Figure 3.5 compares predicted iso-surfaces of the second-invariant of the velocity gradient tensor ($Q=5$) with experimental images obtained from the PIV database. Side views of the 3D streamline patterns at five instances in time are shown in Figure 3.6. Compared with experimental data, the streamline patterns from CFD simulation show the same stage of development of the LEV at each time instance. Overall, the CFD results compare well with the PIV results, giving confidence in the utility of the CFD technique for the present work.

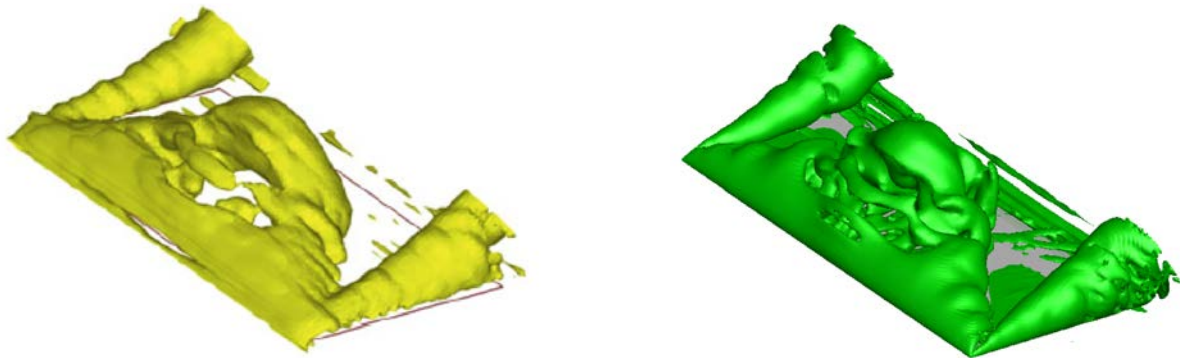
3.4 LES/RANS Modeling Activities

3.4.1 Model Formulation

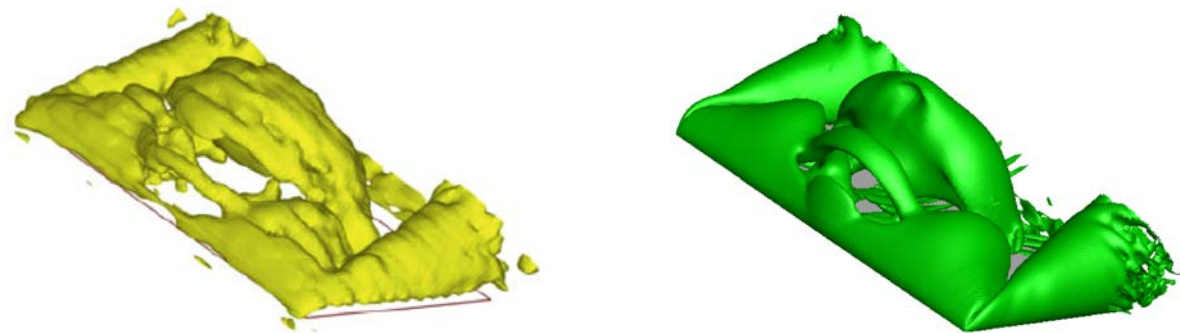
As some three-dimensional calculations were planned for this work, efforts were directed toward developing a hybrid large-eddy simulation / Reynolds-averaged Navier-Stokes method suitable for 3D simulations on moving meshes. In the present study, the transition between a RANS component (used very near solid surfaces) and the LES component (used in the outer parts of developing turbulent boundary layers and in free shear layers) is facilitated by the action of a flow-dependent



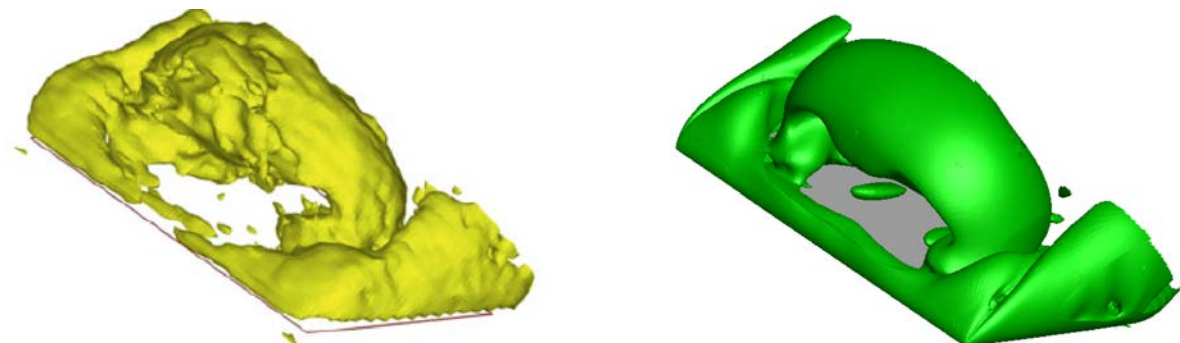
$\alpha = 27 \text{ deg}, t^* = 2.4$



$\alpha = 36 \text{ deg}, t^* = 3.2$



$\alpha = 45 \text{ deg}, t^* = 4.0$



$\alpha = 45 \text{ deg}, t^* = 5.6$

Figure 3.5: Volumes of iso-Q as a function of angle of attack. Left: PIV experiment. Right: CFD simulation.

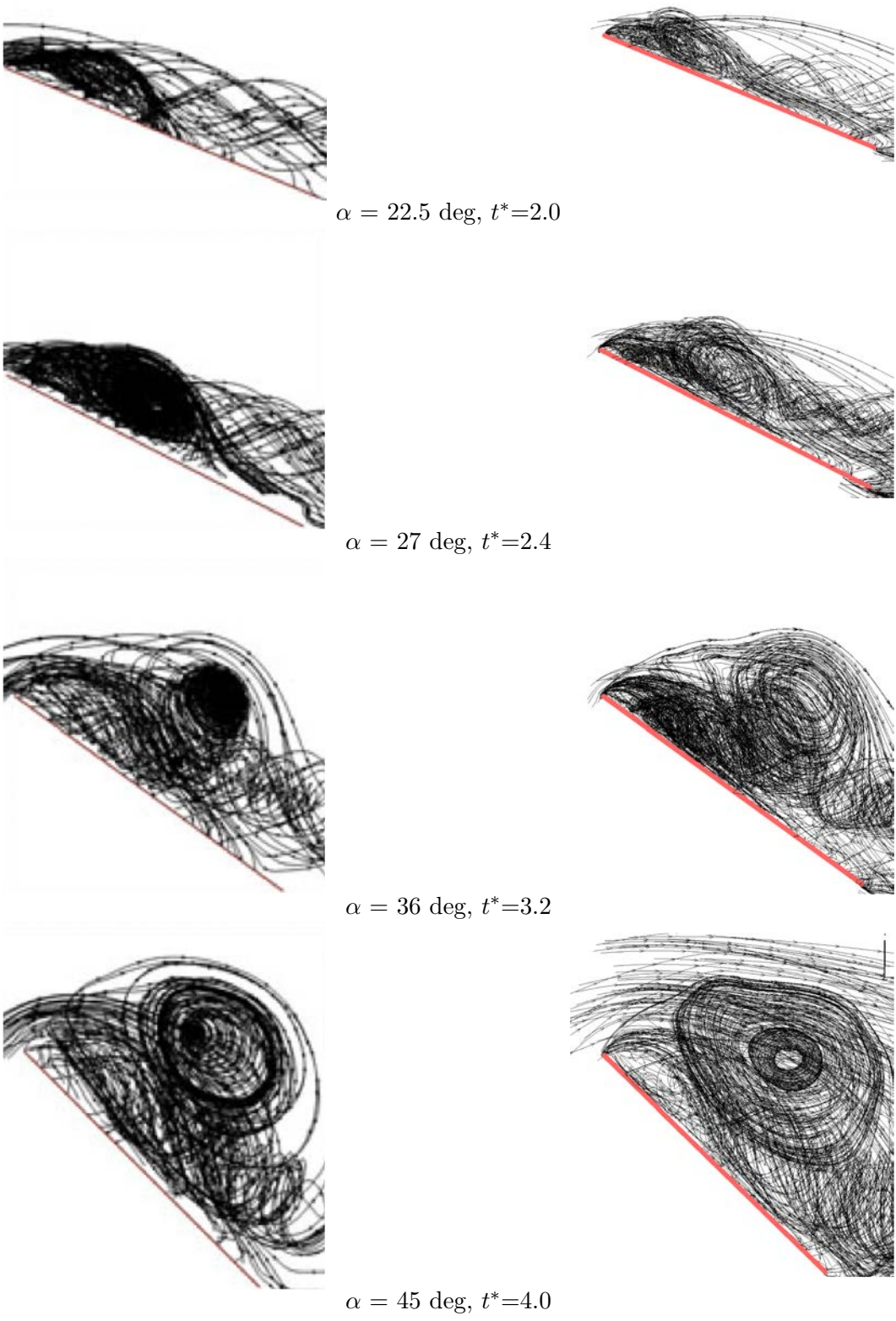


Figure 3.6: Side views of three-dimensional streamline patterns as a function of angle of attack. Left: PIV experiment. Right: CFD simulation.

blending function, which modifies the eddy viscosity field as follows:

$$\mu_f = \rho \left[(1 - \Gamma)\nu_{t,sgs} + \Gamma \frac{k}{\omega} \right] \quad (1)$$

where Γ is a time-dependent blending function that connects the RANS and LES branches. A model due to Lenormand, et al.⁶⁵ is currently used for the subgrid-scale eddy viscosity. The blending function is generally designed to transition the model from RANS to LES approximately as the boundary layer shifts from its logarithmic to its wake-like structure. As such, the RANS component acts as a wall-layer model for the majority of the flow, which is modeled as a large-eddy simulation. The most recent model^{66,67} introduces an outer-layer turbulence length scale into the argument for Γ as a means of removing a calibration procedure required in an earlier version.⁶⁸

$$\Gamma = \frac{1}{2} \left(1 - \tanh \left[15 \left(\frac{1}{\lambda_N^2} - 1 \right) \right] \right) \quad (2)$$

where,

$$\lambda_N = \frac{l_{outer}}{l_{inner}} = C_N \sqrt{\frac{10\nu\bar{\omega} + \bar{k} + \bar{k}_R}{c_\mu^{\frac{1}{2}}\bar{\omega}\omega}} \frac{1}{\kappa d} = C_N \sqrt{10 + \frac{\bar{k} + \bar{k}_R}{\nu\bar{\omega}}} \frac{\nu}{c_\mu^{\frac{1}{4}}\kappa d\sqrt{\omega}} \quad (3)$$

In this expression, \bar{k} is the ensemble-averaged modeled turbulence kinetic energy, \bar{k}_R is the ensemble-averaged resolved turbulence kinetic energy, ω and $\bar{\omega}$ are instantaneous and ensemble-averaged modeled turbulence frequencies, and d is the distance to the nearest wall. The combination of instantaneous and ensemble-averaged data allows the RANS-to-LES transition position $\Gamma = 1/2$ to fluctuate about a mean value that is a function of the local, ensemble-averaged state of the flow. As it is dependent on both inner-layer and outer-layer turbulence length scale information, this model is more capable of adjusting to departures from local equilibrium, and a problem-specific selection of a model constant is not required. The required ensemble averages are currently computed using an exponentially-weighted moving average.

Also tested in this study is an earlier LES/RANS model developed by Choi, et al.⁶⁸ This model differs from the above in that a pre-calibration is needed to calculate a model constant that multiplies $\frac{\sqrt{\nu}}{c_\mu^{\frac{1}{4}}\kappa d\sqrt{\omega}}$ in Eq. 3. This model constant is related to the wall-coordinate distance in which an attached boundary layer transitions from its logarithmic structure to its wake-like structure, and it can be computed as a function of surface distance based on knowledge of the boundary layer thickness and edge conditions.⁶⁸ In addition, a version of REACTMB that couples the LES/RANS formulation of Eq. 3 with the Menter-Langtry transition model⁶⁹ was developed. This model requires the solution of two additional transport equations, one associated with a Reynolds number based on momentum thickness and the other associated with turbulent intermittency. As the Menter-Langtry model only alters the RANS component of the LES/RANS model, the coupling was straightforward and is not described further in this report.

3.4.2 Aérospatiale A-Airfoil

The LES/RANS models described above were used to simulate turbulent flow over an Aérospatiale A-Airfoil near static stall. The free-stream Mach number is 0.15, the Reynolds number based on a chord length of 0.6m is 2.1×10^6 , and the angle of attack is 13.3 degrees. An X-Y snapshot of the computational mesh, which contains approximately 30×10^6 cells, is shown in Figure 3.7. An iso-surface of swirl strength, illustrating the formation of large turbulent eddies on the suction side of the airfoil, is illustrated in Figure 3.8. Extensive flow measurements, including skin friction, surface pressure distributions and velocity and Reynolds-stress profiles obtained using laser Doppler velocimetry measurements are available for comparison.⁷⁰ Wall-resolved large-eddy simulations of this case were conducted by Mary and Sagaut.⁷¹ Other studies include direct numerical simulations of Alam and Sandham⁷² and recent simulations using a LES/RANS formulation with wall modeling from Kawai and Asada.⁷³

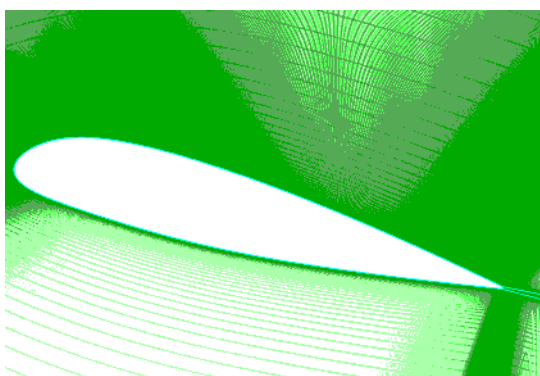


Figure 3.7: X-Y centerplane mesh for A-airfoil.

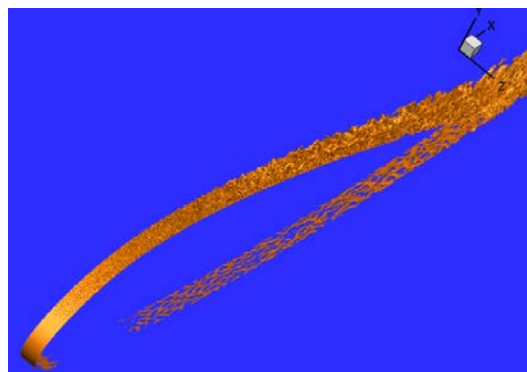


Figure 3.8: Iso-surfaces of swirl strength (2000 s^{-1}) illustrating development of eddy structures in airfoil boundary layer.

Figure 3.9 presents skin-friction and surface pressure results for the three hybrid LES/RANS models tested the model of Choi, et al.⁶⁸ which requires pre-calculation of a model constant, the model of Gieseking, et al.,^{66,67} and Gieseking's model equipped with the Menter-Langtry transition model. Choi's and Gieseking's models under-predict the skin friction, whereas Menter-Langtry transition model under-predicts skin-friction on the front part of the airfoil and over-predicts it on the back part of the airfoil. A large region of laminar flow is not present for either the Choi or Gieseking models but both show indications of a 'numerical' transition region. The use of the Menter-Langtry transition model leads to a large laminar region terminated by a laminar separation bubble. Choi's and Gieseking's models successfully predict the pressure plateau near the trailing edge shown in the experimental data, but Menter's SST with transition model fails to do so. In the leading edge region, the predictions provided by Gieseking's model with Menter-Langtry are in better agreement with the experimental pressure coefficient data than those of Choi's or Gieseking's models.

Figure 3.10 shows a comparison of mean streamwise (tangential) velocity profiles with experimental measurements at various axial stations. The profiles are expressed in a wall-normal coordinate system. Choi's model provides the best predictions of the velocity field, with Gieseking's model slightly under-predicting the level of trailing-edge separation. The use of the Menter-Langtry model promotes flow attachment to the surface near the trailing edge.

Streamwise velocity fluctuation profiles obtained by the hybrid LES/RANS models are shown in

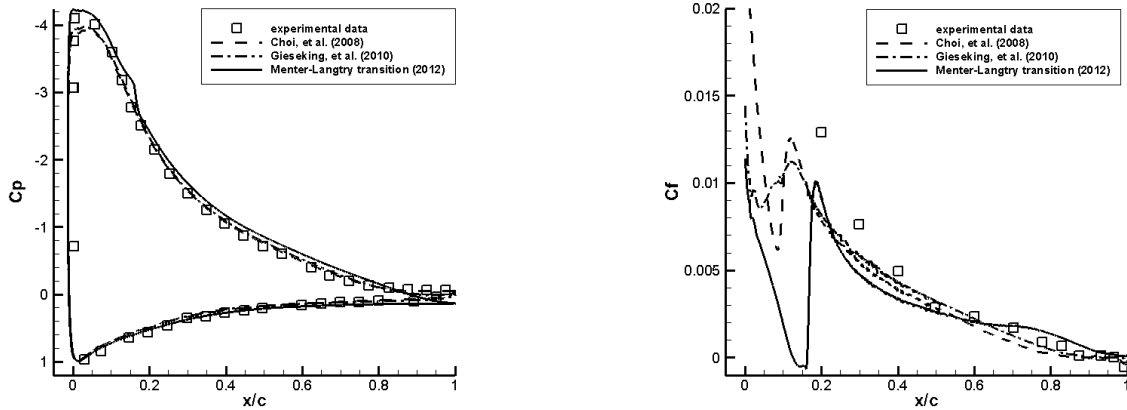


Figure 3.9: Mean pressure coefficient (left) and skin friction coefficient (right) distribution along the airfoil obtained by hybrid LES/RANS computation compared with experimental measurement.

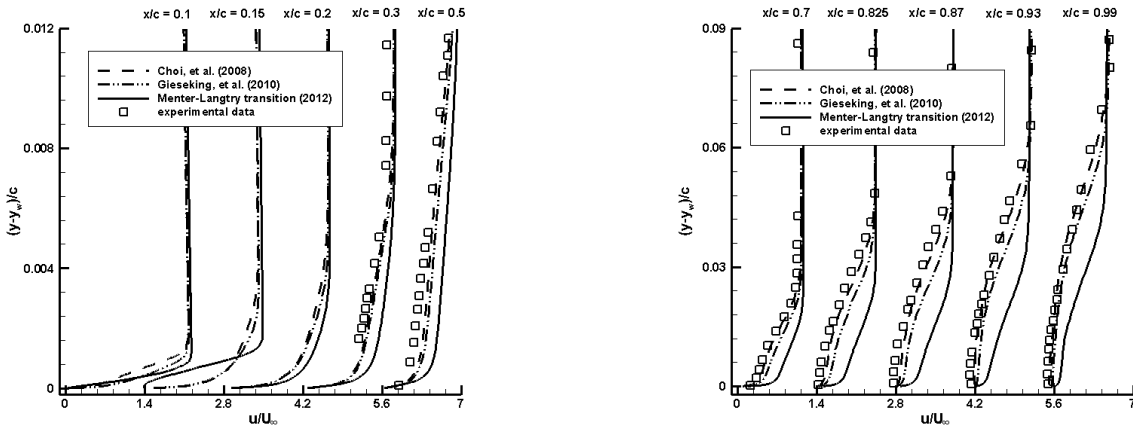


Figure 3.10: Mean streamwise velocity profile as a function of normalized wall-normal distance obtained by hybrid LES/RANS computation; individual profiles are separated by a horizontal profile of 1.4.

Figure 3.11. In the hybrid RANS/LES computations, from $x/c = 0.1$ to 0.15 , the rms streamwise velocity fluctuations are much smaller within the boundary layer when the transition model is included. This is because in this region near leading edge, the flow remains laminar, whereas the flow has already transitioned and has become turbulent in the solutions obtained using Choi's and Gieseking's LES/RANS models. From $x/c = 0.3$ to 0.5 , the effect of including the transition model is to enhance the near-surface axial velocity fluctuation intensity, relative to the other LES/RANS models. This likely contributes to the under-prediction of trailing-edge separation mentioned earlier. From $x/c = 0.7$ to 0.99 , all models again under-predict the rms streamwise velocity. Results from Choi's model are in better agreement with the experimental data than those from Gieseking's model, whereas Gieseking's model with Menter-Langtry transition leads to a thinner boundary layer. This is not surprising, because from the previous mean streamwise velocity analysis, we know that the flow remains attached within the trailing edge region when the transition model is

included.

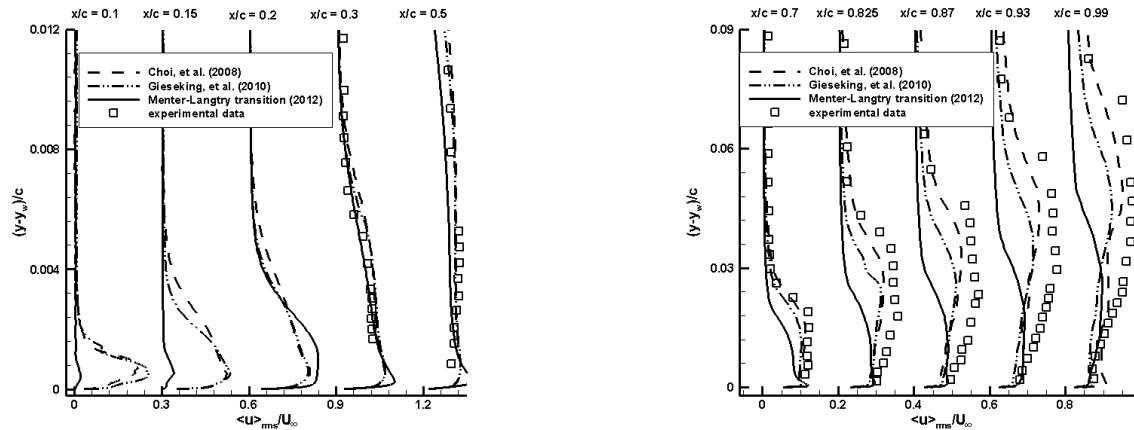


Figure 3.11: Profile of the rms streamwise velocity fluctuations obtained by a hybrid LES/RANS computation; individual profiles are separated by a horizontal profile of 0.3 (left) and 0.2 (right).

The rms wall-normal fluctuation velocity profiles obtained by the hybrid RANS/LES models are shown in Figure 3.12. Trends exhibited in the LES/RANS calculations of the wall-normal velocity fluctuation generally mirror those discussed for the axial velocity fluctuation. Fluctuation growth is suppressed, as expected, near the leading edge when the transition model is used. Further downstream, agreement with experiment is good for both Choi’s and Gieseking’s LES/RANS models. Fluctuation levels in the near wall region are similar among all models, and again, the LES/RANS models provide some improvement in predictive capability, relative to the RANS models.

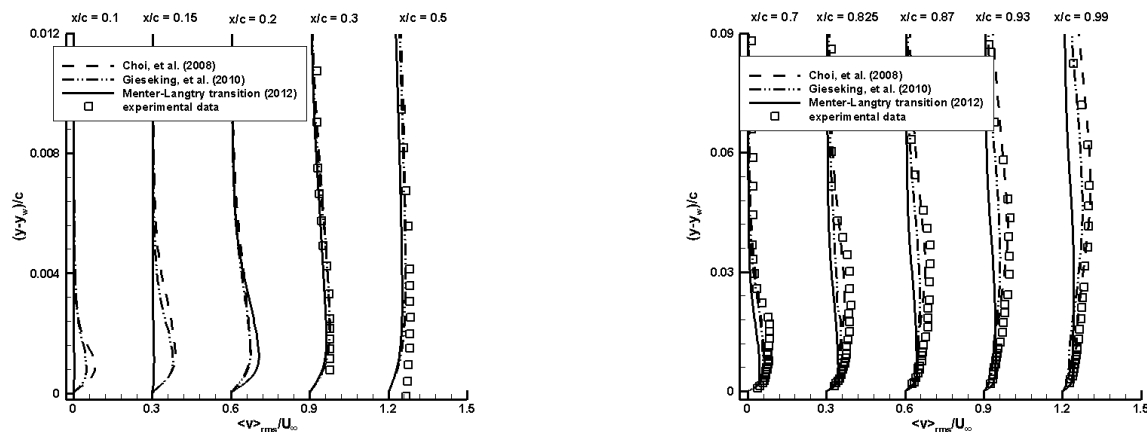


Figure 3.12: Profile of the rms wall-normal velocity fluctuations obtained by a hybrid LES/RANS computation; individual profiles are separated by a horizontal profile of 0.3.

Similar trends are in evidence for the Reynolds shear stress profiles, as shown in Figure 3.13. Here, the normalizing factor is the square of the velocity, which tends to minimize differences among the models. Interesting, the use of the transition model provides the best predictions of the Reynolds shear stress for stations up to $x/c = 0.5$. Further downstream, the predictions are similar to the other fluctuating quantities in that the level of fluctuation intensity in the outer part of the

separated shear layer is less than indicated in the experiment. Agreement with experiment improves nearer to the wall for all models.

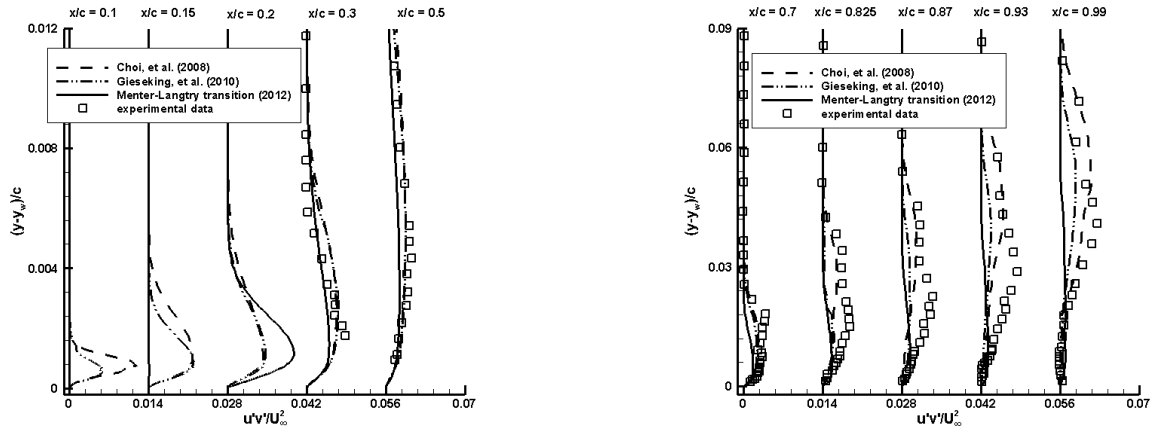


Figure 3.13: Profile of the Reynolds-averaged shear stress obtained by hybrid LES/RANS computation; individual profiles are separated by a horizontal profile of 0.014.

3.5 Interim Conclusions

The results from the computational investigations were critical for the systematic development of the low-order method in the current research effort. These results are presented in the following chapters.

Chapter 4

Experimental Facility and Techniques

The experimental investigations for the current integrated theoretical, computational, and experimental research effort were performed in the U.S. Air Force Research Laboratory's Horizontal Free-surface Water Tunnel. This chapter describes the facility and the techniques for force measurement and flow visualization.

4.1 Facility and Motion Mechanism

The U.S. Air Force Research Laboratory's Horizontal Free-surface Water Tunnel is fitted with a three degree of freedom electric motion rig enabling independent control of pitch or rotation, plunge or heave, and surge or streamwise-aligned translation. Photographs of the tunnel and the model installation are shown in Figure 4.1. More detail on the rig operation is given in Ol et al.⁸ and Granlund et al.,⁷⁴ while the facility is discussed in Ol et al.⁷⁵

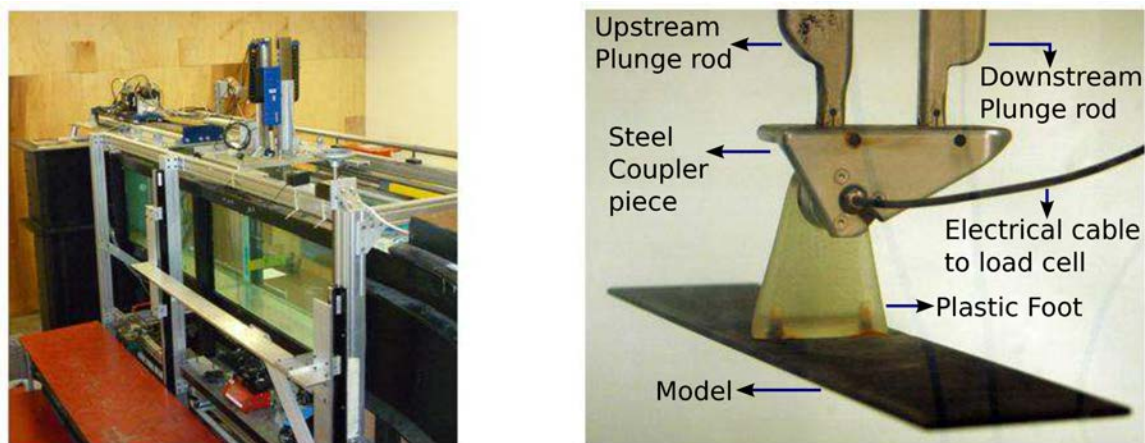


Figure 4.1: Test section and portion of motion rig mounted above test section of the AFRL Horizontal Free-surface Water Tunnel (left). $c = 3$ " flat plate with force balance mounted between steel coupler piece and plastic foot connecting to the plate (right). Dye injection is from a 0.5 mm diameter slot at the plate leading and trailing edges, $\frac{3}{4}$ spanwise location.

The motion rig consists of a triplet of H2W linear motors, driven by AMC DigiFlex servo-drives

controlled by a Galil DMC 4040 4-channel card, with user-selected proportional/integral/derivative (PID) constants for each motion channel. Because the mass of the linear motors and plunge-rods are much larger than the mass of test article and the expected hydrodynamic loads, the PID constants are selected for the rig to move itself, and become largely independent of the load. Generally PIDs suitable for good motion fidelity for high-acceleration motions result in noise for smoother, lower-acceleration motions, and as with all tuning, the final choice is a compromise.

The model's pitch and plunge are controlled via two motors mounted vertically on a plate above the tunnel test section, shown in the left portion of Figure 4.1. Each motor actuates a vertical plunge rod, which connects via a bushing to a coupler piece holding the force balance. The upstream plunge rod is constrained to move purely vertically, whereas the downstream plunge rod is allowed to pivot in the test section vertical plane of symmetry. The pitch pivot point can be varied by suitable choice of phase and amplitude difference in trajectory of front or rear plunge rod. For all cases where the pitch pivot point is not coincident with the bushed end of the front plunge rod, there will be a parasitic streamwise displacement of the plate, which would be unavoidable unless the front plunge rod were to be allowed to pivot similarly to the downstream one. This is removed using the third degree of freedom, surge, which also actuates the fore and aft translating motion of the model. Surge is achieved using a larger linear motor mounted horizontally aft of the pitch-plunge carriage, with 48" peak-to-peak stroke and nominal speed up to 1 m/s.

The desired theoretical pitch history of the plate is converted to position commands for each linear motor. Commanded vs. attained displacement histories of the three motors are compared by interrogating the three motors' optical encoder tapes, at 5000 increments/mm for the two vertical motors, and 1000 increments/mm for the streamwise motor. Peak discrepancy between commanded and attained position are 300 ± 100 increments, which converts to 0.15 deg peak error in incidence angle, if the two vertical motors displacement errors are in the worst-case scenario of anti-phase. However, this is the incidence-angle error at the force balance location, and does not account for vibration or elastic deflection of the plastic coupler piece between the force balance and the model. Manual interrogation of particle image velocimetry raw images in Ol et al.⁸ (not reported here) showing reflection of laser light from the plate suction-side implies an upper bound of incidence angle uncertainty of 0.2 deg.

4.2 Force Measurement

Force data are recorded from an ATI Nano-25 IP68 6-component integral loadcell, oriented with its cylindrical axis normal to the pitch-plunge-surge plane. It is capable of measuring forces in the plane of the airfoil cross-section up to ± 125 N and torque up to ± 3 Nm. The published resolution is 1/48 N for force and 1/2640 Nm for torque. The electrical cable that connects to the loadcell is visible in the right-side photo in Figure 4.1. Load cell strain gage electrical signals are A/D converted in an ATI NetBox interface and recorded over Ethernet LAN UDP protocol to a computer using a Java application. The time-base of the ATI NetBox is slightly inaccurate with the clock operating at a factor of 1.0023 too fast with respect to physical time. This is corrected for in post-processing of data. A disadvantage of the IP68 waterproofing of the loadcell is that it is sensitive to immersion depth in the cylindrical axis direction. Because this direction is normal to the plane of the motion of symmetrical models, the hydrostatic force will not affect either normal force, axial force or pitching moment. Force and motion data are synchronized by polling for the trigger signal every 10 ms and starting the data recording when initial trigger is detected. For

motions that start with no position change, such as the ramp motions, a streamwise $0.001c$ motion step is introduced before the actual ramp start in order to reliably synchronize force and motion data.

The force and moment signals are filtered in three steps. This first is a low-pass filter in the ATI NetBox at $f = 73Hz$, to avoid recording noise not correlated with motion force data, but without attenuating important fast non-circulatory load spikes. These are on the order of a fifth as slow as the $-3dB$ (half amplitude attenuation) point of the filter for the fastest pitch ramp corner acceleration. The second step uses a moving-average of 11 points to smooth the data while preserving as much of the non-circulatory load spikes as possible. This smoothing also makes a more numerically stable final step, which is a 4th order Chebychev II low-pass filter with $-20dB$ attenuation of the stopband. The cutoff frequency is five times the motion frequency and the motion frequency is calculated by taking the ramp motion as a quarter of a periodic motion. It is chosen for maximum passband flatness and high rejection of structural eigenfrequencies which may be just above the desired force frequency information range. To preclude time-shift of useful data in the passband, the forward-backward filtering technique with the Matlab `filtfilt` command is used.

All post-processing is done in Matlab. Before each run, the loadcell is zero-biased at model $\theta = 0$ deg, which is adjusted to horizontal with a bubble level. A static tare sweep over $0 \text{ deg} < \theta < 90 \text{ deg}$, is performed with 500 samples of data every 2 deg. Because the pitch angle is known throughout the motion, and the position error is negligible, the static axial force, normal force and pitching moment due to static model/sting/mount weight can be subtracted from the unsteady force data.

4.3 Flow Visualization

Flowfield visualization of the leading-edge vortex is limited to qualitative inferences from dye injection. In planar laser-induced fluorescence, a high concentration of Rhodamine 6G in water is injected by a positive-displacement medical infusion pump, connecting to a set of 0.5mm internal-diameter rigid lines glued to the surface of the plate, spanwise at the leading- and downstream at the trailing edge at the $\frac{3}{4}$ semispan location. The dye is illuminated by an Nd:YLF 527nm pulsed laser sheet of 2mm thickness at 50Hz and images are recorded with a PCO DiM x high-ed camera through a Nikon PC-E 45mm Micro lens. A Tiffen orange #21 filter is used to remove the incident and reflected laser light, leaving only dye fluorescence. For a larger spanwise visualization, a neutrally buoyant mixture of blue food color and ethanol is injected and backlight illuminated by a Rosco white LED panel. This method images the entire airfoil as well.

4.4 Interim Conclusions

The results from the experimental investigations were critical for the systematic development of the low-order method in the current research effort. These results are presented in Chapter 5.

Chapter 5

Factors Affecting LEV Initiation in Unsteady Airfoil Flows

In this chapter we present a detailed experimental, computational, and low-order study of LEV initiation in airfoil flows, with emphasis on determining the range of validity of the LESP concept. It is shown that, with the exception of slow-rate kinematics which result in significant trailing-edge flow separation, the LESP value for all other kinematics considered falls around a constant critical value. It is also shown that the LESP concept may be used to trigger on-demand or suppress the formation of LEVs by superimposing kinematics such that the required criteria on LESP are met.

5.1 Theoretical approach

This section describes the theoretical methods employed in this research, and the *LESP* hypothesis. The interested reader may refer to references 1 and 2 for greater detail.

5.1.1 Large-angle unsteady thin-airfoil theory

The large-angle unsteady thin-airfoil aims to eliminate the traditional small-angle assumptions in thin-airfoil theory which are invalid in high-amplitude, high-frequency or vortex-dominated flows, such as those considered in this research. The theory builds on the time-stepping approach given by Katz & Plotkin.⁷⁶ In Figure 5.1, the inertial frame is given by $OXYZ$ and the body frame, attached to the moving airfoil, by $Bxyz$. At time $t = 0$, the two frames coincide and at time $t > 0$, the body frame moves toward the left of the page along any prescribed time-varying path (given by pitch and plunge motions). At each time-step, a discrete trailing-edge vortex is shed from the trailing edge.

Analogous to classical thin-airfoil theory, the vorticity distribution over the airfoil, $\gamma(x)$, is taken to be a Fourier series,

$$\gamma(\theta, t) = 2U \left[A_0(t) \frac{1 + \cos \theta}{\sin \theta} + \sum_{n=1}^{\infty} A_n(t) \sin(n\theta) \right] \quad (1)$$

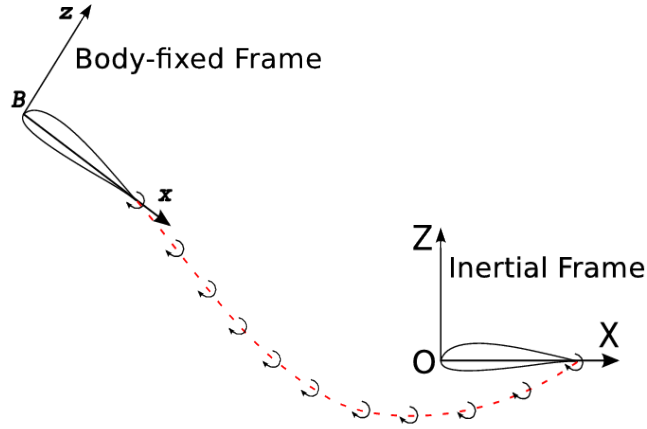


Figure 5.1: Illustration of the time-stepping method in large-angle unsteady thin-airfoil theory.

where θ is a variable of transformation related to the chordwise coordinate x as,

$$x = \frac{c}{2}(1 - \cos \theta) \quad (2)$$

in which $A_0(t)$, $A_1(t)$, ..., $A_n(t)$ are the time-dependent Fourier coefficients, c is the airfoil chord, and U is the component of the airfoil's velocity in the negative X direction. The Kutta condition (zero vorticity at the trailing-edge) is enforced implicitly through the form of the Fourier series. The Fourier coefficients are determined as a function of the instantaneous local downwash on the airfoil by enforcing the boundary condition that the flow must remain tangential to the airfoil surface.

$$A_0(t) = -\frac{1}{\pi} \int_0^\pi \frac{W(x, t)}{U} d\theta \quad (3)$$

$$A_n(t) = \frac{2}{\pi} \int_0^\pi \frac{W(x, t)}{U} \cos n\theta d\theta \quad (4)$$

The induced velocity normal to the airfoil surface, $W(x, t)$, henceforth referred to as downwash, is calculated from components of motion kinematics, depicted in figure 5.2, and induced velocities from vortices in the flowfield.

$$W(x, t) \equiv \frac{\partial \phi_B}{\partial z} = \frac{\partial \eta}{\partial x} (U \cos \alpha + \dot{h} \sin \alpha + \frac{\partial \phi_{tev}}{\partial x}) - U \sin \alpha - \dot{\alpha}(x - ac) + \dot{h} \cos \alpha - \frac{\partial \phi_{tev}}{\partial z} \quad (5)$$

where ϕ_B and ϕ_{tev} are the velocity potentials associated with bound and trailing-edge vorticity, $\eta(x)$ is the camber distribution on the airfoil, $\frac{\partial \phi_{tev}}{\partial x}$ and $\frac{\partial \phi_{tev}}{\partial z}$ are velocities induced tangential and normal to the chord by trailing edge discrete vortices. The motion parameters include the plunge velocity in the Z direction, \dot{h} , and the pitch angle of the chord with respect to the X direction, α . Trailing-edge vortices are shed at every time-step as mentioned earlier, and their strengths are calculated iteratively such that Kelvin's circulation condition is enforced.

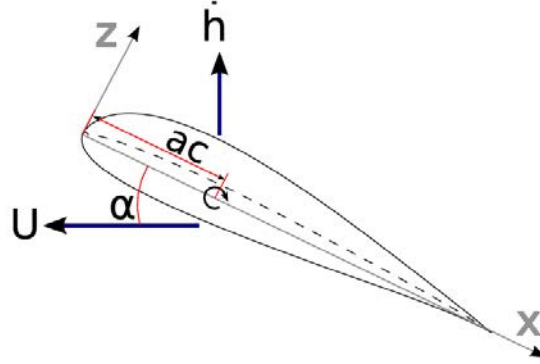


Figure 5.2: Airfoil velocities (positive as shown) and pivot location.

$$\Gamma_b(t) + \sum_{m=1}^{N_{tev}} \Gamma_{tev_m} = 0 \quad (6)$$

where Γ_b is the bound circulation calculated by integrating the chordwise distribution of bound vorticity over the airfoil chord:

$$\Gamma_b = Uc\pi \left[A_0(t) + \frac{A_1(t)}{2} \right] \quad (7)$$

5.1.2 Leading Edge Suction Parameter (LESP)

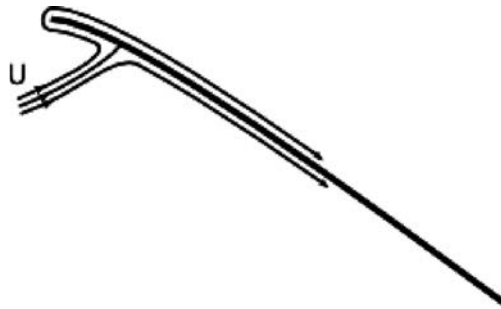


Figure 5.3: Depiction of flow around a thin airfoil's leading edge.

In thin-airfoil theory, the airfoil thickness and hence the leading-edge radius is zero. This requires the flow to turn 180° around the leading edge (figure 5.3), giving rise to a theoretically infinite flow velocity at the leading edge, V_{LE} , of a thin airfoil. From Garrick⁷⁷ and von Kármán & Burgers,⁷⁸ we have that the form of this theoretically infinite velocity is given by,

$$V_{LE}(t) = \lim_{x \rightarrow LE} \frac{S}{\sqrt{x}} \quad (8)$$

where S is a measure of the suction at the leading edge and is given by,

$$S = \lim_{x \rightarrow LE} \frac{1}{2} \gamma(x, t) \sqrt{x} \quad (9)$$

Since $\gamma(x, t)$ is infinite in order of $1/\sqrt{x}$ at the leading edge, the value of S is finite. Evaluating using the current formulation,

$$S = \sqrt{c} U A_0(t) \quad (10)$$

Because the LESP is a nondimensional measure of the suction at the leading edge, S , for given values of c and U , we may simply equate it to the A_0 value as,

$$LESP(t) = A_0(t) \quad (11)$$

As discussed in Katz,²⁰ real airfoils have rounded leading edges which can support some suction even when the stagnation point is away from the leading edge. The amount of suction that can be supported is dependent on the airfoil shape and Reynolds number of operation. Since the LESP (the A_0 value) is a measure of the suction/velocity at the leading edge, it is a logical choice to develop a correlation for initiation of LEV formation based on the LESP.

Using an inviscid parameter to predict trends in viscous behavior is not a new idea. For example, Rival et al.¹³ have shown that LEV detachment/"pinch-off" occurs when the stagnation point of the LEV breaches the airfoil's trailing edge - a phenomenon that may be predicted from inviscid theory. The A_0 term has also been previously used to develop useful correlations in steady aerodynamic theory. It is well known, for instance, that the ideal lift coefficient of a laminar-flow airfoil in steady flow, which usually falls close to the middle of the drag bucket, corresponds to the lift coefficient at which the A_0 coefficient is zero;^{79,80} this idea can be used to estimate the C_l -shift in the drag bucket due to a trailing-edge cruise flap.⁸¹ The A_0 term in thin-airfoil theory is the only term that results in a singularity in the vorticity distribution at the leading edge, and hence is a good measure of the flow at the leading edge.

The research of Morris & Rusak⁸² on inception of leading-edge stall on stationary, two-dimensional, smooth, thin airfoils provides another explanation of why the critical value of the A_0 term should correspond to initiation of LEV formation. In their work, the authors have used matched asymptotic theory with the flow around most of the airfoil chord described in terms of an outer region which is solved using thin airfoil theory. The flow in the vicinity of the leading edge forms the inner region, which is treated as a model problem of a uniform, incompressible and viscous flow past a semi-infinite parabola and solved through numerical simulations of the unsteady Navier-Stokes equations. The flows in the inner and outer regions are made to asymptotically match each other. The far-field circulation for the inner flow is governed by a parameter that is related to the airfoil's angle of attack. This approach allows the determination of the critical angle of attack for leading-edge stall onset as the condition at which a global separation zone is predicted in the solution for the inner flow. For a given airfoil geometry, the A_0 value is linearly related to the angle of attack in stationary flow. This shows that, at a given Reynolds number, leading-edge stall in stationary airfoil flow is related to a critical value of the A_0 coefficient. In the current unsteady thin airfoil theory, the A_0 value accounts not only for the instantaneous angle of attack, but also for the motion kinematics and the effect of vorticity in the flow through the zero-normal flow boundary conditions in equation 5. It follows, therefore, that the critical value of A_0 would correspond to initiation of LEV formation in unsteady flow.

5.2 Study of LEV initiation in low Reynolds-number flows

Trends in LEV initiation for various motion kinematics and the validity of the LESP hypothesis are analyzed in this section using data sets from CFD and experiments. An SD7003 airfoil at a Reynolds number of 20,000 is used for all cases, and a parameter space encompassing a range of values for various kinematic terms is chosen as described in section 5.2.1.

5.2.1 Definition of motion kinematics

Combinations of pitch and plunge maneuvers are considered for the parametric study. Both these motions are generated with a modified version of the Eldredge function which produces a ramp motion with smoothed corners. The pitch histories are given by:

$$\alpha = \alpha_{start} + \frac{K_\alpha}{a_s} \left[\frac{\cosh(a_s(t^* - t_1^*))}{\cosh(a_s(t^* - t_2^*))} \right] + \frac{\alpha_{amp}}{2} \quad (12)$$

, where a_s is the smoothing parameter defined as:

$$a_s = \frac{\pi^2 K_\alpha}{2\alpha_{amp}(1 - \sigma)} \quad (13)$$

and,

$$t_2^* = t_1^* + \frac{\alpha_{amp}}{2K_\alpha} \quad (14)$$

In these equations, t_1^* denotes the time at start of ramp, and t_2^* denotes the time at end of ramp. In all simulations in this paper, t_1^* is taken as 5.0 to generate a steady starting solution and hence minimize the effect of starting vortices on the solution. The parameter σ is a nondimensional measure of smoothing, and is equal to 0.8 in all kinematics considered here. K_α is the reduced frequency of pitch. The term α_{start} is used to generate kinematics where the ramp starts from a non-zero value.

The plunge kinematics are constructed with the same equations, by replacing α with h/c , K_α with K_h and α_{amp} with $(h/c)_{amp}$. h_{start} is not used (always 0). As the plunge motion is in combination with pitch in this study, the reduced frequency for plunge is chosen such that the pitch and plunge ramps occupy the same nondimensional time ($K_h = K_\alpha * (h/c)_{amp}/\alpha_{amp}$). Hence, equations 13 and 14 are not altered. The variation in plunge is given by,

$$\frac{h}{c} = \frac{K_\alpha(h/c)_{amp}}{a_s\alpha_{amp}} \left[\frac{\cosh(a_s(t^* - t_1^*))}{\cosh(a_s(t^* - t_2^*))} \right] + \frac{(h/c)_{amp}}{2} \quad (15)$$

A typical pitch-only ramp motion, starting at $\alpha_{start} = 0$, with pitch amplitude $\alpha_{amp} = 30$ deg, reduced frequency $K_\alpha = 0.2$ and pivoted at quarter-chord is considered as a baseline for the parametric study. The detailed definition of this case is given in table 5.1.

The parameter space for case studies 1-3 is constructed by considering variations in pitch-axis location, pitch reduced frequency and pitch start angles with respect to the baseline case. In case study 4, a pitch-plunge combination is compared to the baseline case. In keeping with the bounds of the experimental apparatus with respect to plunge maneuvers, the K_α for the pitch-plunge

Table 5.1: Base parameter set used to study LEV initiation in low-Reynolds number flow

| Parameter | Symbol | Value |
|---------------------|---------------------------------------|--------|
| Reynolds number | Re | 20,000 |
| Start time of ramp | t_1^* | 5.0 |
| Smoothing parameter | σ | 0.8 |
| Initial pitch angle | $\alpha_{start}(deg)$ | 0 |
| Pitch amplitude | $\alpha_{amp}(deg)$ | 30 |
| Pitch rate | $K_\alpha = \frac{\dot{\alpha}c}{2U}$ | 0.20 |
| Pivot location | x_p/x | 0.25 |
| Plunge amplitude | $(h/c)_{amp}$ | 0.0 |
| Plunge rate | $K_h = \frac{\dot{h}}{2U}$ | 0.0 |

combination was chosen to be 0.1 rather than the baseline value of 0.2. As mentioned previously, the K_h is calculated such that the pitch and plunge ramps occupy the same nondimensional time ($K_h = K_\alpha * (h/c)_{amp}/\alpha_{amp}$). The kinematics for the 4 studies are listed in table 5.2.

Table 5.2: Parameter variations used to study LEV initiation in low-Reynolds number flow (baseline values are in bold)

| Case study | Variable Parameter | Values |
|------------|--|--|
| 1 | Pivot location (x_p/c) | 0.0, 0.25 , 0.75 |
| 2 | Pitch rate (K_α) | 0.01, 0.03, 0.05, 0.1, 0.2 , 0.4 |
| 3 | Initial pitch angle (α_{start}) | 10, 5, 0 , -5, -10, -15 |
| 4 | Pitch-plunge combination | $\alpha_{amp} = 30$, $K_\alpha = 0.1$, $(h/c)_{amp} = -0.1$, $K_h = 0.0191$ |

For all kinematics, the pitch angles at which LEV formation is initiated are determined using experiments and CFD, and the LESP values at these pitch angles are determined from theory. Skin-friction coefficient data from CFD is used to quantitatively identify the initiation of LEV formation. Experimental data is used to mutually validate the CFD and qualitatively study the initiation of LEV formation for all kinematics. The identification of LEV initiation using skin-friction data is illustrated with the baseline case in section 3.2. Four parametric studies are then considered in section 5.3 to study LEV initiation behavior and to establish the envelope of validity of the LESP hypothesis. Section 5.3.5 presents the results from all 4 case studies in combination. Finally, section 5.3.6 discusses two design cases in which plunge motions are added to the baseline pitch motion to alter the occurrence of LEV formation.

5.3 Results of parametric studies of LEV initiation

5.3.1 Case study 1: kinematics with varying pivot locations

In this study, the effect of pitch-axis location on LEV initiation in unsteady maneuvers is examined. In addition to the baseline case (quarter-chord pivot), two cases with modified pivot locations (leading-edge and three-quarter-chord) are considered. The pitch-angle during the ramp-maneuver at which LEV formation is initiated (as determined using the procedure described in section 3.2)

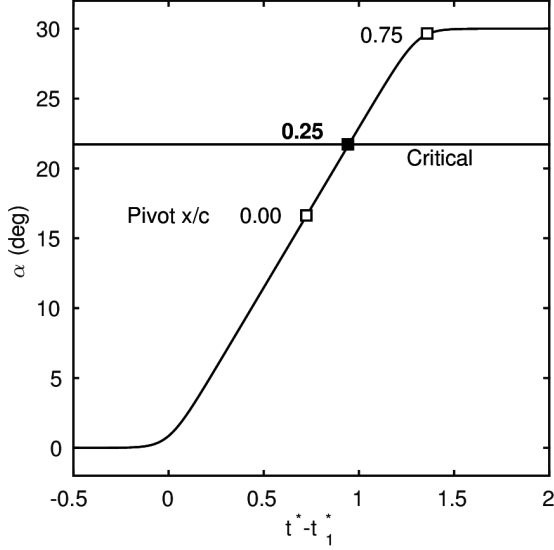


Figure 5.4: Case study 1: pitch-angle variation with time, and pitch-angles at which LEV formation is initiated (kinematics with different pivot locations).

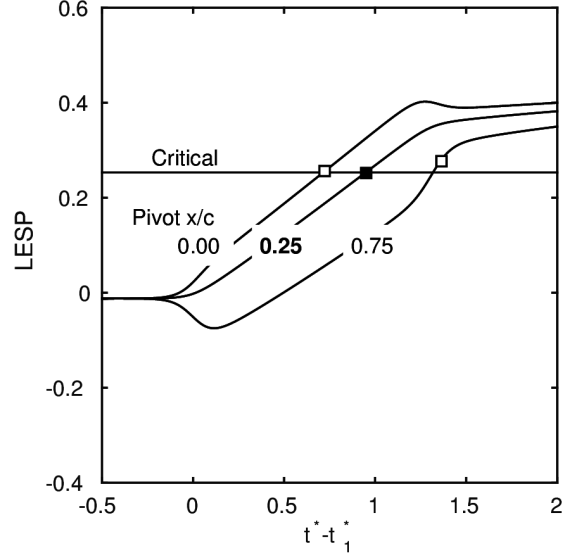


Figure 5.5: Case study 1: LESP variation with time, and LESP values at which LEV formation is initiated (kinematics with different pivot locations).

is plotted for all three cases in figure 5.4. As the pivot location is varied along the chord from leading to trailing edge, the pitch angle at LEV initiation is seen to increase. Clearly, there is no obvious relation between initiation of LEV formation and the values of the pitch angle at that time instant. In figure 5.5, the time variation of $LESP$ for the 3 kinematics from unsteady thin-airfoil theory are co-plotted with the instants of LEV formation marked. It is seen that the initiation of upper-surface LEV formation occurs at a near-constant $LESP$ value. The results for this case study hence confirm the $LESP$ hypothesis that rounded edges can support a certain maximum suction force, beyond which LEV formation occurs.

More insight into the LEV formation and shedding process is gained by analyzing the experimental and numerical results together. Flow visualization plots from experiment, vorticity plots from CFD, pressure coefficient (upper and lower surfaces) and skin-friction coefficient (upper surface) distributions from CFD at the instants of LEV initiation for the three cases are shown in figure 5.6. At the time of LEV initiation, we see that the C_p and C_f distributions for the 3 cases are qualitatively similar. The vorticity and flow visualization plots show that the flow is attached over most of the airfoil for all 3 cases, as is expected for the high reduced frequency $K = 0.2$. This explains the $LESP$ hypothesis holding valid in this case study, as the theory is derived on the basis of an attached flow assumption.

The same plots from CFD and experiment, at some time after the initiation of LEV formation are shown in figure 5.7. The time instant is chosen as that when the inviscid $LESP$ value is greater than $LESP_{crit}$ by a value of 0.1. The $LESP$ is a measure of the velocity at the leading edge and also the velocity at the start of the shear layer emanating from the leading edge. Now, the flux of vorticity into the free shear layer (LEV) may be related to the shear layer edge velocity by the experimentally observed relation of Fage and Johansen,⁸³

$$\frac{d\Gamma_{sh}}{dt} = \frac{1}{2}U_{sh}^2 \quad (16)$$

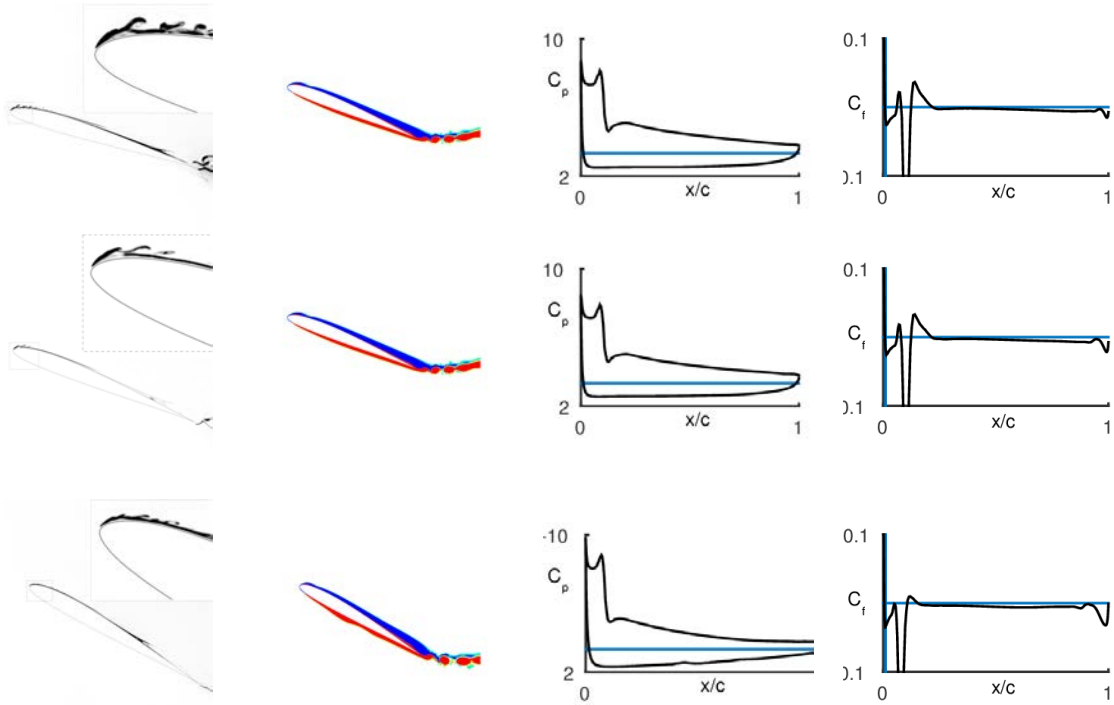


Figure 5.6: Case study 1: left to right - flow visualization from experiment, vorticity plots from CFD, C_p (upper and lower surfaces) and C_f (upper surface) distributions from CFD at the instants of LEV initiation. Top to bottom - pivot location at leading edge, quarter chord and three-quarter chord.

This relation has also been used to model vortex shedding from edges in discrete-vortex methods such as those by Sarpkaya¹⁷ and Katz.²⁰ The instants when the $LESP$ is greater than $LESP_{crit}$ by a certain constant value thus correspond to times when approximately equal vorticity has been shed into the LEVs in all cases. Strictly, the $LESP$ curves in figure 5.5 are only valid until the instant of LEV initiation, as LEV shedding which occurs after this instant is not modeled. Still, $\Delta LESP = 0.1$ is chosen as a measure when all cases would be at approximately the same stage of vortex development, irrespective of motion parameters. Figure 5.7 shows that the LEV structures and C_p distributions are similar for the three cases with different pitch-axis locations. Further, all 3 cases show the presence of a concentrated LEV with no noticeable flow separation over the rest of the airfoil.

5.3.2 Case study 2: kinematics with varying pitch rates

In this case study, the effect of pitch-rate on LEV formation in unsteady maneuvers is investigated. In addition to the baseline case ($K = 0.2$), five cases with modified pitch rates (0.01, 0.03, 0.05, 0.1 and 0.4) are considered.

The pitch-angle during the ramp motion at which LEV formation is initiated (as determined using the procedure described in section 3.2) is plotted for all six cases in figure 5.8. The pitch angle at LEV initiation is seen to increase with increasing pitch rate. High-pitch rates hence serve to keep

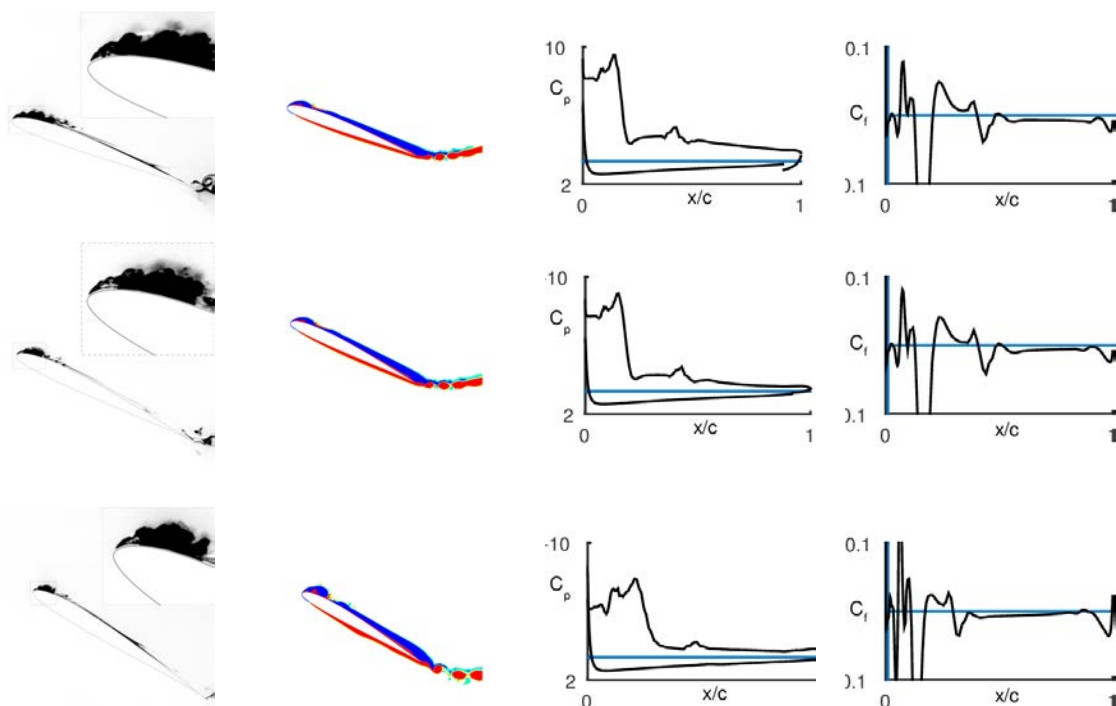


Figure 5.7: Case study 1: left to right - flow visualization from experiment, vorticity plots from CFD, C_p (upper and lower surfaces) and C_f (upper surface) distributions from CFD at $\Delta LES P = 0.1$ after the instants of LEV initiation. Top to bottom - pivot location at leading edge, quarter chord and three-quarter chord.

the flow attached to the airfoil, which is well known from dynamic stall research (for e.g. ref⁸⁴). In figure 5.9, the time variation of $LES P$ for the six kinematics from unsteady thin-airfoil theory are co-plotted with the instants of LEV formation marked. We see that initiation of LEV formation for cases with relatively high pitch rates ($K \geq 0.1$) occurs at a near constant $LES P$ value. The $LES P$ values at LEV initiation for the cases with lower pitch rates ($K < 0.1$) are lower, with the values decreasing for lower pitch rates. This result is analyzed in detail by studying flow features from experiments and CFD below.

Flow visualization plots from experiment, vorticity plots from CFD, pressure coefficient (upper and lower surfaces) and skin-friction coefficient (upper surface) distributions from CFD at the instants of LEV initiation for the six cases are shown in figure 5.10. The first three cases with pitch rates of 0.01, 0.03 and 0.05 respectively, are seen to exhibit significant boundary-layer thickening and flow separation on the airfoil surface at the time of LEV initiation. For these three cases, the flow visualization from experiment shows that flow is separated over more than 50% of the airfoil at the time of LEV initiation. Hence we do not expect the $LES P$ hypothesis to hold true for these cases, as the underlying unsteady thin-airfoil theory assumes attached flow over the whole airfoil and is hence not valid. If trailing-edge separation were modeled in the calculation of $LES P$, the hypothesis may hold true even for the slow pitch-rate cases. The C_p distributions for the six cases show a clear trend, with higher pitch rates resulting in a greater values of pressure coefficient on the airfoil. The C_f distributions and the C_f -spike which is used to identify LEV initiation also show clear trends with the spike moving aft on the airfoil and getting broader/diffused with decreasing

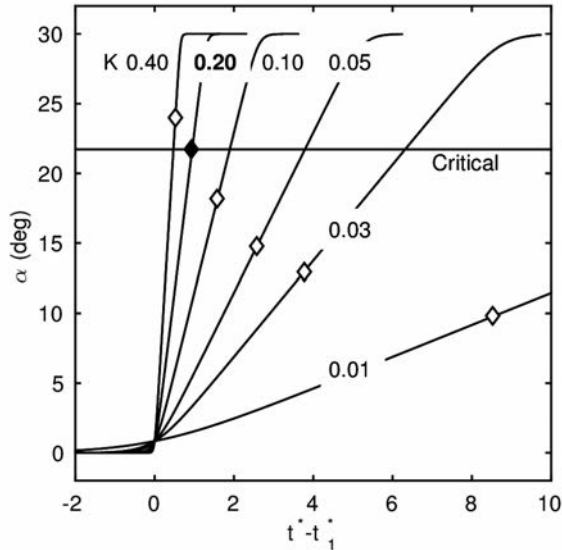


Figure 5.8: Case study 2: pitch-angle variation with time, and pitch-angles at which LEV formation is initiated (kinematics with different pitch rates).

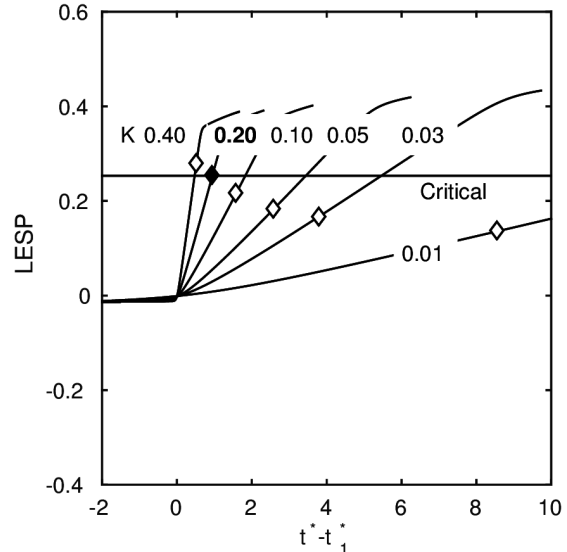


Figure 5.9: Case study 2: LEVP variation with time, and LEVP values at which LEV formation is initiated (kinematics with different pitch-rates).

pitch rate.

The same plots from CFD and experiment, at some time after the initiation of LEV formation are shown in figure 5.7. The time instant, as earlier, is chosen as that when the inviscid $LEVP$ value is greater than $LEVP_{crit}$ by a value of 0.1. The LEV structures for the six cases exhibit a trend of being more concentrated with increasing pitch rate. For the first case with $K = 0.01$, the pitch-rate is so slow that the airfoil is “nearly steady” and displays a bluff-body type flow. The second and third cases show a distinct LEV, along with the presence of flow separation over the rest of the airfoil. The final three cases have a concentrated LEV with no significant separation over the rest of the airfoil surface. From figure 5.9, we see that these cases display LEV initiation at a near constant LEVP value, whereas the LEVP at LEV initiation for the slower cases occurs at progressively lower values.

5.3.3 Case study 3: kinematics with varying initial pitch angles

In case study 3, the influence of boundary layer development and flow separation on LEV initiation is investigated by starting the pitch ramps from non-zero values. In addition to the baseline case (which starts from a pitch angle of 0), five cases starting with starting pitch angles of 10, 5, -5 , -10 and -15 deg are used. The pitch angle histories for these cases and the angles at which LEV formation is initiated are plotted for all six cases in figure 5.12.

In all cases, a steady boundary layer is established at the starting pitch angle before the ramp is initiated. The results show some variation in the pitch angles at which LEV formation is initiated for these cases. There is no clear trend, suggesting that the influence of an established boundary layer on LEV formation is nonlinear. Figure 5.13 displays the time variation of $LEVP$ as determined from theory for the 6 cases. For cases starting with non-zero pitch angles, the $LEVP$ values at LEV

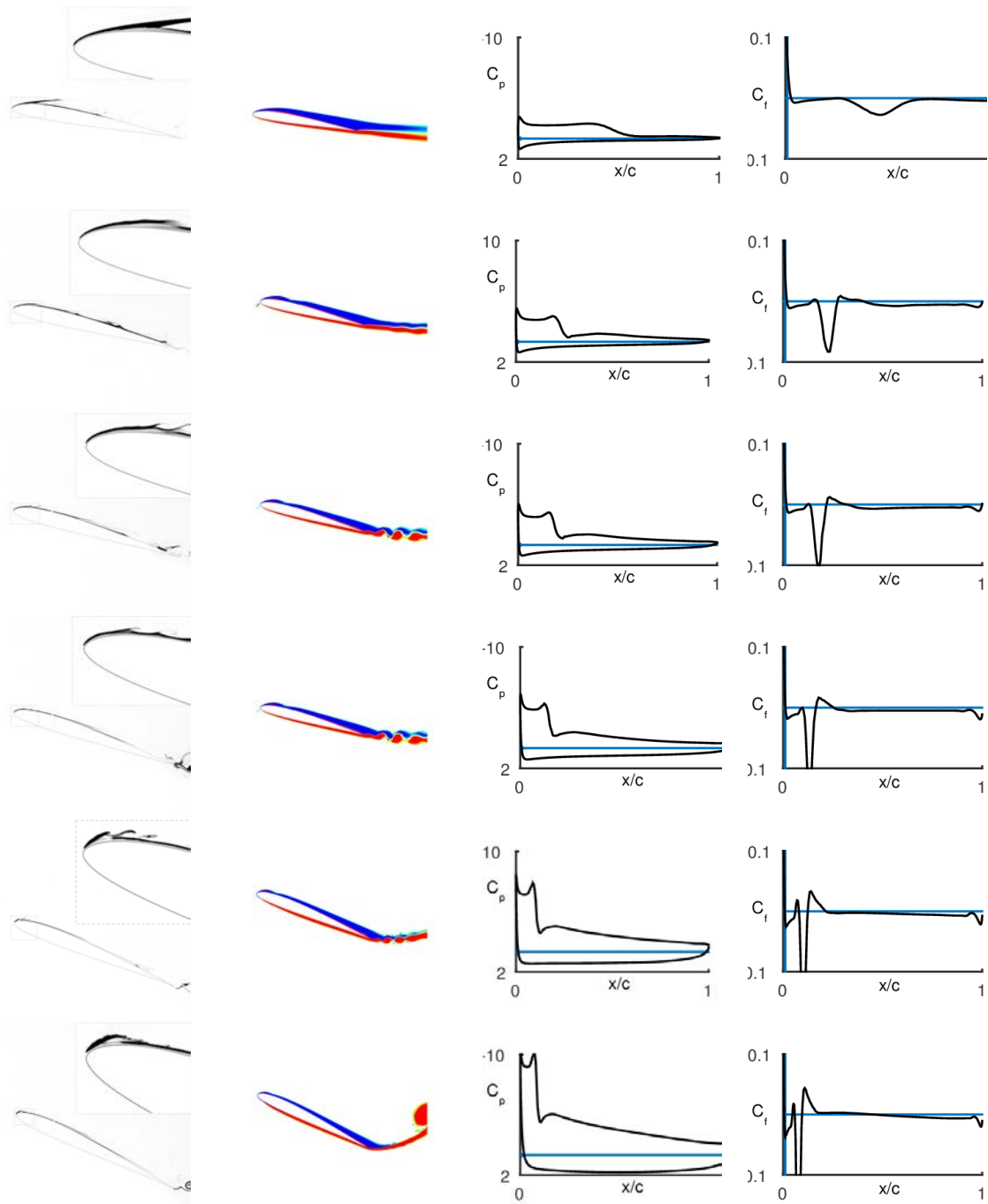


Figure 5.10: Case study 2: left to right - flow visualization from experiment, vorticity plots from CFD, C_p (upper and lower surfaces) and C_f (upper surface) distributions from CFD at the instants of LEV initiation. Top to bottom - pitch rate of 0.01, 0.03, 0.05, 0.1, 0.2 and 0.4).

initiation are lower than that for the baseline case (similar to trend seen in section 5.3.2, though they are still close to the baseline value.

Flow visualization plots from experiment, vorticity plots from CFD, C_p (upper and lower surfaces)

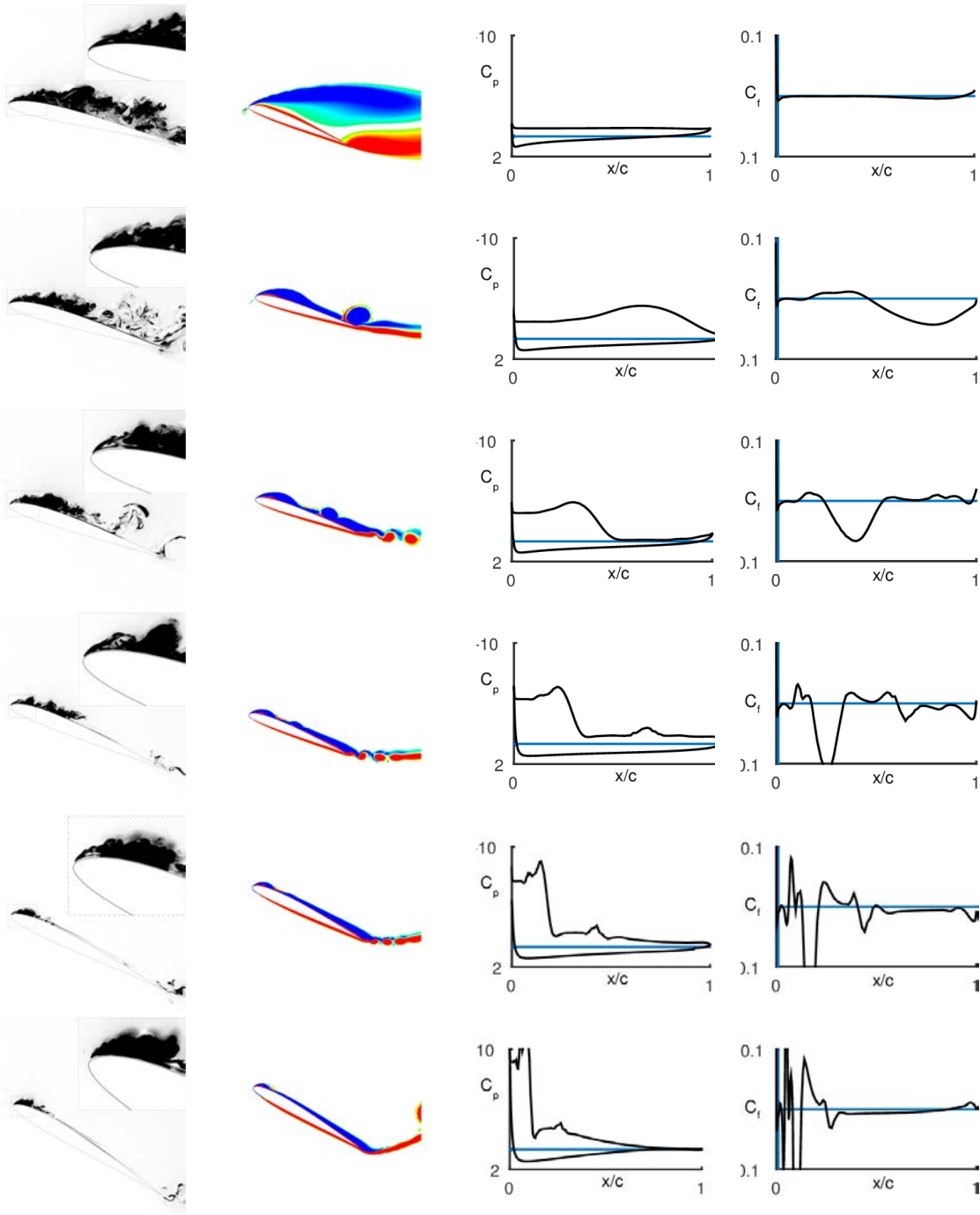


Figure 5.11: Case study 2: left to right - flow visualization from experiment, vorticity plots from CFD, C_p (upper and lower surfaces) and C_f (upper surface) distributions from CFD at $\Delta LES P = 0.1$ after the instants of LEV initiation. Top to bottom - pitch rate of 0.01, 0.03, 0.05, 0.1, 0.2 and 0.4).

and C_f (upper surface) distributions from CFD at the instants of LEV initiation for cases study 3 are shown in figure 5.14. The first 2 cases (starting at 10 and 5 degrees) exhibit flow separation

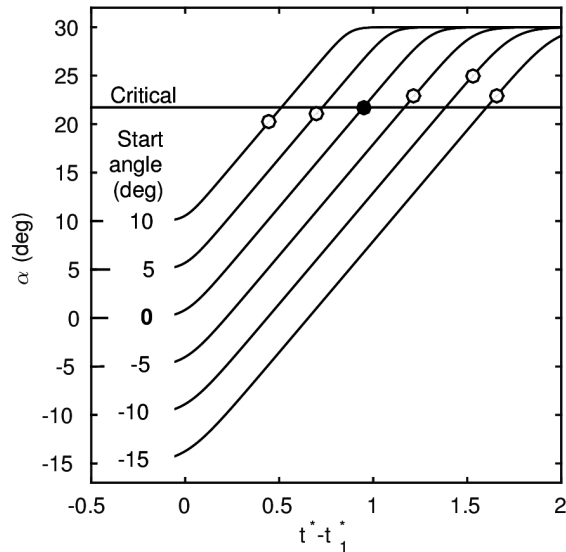


Figure 5.12: Case study 3: pitch-angle variation with time, and pitch-angles at which LEV formation is initiated (kinematics with different start angles).

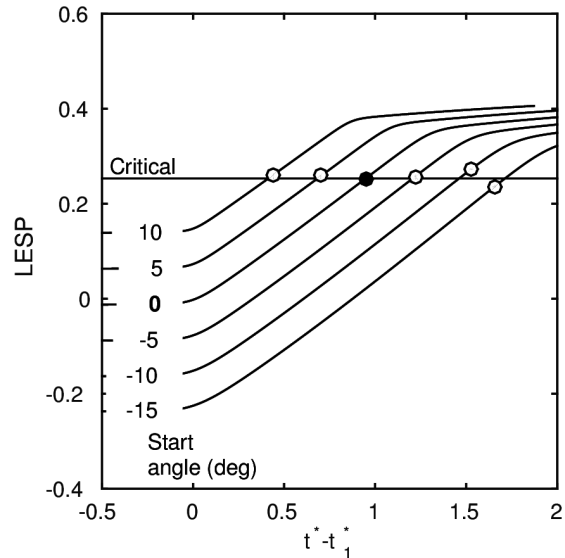


Figure 5.13: Case study 3: LESP variation with time, and LESP values at which LEV formation is initiated (kinematics with different start angles).

on the airfoil upper surface at the time of LEV initiation, while the final 3 cases (starting at -5 , -10 and -15 deg) exhibit separated flow on the lower surface. The LESP values at the instants of LEV formation for these cases were however quite close as observed in figure 5.13.

The same plots from CFD and experiment, at an instant after the initiation of LEV formation when the inviscid $LESP$ value is greater than $LESP_{crit}$ by a value of 0.1, are shown in figure 5.7. All the cases exhibit a concentrated vortex, with the first two also showing significant trailing-edge separation. The LESP hypothesis is however seen to hold for all cases (figure 5.13) in contrast to the slow ramp cases in section 5.3.2 which also had significant trailing-edge separation. Hence the presence of separated shear layers/thick boundary layers as an initial condition does not appear to affect LEV initiation as dynamics flow separation on the airfoil surface progressing from the trailing edge towards the leading edge owing to low pitch rates.

5.3.4 Case study 4: kinematics with pitch-plunge combination

In this study, we aim to establish that the LESP hypothesis (LEV initiation occurring at the same critical value of LESP) applies not only to various pitching maneuvers, but to any arbitrary unsteady maneuver. In addition to the baseline case, a pitch-plunge combination is considered. The latter has a pitch amplitude of 30 deg, plunge amplitude/chord of -0.1 , and reduced frequency (in both pitch and plunge) of 0.1 as given in table 5.2. The pitch angle histories for the two cases and the angles at which LEV formation is initiated are plotted in figure 5.16.

Figure 5.17 displays the time variation of $LESP$ as determined from theory for the two cases, and the LESP values at the instant of LEV initiation as determined from CFD (section 3.2. LEV initiation in both cases is seen to occur at the same LESP value, thereby validating the LESP hypothesis for arbitrary kinematics.

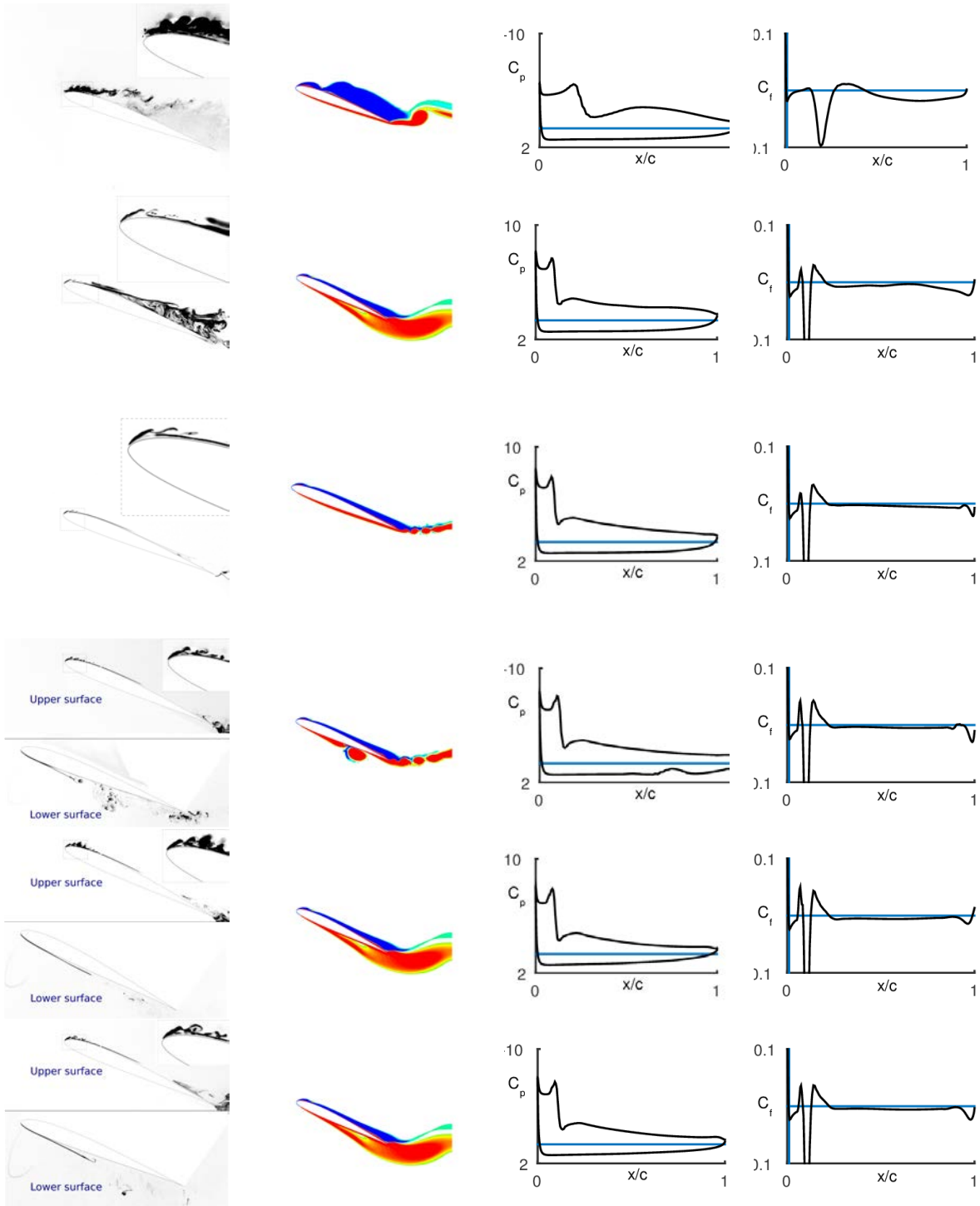


Figure 5.14: Case study 3: left to right - flow visualization from experiment, vorticity plots from CFD, C_p (upper and lower surfaces) and C_f (upper surface) distributions from CFD at the instants of LEV initiation. Top to bottom - starting pitch angles of 10, 5, 0, -5, -10 and -15 deg).

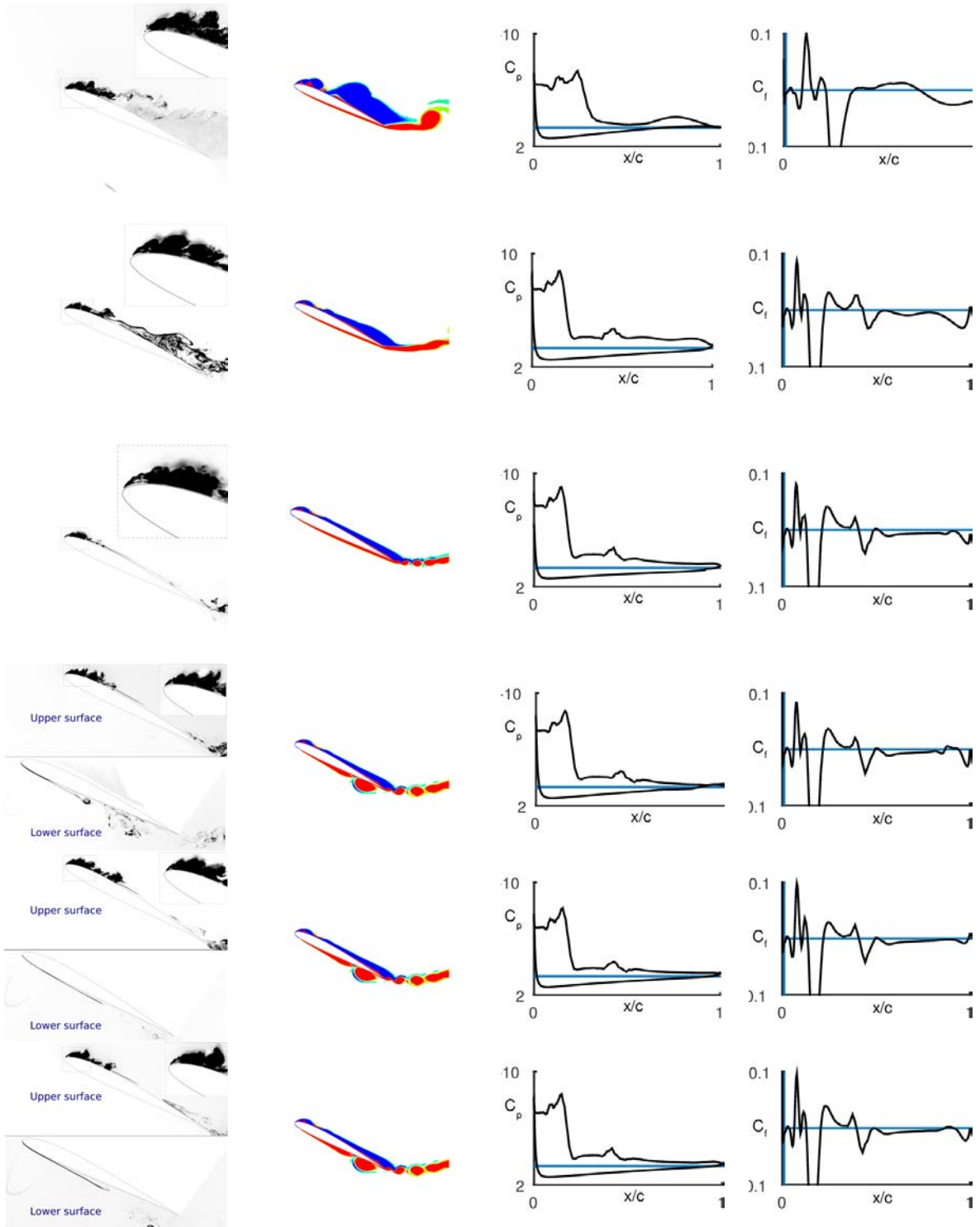


Figure 5.15: Case study 3: left to right - flow visualization from experiment, vorticity plots from CFD, C_p (upper and lower surfaces) and C_f (upper surface) distributions from CFD at $\Delta LES P = 0.1$ after the instants of LEV initiation. Top to bottom - starting pitch angles of 10, 5, 0, -5, -10 and -15 deg).

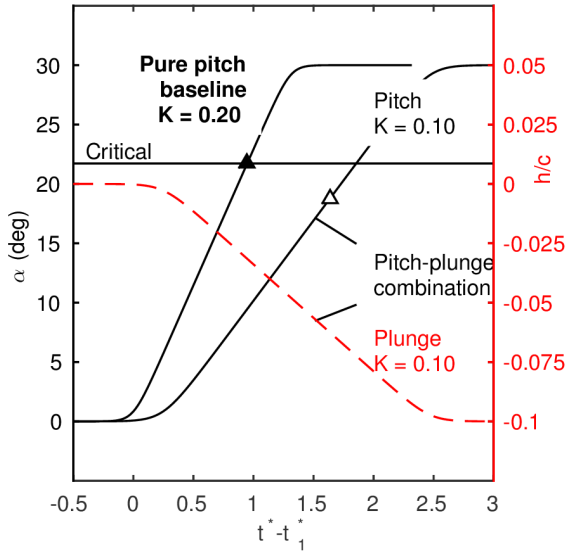


Figure 5.16: Case study 4: pitch angle/plunge amplitude variation with time, and pitch angles at which LEV formation is initiated (baseline case and pitch-plunge combination).

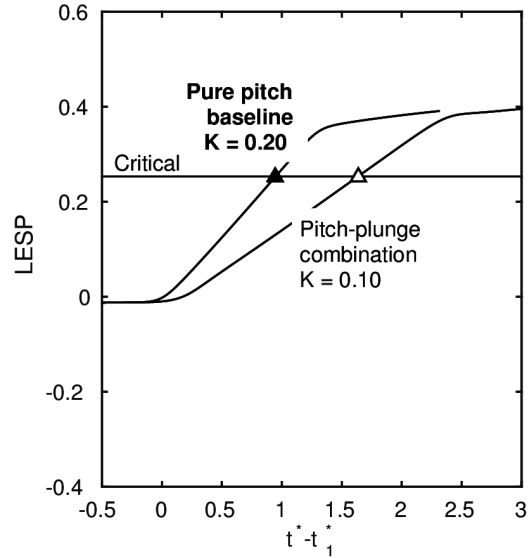


Figure 5.17: Case study 4: LES P variation with time, and LES P values at which LEV formation is initiated (baseline case and pitch-plunge combination).

As for the other case studies, flow visualization from experiment, vorticity plots from CFD, C_p , and C_f distributions from CFD at the instants of LEV initiation for the two cases are shown in figure 5.18. Despite LEV initiation occurring at different angles of attack, the C_f distributions for the two cases are similar at the instant of LEV initiation, which also corresponds to the same critical value of $LES P$ as seen in figure 5.17.

The same plots from CFD and experiment for the two cases, at a time after initiation of LEV formation when the inviscid $LES P$ value is greater than $LES P_{crit}$ by a value of 0.1, are shown in figure 5.19. The vortex development for the two cases is seen to be quite different owing to the different types of motion and the different reduced frequencies. While the baseline case exhibits a small concentrated vortex, the pitch-plunge combination evinces a more diffused LEV accompanied by trailing-edge flow separation.

5.3.5 Compilation of all test cases

The results from all parametric studies performed in this research are compiled here. The applicability of the $LES P$ hypothesis for predicting LEV initiation is demonstrated using figure 5.20. On the y-axis, are the predictions from CFD for angles of attack at LEV initiation in all the kinematics considered. On the x-axis, are angles of attack predicted from inviscid theory, using the critical $LES P$ value. The $LES P$ value of the baseline case at the instant of the LEV initiation is taken to be the critical $LES P$. The instant of LEV initiation for any other case is predicted from theory as the instant when the instantaneous $LES P$ value just crosses the critical $LES P$ value. As seen from figure 5.20, with the exceptions of the three slow pitch-rate cases from case study 2 ($K = 0.01, 0.03$ and 0.05), the predictions from CFD and theory are within an error margin of ± 1 deg for most cases, and within ± 2.5 deg for all cases. This clearly demonstrates the viability of the $LES P$ concept as a tool for predicting LEV initiation using inviscid theory. The critical $LES P$ needs to

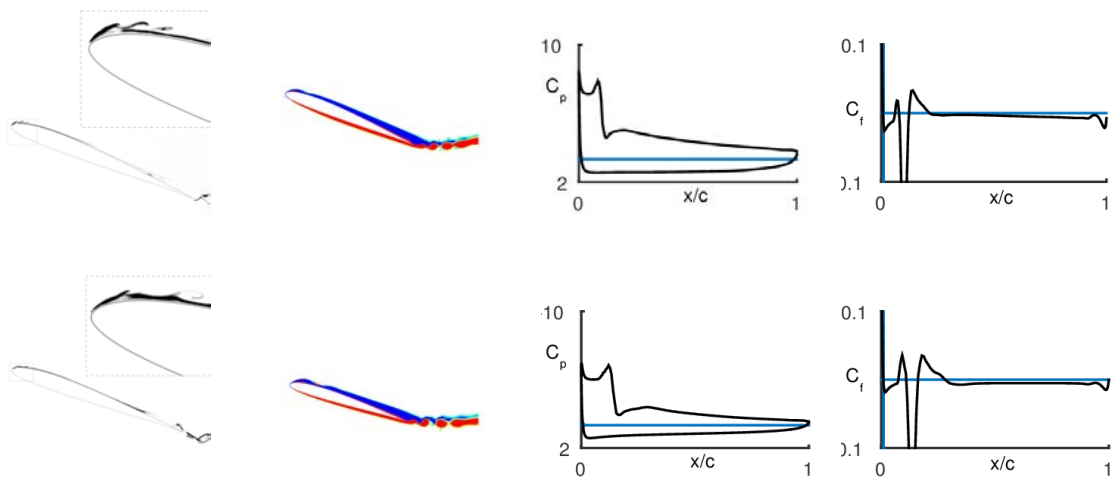


Figure 5.18: Flow visualization from experiment, vorticity plots from CFD, C_p (upper and lower surfaces) and C_f (upper surface) distributions from CFD at the instant of LEV initiation for cases 1 and 15.

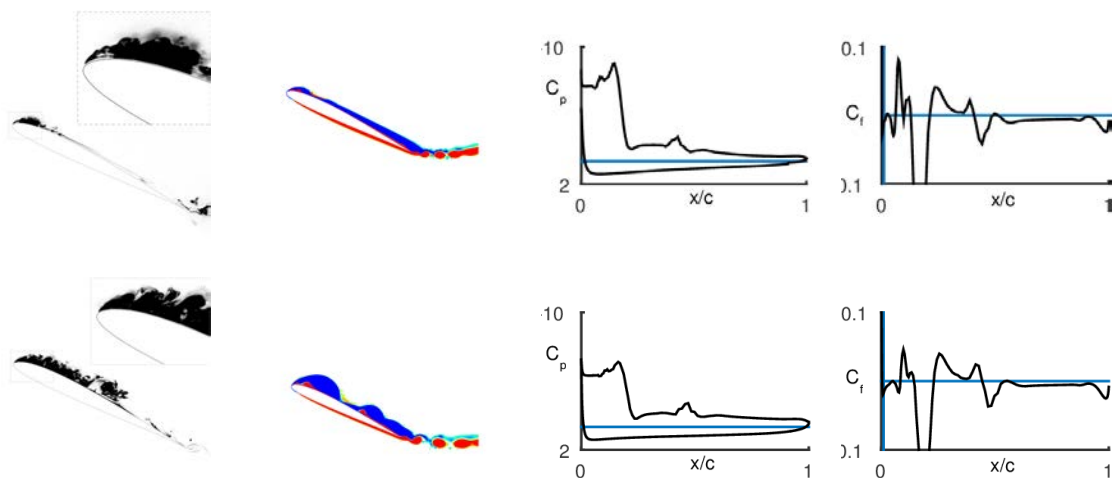


Figure 5.19: Flow visualization from experiment, vorticity plots from CFD, C_p (upper and lower surfaces) and C_f (upper surface) distributions from CFD at some $\Delta LESP$ after the initiation of LEV formation for cases 1 and 15.

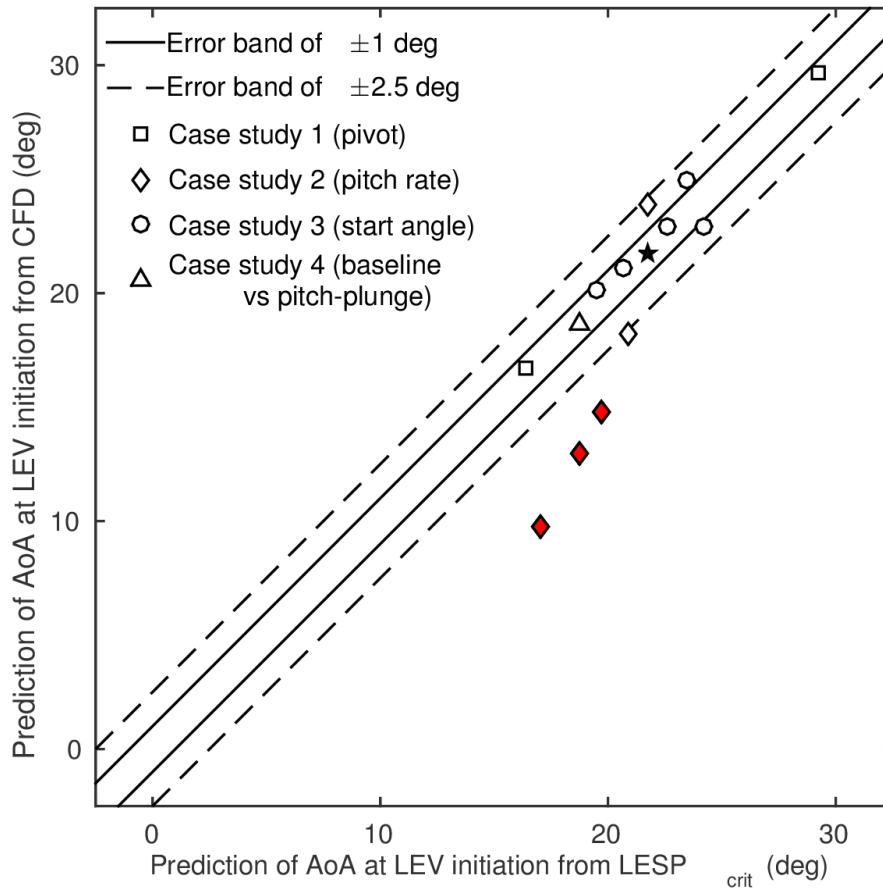


Figure 5.20: Comparison of angle of attack for LEV initiation from low-order and high-order methods.

be calibrating using just one motion for a given airfoil shape and Reynolds number combination. It can then be employed to predict LEV initiation for any other (fast-rate) motion with the same airfoil and Reynolds number combination.

Figure 5.21 shows the $LESP$ values when LEV initiation occurs for all the case studies considered, and further reinforces the $LESP$ hypothesis. With the exception of the 3 slow pitch-rate cases in case study 2 ($K = 0.01, 0.03$ and 0.05), the $LESP$ values for all other cases at the instant of LEV initiation are seen to occur around the same critical value. The figure shows that with the exception of the three outliers, the $LESP$ values at LEV initiation for all cases lies within 14% of the critical value. In the next section, the use of $LESP$ as a low-order tool for manipulating LEV formation is demonstrated.

5.3.6 Trigger/Suppress LEV formation using $LESP_{crit}$

In the preceding sections, we showed that the start of separation at the leading edge is related to the $LESP$ exceeding a certain critical value. The critical $LESP$ value is a function of the airfoil shape and Reynolds number of operation. Once pre-determined using experimental or computational

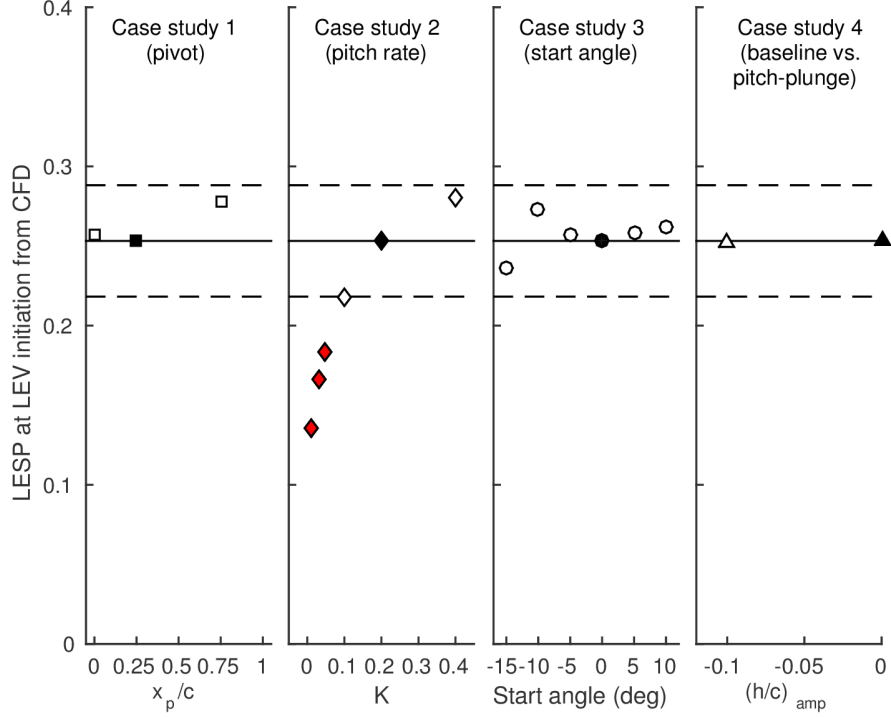


Figure 5.21: LES_p values at the instant of LEV initiation (as determined from CFD), compiled for all cases considered .

methods, the critical LES_p value corresponds to onset of separation at the leading edge, irrespective of motion kinematics. Hence LEV occurrence may be controlled by suitably altering the motion kinematics such that the LES_p critical value is attained at the required time of start of LEV formation.

Consider the baseline case in section 3.2, analyzed with CFD - a pitch motion with amplitude of 30 deg, reduced frequency of 0.2, and pivot about the quarter chord. For these motion kinematics, LEV formation was seen to be initiated on the upper surface at $t^* = 0.95$, $\alpha = 22$ deg. In this section, we modify the occurrence of LES_p variation by superimposing a plunge motion on the baseline case, such that LEV initiation is either advanced or delayed as desired.

As it is well known that (negative) rate of plunge is equivalent to variation in pitch angle,⁷ the plunge rate is taken to be in the form of an Eldredge-ramp function (same as pitch angle).

$$\frac{\dot{h}}{c} = \frac{K_\alpha (\dot{h}/c)_{amp}}{a_s \alpha_{amp}} \left[\frac{\cosh(a_s(t^* - t_1^*))}{\cosh(a_s(t^* - t_2^*))} \right] + \frac{(\dot{h}/c)_{amp}}{2} \quad (17)$$

The plunge motion to be superimposed on pitch is obtained by integrating the Eldredge-form plunge rate,

$$\frac{h}{c} = \int_0^t \frac{\dot{h}}{c} dt \quad (18)$$

A Newton iteration is used to determine the value of (\dot{h}/c) such that criteria on LES_p are satisfied,

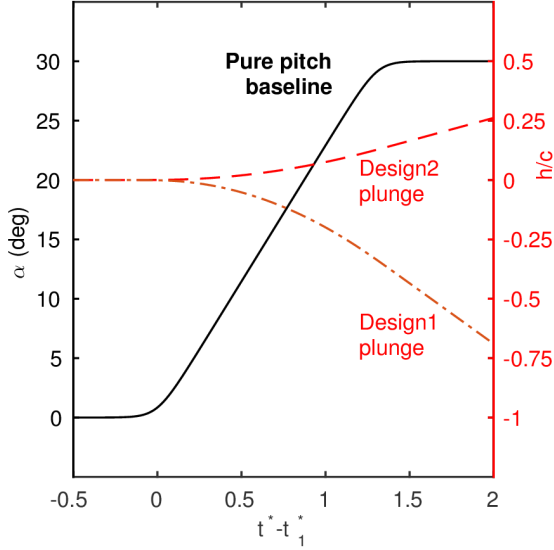


Figure 5.22: Pitch amplitude variation with time for the baseline case, and plunge amplitude variations which are used in combination with baseline pitch to generate the two design cases.

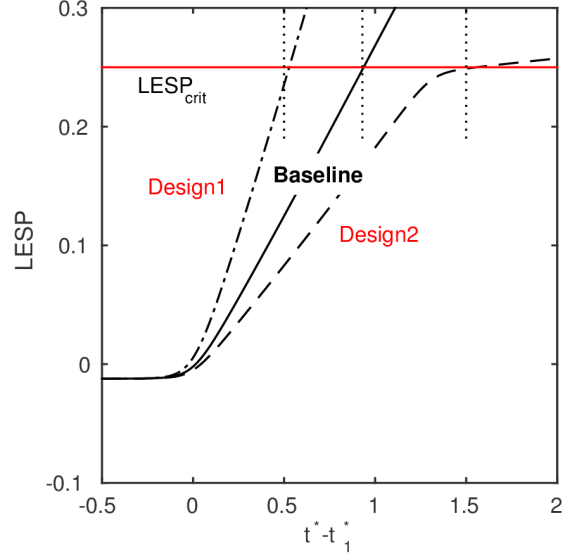


Figure 5.23: LESP variation with time for the baseline case and the two design cases. As required by the design criteria, the intersection of instantaneous $LESP$ with critical $LESP$ is at $t^* - t_1^* = 0.5$ and 1.5 respectively.

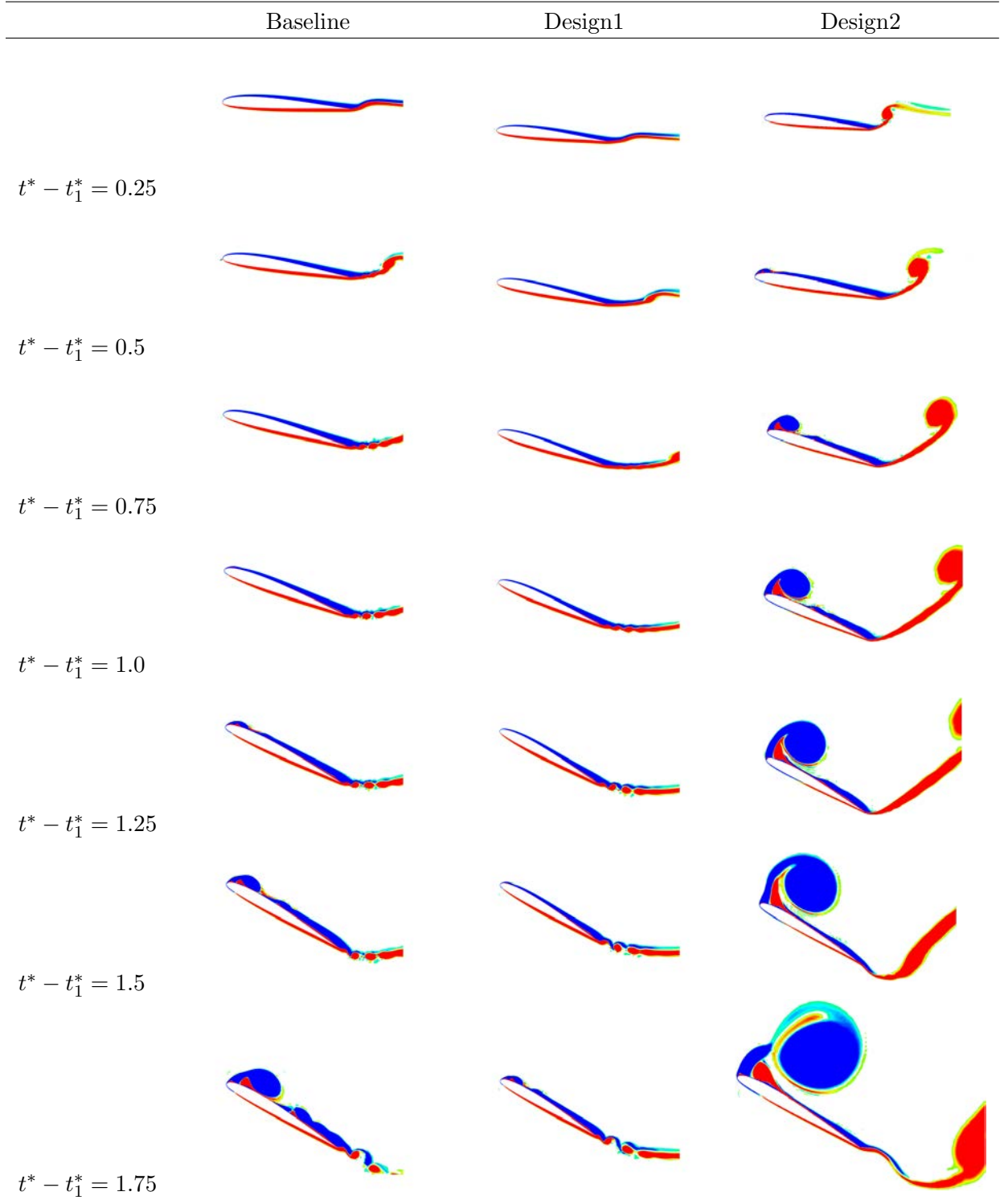
using which the plunge motion is then constructed with eqns. 17 and 18. Recalling that LEV initiation in the baseline case occurs at $t^* - t_1^* = 0.95$, plunge-combined kinematics are constructed such that LEV initiation is shifted to (i) $t^* - t_1^* = 0.5$, and (ii) $t^* - t_1^* = 1.5$. The values of (\dot{h}/c) as determined from the newton iteration for these two cases (hereafter called “design cases”) are -0.5098 and 0.1933 respectively. As expected, the LESP theory predicts a negative plunge (equivalent to positive pitch angle) to advance LEV formation and a positive plunge to delay LEV formation. Figure 5.22 shows the baseline case (pure pitch), and the two design cases which are constructed by combining the baseline pitch with the two plunge motions shown. Figure 5.23 illustrated the LESP histories for the baseline motion and two design motions. As required, the $LESP$ values for the design cases cross the critical value at $t^* - t_1^* = 0.5$ and $t^* - t_1^* = 1.5$.

CFD simulations were performed for the two design cases to validate the viability of the LESP concept for advancing or delaying LEV formation according to specification. Table 5.3 shows vorticity plots for the baseline case and the two design cases, at several equally spaced intervals through the respective motions. The plots confirm that LEV formation can indeed be advanced (as in design1 to $t^* = 0.5$) or delayed (as in design2 in to $t^* = 1.5$) by suitably by superimposing a suitable plunge motion. Using the $LESP$ concept and calculating suitable superpositions, LEV formation for any arbitrary motion may be triggered at will or suppressed entirely.

5.4 Interim conclusions

In this paper, an inviscid theoretical method which handles large amplitudes and non-planar wakes is presented, and used to derive the Leading Edge Suction Parameter (LESP) which is a measure of the suction at the airfoil. Parametric studies with experiments and CFD are used to rigorously

Table 5.3: Vorticity plots from CFD at various instants during the motion



test the LESP hypothesis, that there is a critical value of the LESP for a given airfoil and Reynolds number at which LEV formation is initiated.

In conclusion, the computational method used was seen to reproduce the experimental loads and flow features well. It was seen that there is a critical value of the LESP for a given airfoil and Reynolds number at which LEV formation is initiated, except for slow-rate motions with significant trailing-edge flow separation. The value of critical LESP is completely independent of kinematic parameters such as amplitude and rate of motion, pivot location and type of motion (pitch / plunge). By pre-determining the critical LESP for a given airfoil and Reynolds number it is possible to predict whether LEVs will be formed for any given motion kinematics. Further, the LESP may be used in a design approach to generate motion kinematics which would either prevent LEV formation or generate LEVs as per aerodynamic requirements. The results demonstrate that the LESP is a fundamentally important, albeit simple, theoretical parameter that governs LEV formations.

Chapter 6

Model Reduction in Discrete-Vortex Methods for Unsteady Airfoil Flows

In this chapter, we propose a method for model reduction in discrete-vortex methods for two-dimensional flows on airfoils. Discrete-vortex methods have been successfully employed to model separated and unsteady airfoil flows.² Earlier research² revealed that a parameter called the Leading Edge Suction Parameter (LESP) can be used to modulate leading-edge vortex (LEV) shedding in unsteady flows. The LESP is a measure of suction developed at the leading edge, and whenever the LESP exceeds a critical value, a discrete vortex is released from the leading edge so as to keep the LESP at the critical value. Although the method was successful in predicting the forces on and the flow field around an airfoil in unsteady vortex-dominated flows, it was necessary to track a large number of discrete vortices in order to obtain the solution. The current study focuses on obtaining a model with a reduced number of discrete vortices to model LEVs, thus improving the computation time. Vortex shedding from the leading edge is modeled by a shear layer that comprises a few discrete vortices, and a single concentrated vortex whose strength varies with time. The single vortex at the end of the shear layer accounts for the concentrated vortical structure that comprises several discrete vortex elements in conventional vortex methods. A merging algorithm is initiated when the edge of the shear layer starts rolling up. Suitable discrete vortices are identified using a kinematic criterion, and are merged to the growing vortex at every time step. The reduced order method is seen to bring down the number of discrete vortices required to model LEV structures significantly. The effort described in this chapter, although intended for two-dimensional flows, provided important algorithms for the UVLM-based prediction methods for finite-wing LEV formation, described in Chapter 9.

6.1 Background: The LESP-modulated Discrete Vortex Method (LDVM)

This section briefly describes the 2D low-order LDVM that uses discrete-vortex shedding from the airfoil leading-edge to simulate the intermittent shedding of vorticity from an airfoil leading edge. The method is developed by augmenting the large-angle thin-airfoil theory, described in Section 5.1.1. More details of the LDVM approach, results, and comparison with computational and experimental results are shown in Ref.²

6.1.1 LESP criterion for initiation, shedding, and termination of LEV

It has been shown by Ramesh et. al.² that the initiation and termination of leading-edge vorticity shedding is determined by a nondimensional measure of the suction at the leading edge. It has also been shown that this leading-edge section parameter (LESP) is the same as leading coefficient A_0 in the Fourier series representing the bound vorticity. Thus,

$$LESP(t) = A_0(t) \quad (1)$$

With the LESP criterion, a given airfoil has a critical value of LESP for a given Reynolds number. This value is independent of motion kinematic parameters such as amplitude, reduced frequency, and pivot location. Once the critical value of LESP of a given airfoil is obtained for a given Reynolds number using data from experiment or CFD for a sample motion, LDVM can predict the initiation and termination of intermittent leading-edge vorticity in any arbitrary motion of the airfoil at that Reynolds number.

The instant at which the magnitude of LESP exceeds the critical value marks the initiation of leading edge vorticity shedding. A discrete leading edge vortex (LEV) is shed at every time step after initiation of leading edge vorticity shedding. the strength of the vortex at a time step is determined so as to keep the LESP at its critical value. If the LESP is positive, the sign of the discrete vortex shed at the leading edge is clockwise, and the discrete vortex tends to get convected towards the upper surface. On the other hand, when the LESP is negative, the sign of the discrete vortex is counter clockwise, and it gets convected towards the lower surface. Vorticity shedding terminates when the magnitude of LESP comes below the critical value.

We follow the vortex placement method followed by Ansari et al.⁵¹ to determine the position of the discrete vortex (DV) generated at either edge at any instant of time. It is placed at one third of the distance between the shedding edge and the previously shed vortex. The first DV shed when LEV formation starts is placed using the velocity at the leading edge. Like other discrete vortex methods, the point vortices are convected with the flow velocity at the location of the vortices. A first-order time stepping process is used since the change in accuracy was not much when high-order methods were used. Using a vortex model with core radius v_{core} , we have from Vatistas et al.⁸⁵ that the induced velocities (u and w) by the k^{th} vortex in the X and Z direction are:

$$u = \frac{\gamma_k}{2\pi} \frac{Z - Z_k}{\sqrt{((X - X_k)^2 + (Z - Z_k)^2) + v_{core}^4}} \quad (2)$$

$$w = -\frac{\gamma_k}{2\pi} \frac{X - X_k}{\sqrt{((X - X_k)^2 + (Z - Z_k)^2) + v_{core}^4}} \quad (3)$$

Details of force and moment calculations in the discrete vortex method can be found in Ramesh et al.²

6.2 The reduced order model

This reduced order model is developed to phenomenologically model the evolution of leading vortex structures as revealed by experimental and high fidelity CFD studies. In the early stages of leading-edge vorticity shedding, a shear layer is ejected from the leading edge. The tip of this shear layer

rolls up into a core after some time. Once the roll-up is initiated, the shear layer keeps feeding vorticity into the core until either the vorticity shedding stops, or the core pinches off from the shear layer.

LDVM predicts this flow pattern using discrete vortices shed from the leading edge for the period of time during which the LESP exceeds the critical value. The objective of the reduced order model is to reduce the discrete vortex count in LDVM by merging suitable pairs of discrete vortices shed from the leading edge. In particular, the large number of discrete vortices that represent a huge concentrated vortex core can be replaced by one single vortex that has the combined strength of all the discrete vortices.

We are interested in studying the growth of the core through a model that incorporates a shear layer, and a concentrated vortex at its tip. There are two steps in modeling this phenomenon. The first is the identification of the rollup of the shear layer. Once the shear layer starts rolling up, a vortex that grows in strength with time is introduced at the tip of the shear layer. At each time step, some vorticity is added to this growing single LEV (referred to as SLEV henceforth) by merging an appropriate DV to it. This procedure results in a few point vortices forming a shear layer, from which vorticity is fed into the growing SLEV.

6.2.1 Initial rollup

It is proposed that the shear layer starts rolling up when there is a relative rotation between any two successive vortices near the tip of the shear layer. For identifying the onset of rollup, we keep track of the angular velocity of successive vortex pairs in a shear layer. When the angular velocity $\omega_{i,i-1}$ between the i^{th} and $(i-1)^{th}$ vortices in the shear layer exceeds a threshold value, the shear layer is assumed to have started rolling up at its tip. The i^{th} LEV is declared as the SLEV.

6.2.2 Merging algorithm

As observed by researchers like Moore,³¹ Sarpkaya¹⁷ and Cortelezzi,³⁰ when two like vortices come near each other, they start rotating about the centroid. If one is significantly stronger than the other, the weaker one appears to be revolving about the stronger one since the centroid would nearly coincide with the location of the stronger vortex. In either case, the separation between the vortices keeps decreasing, and tends to a steady state value in the absence of influence from any other external agents or boundaries. Essentially, they behave as a system that can be approximated by a single vortex at the centroid, with a strength that is equal to the combined strength of the two vortices. Following these observations, and deriving insight from the flow pattern predicted by LDVM, we propose a merging algorithm that uses the angular velocity of the line joining the SLEV and a discrete vortex in the LEV, the component of relative velocity along this line and the separation between them as the metrics for determining if the discrete LEV has to be merged with the SLEV.

The relative velocity of two vortices along the line joining can be obtained in terms of the relative distance vector \bar{R}_{21} connecting their positions, and their relative velocity \bar{V}_{21} as,

$$\bar{V}_{rel} = \bar{V}_{21} \cdot \bar{R}_{21} \quad (4)$$

The angular velocity, Ω_{21} between two point vortices can be expressed as,

$$\Omega_{21} = \frac{\bar{V}_{21} \cdot \bar{R}_{21}^\perp}{|\bar{R}_{21}^\perp|} \quad (5)$$

where \bar{R}_{21}^\perp is the vector normal to \bar{R}_{21} .

At every time step after rollup is identified, the algorithm finds a DV within a specified distance $|\bar{R}_{21}|$ from the SLEV that has the maximum angular velocity Ω about the SLEV or the maximum approach speed \bar{V}_{rel} towards the SLEV. This DV is merged to the SLEV, and the combined discrete vortex is convected with the velocity induced at its new location.

The search is necessary in the initial phase of rollup when there can be a quite a few discrete vortices that start rotating about the SLEV. At this stage, the shear layer may even start rolling up very close to the leading edge. However, it has been observed that, within a few time steps after rollup is initiated, the straight shear layer and the concentrated vortex structure become clearly distinguishable. At this stage, the search for a suitable merge candidate is not necessary anymore. Vorticity can be fed into the SLEV by merging the DV at the tip of the shear layer.

We have used a model with a common vortex-core radius for all the discrete vortices, to prevent the induced velocities from becoming unbounded when two point vortices come close to each other.² The distance used for searching in the merging algorithm has been set by trial and error to a value that is 10 times this core radius. The threshold angular velocity to identify initial rollup was set to 0.001 rad/s. Also, it was observed that the search in the merging algorithm could be stopped after 10 discrete vortices were merged to the SLEV.

After this, the DV at the tip of the shear layer is merged to the SLEV at every time step. The number of DVs in the shear layer is approximated by the relation:

$$n_{shear} = \frac{\text{distance of SLEV from LE}}{0.75 * \text{core radius of the DVs}} \quad (6)$$

If the number of DV's in the shear layer is greater than this value at any time step, the DV at the tip of the shear layer is merged to the SLEV. This replicates the shear layer feeding vorticity into the vortex core.

6.2.3 Location of the combined DV

When two DVs of strengths Γ_1 and Γ_2 located at X_1 and X_2 respectively are merged, it has been customary to add their strengths and place the combined vortex at the centroid of the two DVs given by:

$$X_{centroid} = \frac{\Gamma_1 X_1 + \Gamma_2 X_2}{\Gamma_1 + \Gamma_2} \quad (7)$$

However, this approach induces errors in the flow field especially if the merging takes place near the airfoil.³⁰ Cortelezzi (1992) proposed a merging scheme in which the combined vortex is placed at a different location from the centroid so as to conserve the velocity at the shedding location. Following this idea, we propose a novel merging scheme in which the merged DV is placed at a location referred to as the optimal location, (x_{opt}, z_{opt}) . By placing the combined vortex at this

location, we ensure that the Fourier coefficients A_0 and A_1 are conserved before and after merging. This conserves the leading-edge suction, as well as the bound circulation of the airfoil given by

$$\Gamma_b = \pi cU \left[A_0 + \frac{A_1}{2} \right] \quad (8)$$

A 2D Newton iteration is employed to determine (x_{opt}, z_{opt}) that conserves A_0 and A_1 .

6.2.4 Identifying pinch-off

In some cases, the shear layer stops feeding vorticity into the LEV when it attains a maximum strength. This is followed by the LEV getting convected downstream, and the shear layer starting to rollup near the LE to form a new LE vortex structure. We refer to this as LEV 'pinch-off'. To model this phenomenon, we monitor the DVs in the shear layer at every time step. If, at any time step, two adjacent DVs in the shear layer have opposite signs for their angular velocities with respect to the SLEV, a pinch-off is declared to be identified. Following this, the DV in this vortex pair that is close to the LE is declared as a new SLEV. The search algorithm is again initiated to find matching DVs to merge with this SLEV. Meanwhile, the DVs at the edge of the shear layer associated with the first SLEV are merged to it, one at every time step. Thus, the first SLEV represents the LEV structure that pinches off from the shear layer, and the new SLEV models the vortex core that starts rolling up near the LE.

6.2.5 Intermittent LEV shedding

A new LEV is shed each time the LESP reaches the critical value. This is referred to as intermittent LEV shedding. The reduced order model handles this by initiating a new SLEV whenever LESP reaches its critical value. Each SLEV and its shear layer capture the concentrated core and the shear layer structure associated with the individual LEVs.

6.3 Results

In this section, we present a comparison of the results of the reduced order model with those of the LDVM for three cases.

6.3.1 Case 1: Flat plate undergoing 0-90 pitching motion about LE

In Case 1, we study a flat plate that is pitching about its leading edge at a Reynolds number of 1,000. The smoothed ramp motion is generated using Eldredge's canonical formulation.⁸⁶ At the end of the motion, the pitch angle reaches a value of 90 degrees. A non dimensional pitch rate value of $K = 0.2$ is used for this motion. The critical value of LESP for a flat plate at a Re of 1,000 is 0.11.² Fig. 6.1 shows the comparison of LESP variation predicted by the two methods, along with the coefficients of lift, drag and moment. A comparison of the streamline patterns predicted by the two methods at five different instants of time are shown in 6.2.

In this case, the LESP reaches its positive critical value in LDVM during the pitch-up phase of motion, as can be seen from Fig. 6.1. This marks the onset of leading-edge vortex shedding from

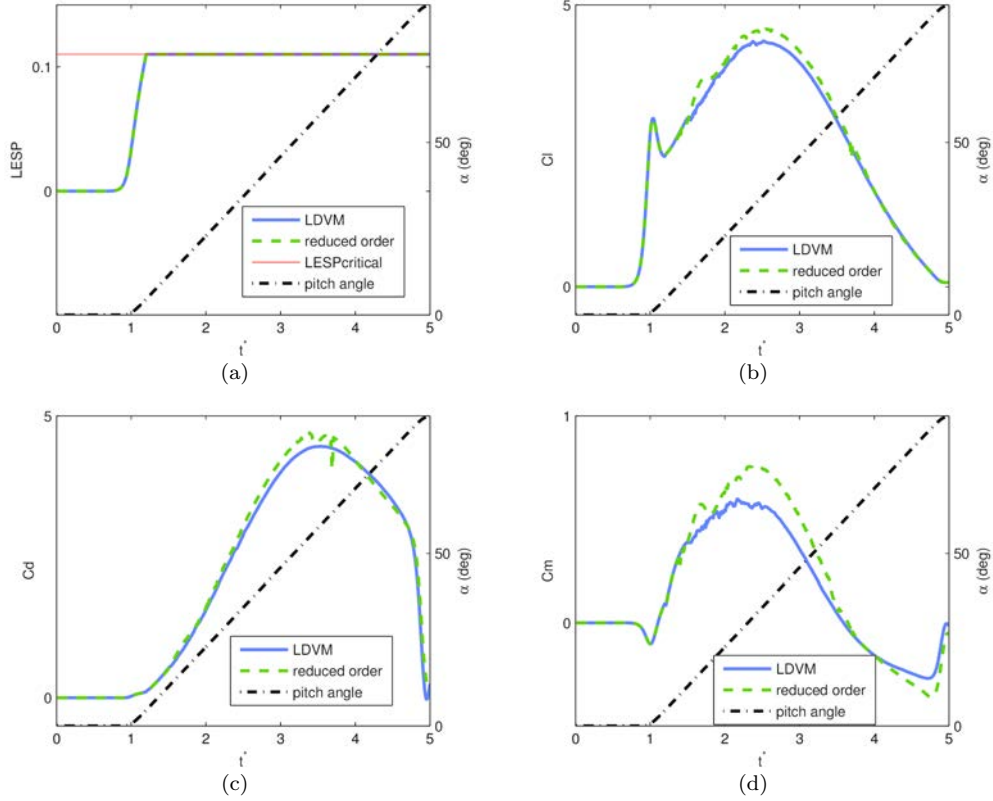


Figure 6.1: Case 1: Comparison of predictions of the reduced order method and LDVM. Variation with $t^* = tU/c$ of: (a) LESP, (b) lift coefficient, (c) drag coefficient, and (d) pitching moment coefficient about the mid chord.

the upper surface of the plate. The LESP remains at the critical value till the end of the motion. This results in an uninterrupted shedding of leading edge vorticity during the remaining span of motion. The evolution of this LEV structure in the LDVM can be observed in the streamline plots in Fig. 6.2. The DVs representing the LEV are also marked in these plots using red dots. The shear layer ejected from the leading edge soon rolls up into a concentrated vortical structure on the upper surface near the leading edge. This structure continues to grow in size as the shear layer keeps rolling up and feeding vorticity into it. A thin shear layer that connects the concentrated core to the leading edge is apparent soon after the shedding starts. This shear layer elongates when the concentrated vortex core convects away from the plate. The concentrated LEV core is attached to the LE through this thin shear layer until the end of the motion.

The reduced order model exactly predicts the onset of LEV shedding and thereafter closely replicates the flow field. This can be seen from the streamline patterns of the reduced order method in Fig. 6.2. An SLEV is initiated as soon as the relative rotation between a pair of DVs at the tip of the shear layer exceeds the threshold value. Following this, one DV is merged to the SLEV at every time step using the search criterion. After 10 DVs are merged to the SLEV, the search is terminated, and the merging is done based on the approximate shear layer length given by (6). By this time, the thin shear layer and the concentrated core structure of the LEV is apparent in LDVM ($t^* = 1.3$). During the later time steps, the SLEV in the reduced order model represents the strength and position of concentrated vortex core of LDVM. The elongated shear layer connects

the SLEV to the leading edge.

The comparison of the results show that lift and drag coefficient histories as well as the history of coefficient of moment about the mid-chord predicted by the reduced order model agree well with those predicted by LDVM. At the last time step, there are 380 DVs in LDVM that accounts for the vorticity shed from the leading edge during the period of time for which LESP was above its critical value. Meanwhile, the reduced order model can predict this flow field by using just 89 DVs. Corresponding to the decrease in the number of discrete LEVs in the flowfield, the run time for the reduced order (20.1 s) is smaller compared to that of LDVM (29.3 s).

6.3.2 Case 2: SD7003 airfoil undergoing 0-90-0 pitching motion about trailing edge

In this study, we consider an SD7003 airfoil undergoing a pitch up-return motion. It undergoes a smoothed 0-90-0 pitch up-return motion with the pivot point at the trailing edge. A non dimensional pitch rate of $K = 0.4$ is used for this motion. The critical value of LESP for an SD7003 airfoil at a Reynolds number of 100,000 is 0.14. The comparison of LESP and the time variations of force and moment coefficients between the two methods are shown in Fig. 6.3. Figure 6.4 presents a comparison of the streamline patterns predicted by the two methods at different instants of time.

The LESP value for this motion reaches the critical value during the pitch-up phase, as shown in Fig. 6.3. It remains at the critical value for some time, and comes down during the return phase. This indicates that vorticity is shed from the leading edge from the middle of the pitch-up phase to the middle of the return phase. The LESP value reaches the negative critical value towards the end of the motion, indicating the shedding of another LEV from the lower surface. Thus, this is a case where intermittent LEV shedding occurs. Fig. 6.4 shows the evolution of the flow field predicted by LDVM for this case. The shear layer associated with the first LEV starts rolling up near the LE. This vortex continues to grow until the vorticity shedding stops. When the shedding terminates, the shear layer detaches from the leading edge. The vortex structure and the shear layer get convected downstream, and they interact with the trailing edge vorticity. Meanwhile, vorticity shedding starts again at the leading edge on lower surface after a short pause. This shear layer can be seen to be rolling up near the leading edge towards the end of the motion.

Comparison of LESP histories of the two methods show that the reduced order model predicts the onset and termination of leading edge vorticity shedding at the same instants of time as LDVM. The reduced order model captures the above mentioned features of the flowfield as can be seen from the streamline plots in Fig. 6.4. It predicts the roll-up of the first shear layer successfully, and models the subsequent growth of the leading edge vortex very closely to the predictions of LDVM using an SLEV. The SLEV remains attached to the leading edge through a shear layer of varying length airfoil until the vortex shedding stops. During this period of time, the shear layer is seen to add vorticity to the SLEV. Upon the termination of vorticity shedding, the shear layer detaches from the leading edge, and the DVs in the shear layer continue to be merged with the SLEV in the following time steps. When the LESP reaches the critical value for the second time, a new SLEV is initiated to capture the new LEV structure. Meanwhile, the DVs in the shear layer associated with the first SLEV are being merged with the first SLEV.

The force coefficient histories of the two methods are in good agreement, except for the slight discrepancy towards the end of the motion when the interaction between LEV and trailing edge vorticity takes place. The coefficient of moment about the quarter chord predicted by the reduced

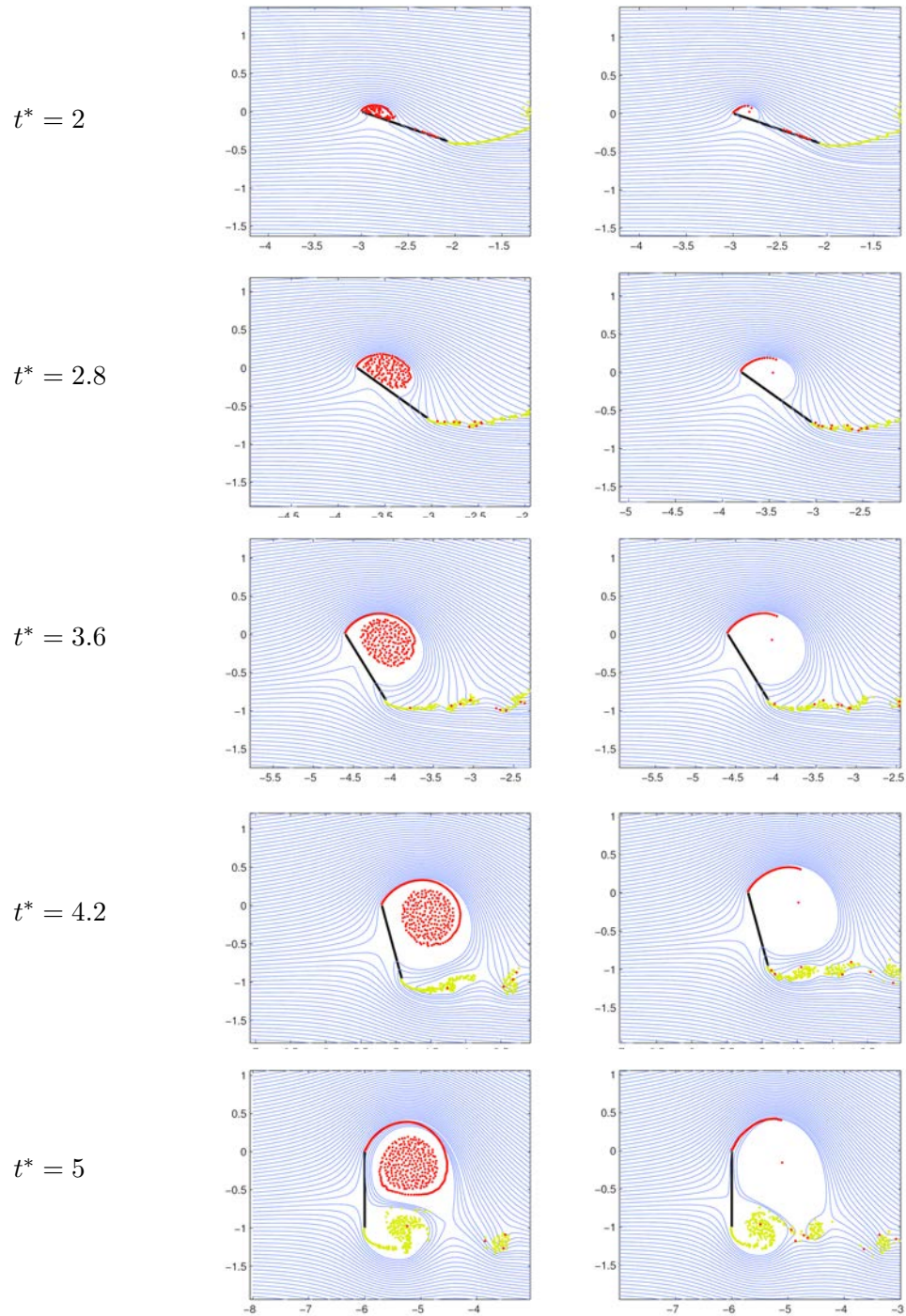


Figure 6.2: Case 1: Streamline patterns predicted by LDVM (left) and the reduced order method (right) at five time instants.

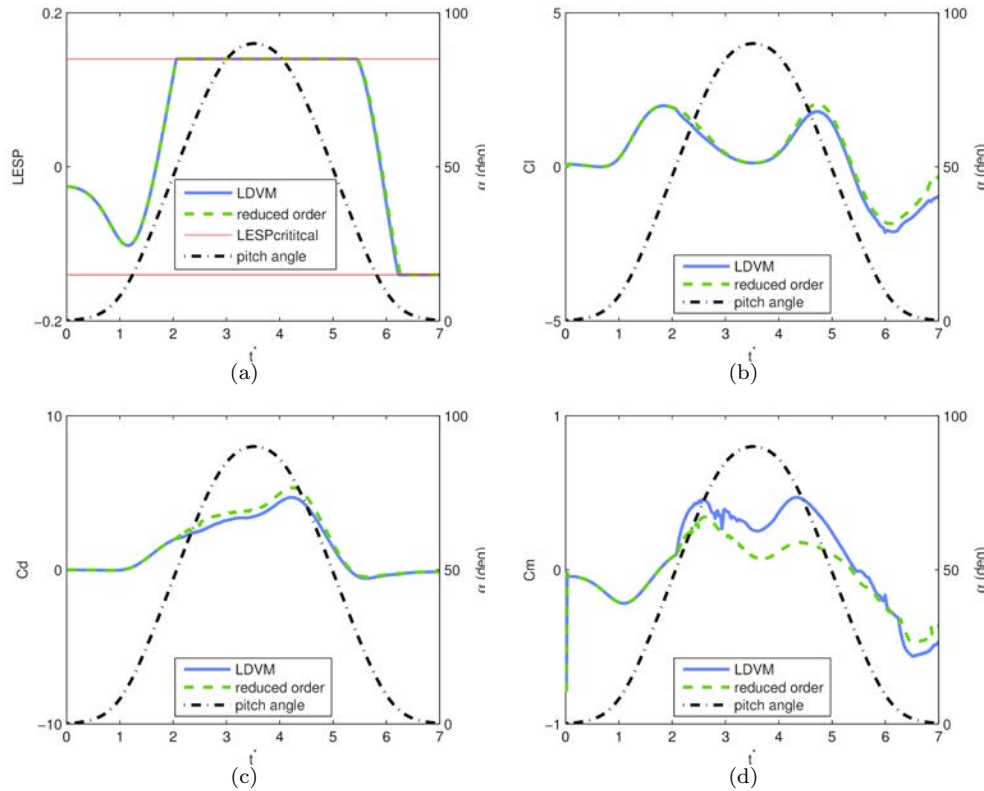


Figure 6.3: Case 2: Comparison of predictions of the reduced order method and LDVM. Variation with $t^* = tU/c$ of: (a) LESP, (b) lift coefficient, (c) drag coefficient, and (d) pitching moment coefficient about the quarter chord.

order method, however, shows slight discrepancy compared to the prediction of LDVM. At the end of the motion, the reduced order model predicts the leading edge vorticity in the flow field using just 36 DVs whereas the LEV structure in LDVM is represented by 274 DVs. Computation time savings in using the reduced order model is evident in the run time of 6.9 s for the reduced order model as compared to 10.6 s for LDVM.

6.3.3 Case 3: Flat plate undergoing 0-45 pitch up-hold motion about leading edge

This case study deals with the pitch up-hold maneuver of a flat plate at a Reynolds number of 1,000. The pitch-ramp motion is generated using an Eldredge function. The flat plate pitches up about the leading edge with a non-dimensional pitch rate of $K = 0.4$. The value of critical LESP for this case is 0.11. The comparison of LESP and the time variation of force and moment coefficients between the two methods are shown in Fig. 6.5. Streamline patterns predicted by the two methods at different instants of time are compared in Fig. 6.6.

The LESP for this motion reaches the critical value when the pitch angle is approximately 3 degrees. From this instant, it stays at the critical value till the end of the motion. Consequently, vorticity is continuously shed from the leading edge from this instant till the end of the motion. The flow field predicted by LDVM is shown in Fig. 6.6. The shear layer starts rolling up near the leading edge,

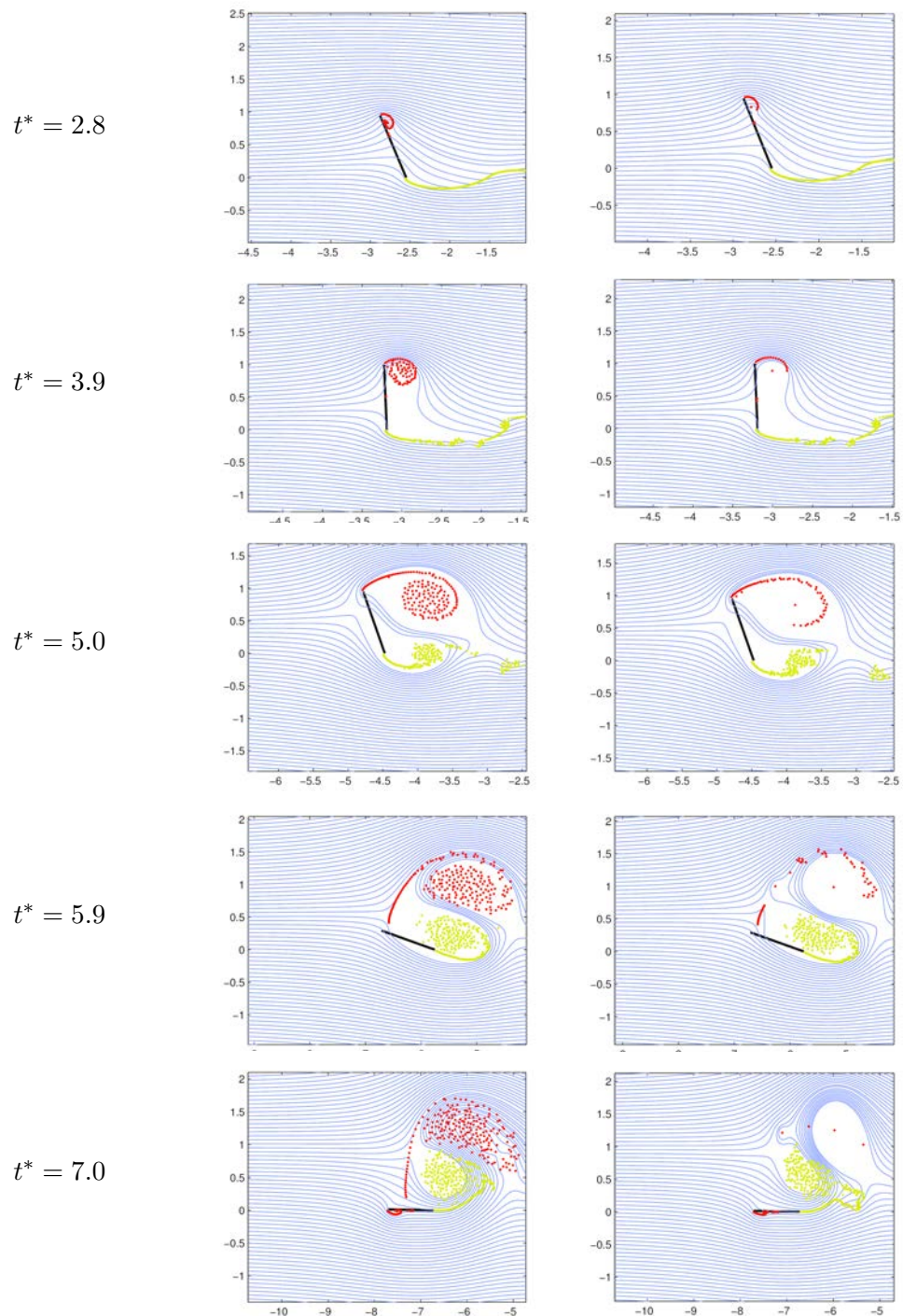


Figure 6.4: Case 2: Streamline patterns predicted by LDVM (left) and the reduced order method (right) at five time instants.

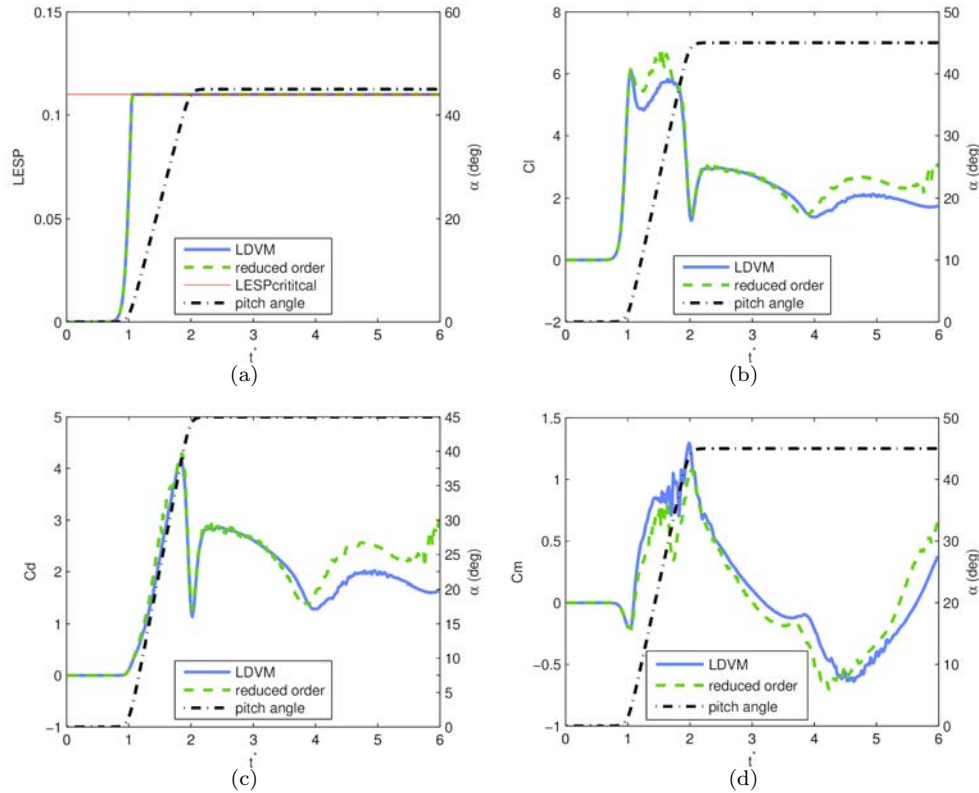


Figure 6.5: Case 3: Comparison of predictions of the reduced order method and LDVM. Variation with $t^* = tU/c$ of: (a) LESP, (b) lift coefficient, (c) drag coefficient, and (d) pitching moment coefficient about the quarter chord.

forming a cluster of discrete vortices. As time progresses, the shear layer feeds more DVs into this core, and the core grows in size. The core is seen to move away from the surface of the flat plate towards the second half of the motion. Later, the concentrated LEV structure pinches off from the shear layer. A part of the shear layer gets convected downstream with the core, while at the same time rolling up into the core. The remaining part of the shear layer that is still attached to the leading edge starts rolling up and forms another concentrated vortex structure near the LE.

It can be observed from Fig. 6.6 that the reduced order model replicates the initial rollup and growth of the LEV as well as its pinch-off. An SLEV is initiated at the instant when the initial rollup is identified. Point vortices from the shear layer are merged to this SLEV at each time step, and hence the shear layer and the concentrated vortex structure are captured by the reduced order model. The reduced order model also successfully identifies the LEV pinch-off and initiates a second SLEV to model the rollup of the tip of shear layer attached to the leading edge. Following this, the DVs in the shear layer associated with the first SLEV are merged to it at every time step. Simultaneously, the ones in the shear layer associated with the second SLEV are merged to the second SLEV. However, the reduced order model predicts pinch-off a little earlier compared to LDVM. This can be noted from the streamline plot at $t^* = 5.1$. At this time instant, a pinch-off is not yet visible according to the predictions of LDVM; but a pinch-off is seen to be taking place according to the reduced order model. A significant interaction of the trailing edge vorticity with the LEV core precedes the pinch-off in LDVM. This may need to be taken care of for eliminating

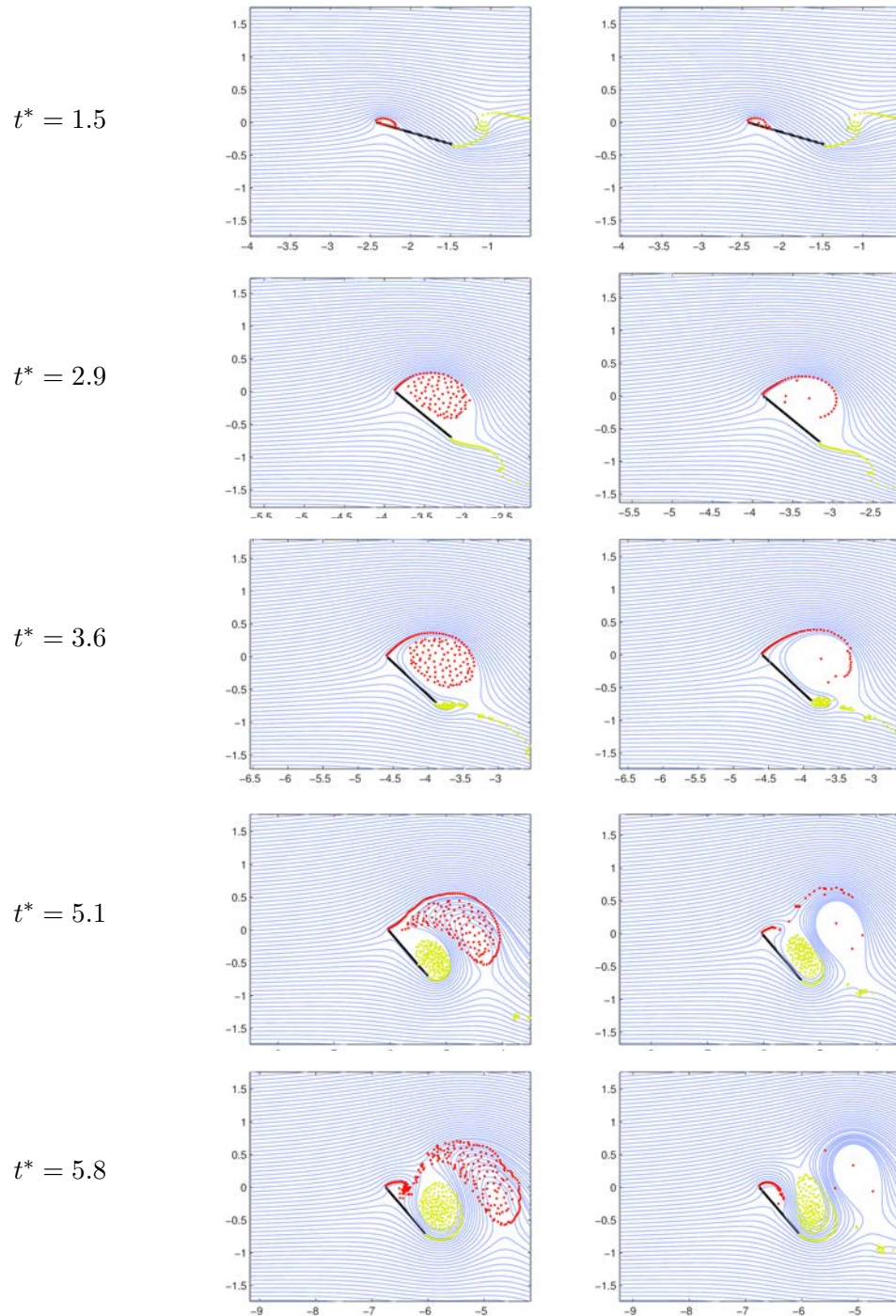


Figure 6.6: Case 3: Streamline patterns predicted by LDVM (left) and the reduced order method (right) at five time instants.

| Case No. | Discrete LEV count LDVM | Discrete LEV count reduced order | Run time LDVM (seconds) | Run time reduced order (seconds) |
|----------|----------------------------|-------------------------------------|----------------------------|-------------------------------------|
| 1 | 380 | 89 | 29.3 | 20.1 |
| 2 | 274 | 36 | 10.6 | 6.9 |
| 3 | 260 | 38 | 17.1 | 13.6 |

Table 6.1: Comparison of run times for the three cases between LDVM and the reduced order method

the discrepancy in the predictions of the reduced order model.

It can be observed from the LESP and force and moment coefficient history plots in Fig. 6.5 that the reduced order model accurately predicts these quantities till there is significant interaction of leading edge vorticity with the LEV in addition to replicating the flow field. However, there are slight discrepancies after the interaction becomes strong. This is evident in the streamline plots. The trailing edge vorticity starts interacting with the LEV after $t^* = 3.6$. The lift and drag coefficient predictions of the reduced order model show mismatch approximately after this instant of time.

At the end of the motion, LDVM has 260 DVs in the simulation for modeling the leading edge vorticity whereas the reduced order model has just 38 DVs. Owing to the reduction in number of discrete vortices compared to the first two cases, a reduction in computational time has been obtained with the reduced order model for this case. The run time of the reduced order model was 13.6 seconds whereas it took 17.1 seconds for the LDVM code to generate the results.

Table 6.1 provides a comparison of performance of the new reduced order model with that of LDVM in terms of the discrete vortex count and run time.

6.4 Interim Conclusions

In this chapter, we presented an approach to reduce the vortex count in discrete vortex methods for modeling unsteady aerodynamic flows. We proposed a phenomenological approach to modeling the leading edge vortex from 2D bodies undergoing unsteady motion. We proposed an algorithm to identify the initial roll-up of the shear layer shed from the leading edge, and to reduce the discrete vortex count by merging suitable pairs of discrete vortices. The model has the capability to handle intermittent LEV shedding and LEV pinch-off. The reduced order model shows promise in terms of reducing the count of discrete vortices compared to the higher order LDVM model, and thus, saving computation time significantly, while also giving predictions of forces and moments close to that of the higher order method. The method is found to be more efficient in cases where there are large number of LEVs in the higher order method.

The predictions of the model deviate from that of the higher order method when there is significant interaction between the vorticity shed from the leading and trailing edges. The model needs to be adapted to better handle such situations. The algorithm can be implemented to reduce the discrete trailing edge vortex count, and achieve faster computation times.

Chapter 7

Unsteady Vortex Lattice Method with Modifications for Prediction of LEV Formation on Finite Wings

In this research, the unsteady vortex lattice method (UVLM) is used as the foundation for the low-order method. The traditional UVLM, intended for inviscid analysis of finite-wing systems undergoing unsteady motions, is well understood and is described in text books.⁷⁶ In the first part of the current work, described in Section 7.1, the UVLM was adapted with minor extensions for prediction of LEV initiation. These extensions relate to (i) calculation of the spanwise distribution of the *LESP* and (ii) an optional separated tip-flow model for improved modeling of the wing tip vortex. In the second part of the current work, described in Section 7.2, the UVLM has been significantly modified to include a spanwise-varying and time-varying vortex sheet that is shed from the leading edge. The former technique is referred to as “UVLM” and the later as “Modified UVLM” in the remainder of this report.

7.1 UVLM for prediction of LEV initiation

This section describes the minor modifications made in the initial portion of this research to the standard UVLM⁷⁶ for prediction of LEV initiation. Figure 7.1 illustrates the discretization of an example wing-tail geometry into vortex rings for UVLM analysis. For unsteady effects, the time-stepping approach⁷⁶ models the shedding of trailing-edge vorticity by adding a new vortex ring (per strip) at each time step, as illustrated in Figure 7.2. The following subsections discuss minor modifications to the UVLM to calculate the spanwise distribution of *LESP* (Section 7.1.1) and the addition of an optional separated tip-flow model (Section 7.1.2).

7.1.1 *LESP* evaluation for finite wing

Of particular interest in the current work is the determination of the spanwise variation of $LESP(y, t)$ along the wing at every time step. For this calculation, the strengths of the bound-vortex filaments on each chordwise strip are considered. Instead of applying thin airfoil theory to UVLM to obtain *LESP*, previous work⁸⁷ derived an approximation of the first-order coefficient $A_0(t)$;

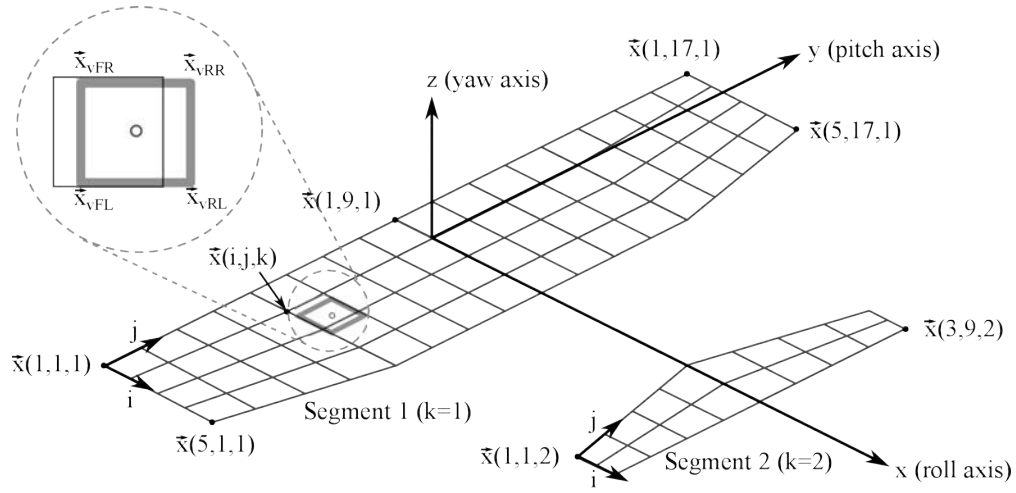


Figure 7.1: Illustration of vortex-lattice discretization of an example wing-tail geometry.

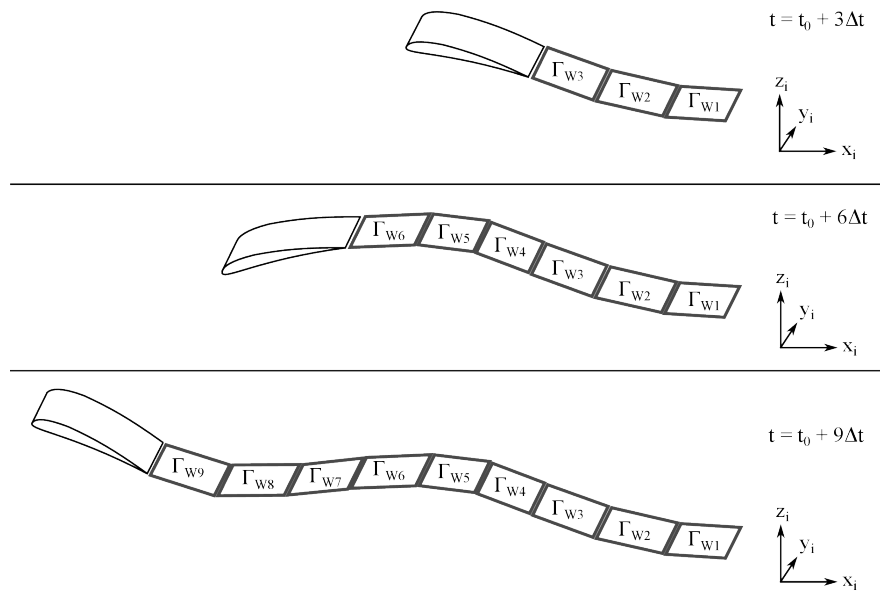


Figure 7.2: Snapshots of TEV shedding in vortex ring representation.

$$A_0(t) = \frac{1.13\Gamma_1(t)}{U_\infty c \left[\cos^{-1} \left(1 - \frac{2\Delta x}{c} \right) + \sin \left\{ \cos^{-1} \left(1 - \frac{2\Delta x}{c} \right) \right\} \right]} \quad (1)$$

The $A_0(t)$ term for each wing strip is taken as the $LESP(y, t)$ for that strip at the time step.

7.1.2 Optional tip-vortex model

Traditional UVLM assumes that the tip vorticity is attached to the tip-edge of the wing, and sheds at the trailing edge of the wing tip. At high angles of incidence, however, experimental and computational flow-visualization images (for example, Figure 3.5) show that the tip vorticity is not attached to the tip, but instead detaches and rolls up while being convected in the approximate direction of the freestream. While the effect of the detached tip vortex does not differ much from that of the attached tip vortex for most high-aspect-ratio wings, discrepancies for low-aspect-ratio wings prompted the development of a “separated tip-flow model” in the current implementation of the UVLM.

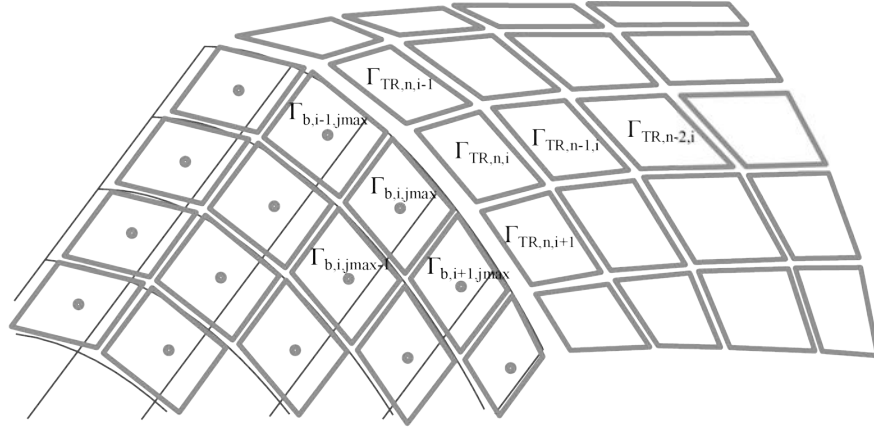


Figure 7.3: Schematic description of separated tip flow model.

Figure 7.3 describes the scheme of tip flow model. A tip vortex ring is shed from the side edge of wing at each time step. The basic idea of separated tip flow model in current UVLM is based on a few conventional models for slender wings, as typified by Levin and Katz.⁸⁸ They assume zero vorticity at the highly swept leading edge similar to the Kutta condition at the trailing edge. Considering these analogies, the strength of tip vortex ring Γ_{TR} can be approximated by Kelvin’s theorem for a spanwise direction at wing tip, as follows.

$$\Gamma_{TR,n} = \Gamma_{b,jmax}^{n-1} \quad (2)$$

It is noteworthy that the analogy has some discrepancies. For example, most of slender-wing systems have sharp leading edges but the wing tip of a typical wing is not always sharpened, which does not support the use of a Kutta-condition-like situation at wing tip. However, modelling the tip flow is beyond the scope of this project and current UVLM employs this simple model when evaluating the influence of tip vortices. For the location of tip vortex shedding, Levin and Katz also

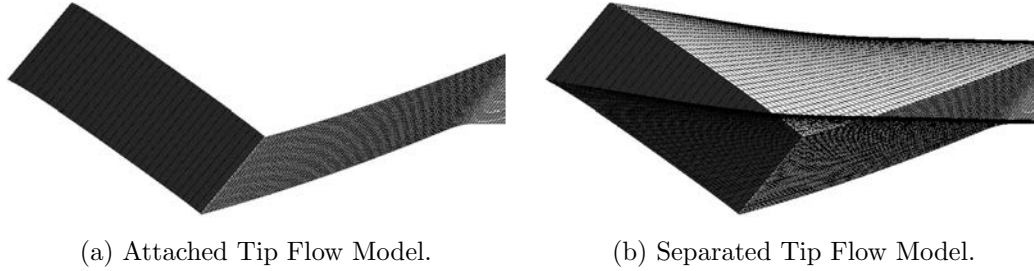


Figure 7.4: Comparison of distribution of vortex lattices.

proposes to place the newly shed vortex ring at the half interval of translation distance $U_\infty \Delta t / 2$ from the tip edge and current UVLM adopts the same idea.

To avoid the significant difficulties with modeling the roll up of the separated tip flow and likely interference of the rolled-up vortex sheet with the wing surface, the current separated tip flow model is based on straight wake sheet, as shown in figure 7.4. Figure 7.4 compares the vortex-sheet geometries for the attached-tip-flow model and the separated-tip-flow model.

7.2 Modified UVLM for prediction of LEV formation

7.2.1 Leading edge vortex

Leading edge vortex (LEV) refers to vorticity shed from the leading edge. While TEV and tip vortices are shed from respective edge in every time step, LEV shedding in UVLM is implemented only when $LESP(t) > LESP_{crit}$.

Modelling of LEV for a three-dimensional unsteady flow is a challenge because there are few prior successful works using vortex-ring representation, in contrast to the two-dimensional LEV model in which discrete-vortex representation has large popularity. On the other hand, there are several successful implementations of LEV models for delta wings. In such applications, it is well known that LEV sheet distribution of slender wing results in a pair of steady vortical structure from the shedding edges, and these are easily modelled by a pair of vortex cores representing the center line of the turn, as typified by Brown and Michael.²³ In another example, Kandil *et al.*⁸⁹ use multiple vortex filaments shed from the leading edge of the delta wing in place of LEV sheets. The other example is a hybrid method of discrete-vortex model and vortex ring representation. Katz⁹⁰ assumes a large vortex ring extending from the leading edge to the trailing edge in which the front edge of the ring behaves as a single LEV filament and the aft edge performs as a single TEV filament. Although these prior works give a lot of insights, the current UVLM cannot directly employ these models because of their limited generality. Also, line-vortex model will need a new formulation to evaluate the representative circulation strength and line distribution in three-dimension. Considering the trade-off between the merit and the difficulties of both models, vortex-ring representation was chosen for the LEV model in current work.

The main issue of modelling LEV is the evaluation of the strength of circulation shed from the leading edge. It is an ambiguous problem in UVLM because the velocity field at the leading edge becomes numerically infinite, but it must be a bounded value. The numeric singularity at the leading edge results from the postulate of inviscid flow. Thus, an additional condition to determine

the bound circulation and LEV strength around the leading edge is necessary.

The simplest LEV model is to assume the same Kutta condition at the leading edge. Imposing Kutta condition at the leading edge, the strength of nascent LEV element is simply obtained from the adjacent wing bound circulation closest to the leading edge by Kelvin's theorem and LEV sheet is shed upstream, like TEV is shed downstream. This method is broadly used to model LEV of delta wings with sharp leading edges, for example, by Levin and Katz.⁸⁸ Ansari *et al.*, in their discrete-vortex model, derived LEV distribution from Kelvin's theorem to obtain the flow field which enabled Kutta condition (zero vorticity) at the leading edge.⁵⁰ However, in inviscid flow modelled by vortex-ring representation, the wing bound circulation at the leading edge cannot be defined clearly because the leading edge is a singular point and the vorticity at the leading edge becomes infinite, i.e. numeric solution of the leading edge circulation strongly depends on the resolution of discretization. In addition, application of Kutta condition to describe the flow field around the leading edge is still an open question. Smith⁹¹ pointed out that the flow velocity behind the separation line must be parallel to the stream line because vortex sheets form the separated stream surface. Wu *et al.* proposed an asymptotic viscous theory to model boundary layer separation.⁹² Comprehensive discussion about applicability of Kutta condition in various cases was provided by Crighton.⁹³ After a comparative investigation about flow perturbation relating to geometry, unsteadiness, separation, compressibility, instability wave, and oncoming turbulence, he concluded that Kutta condition would be valid in a low Re and St cases, but it is still an open matter about whether to apply Kutta condition to the flow around the leading edge.

In the current work, the LESP concept does not explicitly account for a Kutta-type condition in LEV simulation but has a criterion to enforce the flow field at the leading edge. The LESP concept is intended for application to rounded-leading-edge geometries. In these cases, there must be attached flow turning around the leading edge before LEV formation, and this flow generates the leading-edge suction. According to the work of Ramesh *et al.*,² there should be a finite vorticity distribution at the leading edge even under LEV formation because it is known that the leading-edge suction does not vanish but converges to a finite value. For example, according to Pinkerton⁹⁴ the leading-edge suction force in post-stall condition, converted from the raw pressure data, asymptotically approached to a finite value even though the stagnation point retreated. LESP is a measure of suction and it will also give a direction for the vorticity at the leading edge after initiation of LEV formation. Ramesh *et al.* established a new LEV model that the vorticity field around the leading edge saturates at $LESP(t) = LESP_{crit}$, and the strength of shed LEV is determined by the suction parameter $LESP(t)$ holding an appropriate finite value $LESP_{crit}$. Considering the permanent continuity of vorticity, because the bound circulation can maintain the flow field around the leading edge until the onset of LEV initiation ($LESP(t) < LESP_{crit}$), it is reasonable to think that the vorticity field around the leading edge preserves the flow ($LESP(t) = LESP_{crit}$) and the surplus of vorticity is eventually shed to the fluid as LEV. The current UVLM employs the LESP concept including this LEV model. The strength of shed LEV is determined using an iteration in which $LESP(t)$ saturates at $LESP_{crit}$ for every wing strip in which $LESP(t)$ exceeds $LESP_{crit}$. Denoting superscript k as iteration number, the strength of LEV sheet for a wing strip can be evaluated by Newton-Raphson method as follows:

$$\Gamma_L^k = \frac{\Gamma_L^{k-1} - \Gamma_L^{k-2}}{LESP^{k-1} - LESP^{k-2}}(LESP_{crit} - LESP^{k-1}) + \Gamma_L^{k-1} \quad (3)$$

Due to the assumption of nonzero vorticity at the leading edge under LEV formation, LEV sheet is tangentially shed, which means LEV sheet leaves in the z direction in body frame of reference.

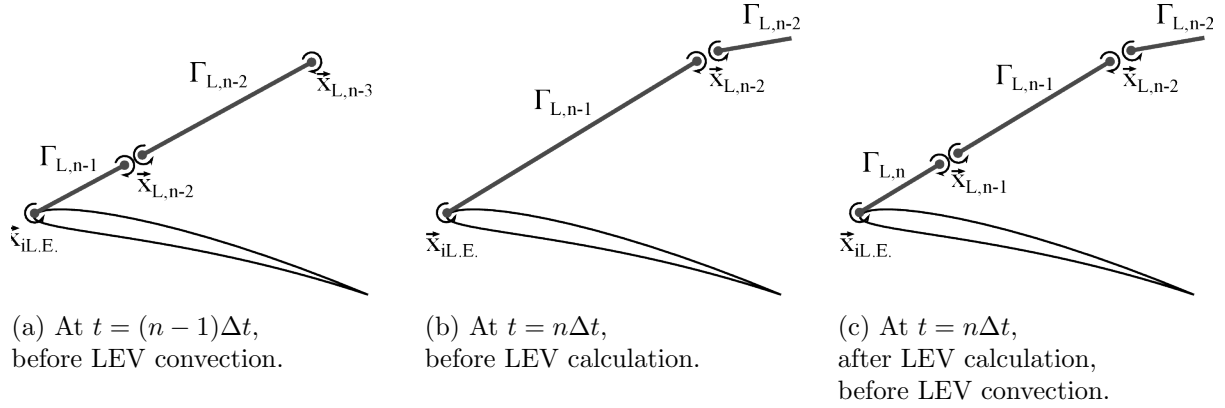


Figure 7.5: Placement of LEV ring vortex.

In order to place the new LEV sheet, the current UVLM employs a method of LEV placement proposed by Ansari *et al.*⁵¹ The idea is to place new point-vortex of LEV at one-third distance from the leading edge to the last LEV. It can be formulated as below,

$$\vec{x}_{L,n-1} = \frac{2}{3}\vec{x}_{i,L.E.} + \frac{1}{3}\vec{x}_{L,n-2} \quad (4)$$

This formulation is an approximated conversion from grid-based vortex sheet model to discrete vortex model and is advantageous in sense that it can simultaneously follow the wing motion and vortex convection.

As shown in figures 7.5b–7.5c, the placement of a new LEV panel is implemented by splitting a previously shed LEV panel into two LEV panels at the point determined by equation 4. Then, in figure 7.5, a nascent LEV $\Gamma_{L,n}$ is defined as the vortex ring lying across the leading edge and $\vec{x}_{L,n-1}$. However, as shown in figures 7.5, the front end of the new LEV ring coincides with the leading edge and this component of the LEV ring violates the precedent Kutta-type assumption because it behaves as a large and negative circulation on flow field.

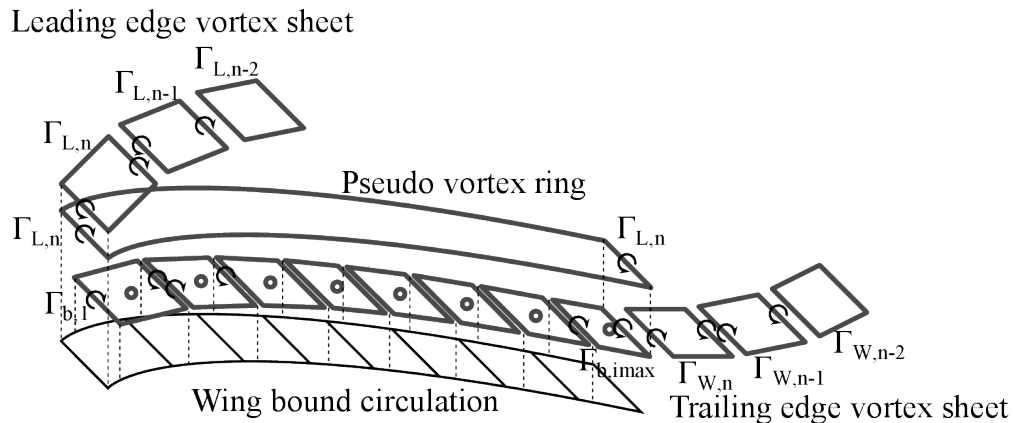


Figure 7.6: Schematic description of pseudo vortex ring.

In order to prevent this numerical side effect, the current UVLM introduces a pseudo vortex ring to the distribution of the wing bound circulation. Figure 7.6 shows the alignment and the strength of

the pseudo vortex ring. The pseudo vortex ring is a fictitious vorticity distribution and compensates for the mathematical discontinuity caused by LEV rings at the leading edge. The pseudo vortex ring is overlaid on the wing bound circulation from separation line (the leading edge) to the trailing edge shedding point (not always the same as the trailing edge). Considering Helmholtz law at the leading edge, the strength of the pseudo vortex ring can be derived as the current Γ_L at the wing strip. The presence of the pseudo vortex ring affects the circulation conservation (Kelvin's theorem), i.e. it provides the circulation component Γ_L^n at the trailing edge shedding point, which is accounted for in the modified UVLM.

7.2.2 Solution of linear system

As noted in previous section, the distribution of wing bound circulation is derived by boundary condition on wing surface which specifies that zero normal component of the velocity on the surface is enforced. This boundary condition can be described by linear equation 5.

$$(\vec{v}_b + \vec{v}_\infty + \vec{v}_m + \vec{v}_W + \vec{v}_{TL} + \vec{v}_{TR} + \vec{v}_L) \cdot \vec{n} = 0 \quad (5)$$

As mentioned in previous sections, velocity induced by motion \vec{v}_m is determined by given motion kinematics, velocity induced by shed vortices \vec{v}_W , \vec{v}_{TL} , \vec{v}_{TR} , and \vec{v}_L are given by application of Biot-Savart law to each shed vortex ring in the flow field. Thus, unknown values are only wing bound circulation Γ_b and equation 5 is rewritten for K th wing bound vortex ring and the other known vortices using influence coefficient as below.

$$\sum_{n=1}^N a_{b,Kn} \Gamma_{b,n} + (\vec{v}_\infty + \vec{v}_{m,K}) \vec{n}_K + \sum a_W \Gamma_W + \sum a_{TL} \Gamma_{TL} + \sum a_{TR} \Gamma_{TR} + \sum a_L \Gamma_L = 0 \quad (6)$$

$$\begin{aligned} & [a_{b,nm}] \begin{pmatrix} \Gamma_{b,1} \\ \vdots \\ \Gamma_{b,K} \\ \vdots \\ \Gamma_{b,N} \end{pmatrix} + \begin{pmatrix} (\vec{v}_\infty + \vec{v}_{m,1}) \vec{n}_1 \\ \vdots \\ (\vec{v}_\infty + \vec{v}_{m,K}) \vec{n}_K \\ \vdots \\ (\vec{v}_\infty + \vec{v}_{m,N}) \vec{n}_N \end{pmatrix} + [a_{W,nm}] \begin{pmatrix} \Gamma_{W,1} \\ \vdots \\ \Gamma_{W,K} \\ \vdots \\ \Gamma_{W,N} \end{pmatrix} \\ & + [a_{TL,nm}] \begin{pmatrix} \Gamma_{TL,1} \\ \vdots \\ \Gamma_{TL,K} \\ \vdots \\ \Gamma_{TL,N} \end{pmatrix} + [a_{TR,nm}] \begin{pmatrix} \Gamma_{TR,1} \\ \vdots \\ \Gamma_{TR,K} \\ \vdots \\ \Gamma_{TR,N} \end{pmatrix} + [a_{L,nm}] \begin{pmatrix} \Gamma_{L,1} \\ \vdots \\ \Gamma_{L,K} \\ \vdots \\ \Gamma_{L,N} \end{pmatrix} = 0 \end{aligned} \quad (7)$$

In equation 7, the symbol $[\]$ means a $N \times N$ matrix. As a result, the boundary condition for wing bound circulation reduces to an $N \times N$ matrix equation, and the unknown Γ_b is derived by a linear solution technique, such as LU decomposition method.

7.2.3 Calculation of aerodynamic load

Aerodynamic loads are obtained from pressure distribution on wing surface and the leading-edge suction force. The pressure distribution is derived from the wing bound circulation distribution and the suction force is evaluated from the A_0 value for each wing section.

$$C_L = C_N \cos \alpha + C_S \sin \alpha \quad (8)$$

7.2.4 Vortex sheet roll up

Vortex roll up in UVLM is a model for wake vorticity convection. Vorticity distribution moves by the local flow velocity. Vortex roll up is important in situations in which shed vortices directly interact with the lifting body. Under LEV formation, roll up becomes a dominant feature of aerodynamics⁹¹ because the LEV structure develops near the wing and generates vortex lift. On the other hand, vortex roll up is often problematic due to a numeric instability. Characteristic numeric instability in UVLM is caused by singularity of vortex model and geometric discrepancy, which are discussed in the following subsections.

7.2.4.1 Numerical process of vortex roll up

Vortex wake roll up calculates a displacement of distribution of vortex sheet driven by local velocity field \vec{v}_r . The displacement of a grid point of a vortex ring during a unit time-step in inertial frame of reference $\Delta\vec{x}$ is simply described as

$$\Delta\vec{x} = \vec{v}_r \Delta t, \quad (9)$$

where $\vec{v}_r = (\vec{v}_b + \vec{v}_W + \vec{v}_{TL} + \vec{v}_{TR} + \vec{v}_L)$. Each velocity term is given by Biot-Savart law, but the finite difference method (FDM) for the time advancing scheme has a number of options. Several kinds of numerical schemes are applicable to UVLM and the simplicity of the scheme is proportional to computational speed and numeric instability. A basic way to calculate the time-marching vortex roll up is Euler method which estimates the displacement only by information from the current time-step,⁷⁶ shown below.

$$\Delta\vec{x} = \vec{v}_r^n \Delta t \quad (10)$$

The well-known multi time-step method to solve ODE is Runge-Kutta method. Runge-Kutta method is based on Taylor expansion and fourth-order Runge-Kutta method is especially popular in use;

$$\Delta\vec{x} = \frac{1}{6} \left(\vec{K}_1 + \vec{K}_2 + \vec{K}_3 + \vec{K}_4 \right) \quad (11)$$

where each coefficient vectors are available as

$$\begin{cases} \vec{K}_1 = \Delta t \cdot \vec{v}_r(t, \vec{x}) \\ \vec{K}_2 = \Delta t \cdot \vec{v}_r \left(t + \frac{1}{2} \Delta t, \vec{x} + \frac{1}{2} \vec{K}_1 \right) \\ \vec{K}_3 = \Delta t \cdot \vec{v}_r \left(t + \frac{1}{2} \Delta t, \vec{x} + \frac{1}{2} \vec{K}_2 \right) \\ \vec{K}_4 = \Delta t \cdot \vec{v}_r \left(t + \frac{1}{2} \Delta t, \vec{x} + \vec{K}_3 \right). \end{cases} \quad (12)$$

However, Dovgii and Shekhovtsov⁹⁵ pointed out that conventional multi-step method would likely spoil the accuracy in UVLM. The paradox that high-order scheme enlarges the error results from the fact that major source of error in UVLM is an input error, and a high-order scheme with multiple references increases the chance of input error. For example, fourth-order Runge-Kutta method requires us to calculate the derivative four times to estimate the four unknown coefficients, and this process accumulates the input errors. In order to prevent this paradoxical error in multi-step method, the UVLM has to employ a method with single reference. It is known that some multi-step method with variable coefficients are replaced by constant coefficients by approximating the reference function as an algebraic series. For example, Paul *et al.*⁹⁶ employed Adams-Bashforth method in UVLM.

In addition, according to Dovgii and Shekhovtsov,⁹⁵ the order of time-marching method in UVLM does not determine the numeric accuracy and they proposed two low-order FDMs as an alternate of predictor-corrector scheme. One FDM that they proposed is a two-step Euler method with second order approximation, as shown below.

$$\Delta \vec{x} = \vec{v}_r^n \left\{ 1 + \frac{t^{n+1} - t^n}{2(t^n - t^{n-1})} \right\} - \vec{v}_r^{n-1} \left\{ \frac{t^{n+1} - t^n}{2(t^n - t^{n-1})} \right\} \quad (13)$$

Equation 13 takes into account an acceleration of vortices by putting weight in present velocity term. Another FDM is a balanced FDM of equation 13.

$$\Delta \vec{x} = \frac{\vec{v}_r^n + \vec{v}_r^{n-1}}{2} \Delta t \quad (14)$$

The FDM of equation 14 consists of the present and the previous-time-step information, and it is a first-order approximation. After investigations and tests of these schemes in current UVLM problem, it was shown that high-order scheme gives less improvement in accuracy. For this reason, current UVLM takes the opinion of Dovgii and Shekhovtsov⁹⁵ and employs equation 14 as the time-advancing method for vortex roll up.

7.2.4.2 Desingularized vortex model

As seen in previous sections, UVLM employs vortex ring (closed vortex filament) discretization. However, a mathematically-derived vortex filament is a singularity at the center which could cause extremely large velocity and physically impossible vortex sheet intersection. This discrepancy results from the assumption of inviscid flow and vortex lumping in that all intensity of three-dimensionally distributed vorticity is concentrated on a line. The velocity field induced by vortex sheets obeys Biot-Savart law and this has $O(-1)$ order in distance between vortex filaments as variable. When they are close each other and $r \rightarrow 0$, a great error occurs in the magnitude of velocity, namely an input data error.⁹⁵ According to an error analysis for Cauchy problem reported by Dovgii and Shekhovtsov,⁹⁵ the input errors in the system of VLM become far greater than the truncation errors. Thus, some viscous model is required to eliminate the mathematical singularity.

Real vortex structure has a finite vorticity distribution around the center.⁹⁷ As the vortex model which guarantees finite value in vortex center, Rankine model (equation 15) and Lamb-Oseen model (equation 16) are well-known.

$$v_\theta = \begin{cases} \frac{\Gamma}{2\pi r} & (r > r_c) \\ \frac{\Gamma}{2\pi r} \left(\frac{r}{r_c} \right)^2 & (r \leq r_c) \end{cases} \quad (15)$$

$$v_{\theta} = \frac{\Gamma}{2\pi r} \left(1 - e^{-\frac{r^2}{4\nu t}} \right) \quad (16)$$

Both models consist of the original Biot-Savart law and an additional nondimensional cutoff function.

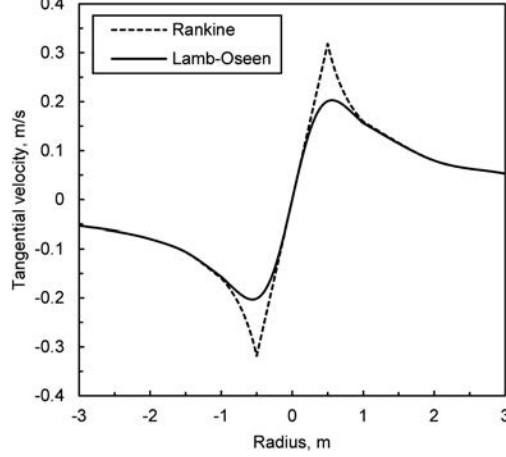


Figure 7.7: Comparison of tangential velocity distribution of Rankine and Lamb-Oseen model (Assuming $\Gamma = 1, r_c = 2\sqrt{\nu t} = 0.5$).

As shown in figure 7.7, the Rankine vortex model has C^1 discontinuity at the cutoff radius r_c , dividing internal Couette flow region and external circulation flow region. In contrast, Lamb-Oseen vortex model shows a continuous distribution with time-dependent viscous diffusion distance $2\sqrt{\nu t}$. (It should be noted that, Lamb-Oseen equation 16 is known as a particular solution of Navier-Stokes equation for a single vortex but not general solution for multiple vortex system.⁹⁸) Rankine vortex model is $O(r^3)$ approximation of Lamb-Oseen model, which is confirmed by the assumption that $r_c = 2\sqrt{\nu t}$ and applying Taylor expansion to the cutoff function of equation 15 and 16 as follows.

$$1 - e^{-\frac{r^2}{4\nu t}} = \left(\frac{r}{r_c} \right)^2 - \frac{1}{2} \left(\frac{r}{r_c} \right)^4 \dots$$

As an example to use Rankine vortex model in UVLM, Gennaretti and Bernardini⁹⁹ reported a reasonable accuracy in accordance with their numerical investigation. It is known that the discontinuity of Rankine model is solved by adding a limit radius in radial coordinate r of denominator of vortex model. Vatisas *et al.*⁸⁵ attempted a comprehensive analysis of application of Rankine vortex model and proposed an empirical formula as below.

$$v_{\theta} = \frac{\Gamma}{2\pi r} \frac{\left(\frac{r}{r_c} \right)^2}{\left\{ 1 + \left(\frac{r}{r_c} \right)^{2n} \right\}^{\frac{1}{n}}} \quad (17)$$

Equation 17 was utilized by Ansari *et al.*⁵¹ and Ramesh *et al.*² and proven good performance. The cutoff function of equation 17 is suitable for scalar form but not always easy to apply in

vector form. Thus, Lamb-Oseen vortex model is useful in current work. The application of Lamb-Oseen vortex model to a vortex method was reported by Kuwahara and Takami⁹⁸ and Summa.¹⁰⁰ According to their study about vortex roll up, Lamb-Oseen vortex model performs good convergence when $\nu \geq 0.002$ and shows numeric instability in a smooth media $\nu < 0.002$. This result proves that Lamb-Oseen vortex model can alleviate the singularity of vortex model but brings a new arbitrariness to UVLM in the sense that the viscosity of fluid ν numerically influences the result of inviscid flow model. About this arbitrariness in UVLM, Dovgii and Shekhovtsov proposed to employ singular radius as the cutoff radius of the artificial viscosity r_c .⁹⁵ To contrast that viscous diffusion in Lamb-Oseen vortex model is evaluated physically, singular radius is derived by numerically expected precision determined by resolution of discretization. Dovgii and Shekhovtsov pointed out that it is impossible to expect correct value from Biot-Savart law at distance less than half of panel size, since nobody can require a higher precision of the model than that given by the boundary-value condition at the surface.⁹⁵ Accordingly, the viscous diffusion distance in equation 16 can be replaced by r_c without numeric setback. For these reasons, Lamb-Oseen model restricted by singular radius is thought as the most suitable cutoff function to desingularize current UVLM and Biot-Savart law is modified as follows.

$$\vec{v}(\vec{r}) = \frac{\Gamma}{4\pi} \frac{\vec{r}_s \times \vec{r}_e}{|\vec{r}_s \times \vec{r}_e|^2} (|\vec{r}_s| + |\vec{r}_e|) \left(1 - \frac{\vec{r}_s \cdot \vec{r}_e}{|\vec{r}_s||\vec{r}_e|} \right) \left\{ 1 - e^{-\left(\frac{r}{r_c}\right)^2} \right\} \quad (18)$$

7.2.4.3 Impingement of vortex sheets

In vortex roll up, discrete vortices or grid of vortex rings tend to congest in a place and form spiral structure.¹⁰¹ The cutoff function (Equation 18) mitigates the overestimation of velocity induced by proximal vortex filament but does neither inhibit this tendency of vortex congestion and nor prevent the eventual irregularity in highly concentrated vortex region.⁹⁷ Thus, vortex-sheet impingement could happen in fully developed vortex structure even if the UVLM used a desingularized vortex model. For some aerodynamic problem in which the type of wing is inevitably exposed to a vortical wake, such as LEV, rotor craft, and turbine system, this vortex-wing impingement matters. For wing-wake impingement, several directions of solution has been proposed. Gennaretti and Bernardini⁹⁹ solved the vortex-blade interaction in rotor craft by UVLM. In their work, the trailing edge wakes were divided to the near-wake and the far-wake segment from the shedding edge. According to their investigation, the velocity component induced by the far-wake segment was represented by blade bound circulation and the near-wake segment. The threshold for distinguishing between near-wake and far-wake, however, was not clearly introduced. Eventually, their UVLM simulation showed the rotor blades immersed in vortex wake sheets but it does not impair the calculation result. The same problem was solved by Wie *et al.*,¹⁰² in which they proposed to realign the trailing edge wake potential by integrating velocity field through an arbitrary path, where the velocity field was determined by original vortex distribution. This method does not provide direct solution of velocity field but performed reasonably. These solutions are successful but brings another arbitrariness in calculation and it is not preferable for the present work. Then, for current UVLM, a special treatment for unreal vortex sheet penetration to wing is employed. The idea of the treatment is to assume a slip-wall condition, which is originally proposed by Suresh Babu *et al.* (from a personal suggestion). In computation of vortex roll up, the displacement for a grid of vortex sheet which is closer to the wing surface than singularity radius r_c was evaluated as surface tangential velocity as below.

$$\Delta \vec{x} = (\vec{v}_\infty + \vec{v}_m + \vec{v}_W + \vec{v}_{TL} + \vec{v}_{TR} + \vec{v}_L + \vec{v}_\tau) \Delta t \quad (19)$$

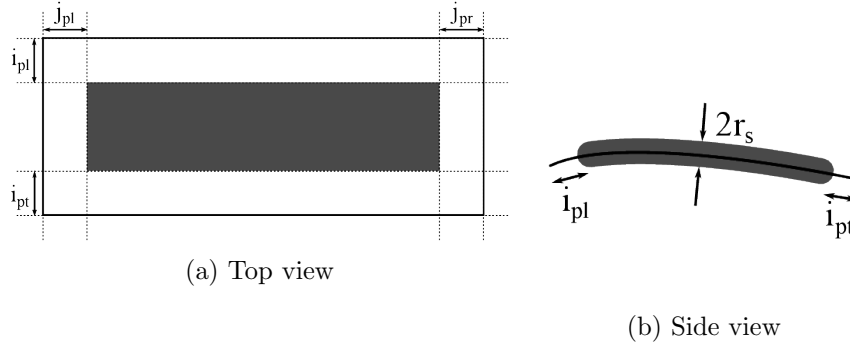


Figure 7.8: Range of application (colored by gray).

This solution forces vortex sheet near the wing surface to slide in the tangential direction but would interrupt vortex shedding around the wing edges. Therefore, the range of application for the prevention of impingement must have a padding through the edge lines, as shown in figure 7.8. In figure 7.8, gray regions denote the region where equation 19 is applied, and about 20% of padding in chord is used in the present work.

7.2.5 Amalgamation of vortex sheets

In the context of vortex methods, amalgamation means to merge some discrete vortices. The motivation of amalgamation method for vortex roll up are roughly categorised into physical reason, numeric reason, and economic reason. First, potential flow theory and UVLM do not simulate viscous dissipation and turbulence. Thus, the shed wakes are eternally preserved in the flow field. In case the preservation of vortex sheets is not preferable, amalgamation method should be used. Second, vortex roll up develops the vortex structure but it tends to cause an irregular distortion and intersection in vortex sheet distribution. Amalgamation method can smoothen these geometric discrepancies. Third, merging vortex sheets reduces the number of vortex rings and contributes to save computation time.

According to Sarpkaya,⁹⁷ the idea of amalgamation was suggested by Ham¹⁰³ to inhibit the error in calculation of induced velocity by proximal discrete vortices. Ham provided the basic scheme of vortex sheets amalgamation and the basis of the scheme has not been largely changed by successor methods. The main idea of amalgamation of vortex sheets is to give a united circulation which has the summation of the strength of the merged circulations and is located at their centroid. Considering amalgamation from N th to M th of discrete vortices into new one, the strength and the location of the new representative discrete vortex Γ_{new} and $\vec{x}_{i,new}$ is formulated as follows.

$$\Gamma_{new} = \sum_{n=N}^M \Gamma_n \quad (20)$$

$$\vec{x}_{i,new} = \frac{\sum_{n=N}^M \Gamma_n \vec{x}_{i,n}}{\sum_{n=N}^M \Gamma_n} \quad (21)$$

The formulation of amalgamation method as shown in equation 20 and 21 must guarantee the far field boundary flow condition.¹⁰⁴ Although amalgamation method brings aforementioned benefits in UVLM, the process is fundamentally a nonlinear and irreversible approximation in the sense that, though the circulation strength is conserved, the resulting velocity field around the region of amalgamated vortices is not identical to that prior to amalgamation.⁹⁷ Further, it is known that the merging vortices near the lifting body could cause a discontinuity in force calculation.⁹⁷ Thus, amalgamation method should be used with care.

Amalgamation schemes have been studied by several engineers from various perspectives. Spalart¹⁰⁴ provided a theoretical reinforcement to the basic scheme as shown in equation 20 and 21 by Taylor expansion analysis and derived a merging criterion to minimize the truncation error. Spalart's criterion was largely simplified and employed in the work of Ansari *et al.*⁵¹ Moore³¹ focused on the geometry of the rolled up vortex structure and established another amalgamation criterion considering numeric resolution. In his investigation, there must be a minimum number of discrete vortices to be able to depict the spiral structure of rolled up vortex and main numeric discrepancy was caused by low resolution to capture the internal spiral structure. Thus, the amalgamation was carried out in case that the number of grid of vortex rings cannot correctly capture the spiral distribution. The idea to solve the amalgamation criteria from geometric viewpoint was modified by Lamarre and Paraschivoiu,¹⁰⁵ in which the highly rolled up portion was detected by bending angle of vortex rings and merged. Lamarre and Paraschivoiu also proposed adaptive panelling scheme, namely to compensate the lack of discrete vortex by reproducing another vortex filament in different area. More intuitive approach was attempted by Suresh Babu *et al.*¹⁰⁶ According to the observation of Suresh Babu *et al.*, a vortex structure can be represented by a strong vortex core and it is grown by absorbing the surrounding discrete vortex components which is detected by relative angular velocity.

For the present work, the current UVLM implementation aims to mitigate a numeric instability and to equip a geometrically fundamental function to calculate the development of free wake. The numeric instabilities in UVLM is typical due to the intersection. On the one hand the intersection of vortex and wing has been introduced in previous sections. On the other hand the object of amalgamation method is to solve the intersection of vortex sheets itself, which is often observed in the spiralling region of rolled up vortex sheets. The geometrically fundamental function deform the two-dimensional vortex sheets to the three-dimensional manifold and this problem is discussed in the subsequent section.

In order to detect these unrealistic features in vortex sheet distribution, current UVLM uses a modification of past methods proposed by Moore³¹ and Lamarre and Paraschivoiu.¹⁰⁵ The external angle formed by adjacent vortex rings are evaluated in every time-step and if this shows characteristics of adverse features like wave and intersection, the amalgamation scheme is applied to the region at hand. The external angle consists of three components: angle measured on a XY plane, YZ plane, and XZ plane. Denoting a pair of vectors \vec{a} and \vec{b} on a plane, the external angle θ which they forms is calculated by an intrinsic functions as follows.

$$\theta = \text{sgn}(\vec{a} \times \vec{b}) \cdot \cos^{-1} \left(\frac{\vec{a} \cdot \vec{b}}{|\vec{a}||\vec{b}|} \right) \quad (22)$$

From discrete geometry, the source of vortex sheets intersection can be defined as pleat structure and turn structure. Turn structure forms spiral pattern in tip vortex (assuming no secondary vortex) and wave pattern in TEV and LEV except for the starting vortex. Figure 7.9 describes these two structures. The pleat structure can be detected as the condition that the sign of the

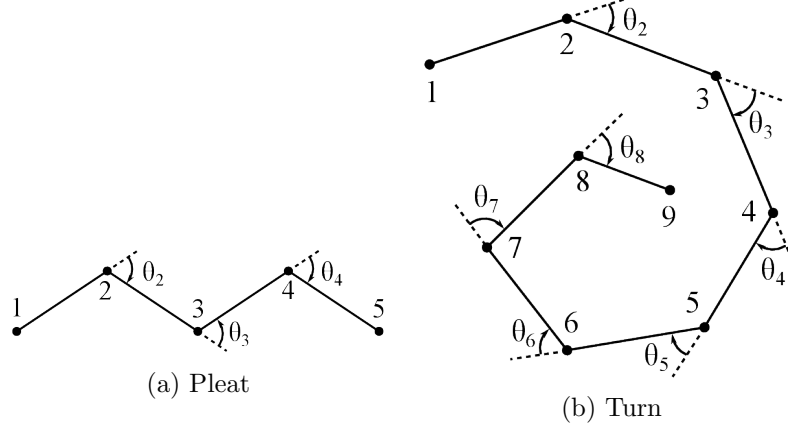


Figure 7.9: Schematic description of vortex sheet structure to be amalgamated.

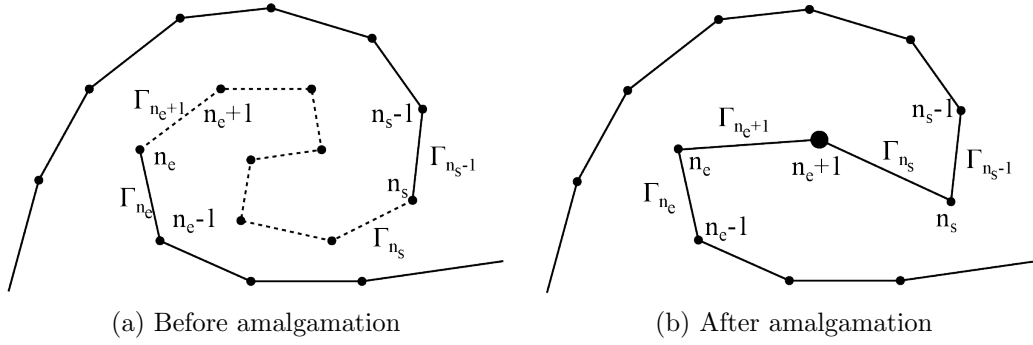


Figure 7.10: Schematic description of implementation of amalgamation.

external angle changes in three times in a row. The structural condition of pleat can be described as

$$\begin{cases} \theta_{N-1} > 0, \theta_N < 0, \theta_{N+1} > 0 \\ \theta_{N-1} < 0, \theta_N > 0, \theta_{N+1} < 0 \end{cases} \quad (23)$$

Taking figure 7.9a as an example, $\theta_2 < 0, \theta_3 > 0, \theta_4 < 0$, the 3rd grid of vortex sheets should be merged. The turn inside of the spiral vortex sheet structure can be detected by the region whose summation of a series of the external angles exceeds a threshold θ_a . If $\theta_a = 2\pi$, the amalgamation scheme would merge the inner turn and the only outermost circle would remain. It can be described by

$$\left| \sum_{n=N}^M \theta_n \right| \geq \theta_a \quad (24)$$

and the vortex rings which is from N th to M th should be amalgamated.

The procedure of amalgamation is illustrated in figure 7.10. Figure 7.10 shows that the inner turn indicated by dashed line and vortex rings with suffix from n_s to $n_e + 1$ is merged into one circulation denoted by suffix $n_e + 1$. The detailed procedure is explained in figure 7.11. As mentioned before, UVLM is based on vortex ring discretization and physically conserved parameter is not the strength of vortex ring Γ_n but the difference of circulation between adjacent vortex rings $\Gamma'_n = \Gamma_{n+1} - \Gamma_n$. Therefore, converting equation 20 to the vortex ring discretization, representative circulation at the centroid must be $\Gamma_{n_s} - \Gamma_{n_e+1}$. As shown in figure 7.11b, this means that the amalgamation

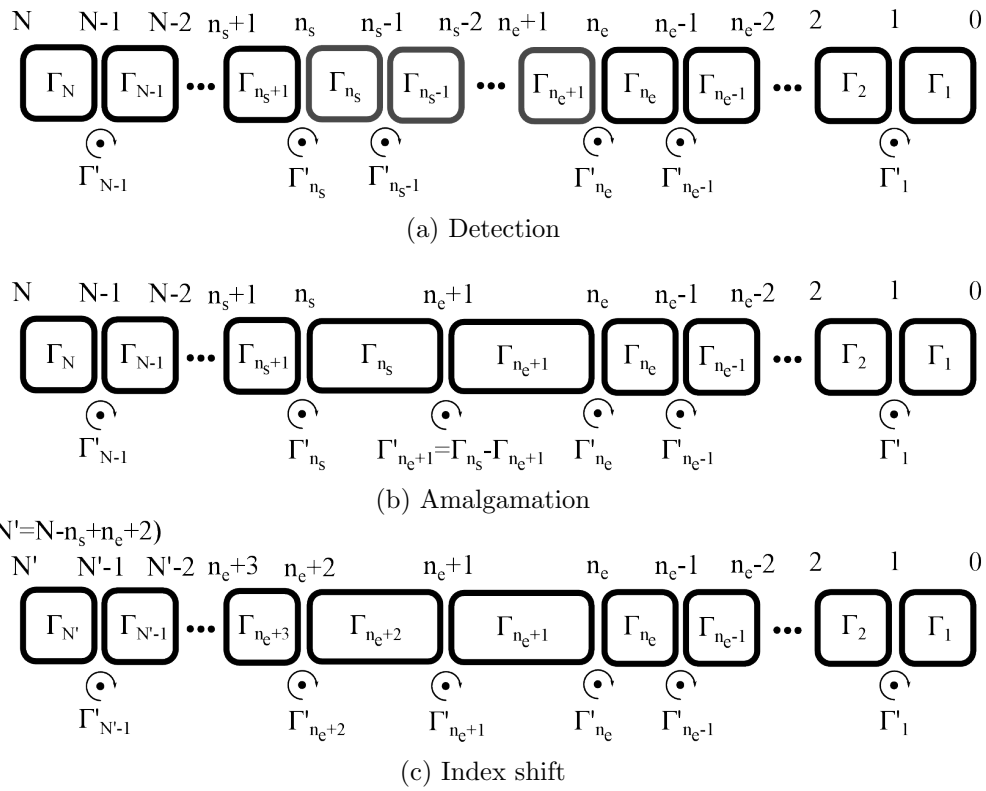


Figure 7.11: Schematic description of procedure of amalgamation.

process simply eliminates the vortex rings from index $n_s - 1$ to $n_e + 2$ and connects the n_s th and $n_e + 1$ th vortex ring at the centroid

$$\vec{x}_{n_e+1,new} = \frac{\sum_{n=n_e+1}^{n_s-1} \vec{x}_n(\Gamma_{n+1} - \Gamma_n)}{\sum_{n=n_e+1}^{n_s-1} (\Gamma_{n+1} - \Gamma_n)} = \frac{\sum_{n=n_e+1}^{n_s-1} \vec{x}_n(\Gamma_{n+1} - \Gamma_n)}{\Gamma_{n_s} - \Gamma_{n_e+1}}. \quad (25)$$

After the amalgamation scheme is processed, the indices of vortex rings which are located in upstream from the amalgamation centroid are shifted as shown in figure 7.11c.

7.3 Summary of Modified UVLM

Figure 7.12 shows a flowchart for the modified UVLM algorithm. The algorithm for the conventional UVLM roughly consists of three main steps: (1) evaluation of the velocity induced by free stream, motion, and wakes, (2) derivation of the wing bound circulation distribution from surface boundary condition, and (3) calculation of the pressure distribution from the obtained velocity field on the surface. The modified UVLM from the present work includes new contributions for simulating LEV formation using the LESP concept proposed for 2D flows by Ramesh *et al.*,² and incorporates capability for flow simulation of LEV-dominated unsteady finite wing system.

Results from the UVLM are applied to prediction of LEV initiation in chapter 8 and to prediction of LEV formation in chapter 9.

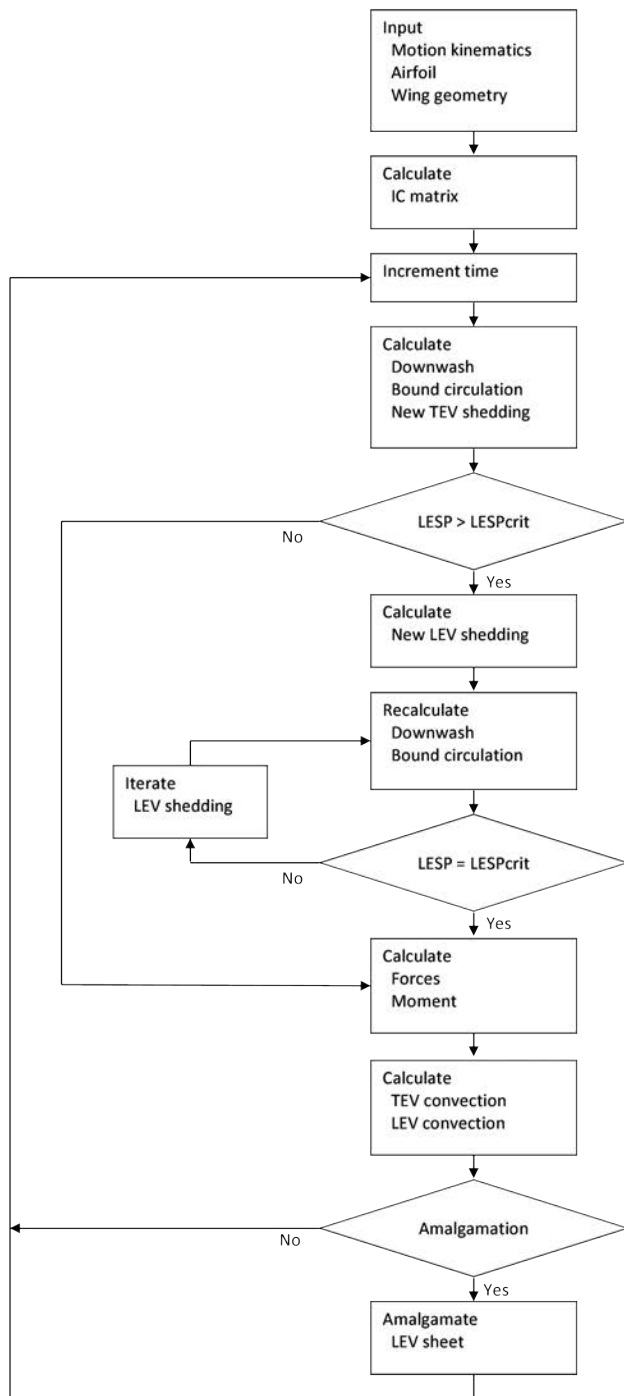


Figure 7.12: Schematic flowchart of UVLM.

Chapter 8

Low-Order Prediction of LEV Initiation on Finite Wings

This chapter presents the results of studies on LEV initiation on finite wings, with emphasis on the effectiveness of the low-order prediction capability using the UVLM code. The studies in this portion of the effort were carried out with the objective of answering the following key questions:

- (i) For any wing shape and motion, what are the values for time instant, angle of attack, and spanwise location at which CFD predicts initiation of LEV formation? How do these values vary with wing-geometry and motion-kinematic parameters?
- (ii) For any wing shape and motion, how does the maximum in the UVLM-predicted spanwise variation in the LESP at the time instant corresponding to the CFD-predicted LEV initiation (referred to as “ $LESP_{max}$ ”) agree with the critical value of LESP for the corresponding 2D airfoil (referred to as “ $LESP_{crit}$ ”)? And how does the spanwise location of the maximum in the spanwise LESP distribution agree with the CFD-predicted spanwise location for initiation of LEV formation?
- (iii) if the agreements in (ii) are good, can the critical value of LESP, obtained from 2D studies, be used to predict the time instant, angle of attack, and spanwise location for LEV initiation using UVLM (without using 3D CFD studies), and how closely will these predicted values agree with the corresponding CFD predictions?

The following section presents the methodology for carrying out the LEV initiation study and the case studies used to assess the effectiveness of the low-order prediction using the UVLM code. The subsequent section presents the results from the low-order and high-order methods.

8.1 Methodology and Case Studies

A total of 13 finite-wing geometries and two airfoil sections are considered in this effort. The two airfoil sections are the SD 7003 (see the reference¹⁰⁷) and a modified SD 7003 with a sharpened leading edge having a 50% reduction in the leading-edge radius compared to the original SD 7003 airfoil. The two airfoil sections, referred to as the SD7003 and sharpened SD7003 in this thesis, are shown in figure 8.1.

The 13 finite wing cases, labelled cases 1–13, have different taper ratios, tip-twist angles, aspect ratios, and pivot locations, with sections formed using one or both of the two airfoils, SD7003 and

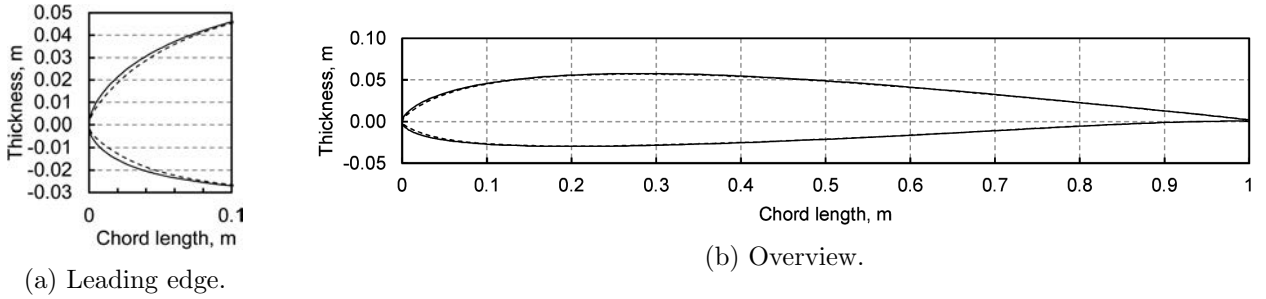


Figure 8.1: Comparison of SD 7003 (solid line) and sharpened SD 7003 (dashed line)

sharpened SD7003. Table 8.1 lists the details of the two airfoils and the 13 finite-wing cases used in this paper. Figures 8.2 show the ten wing geometries that are used in the 13 cases.

Table 8.1: Test cases.

| Case | Taper ratio | AR | Pitch rate K | Pivot point (x/c_{ave}) | Tip twist [deg] | Sweep angle [deg] | Inboard incidence [deg] | Airfoil |
|------|-------------|----|----------------|---------------------------|-----------------|-------------------|-------------------------|---------------------|
| 2D1 | - | 2D | 0.3 | 0.25 | - | - | 0 | SD7003 |
| 2D2 | - | 2D | 0.3 | 0.25 | - | - | 0 | Sharpened SD7003 |
| 1 | 1 | 6 | 0.3 | 0.25 | 0 | 0 | 0 | SD7003 |
| 2 | 1 | 6 | 0.3 | 0.75 | 0 | 0 | 0 | SD7003 |
| 3 | 1 | 6 | 0.2 | 0.25 | 0 | 0 | 0 | SD7003 |
| 4 | 1 | 6 | 0.4 | 0.25 | 0 | 0 | 0 | SD7003 |
| 5 | 0.5 | 6 | 0.3 | 0.25 | 0 | 0 | 0 | SD7003 |
| 6 | 1 | 6 | 0.3 | 0.25 | 10 | 0 | 0 | SD7003 |
| 7 | 1 | 2 | 0.3 | 0.25 | 0 | 0 | 0 | SD7003 |
| 8 | 1 | 4 | 0.3 | 0.25 | 0 | 0 | 0 | SD7003 |
| 9 | 1 | 8 | 0.3 | 0.25 | 0 | 0 | 0 | SD7003 |
| 10 | 1 | 6 | 0.3 | 0.25 | 0 | 30 | 0 | SD7003 |
| 11 | 1 | 6 | 0.3 | 0.25 | 0 | 0 | 0 | Sharpened SD7003 |
| 12 | 1 | 6 | 0.3 | 0.25 | 0 | 0 | 4 ^a | SD7003 |
| 13 | 1 | 6 | 0.3 | 0.25 | 0 | 0 | 0 | SD7003 ^b |

a) Inboard third of wing has a 4-degree larger incidence compared to the rest of the wing.

b) Inboard third of wing has the sharpened SD7003 airfoil, with the SD7003 used on the rest of the wing.

All the studies in this work have been performed for a chord Reynolds number of 20,000. This value was chosen because our previous studies have shown that the LESP criterion successfully predicts initiation of LEV formation on airfoils (in two-dimensional flow) at Reynolds numbers between 10,000 and 40,000. In this range of Reynolds numbers, the RANS CFD analysis using the Spalart-Allmaras turbulence model, as implemented in REACTMB-INS flow solver, has also been shown to agree well with experimental results for LEV initiation and formation on airfoils. The only case with a non-constant chord is case 5; for this case, the leading-edge has zero sweep, and the average chord (at the mid-semi-span location) has been used as the length scale to set the Reynolds number and the non-dimensional pitch rate. For the tapered wing (case 5), the pivot

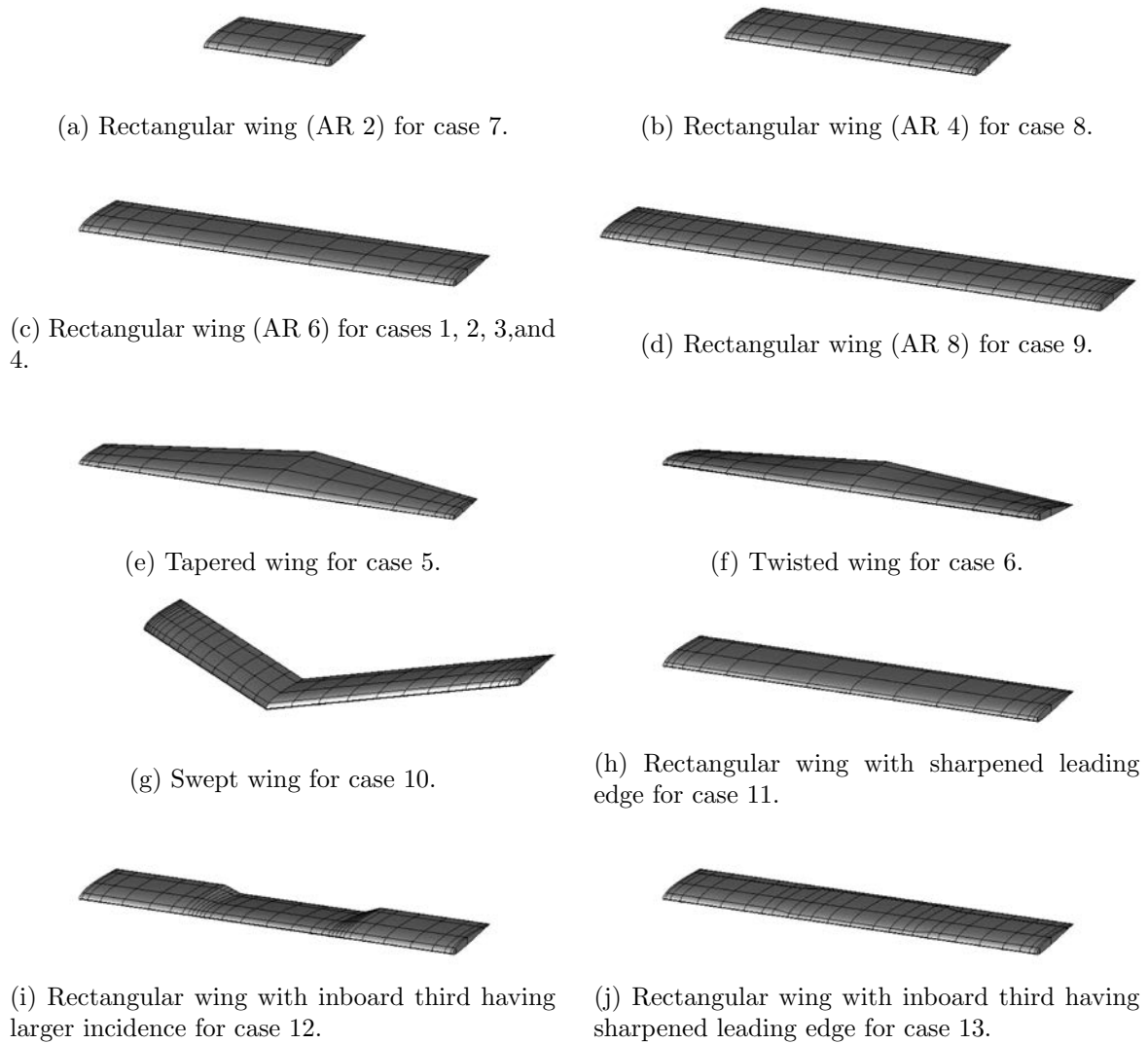


Figure 8.2: Geometries of the ten wings used in the 13 cases.

location for the pitching motion is at the 25% of the chord at the mid-semi-span location, while for the swept wing (case 10), the pivot is at the quarter-chord location of the root section. Cases 12 and 13 comprise wings that have abrupt changes in geometry demarcating the inboard third of the wing span from the outboard regions. Case 12 has a 4-degree higher incidence on the inboard third of the wing compared to the rest of the wing, and case 13 has the sharpened SD7003 airfoil over the inboard third of the airfoil and the original SD7003 section on the outboard portions. The swept-wing geometry in case 10 has been defined using the airfoil section parallel to the plane of symmetry.

8.1.1 Motion parameters

Although the LESP criterion has been verified for arbitrary pitching, plunging, surging, and combination motions,² the current work, owing to the large number of geometry cases, focusses on a pure pitching motion. Thus, for all wing geometries in this work, a 0–45-degree pitch-ramp motion is considered, with a non-dimensional pitch rate of $K = 0.3$ used in most cases, except for cases 3 and 4, which have $K = 0.2$ and 0.4 , respectively. Figure 8.3 shows the time variations of the angle of attack (same as pitch angle in this work) for the three pitch rates. The equation for the pitch ramp motion is from Granlund *et al.*¹⁰

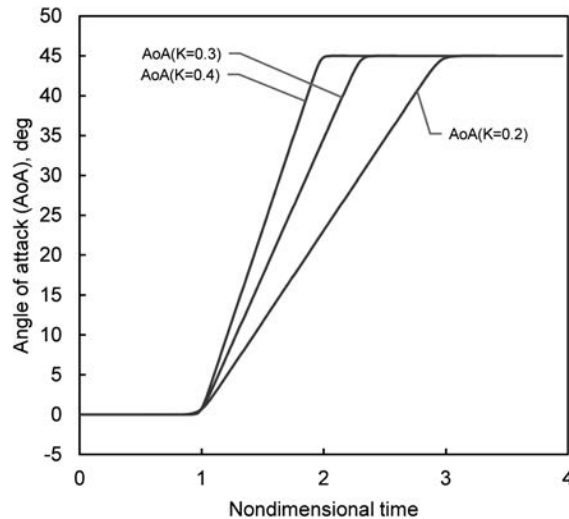


Figure 8.3: Pitch-up motions used in this study.

8.1.2 Determination of LEV initiation and $LESP_{max}$ from CFD and UVLM

An important element of the current work is the quantitative determination of the time instant of LEV initiation from CFD results. In past research, experimental studies (¹⁰⁸ and ³⁸ for example) have used the movement of the minimum-pressure location to track movement of the LEV, and the computational study of Ref.⁴⁸ brought to light the behavior of critical points in the velocity field near an LEV. Guided by these results in the literature, in our earlier work on LEV initiation on airfoils,² we showed that a skin-friction signature near the leading edge from CFD results could be consistently used to identify LEV initiation. In the current work, we adapt this skin-friction

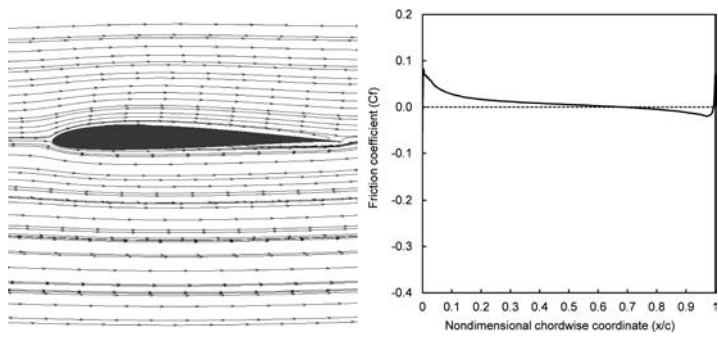
signature to predict LEV initiation on finite-wing flows. In the remainder of this subsection, we discuss this skin-friction signature, first for airfoil flows and next for finite-wing flows.

In order to provide an overview of the events leading up to LEV formation, Figure 8.4 shows a series of representative CFD snapshots of streamlines and upper-surface C_f plots for the SD 7003 undergoing pitch up motion (Case 2D1). At the start of the pitching motion, the airfoil has attached flow over most of the upper surface, with the upper-surface C_f becoming negative past $x/c = 0.7$ indicating the presence of a small region of reversed flow over the aft 30% of the chord in Figure 8.4a. At the higher angle of attack of 18.2 degrees, as seen from Figure 8.4b, the trailing-edge reversed flow region extends from $x/c = 0.5$. Of interest, however, is the tiny region near the leading edge over which C_f is negative, indicating the beginning of flow reversal at the leading edge. At a higher pitch angle of 23.4 degrees, the C_f distribution in Figure 8.4c shows a positive spike reaching up to $C_f = 0$ within the negative- C_f region near the leading edge. In the approach developed in our earlier work,² this first occurrence of positive C_f within the negative- C_f region near the leading edge is taken as the time instant corresponding to initiation of LEV formation. The LEV becomes discernable in the streamline plot at the higher pitch angle of 26.0 degrees in Figure 8.4d, and clearly visible at even higher pitch angles (not shown). As the LEV grows, multiple vortices near the primary vortex are formed, resulting in the occurrence of several positive spikes with the negative- C_f region near the leading edge. The structures observed in our CFD results are similar to those observed by Ghosh-Choudhuri *et al.*⁴⁸ In the current work, however, the focus is on the initiation of LEV formation rather than on the flow features that occur subsequent to LEV initiation.

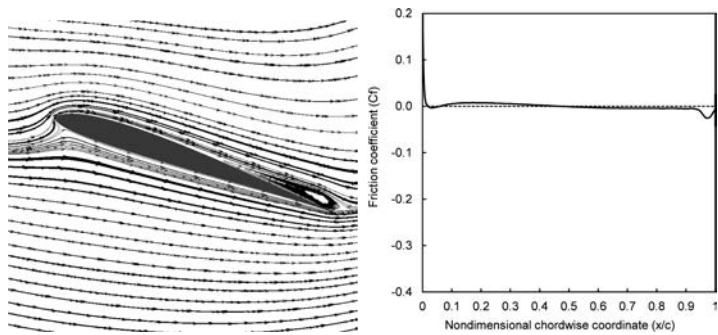
In extending the skin-friction signature for LEV initiation to finite-wing flows, we examine the CFD plots of the skin-friction lines on the upper-surface at successive time instants. The objective is to find the time instant corresponding to the first occurrence of a region of positive skin-friction within the negative skin-friction region near the leading edge. To illustrate the procedure, Figures 8.5a and 8.5b show the upper-surface skin-friction lines on the wing used in case 1 at two successive time instants from CFD output corresponding to just prior to LEV initiation and just after LEV initiation, respectively. Figure 8.5a indicates that there are roughly four flow regions at $t^* = 1.695$: (i) a small region of reversed flow near the leading edge with negative chordwise C_f , which is usually a precursor to LEV formation; (ii) a thin layer of reversed flow in the vicinity of the trailing edge, indicating trailing-edge flow reversal; (iii) the triangle-shaped region at the right edge resulting from surface flow caused by the tip vortex; and (iv) the intermediate flow region with flow having a chordwise component that is from leading to trailing edge corresponding to positive chordwise C_f .

Figure 8.5b shows the surface streamlines for the very next time instant ($t^* = 1.710$) from CFD output for case 1. It is seen that there is a new region near the leading edge of the root area. This small region is the first occurrence of positive chordwise skin friction within the reversed-flow region near the leading edge. By analogy to the skin-friction signature in the airfoil case, it can be said that the t^* corresponding to LEV initiation for the finite-wing case 1 is between 1.695 and 1.710. It is also seen that the LEV initiation occurs at the wing root for this wing, i.e., at $2y/b = 0$, with the LEV starting to form over a spanwise region extending approximately from $2y/b = -0.3$ to 0.3.

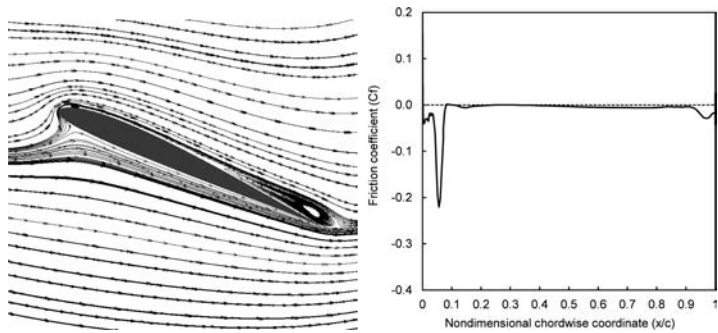
Figure 8.6 shows the spanwise distributions of LESP for case 1 for $t^* = 1.710$ (solid curve, for CFD frame just after LEV initiation) and for $t^* = 1.695$ (dashed curve, for CFD frame just prior to LEV initiation). These spanwise LESP distributions were obtained from the UVLM analysis. The spanwise-maximum LESP value, corresponding to LEV initiation, for case 1, therefore, occurs between the maximum values for these two spanwise LESP distributions. Thus, the solid black



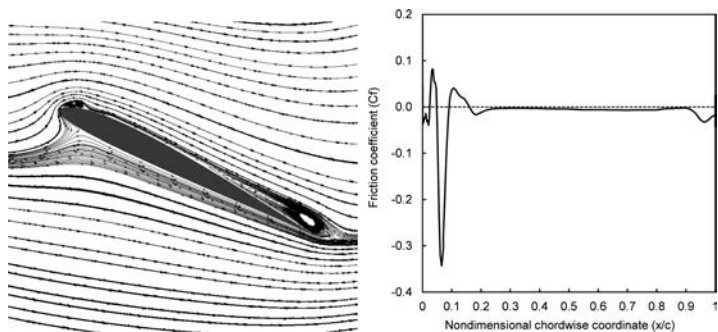
(a) $\alpha = 0.1$ deg.



(b) $\alpha = 18.2$ deg.



(c) $\alpha = 23.4$ deg.



(d) at $\alpha = 26.0$ deg.

Figure 8.4: Sequence of events associated with LEV initiation and growth on an airfoil. Streamlines and C_f at different angles of attack.

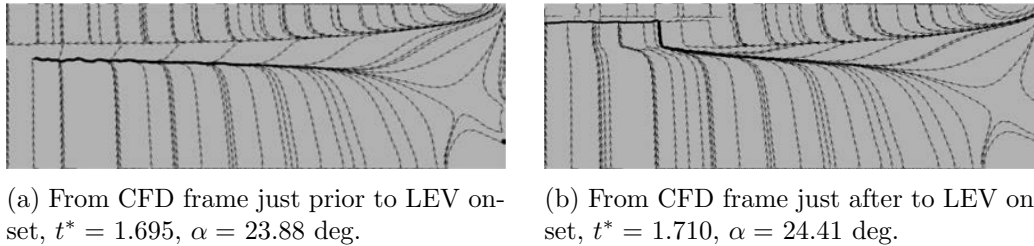


Figure 8.5: Upper-surface skin-friction lines for case 1. Right half of wing shown. In each snapshot, leading edge is on the top, wing tip is on the right, trailing edge is on the bottom, wing root is on the left.

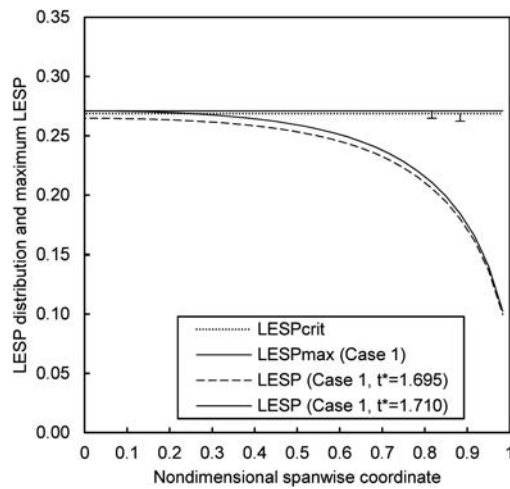


Figure 8.6: Spanwise variation of $LESP$ and determination of $LESP_{max}$ for case 1.

horizontal line in figure 8.6 indicates the $LESP_{max}$ value, with the black error bar denoting uncertainty, corresponding to initiation of LEV for case 1. Also plotted as a horizontal line is the $LESP_{crit}$ from 2D airfoil CFD result, intended to be compared with the $LESP_{max}$ line.

In the remainder of the paper, results for initiation of LEV formation on any arbitrary wing will be presented using a plot of upper-surface skin-friction lines from a CFD frame corresponding to the instant of time just after LEV onset. The $LESP$ distribution from UVLM will also be presented for the t^* corresponding to this frame. The $LESP_{max}$ for the wing and 2D $LESP_{crit}$ for the airfoil with error estimates will be denoted by horizontal line with vertical error bars in the $LESP$ vs. spanwise coordinate plots.

8.2 Results and Discussion

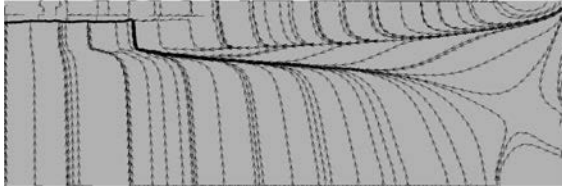
The following subsection presents the values of $LESP_{crit}$ for the SD 7003 (case 2D1) and the sharpened SD 7003 (case 2D2) airfoils used in this study. The next subsection presents the results for the baseline finite-wing geometry (case 1), in which the finite-wing results are compared with the 2D results for LEV initiation. The subsequent results are presented as seven case studies to illustrate the effects of pivot location (case study A), pitch rate (case study B), wing taper ratio (case study C), wing-tip twist (case study D), aspect ratio (case study E), sweep angle (case study F), leading-edge shape (case study G), abrupt change in section incidence (case study H), and abrupt change in section leading-edge radius (case study I), on initiation of the LEV formation. A summary of all case studies is then discussed. In each case study, case 1 is used as the baseline case for reference, and all the finite-wing results are compared with the corresponding 2D results for LEV initiation.

8.2.1 Two-dimensional cases 2D1 and 2D2

The two airfoils used in the study, the original and the sharper-leading-edge versions of the SD 7003, were studied for the pitching motions listed under cases 2D1 and 2D2 in Table 8.1. For each case, results from two-dimensional CFD analysis were studied to determine the time instant and angle of attack for LEV initiation using the approach described in Section 8.1.2. The time-variation of $LESP$ for each case was determined using the unsteady thin airfoil theory of Ref.¹ From the results for case 2D1, the time instant, angle of attack and $LESP$ at LEV initiation were found to be 1.680, 23.38 degrees, and 0.269, respectively. Similarly, the results for case 2D2 yield the time instant, angle of attack, and $LESP$ to be 1.605, 20.80 degrees, and 0.237 at LEV initiation. Because case 2 uses the sharpened-leading-edge airfoil, the LEV initiation occurs at an earlier time in the motion. Thus, the $LESP_{crit}$ values for the SD7003 and the sharpened SD7003 airfoils, used in the remainder of this report, are 0.269 and 0.237.

8.2.2 Baseline: case 1

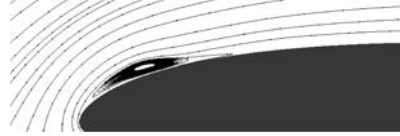
The results for case 1 are presented in Figure 8.7. Figure 8.7a, shown earlier as Figure 8.5b and repeated here for completeness, shows the upper-surface skin-friction lines from CFD analysis at the time instant just after LEV initiation. Using the skin-friction signature described earlier in Section. 8.1.2, it is seen that the LEV starts forming at the wing root. Figures 8.7b, 8.7c, and 8.7d show the leading-edge flow streamlines (for velocities relative to the body frame) at the tip,



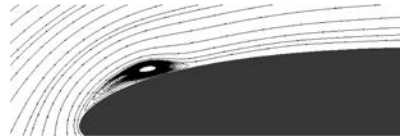
(a) Upper-surface skin-friction lines for case 1, $t^* = 1.710$, $\alpha = 24.41$ deg.



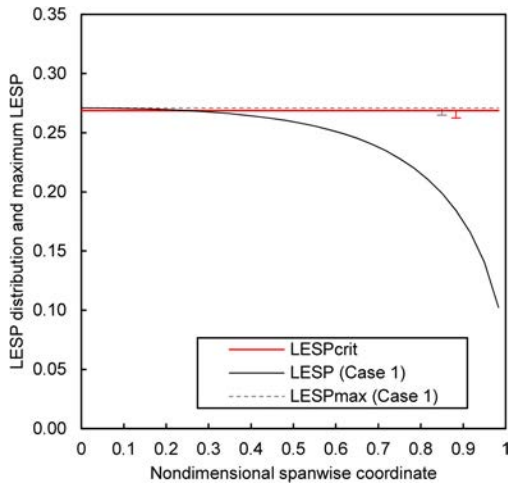
(b) Streamlines near wing tip, leading edge.



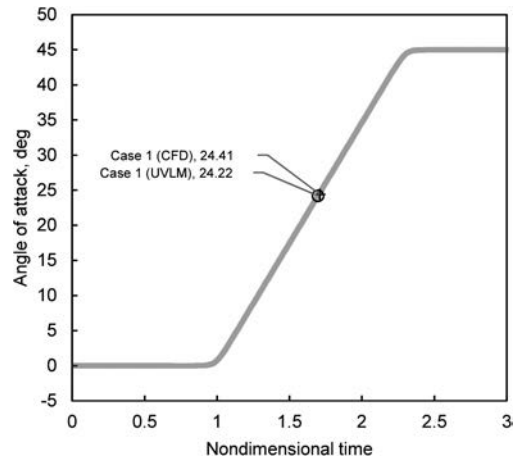
(c) Streamlines at $2y/b = 0.5$, leading edge.



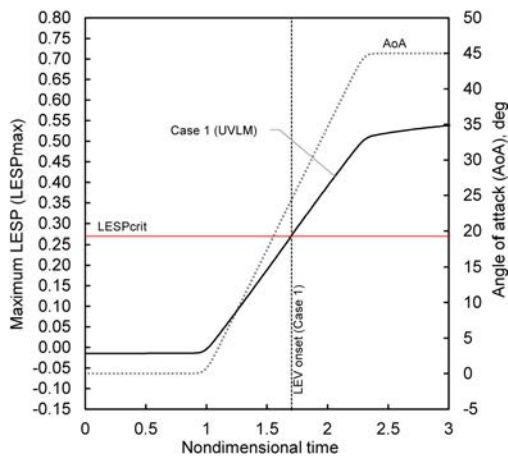
(d) Streamlines at wing root, leading edge.



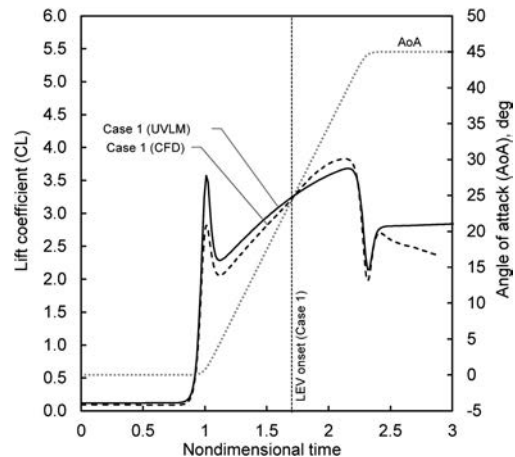
(e) LESP distribution at LEV initiation.



(f) Motion histories and LEV initiation.



(g) $LESP_{max}$ vs. t^* from UVLM.



(h) C_L vs. t^* from CFD and UVLM.

Figure 8.7: Result of baseline (case 1)

mid-semi-span, and root locations, respectively. These streamline plots show the LEV formation, in the early stages, visible only over the inboard portion of the wing. The fact that the surface skin-friction plot in Figure 8.7 does not show evidence of LEV formation at $2y/b = 0.5$ is probably because of a small time lag in the signature registering on the surface.

The general features of LEV structure at the initiation for the baseline case agree with the observations of Freymuth,⁵⁷ Yilmaz and Rockwell⁵⁹ and Spentzos *et al.*^{109,110} in that, for a pitching rectangular wing, the LEV structure is parallel to the leading edge over the inboard portion of the wing, with its maximum strength around wing root. The corner portion of LEV structure tends to attach to the wing surface, whereas the inboard portion of LEV structure is lifted up and gets convected downstream, as reported by Granlund *et al.*¹¹¹ As shown in figures 3.5, the LEV subsequently forms a three-dimensionally distorted vortex structure, which is often called an Ω -shaped structure, bounded at the leading edge of the wing tips. This characteristic LEV structure has been observed in different motion kinematics such as plunging maneuver by Visbal *et al.*¹¹² and the flapping cycle maneuver by Gordnier and Demasi.¹¹³

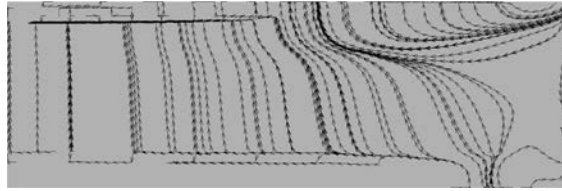
Figure 8.7e shows the spanwise distribution of $LESP$ on the right side of the wing at the time instant of LEV initiation. The occurrence of maximum $LESP$ at the wing root agrees well with the initiation of LEV at the wing root in the CFD prediction. This spanwise $LESP$ distribution is also consistent with the variation of suction pressure on leading edge observed by Schreck and Helin.⁵⁸ Also plotted are the horizontal line at the maximum value and an error bar denoting the change in maximum value between two consecutive output frames from CFD. The value of $LESP_{crit}$ for the 2D airfoil is also plotted using a dashed line with its error bar. The excellent agreement between the 3D $LESP_{max}$ and 2D $LESP_{crit}$ shows that the initiation of LEV formation on the finite wing could have been predicted using a low-order analysis and the $LESP_{crit}$ value. This type of low-order prediction is referred to as “UVLM prediction” in the remainder of this chapter. Figure 8.7f shows the motion history for this case with comparison of the prediction of LEV initiation from UVLM and CFD. The agreement is seen to be excellent.

The time variation of $LESP_{max}$ from UVLM is shown in Figure 8.7g, with the dotted vertical line denoting the time instant of LEV initiation from CFD prediction, and dotted horizontal line representing the $LESP_{crit}$ from 2D CFD. It is seen that $LESP_{max}$ increases with constant slope during pitch-ramp motion. Figure 8.7h shows the lift-coefficient variation with time. At the start of pitching, both CFD and UVLM predict a spike in C_L . This is due to apparent-mass effects. During the linear pitch up, although C_L from CFD and UVLM monotonically increase with the angle of attack, the CFD result is lower than UVLM because UVLM is based on inviscid flow while CFD is a viscous-flow solution. However, after the onset of LEV, the C_L from CFD is higher than that from UVLM. After LEV initiation, CFD takes into consideration the vortex lift due to LEV formation, while current UVLM does not model the LEV effects. Overall, it is seen that prior to LEV initiation, the C_L prediction between CFD and UVLM are in good agreement.

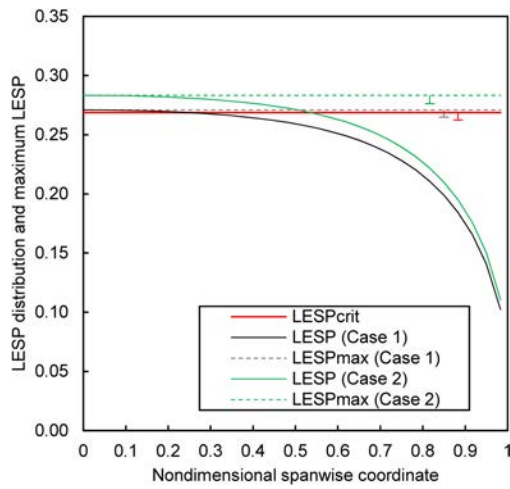
8.2.3 Case Study A: Effect of pivot location

In case study A, the initiation of the LEV for the baseline case (case 1, pivot at $x/c = 0.25$) is compared with that for the same wing with pivot at $x/c = 0.75$ (case 2).

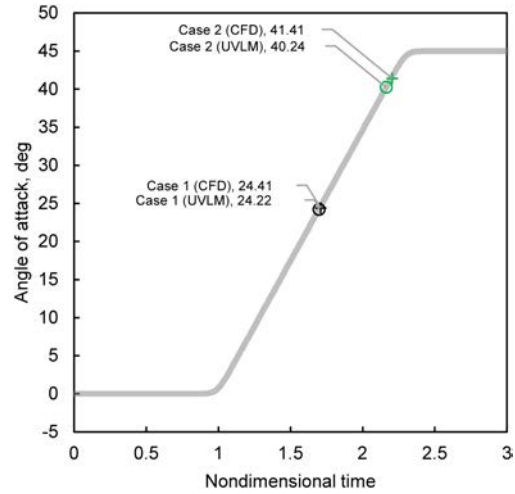
Figure 8.8 shows the comparison of results for the two pivot locations. While the spanwise location for initiation of the LEV for case 2 (as deduced from the skin-friction plot in Figure 8.8a) is similar to that for the baseline case 1, it is seen that case 2 has a larger region of trailing-edge reversed



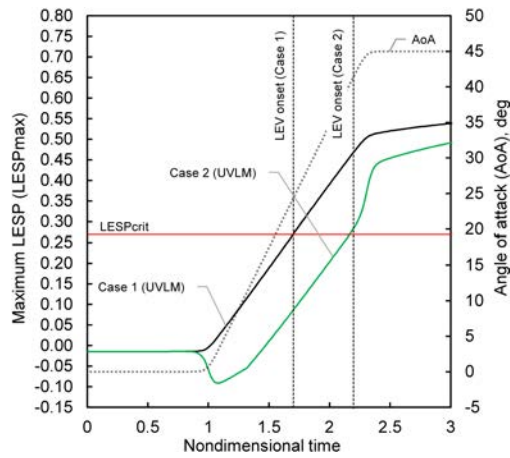
(a) Upper-surface skin-friction lines for case 2, $t^* = 2.205$, $\alpha = 41.14$ deg.



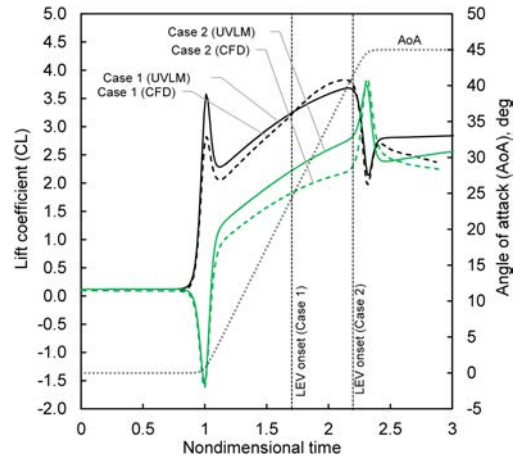
(b) LESP distribution at LEV initiation.



(c) Motion histories and LEV initiation.



(d) $LESP_{max}$ vs. t^* from UVLM.



(e) C_L vs. t^* from CFD and UVLM.

Figure 8.8: Case study A: Effect of pivot location. Comparison of cases 1 and 2 at CFD frames just after LEV onset.

flow that extends to almost the reversed flow at the leading edge. The major difference from the baseline, however, is that LEV initiation is largely delayed due to motion-induced “downwash” at the leading edge. This trend of delayed LEV formation with aft movement of the pivot point is not new. The trend and the reasoning have been reported by several researchers including Ham and Garelick,⁴⁵ Visbal and Shang,⁴⁶ Visbal and Gordnier,¹¹⁴ Ol,⁴⁹ and Granlund *et al.*^{10,111} Furthermore, according to Ericsson,¹¹⁵ rearward pivot location increases the pitching speed at the leading edge and the moving wall effect gives more beneficial effect in boundary layer around the leading edge and thus delays LEV formation.

In figure 8.8b, the spanwise variation of $LESP$ is similar to that for the baseline, but there is slight discrepancy between the $LESP_{max}$ for case 2 and the 2D $LESP_{crit}$. This discrepancy manifests as an approximately 1.2-degree discrepancy between the CFD and UVLM predictions for the AoA for LEV initiation (Figure 8.8c). The motion-induced downwash due to the aft pivot location in case 2 also reduce the $LESP_{max}$ (Figure 8.8d) and the lift coefficient (Figure 8.8e) in comparison to those for case 1. As seen in case 1, the UVLM-predicted C_L for case 2 is higher than the CFD-predicted value until LEV initiation, beyond which the UVLM predictions become progressively invalid.

8.2.4 Case Study B: Effect of pitch rate

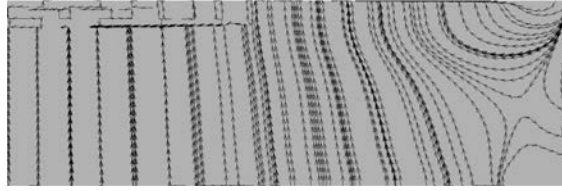
In case study B, the initiation of the LEV for the baseline case (case 1, $K = 0.3$) is compared with that for the same wing with $K = 0.2$ (case 3) and $K = 0.4$ (case 4).

The results for the case study for three pitch rates is shown in figure 8.9. The upper-surface skin-friction lines, plotted in Figures 8.9a and 8.9b for $K = 0.2$ and 0.4, respectively, show that the LEV initiation starts at the wing root like for case 1. It is also seen that, with increasing pitch rate, the chordwise extent of the trailing-edge reversed-flow region progressively reduces. There is a small increase in AoA for LEV initiation with increase in pitch rate. Increase in pitch rate increases the motion-induced downwash at the leading edge, causing the small delay in LEV initiation. This trend between the pitch rate and the time instant of LEV onset is consistent with the features and explanations in the literature: Ham and Garelick,⁴⁵ Johnson and Ham,¹¹⁶ McCroskey *et al.*,^{117–119} Walker *et al.*,¹²⁰ Carr,¹²¹ Visbal and Shang,⁴⁶ Acharya and Metwally,¹²² Schreck and Helin,⁵⁸ Choudhuri and Knight,⁴⁷ Lian,¹²³ and Jantzen *et al.*¹²⁴

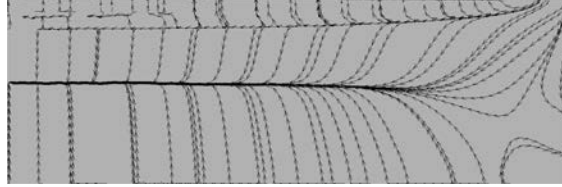
Figure 8.9c shows the spanwise $LESP$ distributions at LEV initiation for cases 3 and 4. The maximum values for the $LESP$ distributions are at $2y/b = 0$, which agrees with the CFD-predicted behavior of LEV initiation starting at the wing root. The figure also shows that the $LESP_{max}$ value for the slow pitch rate (case 3, dashed line) is lower than $LESP_{crit}$ and $LESP_{max}$ for the fast pitch rate (case 4, dotted and dashed line) is higher than $LESP_{crit}$. As a result, as seen in Figure 8.9d, the UVLM predictions for the AoA for LEV initiation for cases 3 and 4 are respectively higher and lower than the CFD-predicted values. Figure 8.9e shows the variations of $LESP_{max}$ for cases 1, 3, and 4. Figure 8.9f shows the effect of pitch rate in C_L . Generally speaking, the faster pitch rate generates higher C_L and this trend is consistent with the observations of McCroskey and Pucci¹¹⁹ and Granlund *et al.*^{10,111}

8.2.5 Case Study C: Effect of taper ratio

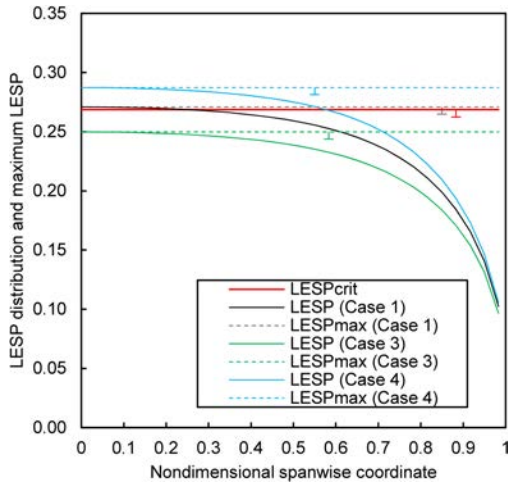
In case study C, the initiation of the LEV for the tapered wing of case 5 (taper ratio of 0.5, with unswept leading edge) is compared with that for the baseline case.



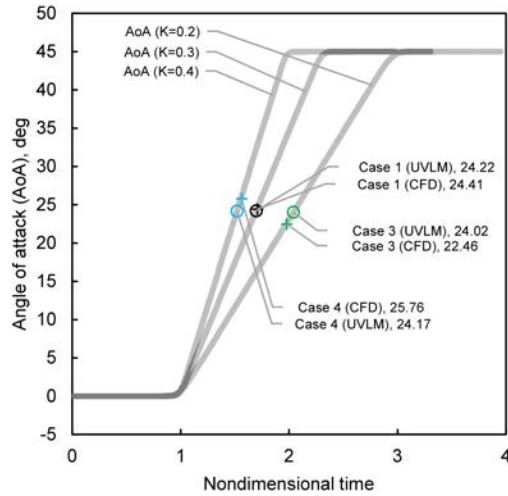
(a) Upper-surface skin-friction lines for case 3, $t^* = 1.980$, $\alpha = 22.46$ deg.



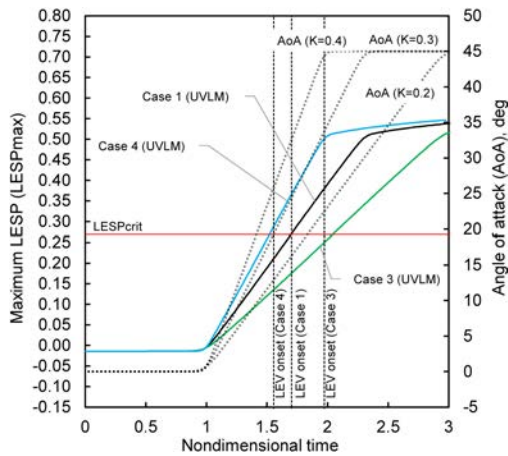
(b) Upper-surface skin-friction lines for case 4, $t^* = 1.562$, $\alpha = 25.76$ deg.



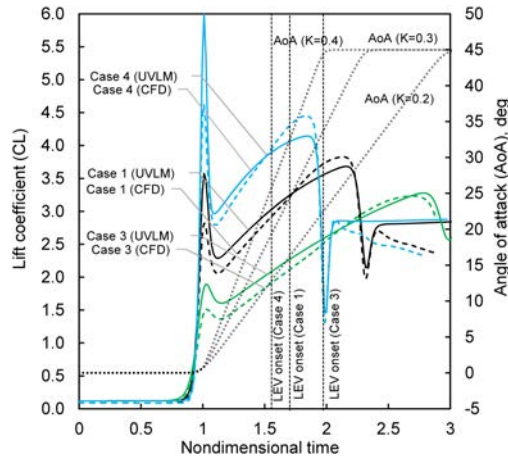
(c) LESP distribution at LEV initiation.



(d) Motion histories and LEV initiation.

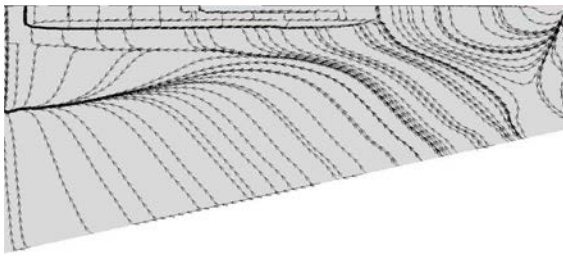


(e) $LESP_{max}$ vs. t^* from UVLM.



(f) C_L vs. t^* from CFD and UVLM.

Figure 8.9: Case study B: Effect of pitch rate. Comparison of cases 1, 3, and 4 at CFD frames just after LEV onset.



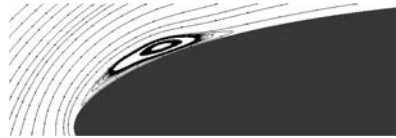
(a) Upper-surface skin-friction lines for case 5, $t^* = 1.725$, $\alpha = 24.92$ deg.



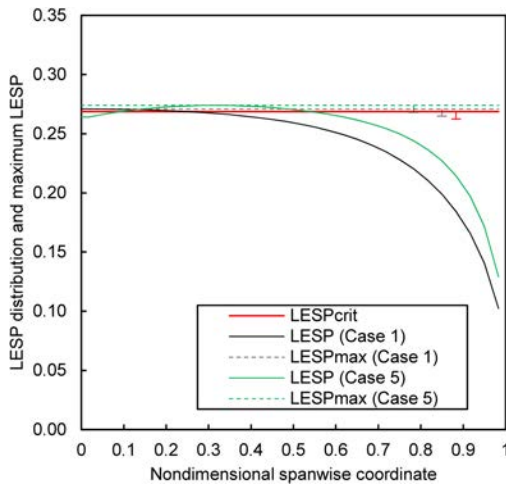
(b) Streamlines near wing tip, leading edge.



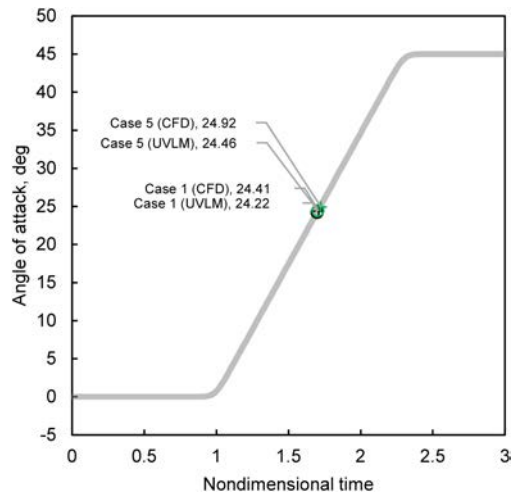
(c) Streamlines at $2y/b = 0.3$, leading edge.



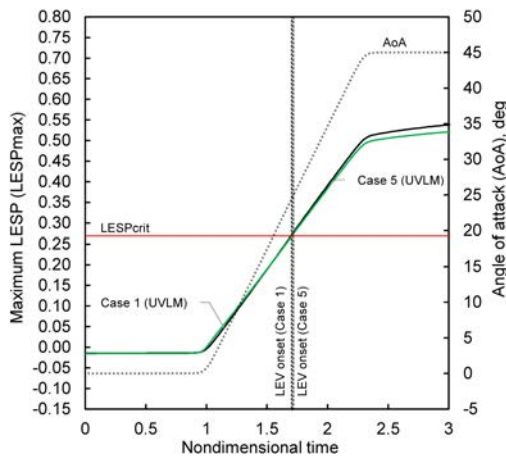
(d) Streamlines at wing root, leading edge.



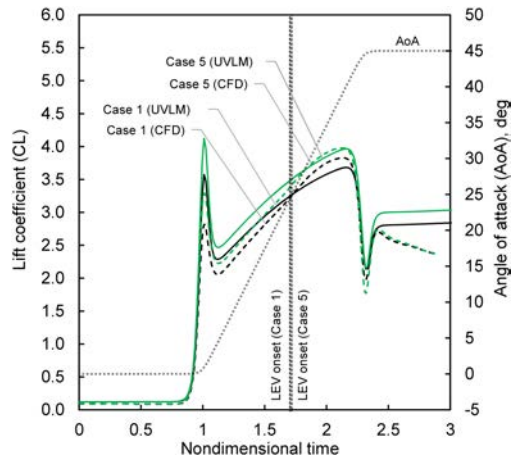
(e) LESP distribution at LEV initiation.



(f) Motion histories and LEV initiation.



(g) $LESP_{max}$ vs. t^* from UVLM.



(h) C_L vs. t^* from CFD and UVLM.

Figure 8.10: Case study C: Effect of taper ratio. Comparison of cases 1 and 5 at CFD frames just after LEV onset.

Figure 8.10a shows the skin-friction lines on upper surface for case 5 at LEV initiation. It is seen that the LEV initiation starts at around $2y/b = 0.3$, which is qualitatively confirmed by the streamline plots around the leading edge at the three spanwise locations in Figures 8.10b–8.10d and is similar to the observation of Spentzos *et al.*¹¹⁰ that LEV initiation on a tapered wing appeared to be closer to the wing tip. Figure 8.10e compares the spanwise $LESP$ distribution for case 5 with that for case 1. In contrast to the results for case 1, the spanwise $LESP$ distribution for the tapered wing has a maximum near $2y/b = 0.3$, which agrees well with the CFD-predicted spanwise location for LEV initiation. The $LESP_{max}$ value also agrees well with the 2D $LESP_{crit}$ value. Because of this agreement, the UVLM-predicted AoA for LEV initiation agrees excellently with the CFD prediction (Figure 8.10f). Figures 8.10g and 8.10h show that the time variations of the $LESP_{max}$ and C_L for case 5 are largely similar to those for case 1.

8.2.6 Case Study D: Effect of tip twist

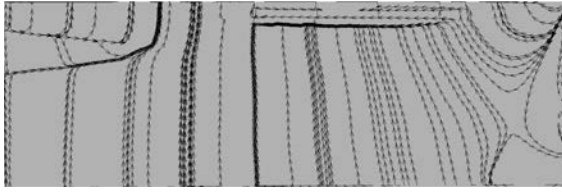
In case study D, the initiation of the LEV for the twisted wing with 10-degree tip twist (case 6) is compared with the results for case 1. The twisted wing in case 6 has a linearly increasing section incidence angle from root to tip.

Figure 8.11a shows the upper-surface skin-friction lines from CFD at the time instant of LEV initiation, showing that LEV starts forming for this wing from $2y/b$ of approximately 0.6. The chordwise streamline plots for the three sections, shown in Figures 8.11b, 8.11c, and 8.11d, confirm this observation. As seen in Figure 8.11g, the UVLM-predicted spanwise $LESP$ distribution of case 6 (dashed line) has a clear maximum around the spanwise location of $2y/b$ of 0.6, which agrees excellently with the CFD prediction. The $LESP_{max}$ value from UVLM agrees excellently with the 2D $LESP_{crit}$ value. As a result of this agreement, the UVLM-predicted value for the AoA for LEV initiation also agrees excellently with the CFD prediction, as seen from Figure 8.11f. From Figure 8.11f, it is also seen that the AoA for LEV initiation for case 6 is approximately five degrees less than that for case 1. This early initiation of the LEV formation is the result of higher incidence of the outboard sections due to tip twist. The behavior of the $LESP_{max}$ and C_L time variations, shown in Figures 8.11g and 8.11h, are largely similar to those for case 1, except for an offset resulting from the wing twist.

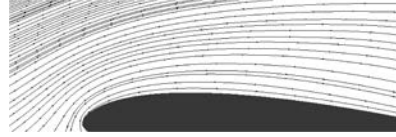
8.2.7 Case Study E: Effect of aspect ratio

In case study E, the initiation of the LEV for the rectangular wing cases 7, 8, and 9 ($AR = 2, 4, 8$ respectively) are compared with that for the baseline case (case 1, rectangular wing of $AR = 6$).

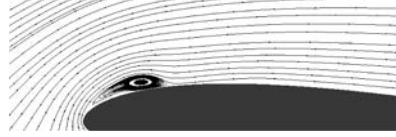
The results of the investigation of AR effects on LEV initiation are presented in Figure 8.12. Figures 8.12a, 8.12b, and 8.12c show the skin friction lines for the rectangular wings with $AR = 2, 4, 8$, respectively. These three figures indicate that the onset location of LEV initiation is at the wing root for all these wings. Also seen is that, although the region near the wing tip for each wing where the skin-friction lines are influenced by the tip vortex are roughly of the same size for these three wings, the fraction of the wing occupied by this region is clearly the largest for the lower aspect ratio wing. Thus it can be expected that the lower aspect ratio wings will be more influenced by the tip vortex effects. Figure 8.12d shows the spanwise distributions of $LESP$ for the four cases: $AR = 2, 4, 6, 8$. Each of the four cases has the maximum in $LESP$ variation at the root, which agrees with the CFD-predicted root location for the onset of LEV formation for each wing. While the $AR = 4, 6, 8$ wings have $LESP_{max}$ values agreeing excellently with the 2D



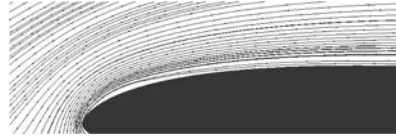
(a) Upper-surface skin-friction lines for case 6, $t^* = 1.575$, $\alpha = 19.75$ deg.



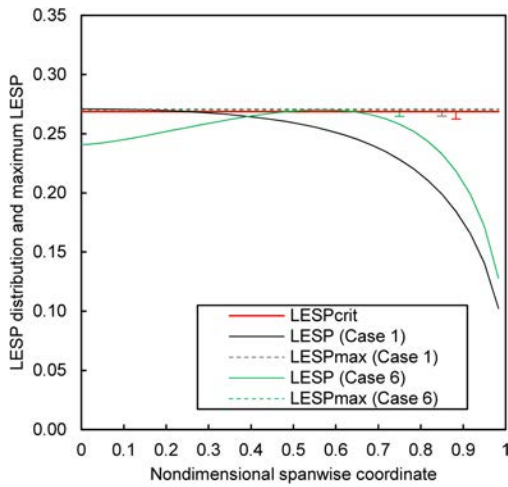
(b) Streamlines near wing tip, leading edge.



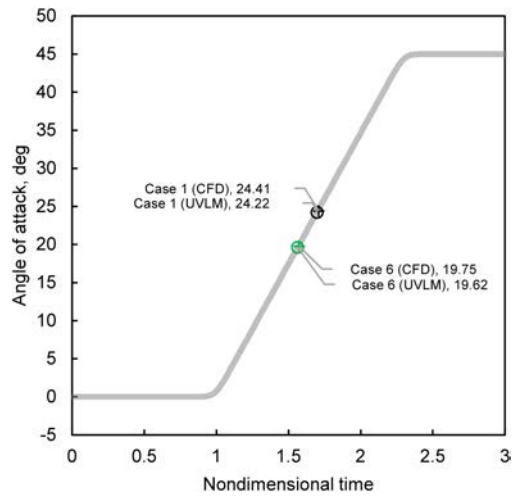
(c) Streamlines at $2y/b = 0.6$, leading edge.



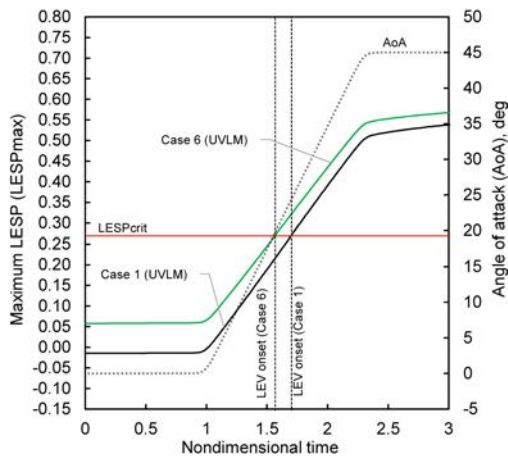
(d) Streamlines at wing root, leading edge.



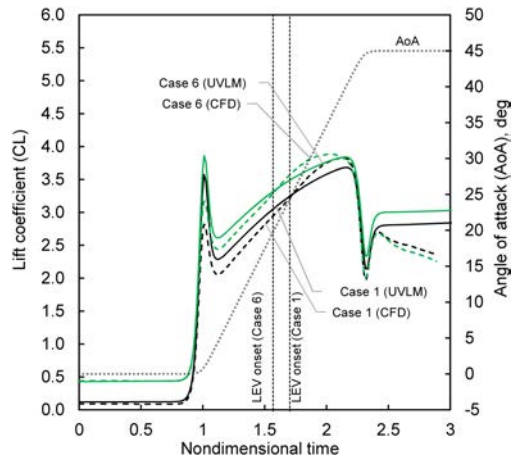
(e) LESP distribution at LEV initiation.



(f) Motion histories and LEV initiation.

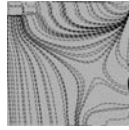


(g) $LESP_{max}$ vs. t^* from UVLM.



(h) C_L vs. t^* from CFD and UVLM.

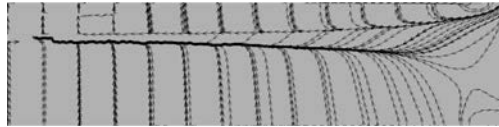
Figure 8.11: Case study D: Effect of tip twist. Comparison of cases 1 and 6 at CFD frames just after LEV onset.



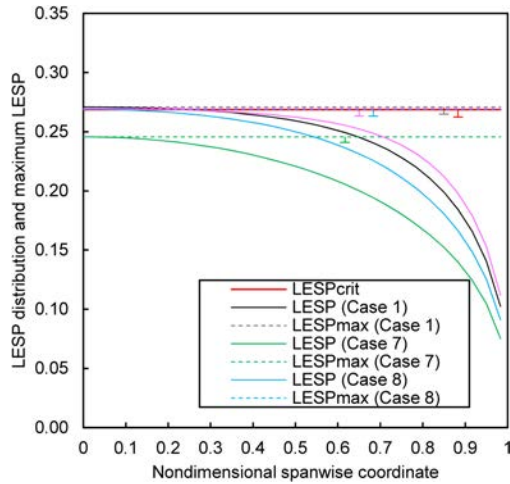
(a) Upper-surface skin-friction lines for case 7, $t^* = 1.830$, $\alpha = 28.53$ deg.



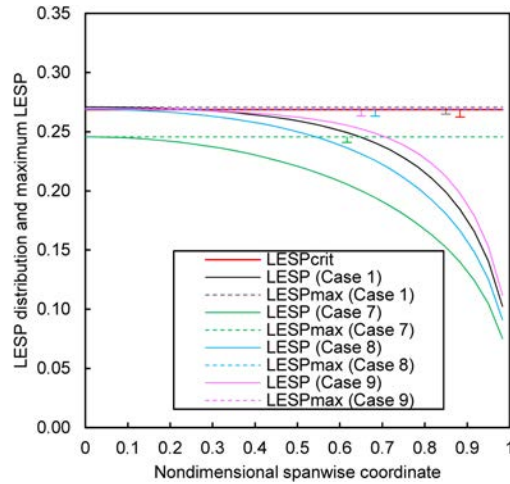
(b) Upper-surface skin-friction lines for case 8, $t^* = 1.740$, $\alpha = 25.44$ deg.



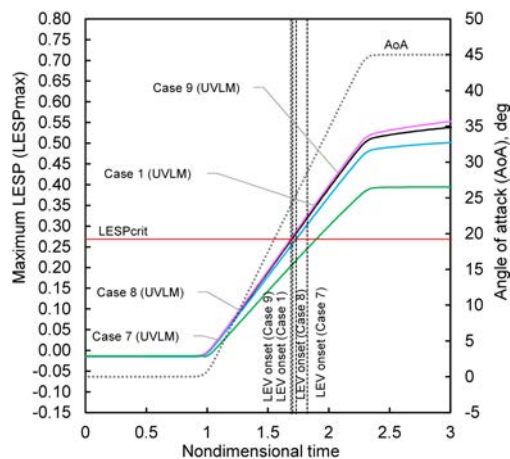
(c) Upper-surface skin-friction lines for case 9, $t^* = 1.695$, $\alpha = 23.89$ deg.



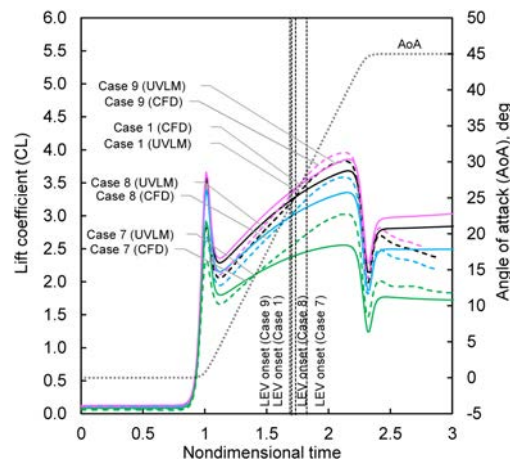
(d) LESP distribution at LEV initiation.



(e) Motion histories and LEV initiation.



(f) $LESP_{max}$ vs. t^* from UVLM.



(g) C_L vs. t^* from CFD and UVLM.

Figure 8.12: Case study E: Effect of aspect ratio. Comparison of cases 1, 7, 8, and 9 at CFD frames just after LEV onset.

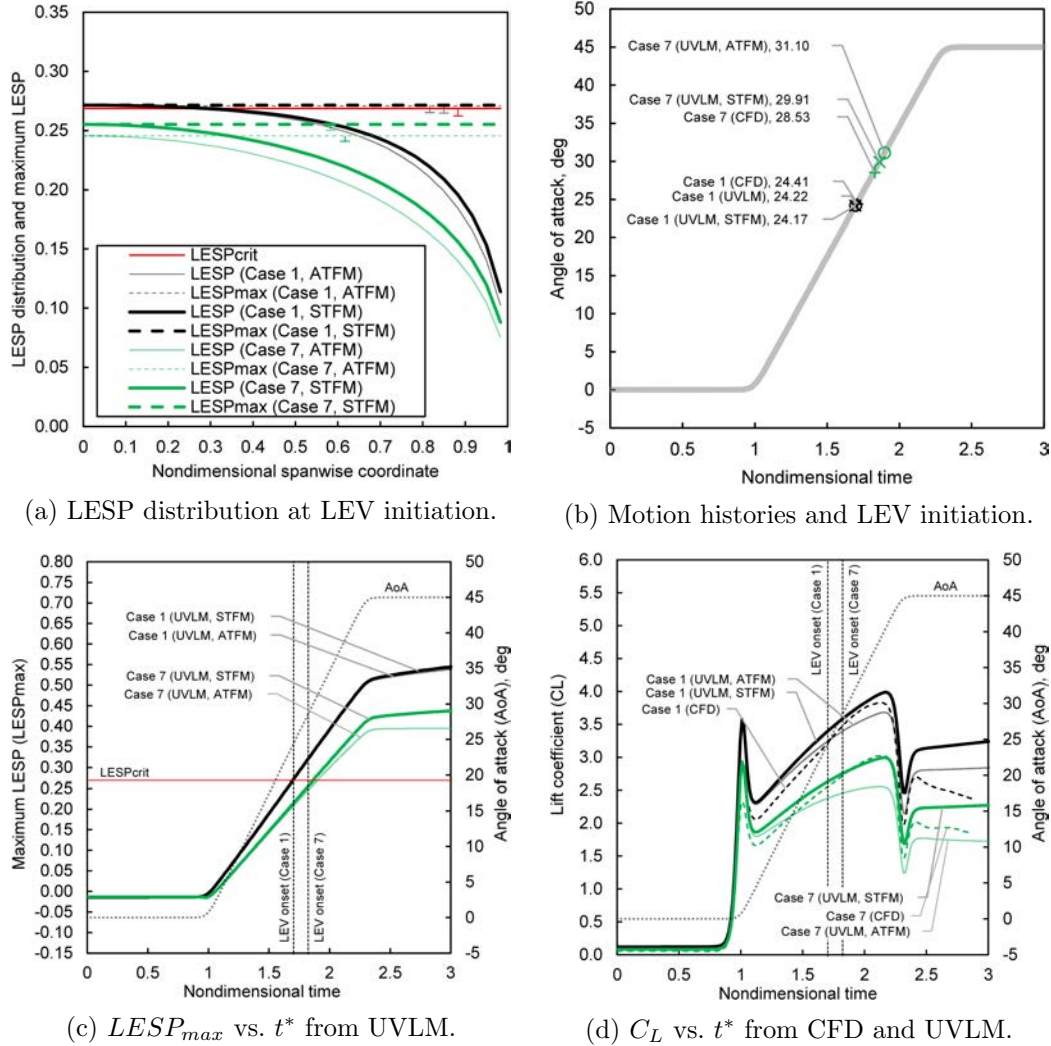


Figure 8.13: Comparison of separated tip flow model and attached tip flow model for case 1 and 7.

$LESP_{crit}$, the $LESP_{max}$ for the AR 2 wing is noticeably less than the 2D $LESP_{crit}$. In concert with this observation, Figure 8.12e shows that the AoA for LEV initiation for the AR 4, 6, and 8 wings from both CFD and UVLM predictions are very close to each other. On the other hand, the AR 2 wing has CFD prediction for LEV initiation occurring at a higher AoA compared to the UVLM prediction. This discrepancy can be attributed to the increased effect of the “lifted-up” tip vortex structure on the downwash at the leading edge for the AR-2 case due to the proximity of the tip vortex to the wing root. Because the UVLM does not take the lifting-up of the tip vortex into consideration, and instead assumes an attached tip vortex, the UVLM-predicted AoA for LEV initiation on the AR-2 wing differs from the CFD prediction by almost 2.5 degrees. Figures 8.12f and 8.12g show the time variations of $LESP_{max}$ and C_L for the four cases. Except for the AR-2 wing, the results for the other cases mostly follow expected trends.

To investigate the influence of the tip-vortex structure on the UVLM predictions, the UVLM code was used to study the AR-2 (case 7) and AR-6 (case 1) wings using the “attached tip-flow model, or ATFM” option (Figure 7.4a) and the “separated tip-flow model, or STFM” option (Figure 7.4b). Figure 8.13 presents the results from this study. It is seen that the results for AR-6 wing are mostly

independent of the tip-flow model used. On the other hand, for the AR-2 wing, the results of the UVLM have better agreement with the CFD prediction when the separated tip-flow model is used than when the attached tip-flow model is used. This trend confirms the hypothesis that, for very low aspect ratio wings, it is important to capture the effects of the “lifted-off” tip vortex structure for improved predictions from the UVLM.

8.2.8 Case Study F: Effect of sweep angle

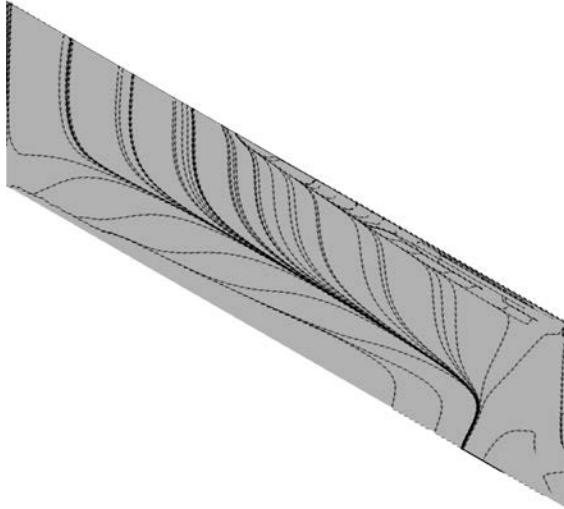
In case study F, the initiation of the LEV for the 30-degree swept-wing case 10 is compared with the baseline case (case 1, 0-degree sweep). It is to be noted that the pivot point for the swept wing is at the quarter-chord location of the root section.

The results for the effects of sweep on LEV initiation are shown in figure 8.14. Figure 8.14a shows the CFD-predicted skin-friction lines on the upper-surface at LEV initiation. In contrast to the results for all the other wings, this swept wing case exhibits LEV initiation that starts close to the wing tip, and at a very small AoA of 2.8 degrees. The streamline plots of the leading-edge regions in Figures 8.14b, 8.14c, and 8.14d show an LEV structure for the sections near the wing tip and none for the root section, confirming this observation. The likely reason for this behavior is that a pitch-up motion about the root quarter-chord location causes a significant motion-induced upwash towards the wing tips, causing the leading edge near the wing tip to become critical even at an early stage of the motion. Figure 8.14e compares the spanwise distributions of $LESP$ at LEV initiation for the swept wing with the unswept wing. It is seen that the $LESP$ distribution for the swept wing is distinctly different from that for the unswept wing; it has a clear maximum near $2y/b = 0.9$, which shows that, like CFD, the UVLM also predicts LEV initiation very close to the wing tip. There is a significant discrepancy between the $LESP_{max}$ for the swept wing and the 2D $LESP_{crit}$. One possible reason for this discrepancy is that, like with the AR-2 wing, the LEV occurs very close to the tip vortex. Because the UVLM models the tip vortex using an “attached-tip-flow” model (Figure 7.4a), there is error in the predicted value of $LESP$ near the wing tips. Another reason could be that spanwise pressure gradient or spanwise flow, which have both been discussed by other researchers in the context of LEV initiation,^{33,60,125} could be causing the discrepancy.

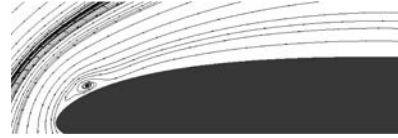
Figure 8.14f compares the CFD- and UVLM-predicted AoA for LEV initiation on the swept wing with those for the unswept wing (case 1). In spite of the discrepancy between the $LESP_{max}$ and 2D $LESP_{crit}$ for case 10, it is seen that the UVLM-predicted AoA is a small value of 1.5 degrees, which is within 1.3 degrees of the CFD-predicted AoA. Figure 8.14g shows the time-variation of $LESP_{max}$ for the swept and unswept-wing cases. In contrast to the other cases, the swept wing is seen to have a rapid increase in the $LESP_{max}$ even during the very early stages of the pitch-up motion. Perhaps for this reason, the fairly significant discrepancy of 0.08 between $LESP_{max}$ and 2D $LESP_{crit}$ translates to only a small AoA discrepancy of 1.3 degrees between UVLM and CFD. Figure 8.14h shows the time variation of C_L from UVLM and CFD for the two cases. Because the LEV initiation occurs very early in the motion and UVLM does not model the LEV formation and its effects, there is considerable lack of agreement between UVLM and CFD for much of the pitch-up portion of the motion.

8.2.9 Case Study G: Effect of leading-edge curvature

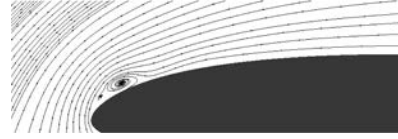
In case study G, the initiation of the LEV for the wing with sharpened leading edge (case 11, sharpened SD7003 airfoil) is compared with the baseline case (case 1, SD7003).



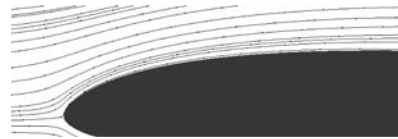
(a) Upper-surface skin-friction lines for case 10, $t^* = 1.080$, $\alpha = 2.79$ deg.



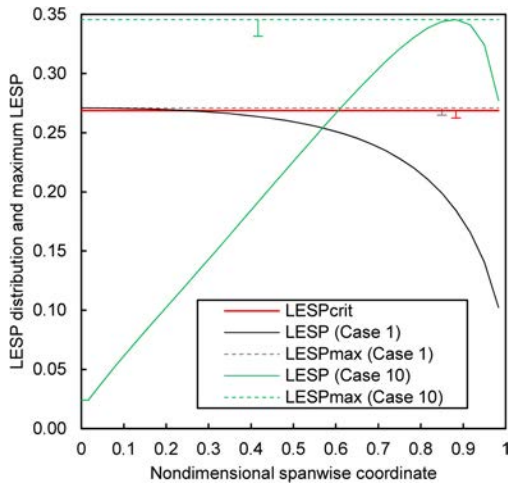
(b) Streamlines near wing tip, leading edge.



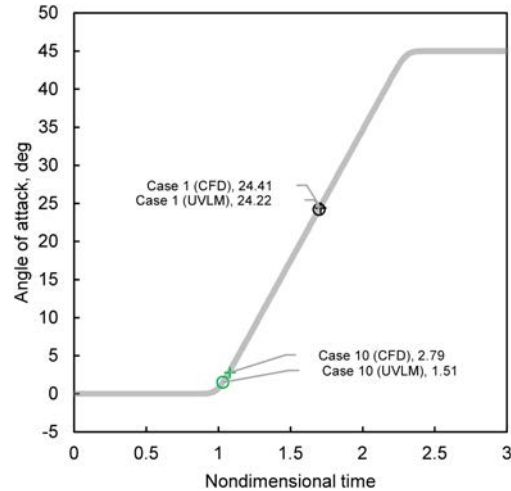
(c) Streamlines at $2y/b = 0.9$, leading edge.



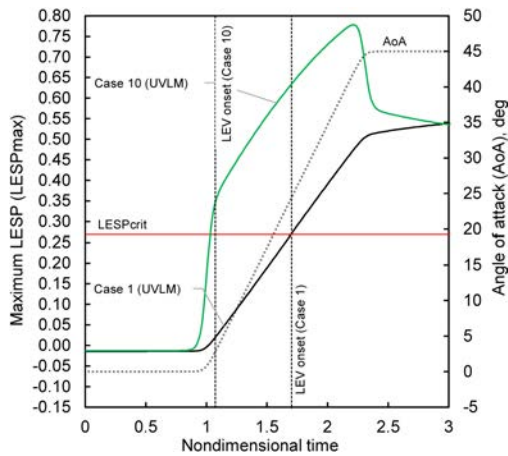
(d) Streamlines at wing root, leading edge.



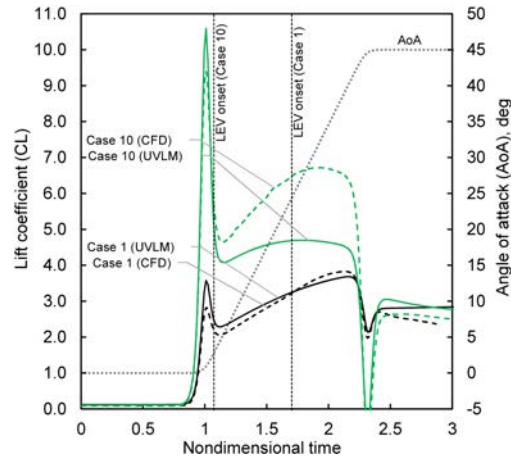
(e) LESP distribution at LEV initiation.



(f) Motion histories and LEV initiation.

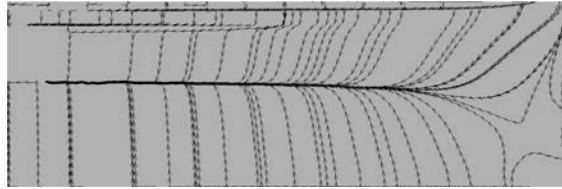


(g) $LESP_{max}$ vs. t^* from UVLM.

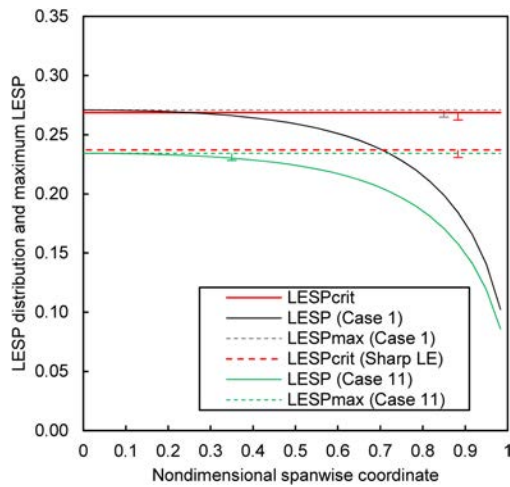


(h) C_L vs. t^* from CFD and UVLM.

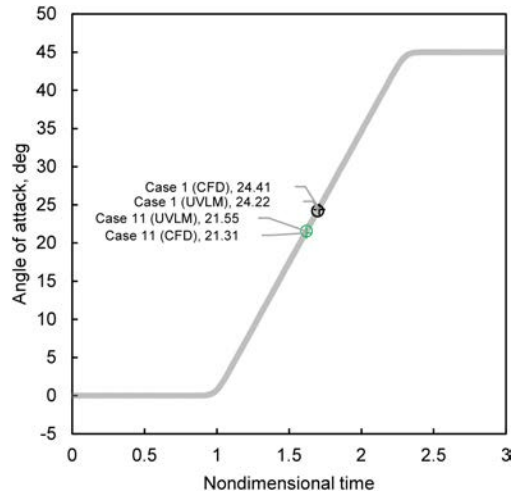
Figure 8.14: Case study F: Effect of sweep angle. Comparison of cases 1 and 10 at CFD frames just after LEV onset.



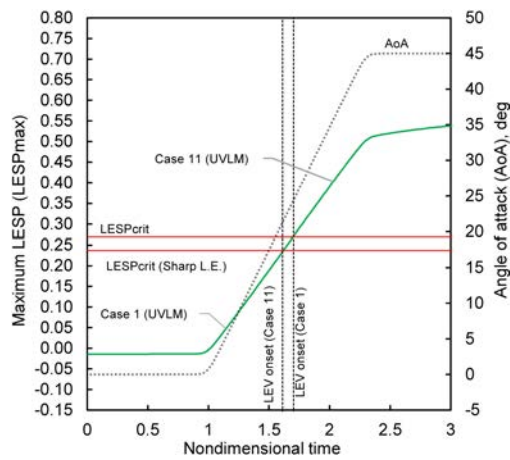
(a) Upper-surface skin-friction lines for case 11, $t^* = 1.620$, $\alpha = 21.31$ deg.



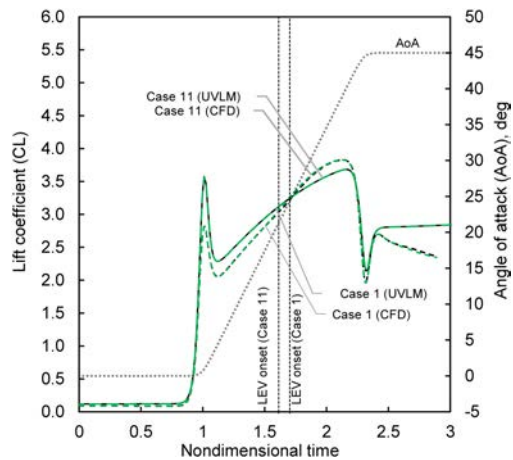
(b) LESP distribution at LEV initiation.



(c) Motion histories and LEV initiation.



(d) $LESP_{max}$ vs. t^* from UVLM.



(e) C_L vs. t^* from CFD and UVLM.

Figure 8.15: Case study G: Effect of leading edge curvature. Comparison of cases 1 and 11 at CFD frames just after LEV onset.

Figure 8.15 presents the result for this case study. The results largely agree with the expected behavior that airfoils with sharper leading edges tend to have earlier leading-edge separation or initiation of vortex shedding.^{39,44} Figure 8.15a shows the upper-surface skin-friction lines for case 11. It is seen that LEV initiation starts at the root, like with case 1, but at a smaller AoA due to the sharper leading edge. Compared to case 1, the chordwise extent of trailing-edge reverse flow region is smaller because of the smaller AoA. The spanwise variation of $LESP$ for the two cases are shown in Figure 8.15b. The $LESP_{max}$ for case 11 compared excellently with the 2D $LESP_{crit}$ value for the sharpened SD7003. This excellent agreement translates to excellent agreement between the UVLM and CFD predictions for the AoA for LEV initiation for case 11 (Figure 8.15c). Figure 8.15d shows that the time variations of $LESP_{max}$ for cases 1 and 11 are identical. Likewise the time variations of C_L for the two cases from UVLM predictions are also identical. This behavior is because the two airfoils have the same camberline, and the UVLM results do not depend on leading-edge radius. The CFD predictions for time variation of C_L for case 11 is seen to be very similar to that for case 1.

8.2.10 Case Study H: Effect of abrupt change in incidence

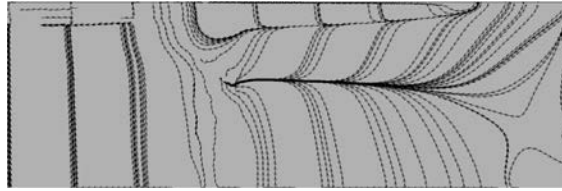
In case study H, the initiation of the LEV for case 12, for which the wing geometry has a four-degree higher incidence over the inboard third of the span, is compared with that for case 1.

Figure 8.16 shows the results for this case study. The upper-surface skin-friction lines for case 12 in Figure 8.16a shows the abrupt change in sectional skin-friction lines at $2y/b = 0.33$, which is clearly related to the incidence change. It is seen that the LEV initiation starts at the wing root, which is also to be expected owing to the increased incidence in that region. Figure 8.16b shows the spanwise distributions of $LESP$ for the two cases. It is seen that case 12 has a distinctly higher $LESP$ over the inboard portion of the wing. The $LESP_{max}$ for case 12 is seen to agree closely with the 2D $LESP_{crit}$. From Figure 8.16c, it is seen that the UVLM and CFD predictions for AoA for LEV initiation on case 12 agree well with each other, and that case 12 has LEV initiation approximately 4 degrees earlier than case 1. Figure 8.16d shows that the time variation of $LESP_{max}$ for case 12 is quite similar to that of case 1, except for an offset resulting from the increased incidence. Similarly, Figure 8.16e shows that the time variation of C_L for case 12 is similar to that for case 1, except for an offset due to the incidence change.

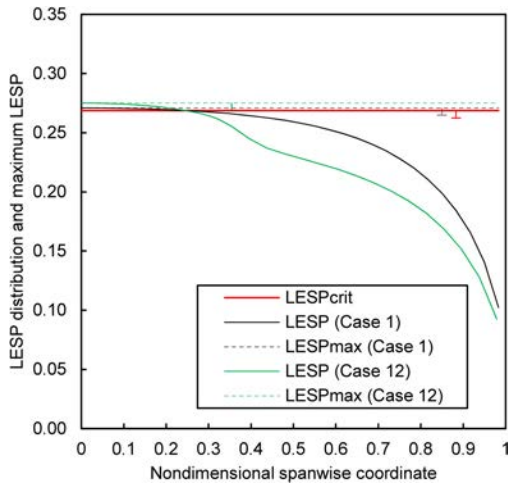
8.2.11 Case Study I: Partially sharpened wing

In case study I, the initiation of the LEV for case 13, with the wing having the sharpened leading-edge over the inboard third of the wing span, is compared with the baseline case 1.

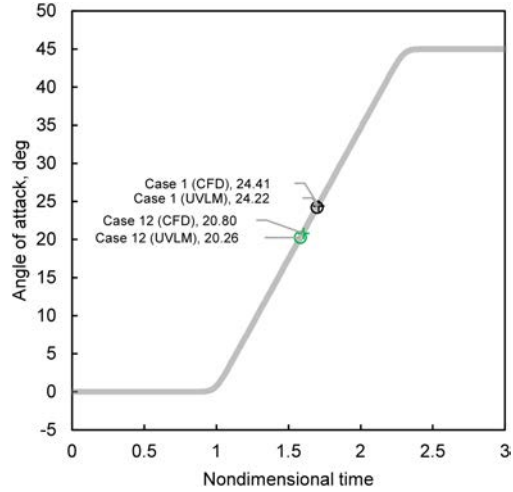
Figure 8.17 presents the results for this case study. The upper-surface skin-friction lines for case 13, in Figure 8.17a, shows that the LEV initiation starts at the wing root at AoA of 21.3 degrees. Figure 8.17b compares the spanwise variations of $LESP$ and $LESP_{crit}$ for case 13 with those for the baseline. Because of the abrupt change in airfoil between the inboard and the outboard portions of the wing, the 2D $LESP_{crit}$ value also changes from the value of $LESP_{crit} = 0.269$ for the SD 7003 airfoil in the outboard portions to the value of $LESP_{crit} = 0.237$ for the sharpened SD 7003 airfoil in the inboard portion. It is seen that the $LESP_{max}$ agrees well with the inboard value of the 2D $LESP_{crit}$, resulting in an excellent agreement between the UVLM and CFD predictions for the AoA for LEV initiation (Figure 8.17c). In contrast with case study H in which the abrupt change in section incidence caused a sudden change in the spanwise variation of $LESP$, the abrupt



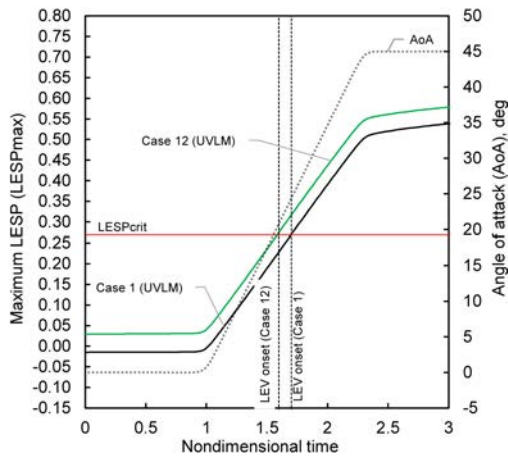
(a) Upper-surface skin-friction lines for case 12, $t^* = 1.605$, $\alpha = 20.80$ deg.



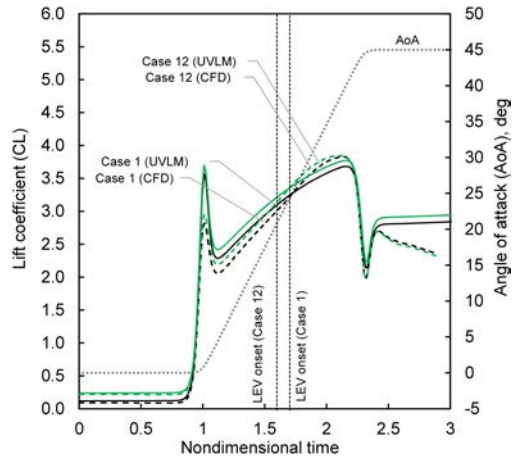
(b) LESP distribution at LEV initiation.



(c) Motion histories and LEV initiation.

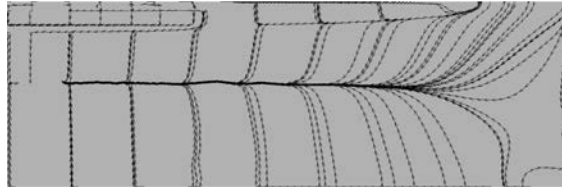


(d) $LESP_{max}$ vs. t^* from UVLM.

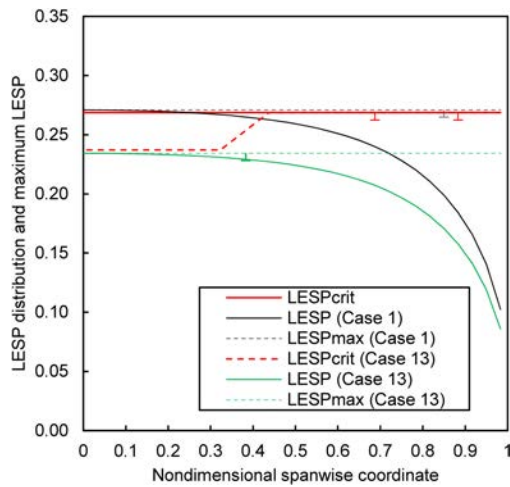


(e) C_L vs. t^* from CFD and UVLM.

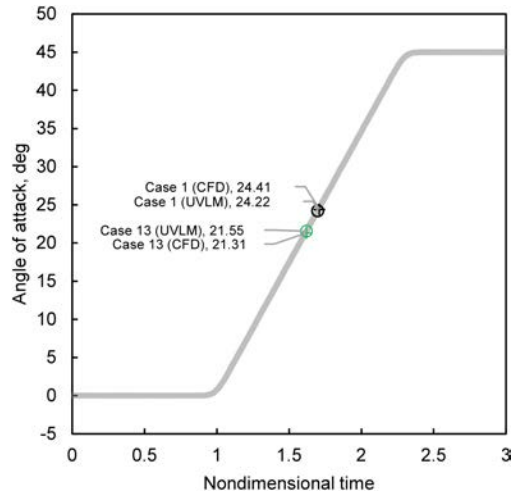
Figure 8.16: Case study H: Partially deflected wing. Comparison of cases 1 and 12 at CFD frames just after LEV onset.



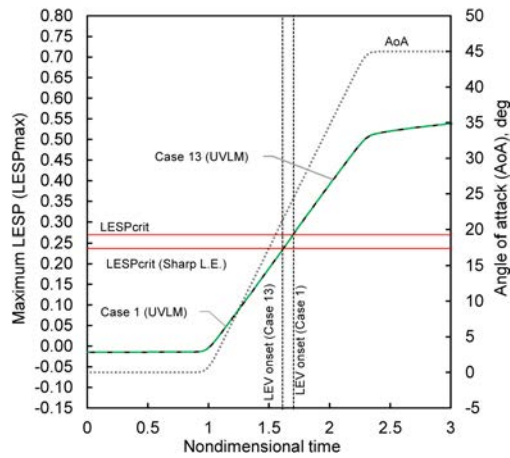
(a) Upper-surface skin-friction lines for case 13, $t^* = 1.620$, $\alpha = 21.31$ deg.



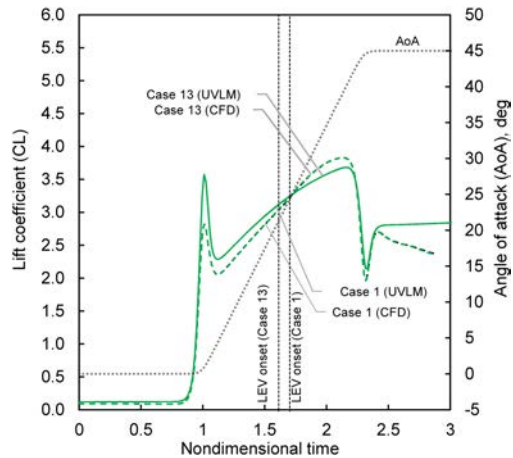
(b) LESP distribution at LEV initiation.



(c) Motion histories and LEV initiation.



(d) $LESP_{max}$ vs. t^* from UVLM.



(e) C_L vs. t^* from CFD and UVLM.

Figure 8.17: Case study I: Partially sharpened wing. Comparison of cases 1 and 13 at CFD frames just after LEV onset.

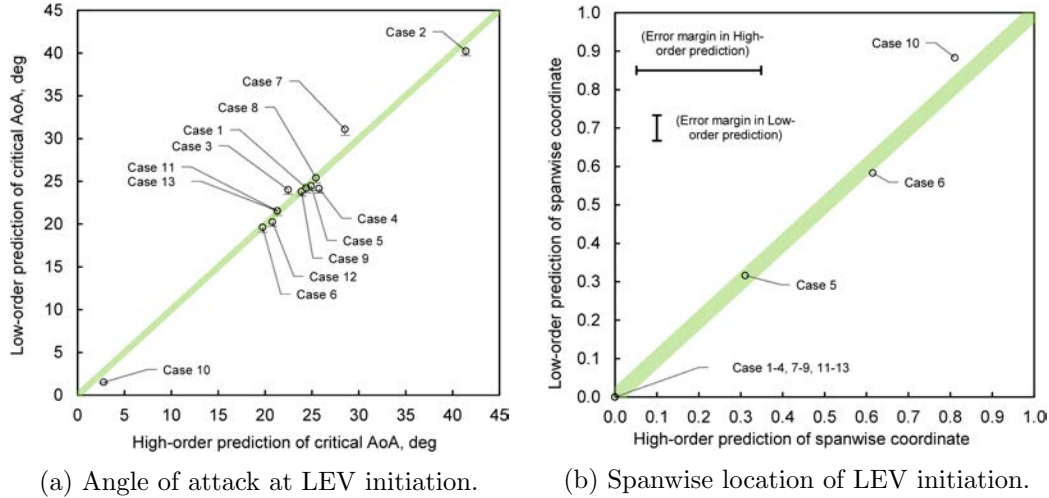


Figure 8.18: Comparison of low-order (UVLM) predictions with high-order (CFD) results for all the finite-wing cases.

change in leading-edge radius in this case study causes an abrupt change in $LESP_{crit}$. Thus, while both cases 12 and 13 have a roughly 3–4-degree earlier LEV initiation compared to the baseline case, the earlier LEV initiation is achieved in different ways. As seen from Figure 8.17d, the time variations in $LESP_{max}$ for both cases are identical, because the UVLM prediction is not altered by changes in leading-edge radius as long as section camber is not altered. Figure 8.17e shows that the time variations in C_L for the two cases are also nearly identical.

8.2.12 Summary

Figure 8.18 presents a comparison of low-order (UVLM) predictions for all the 13 finite-wing cases with the respective high-order (CFD) predictions. In Figure 8.18a, the AoA values for LEV initiation from UVLM are plotted as symbols for the 13 cases against the CFD predictions. The 45-degree line is co-plotted to denote perfect correlation, with the thickness of the line chosen to denote the measuring error in the CFD observation. Each symbol has an error bar to denote the resolution error in the UVLM prediction. It is seen that the AoA for LEV initiation has a spread of almost 40 degrees varying from 2.8 degrees for case 10 to 41.4 degrees for case 2. This shows that AoA itself is not a good measure for LEV initiation, as it varies significant from case to case. In contrast, when the low-order prediction is made using the 2D $LESP_{crit}$ value, the UVLM-to-CFD correlation for AoA for LEV initiation is seen to be very good for all the cases as the symbols are all close to the 45-degree line. The error in UVLM-to-CFD correlation for AoA is a maximum of 2.6 degrees for case 7, which is the AR-2 wing, with most of the other cases having much smaller error. Figure 8.18b shows a plot of the low-order (UVLM) prediction of the spanwise location of LEV initiation against the corresponding CFD prediction, using symbols to denote the 13 cases. In this figure too, the 45-degree line is plotted to show perfect correlation with the thickness of this line chosen to represent the resolution error of the UVLM. The spanwise width over which LEV initiation was observed in the CFD, averaged over the 13 cases, is shown as an error bar in the figure. It is seen that, although the spread for the spanwise locations ranges from the wing root to almost the wing tip, the UVLM predictions for all cases agree remarkably well with the corresponding CFD observations. These excellent correlations in (i) AoA for LEV initiation, with a

highest error of 2.6 degrees for cases that are spread over a range of 41.4 degrees, and (ii) spanwise location with a highest error of approximately $2y/b = 0.1$ for cases that are spread of a range of $2y/b = 0.9$ demonstrate the power of the LESP concept in predicting the LEV initiation on a range of finite-wing geometries using just the 2D $LESP_{crit}$ values for the sections used in the wings along with a low-order method like the UVLM.

8.3 Interim Conclusions

In this chapter we presented a study to extend the concept of LESP, which is a measure of leading edge suction in 2D airfoils, as a criterion for LEV initiation on finite wings. In order to assess the effectiveness of this idea, the maximum values of the spanwise $LESP$ variations for the wings at LEV initiation were studied for 13 wings with variations in planform geometry, pivot location, pitch rate, twist angle, aspect ratio, and cross-section shape. It was seen that, for any given airfoil shape and Reynolds number, this maximum $LESP$ value for all the wings and motions was acceptably close to the critical $LESP$ (obtained from 2D CFD). It was shown that the LESP concept was successful in predicting the angle of attack for the onset of LEV initiation within ± 1.6 degrees accuracy against a 39-degree spread in the angle of attack for the LEV onset for the cases examined. Additionally, the LESP concept is also able to predict the spanwise location for LEV initiation with good accuracy. Thus, the results of this portion of the research effort provided the confidence to extend the LESP concept to prediction of LEV formation (LEV growth after initiation), which is discussed in the next chapter.

Chapter 9

Low-Order Prediction of LEV Formation on Finite Wings

This chapter presents the results from the modified UVLM to model LEV formation on finite wings. The prediction of LEV structure and aerodynamic loads derived by new modified UVLM are verified with the observation of CFD.

9.1 Development of LEV structure

In this section, distribution of LEV sheet predicted by new LEV model is reported and verified by CFD observation. As mentioned before, the motion of vortex sheets are determined by local velocity field. For this reason, the sheet distribution can be thought of as a plane swept by local streamlines and the figure of vortex sheets represents the flow structure. This section discusses the accuracy of predicted flow structure by verifying with CFD observation and shows the development of inner vortical structure of LEV.

Figure 9.1 shows chronological snapshots of LEV development for case 1 (baseline). Because the flow is symmetric, all pictures show the left side of wing and its flow structure. The left and the right column of figure 9.1 respectively shows the observation of CFD and the prediction of UVLM. Herein, CFD observation is rendered by iso-surface of Q -criterion to depict the vortex structure. Although iso- Q surface is not quantitatively equivalent to the vortex sheet distribution, it allows for qualitative comparison of vortex flow structure. Figure 9.1a shows the initiation of LEV formation. The LEV sheet starts shedding from the leading edge around the wing root, which is the onset location of LEV formation, and it corresponds with the CFD observation. In figure 9.1b, the front line of LEV progresses to the spanwise direction. The predicted spanwise progression of LEV qualitatively matches the CFD observation but UVLM prediction is slightly delayed. CFD observation captures a few chordwise shear waves (Kelvin-Helmholtz wave) behind the leading edge while UVLM prediction shows a convection of LEV sheet with small crease at the edge of LEV sheet, which indicates the trace of the starting vortex of LEV shedding. UVLM employs the cutoff function to remove the singularity effect and small shear waves observed in CFD are not simulated in UVLM prediction. (Note that the influence of shear waves are not important compared to that of primary LEV in present work.) According to CFD observation, LEV shedding region has covered the whole leading edge in figure 9.1c, however UVLM prediction is slightly delayed and the spanwise

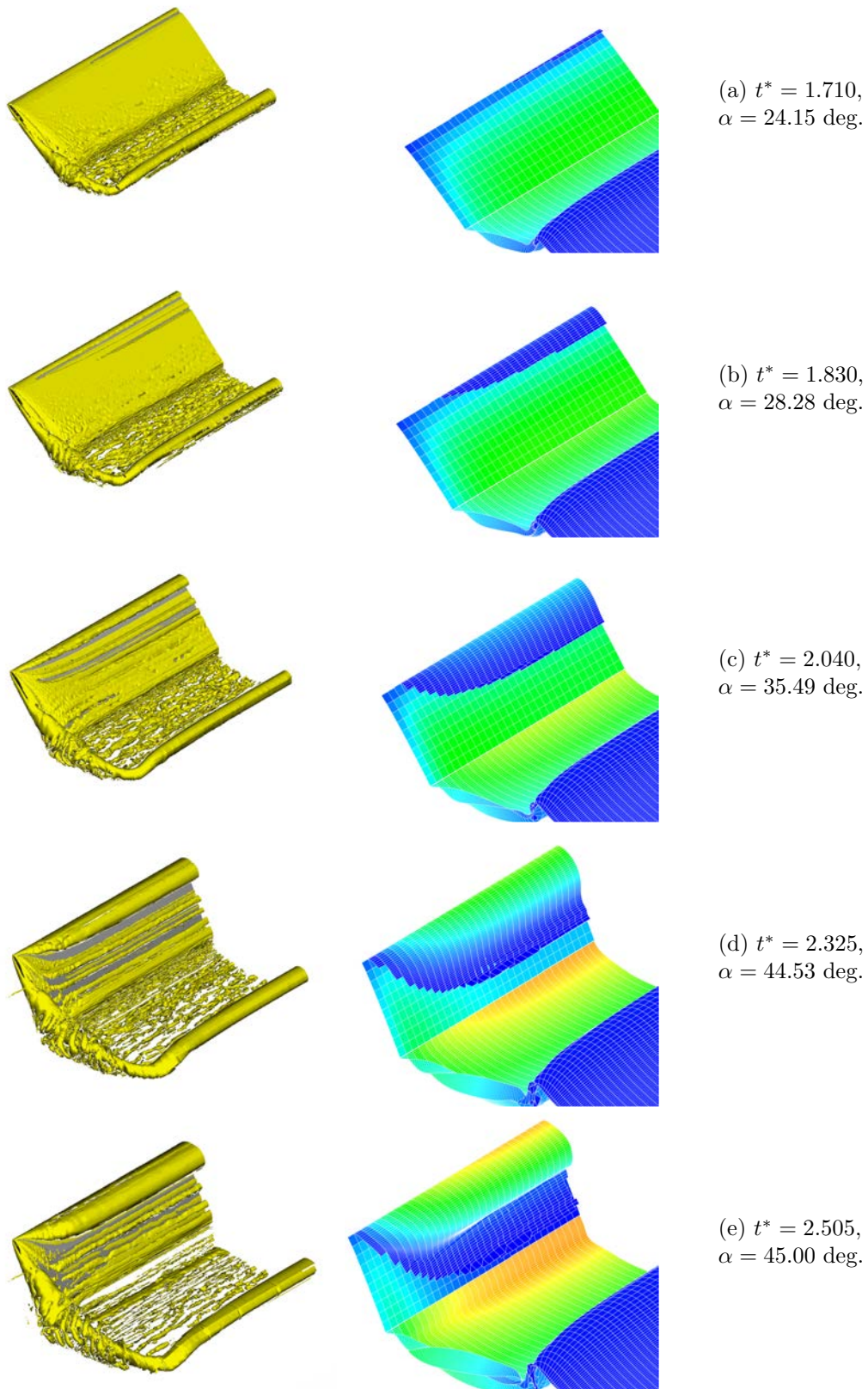


Figure 9.1: Comparison of LEV structure of CFD (left) and UVLM (right) for case 1.

progression of LEV has not yet reached the wing tip. This delay of spanwise development of LEV structure probably results from the lack of tip vortices, which could pull the surface flow structure to the tip side. In figure 9.1d, both CFD observation and UVLM prediction shows the primary LEV build up around the leading edge. At the trailing edge, CFD observation shows relatively large shear wave and it is also predicted by UVLM. In figure 9.1e, both CFD observation and UVLM prediction shows one developed primary LEV and several smaller waves on wing surface. CFD observation in figure 9.1 shows that the tip vortex shed from the wing tip and it directly connects with the trailing vortex of TEV. They eventually forms one large and closed circle, whereas UVLM prediction does not have this feature because UVLM does not simulate a detached or rolled up tip vortex. The problem with simulation of the tip vortices in UVLM is discussed in subsequent section. Overall, figure 9.1 provides a good demonstration of the prediction performance of UVLM in the sense of LEV onset time, onset location, chordwise convection, and the basic pattern of LEV structure composed by the primary LEV. On the other hand, it shows a slight delay of spanwise development of LEV in an early phase of LEV formation.

Figure 9.2 shows the verification of predicted and observed LEV structure for case 6 (tip twist wing). To sum up, it can be said that the accuracy of UVLM prediction is good to capture the time-dependent structural feature of LEV. As mentioned in previous section, one outstanding character of twisted wing is that the onset of LEV formation initiates at the semi-half-span in both left and right wing and spanwise LESP distribution has an M-shaped profile. As shown in figure 9.2a, LEV onset mark is indicated at around $2y/b = 0.6$ in both CFD observation and UVLM prediction. In figure 9.2b, the span of LEV shedding area rapidly progresses towards wing root and wing tip and covers the whole leading edge in CFD observation. On one hand, the UVLM prediction shows that spanwise progression of the LEV has reached the wing root, on the other hand, it delays toward the wing tip, similar to the verification of case 1. As discussed in previous section, the onset of LEV formation of the twisted wing starts from the semi-half-span. The strength of the leading edge suction has twin peak (called M-shaped profile) at the point and the trace of profile is preserved for a few seconds. As a result, the primary LEV forms a slightly distorted shape, which would be illustrated as a hyperbolic hyperboloid in full wing model, as shown in figure 9.2e. (This hyperboloid structure is easily understood by comparing the line of the leading edge and the outline of primary LEV.) UVLM correctly predicts the structural feature of LEV for the twisted wing. The M-shaped LEV structure seems to be transient and soon converges into one cylindrical LEV soon after a second. According to UVLM prediction at $t^* = 3.300$ as shown in figure 9.3, it can be confirmed that the hyperboloid structure has been absorbed by new major cylindrical LEV and it finally attains the same LEV structure as that of baseline case.

Figure 9.4 shows the comparison of LEV structure of CFD observation and UVLM prediction through the time sequence. As mentioned in previous section, the onset of LEV in the swept wing occurs near the wing tip. This behavior is confirmed through figures 9.4a and 9.4b. UVLM prediction captures well with CFD observation for the LEV formation and development towards the wing root, as seen in figures 9.4b and 9.4c. Finally, as shown in figures 9.4d and 9.4e, the LEV forms a conical shape which is well known in delta wings. To sum up, UVLM successfully predicts the LEV structure compared to CFD observation in case 10. However, CFD also shows the interaction between LEV and the tip vortices. Figure 9.5 is the same snapshot of figure 9.4e rendered from the front-left viewpoint. According to figure 9.5, primary LEV shows a conical shape from the wing root (left side of the picture) to the wing tip (bottom-right corner of the picture) and contacts the tip vortex. Considering Helmholtz law, LEV would feed itself to the tip vortex there and they eventually connect with each other at the corner of the wing tip. It could be geometrically important feature to simulate in UVLM prediction and is discussed in subsequent section.

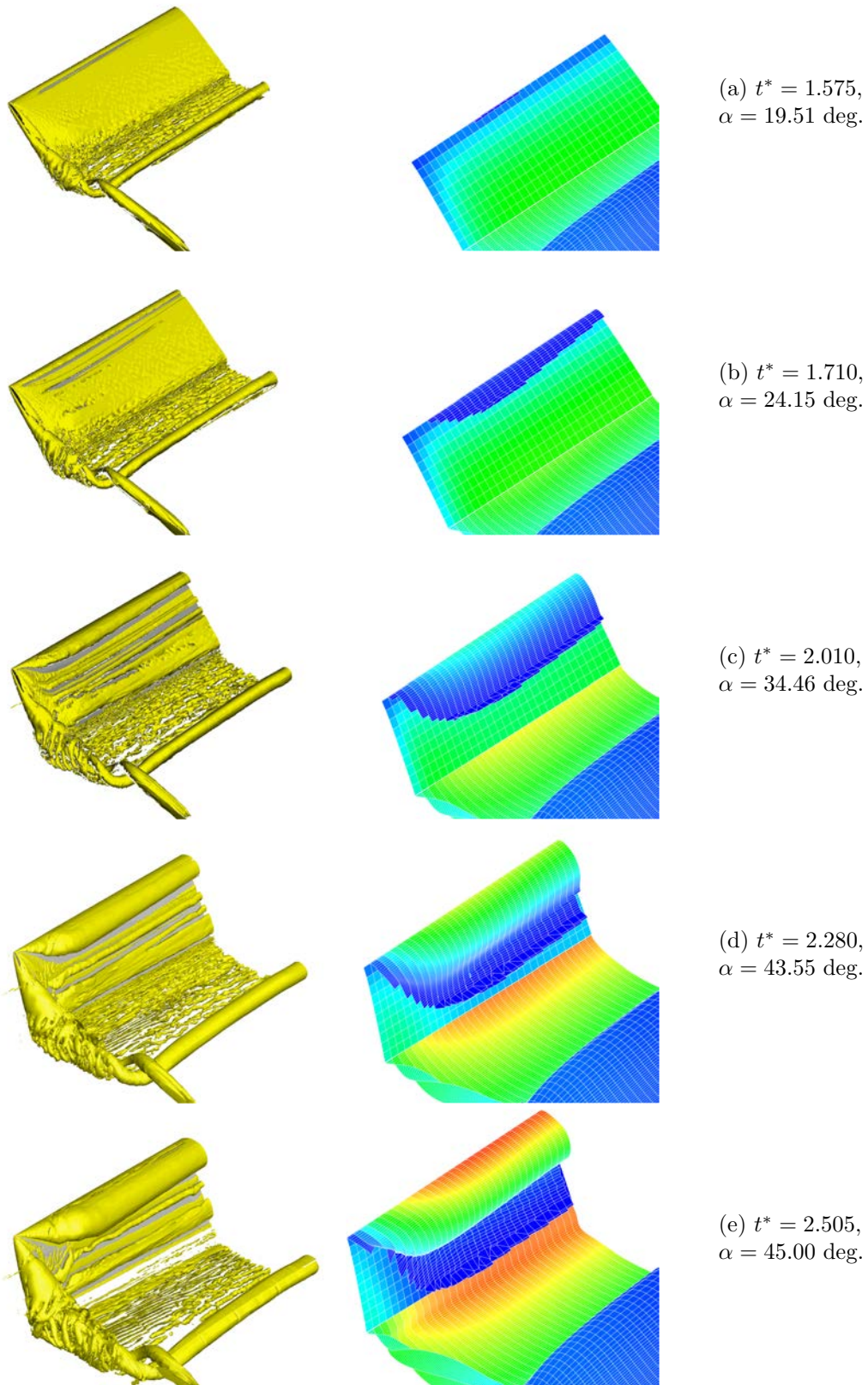


Figure 9.2: Comparison of LEV structure of CFD (left) and UVLM (right) for case 6.

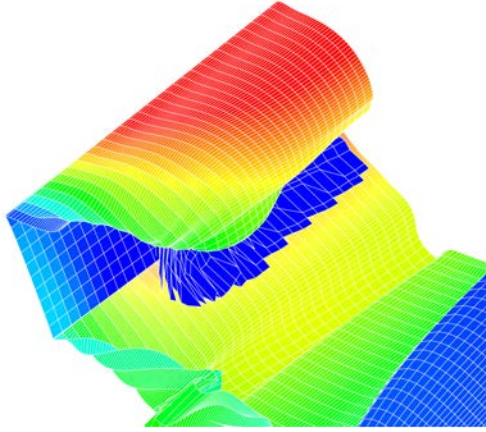


Figure 9.3: LEV structure at $t^* = 3.300$, $\alpha = 45.00$ deg, predicted by UVLM

Lastly, the result of UVLM prediction of LEV development with inner structure is presented. Figure 9.6 shows a series of half-cut snapshots of LEV sheet distribution predicted by UVLM for case 1 (baseline). UVLM prediction successfully captures the process of LEV formation; the onset of LEV formation initiates from the wing root (figure 9.6a), the LEV shedding area progresses to span-wise direction and the shed LEV sheet convects to downstream (figure 9.6b), LEV structure starts building up (figure 9.6c), an reattached region of LEV sheet retreats (moves forward) at around mid-chord (figure 9.6d), a first inner turn is formed in the primary LEV structure (figure 9.6e), and major vortical structure is finally developed on the wing upper surface (figure 9.6f). Though a verification of inner structure of vortex is technically difficult in present work, the prediction result of UVLM seems reasonable, considering several fundamental laws and some experimental observation of LEV structure, for example the reference.⁵⁷

9.2 Prediction of aerodynamic loads with LEV

Verification of lift coefficient C_L and momentum coefficient about aerodynamic center C_M for case 1 (baseline) is presented in figure 9.7. When the wing starts pitching at around $t^* = 1$, C_L increases sharply due to the effect of apparent mass and C_M drops because of the moment of apparent mass is loaded about the half chord. Predicted C_M is overestimated compared to CFD observation during this period because UVLM is based on inviscid flow model. The apparent mass subsides after the end of pitch acceleration and C_L rises as the angle of attack α increases. C_M of CFD observation gradually decreases with increase of α while the C_M in UVLM prediction is nearly constant because UVLM is based on potential flow theory and C_M is defined at aerodynamic center. After the onset of LEV formation, both observed C_L and predicted C_L keeps increasing but the rate of increase gets weaker in UVLM prediction whereas the slope of C_L of CFD observation does not change through the LEV initiation. This difference in C_L slope eventually results in a maximum of about 15% discrepancy in C_L . For C_M , the predicted C_M turns its variation from up to down at the onset of LEV formation and the trend becomes the same as CFD observation after LEV formation. At around $t^* = 2.3$, the pitching wing decelerates and both predicted and observed C_L drop due to negative apparent mass. On the other hand, due to the location of pitch axis, this negative apparent mass raises the C_M . Since the wing attains the end of motion ($\alpha = 45$ deg) and stops pitching,

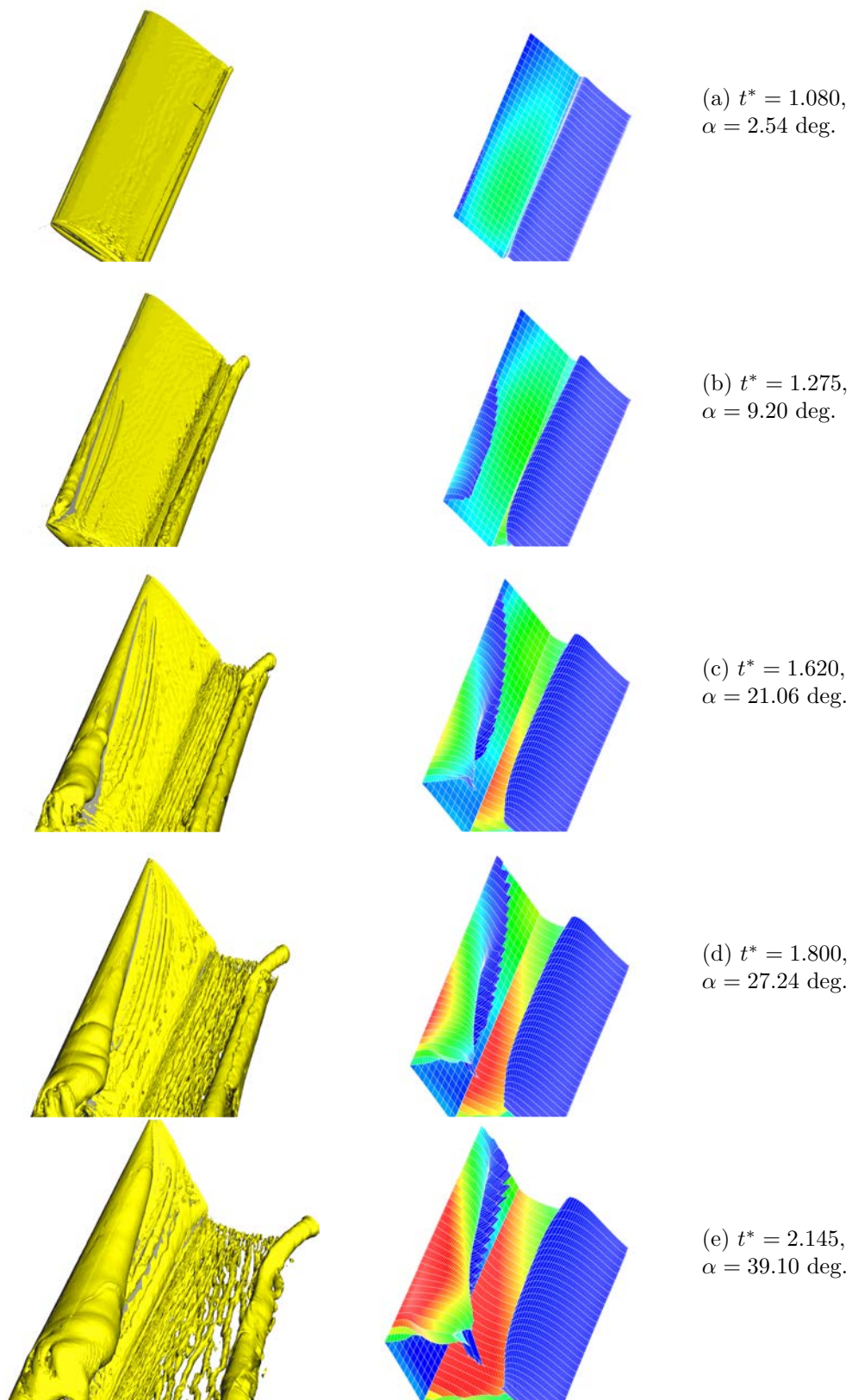


Figure 9.4: Comparison of LEV structure of CFD (left) and UVLM (right) for case 10.

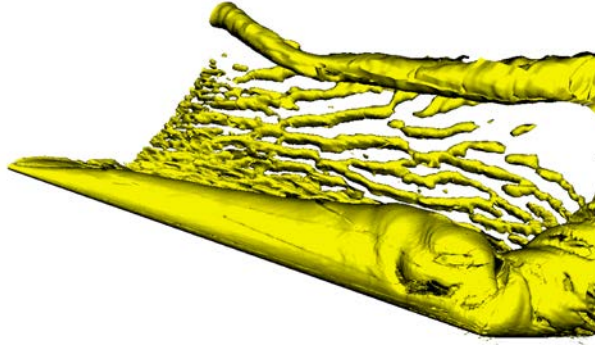


Figure 9.5: Interaction of LEV and tip vortex, $t^* = 2.145$, $\alpha = 39.10$ deg.

C_L decreases by development of LEV on wing surface. According to figure 9.6, LEV keeps growing and moves downstream. Thus, C_M in UVLM prediction decreases after the wing stops pitching. A fluctuation is found in predicted C_L and C_M for this period and it can be thought as an influence of instability waves on the wing surface. As the primary LEV develops its structure, the lower surface of LEV pushes the circulation flow to the wing surface. The circulation has Kelvin-Helmholtz wave due to shear force near the surface and they are observed as a fluctuation pattern in C_L and C_M .

Analysis of the aforementioned discrepancy in C_L about LEV formation has centered on three probable causes. First probable cause is the underestimation of the leading edge suction force F_S . LESP concept postulates that the flow around the leading edge must be preserved under LEV formation. Then, the value of $LESP(t)$ plateaus at $LESP_{crit}$ during LEV shedding. Figure 9.8 is a comparison of maximum $LESP$ between UVLM and CFD. The method of conversion from CFD data to $LESP$ is introduced by Narsipur *et al.*¹²⁶ In figure 9.8, CFD observation shows that the leading edge suction does not necessarily plateau since LEV initiation and keeps increasing for a while, whereas $LESP_{max}(t)$ of UVLM forced to be plateaued. The period of this discrepancy in $LESP$ between UVLM prediction and CFD observation corresponds with the period of high incidence ($\alpha \simeq 45$ deg) in which the suction force F_S becomes predominant in C_L .

Second probable cause is the fact that current UVLM does not simulate the influence of tip vortices. Current UVLM does have a tip vortex model as an option but it is not usually activated because it is still under development. In addition, previous case studies showed that tip vortices did not largely affect the prediction of LEV onset time and location except for a short span wing. However, tip vortices would positively influence the forces on the lifting surface to some extent, even if the wing geometry has broad wing span. Thus, the improvement of the tip vortex model could reduce the discrepancy in C_L after LEV formation.

Third probable cause is the delay of development of LEV. As be seen in previous section, UVLM prediction shows qualitatively good agreement with CFD observation. However, it is also confirmed that the prediction of LEV development in spanwise direction is somewhat slower than the result of CFD observation. The delay in spanwise progression of LEV onset must cause underestimation of the influence of LEV. In order to assess the LEV model quantitatively, one more verification is implemented about the strength of circulation variation, using LESP-modulated discrete-vortex method (LDVM, see the reference²). In this investigation, because LDVM is two-dimensional flow solution, current UVLM calculates for a pseudo-infinite wing ($AR = 20,000$) to simulate approximately two-dimensional flow field. (This method is introduced in the reference.¹²⁷)

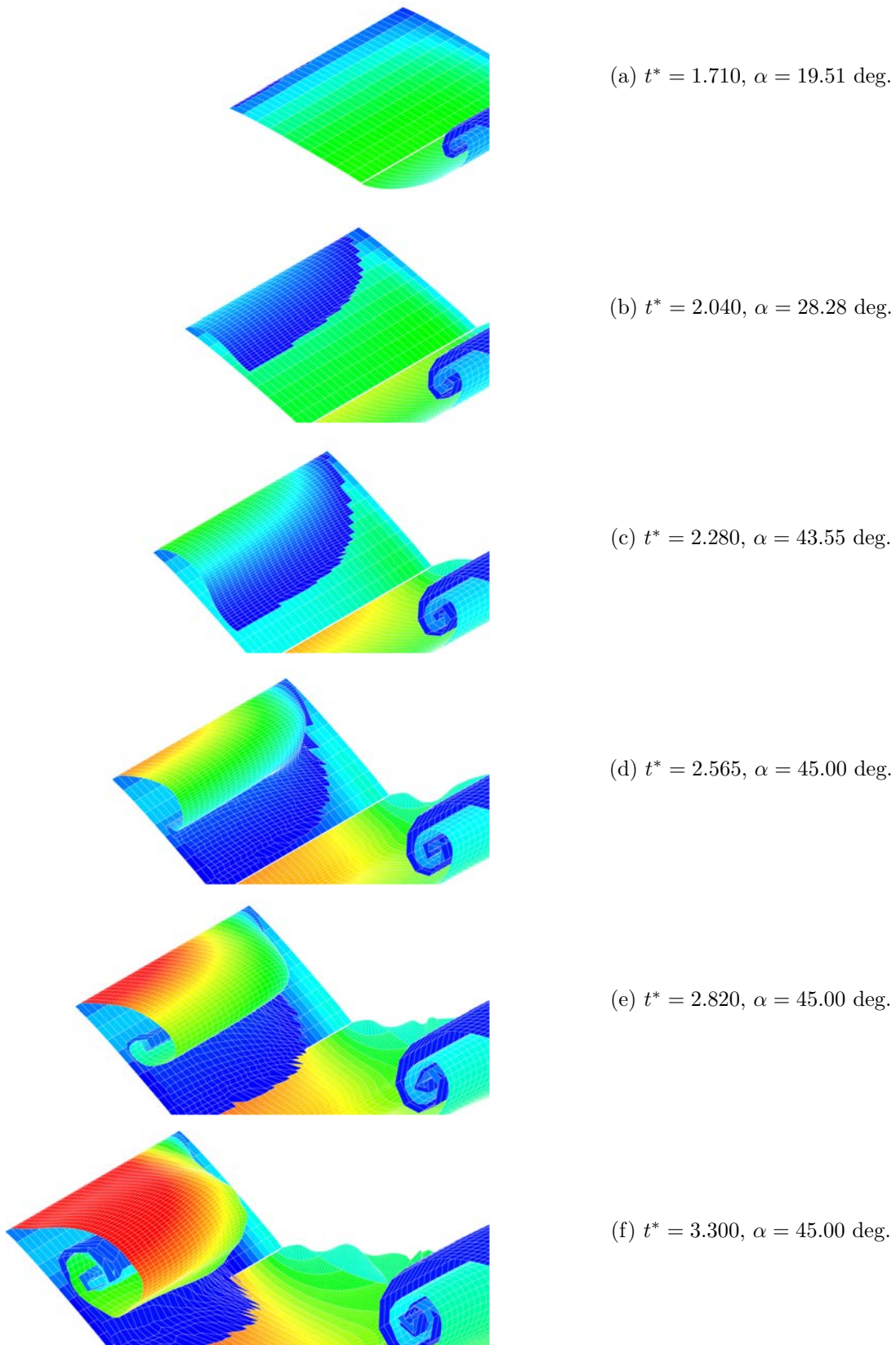
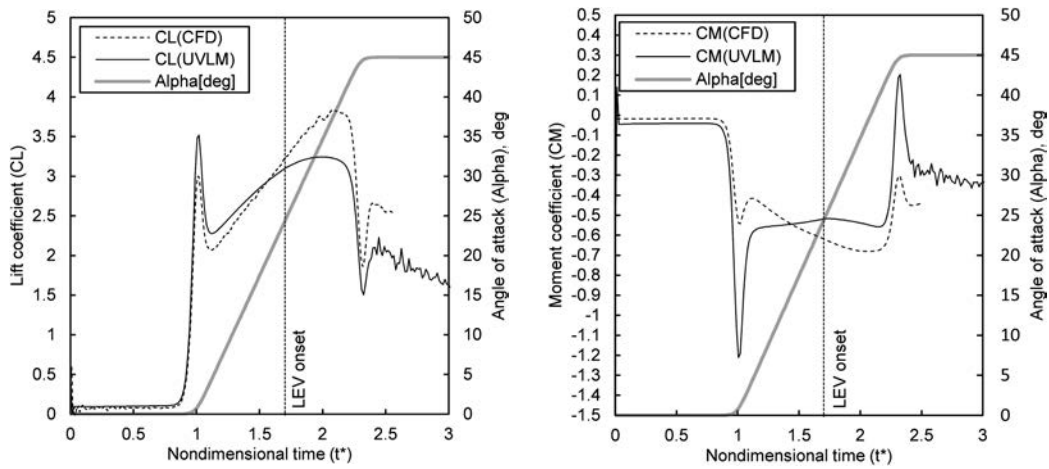


Figure 9.6: Time variation of development of LEV structure (case 1).



(a) Comparison of C_L .

(b) Comparison of C_M .

Figure 9.7: Result of aerodynamic loads for case 1 (baseline)

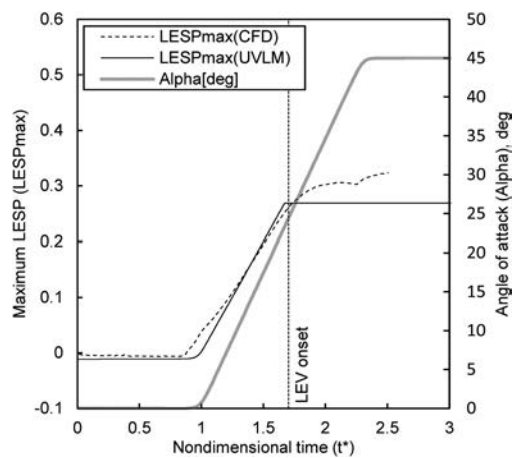


Figure 9.8: Comparison of $LESP_{max}(t)$ for case 1.

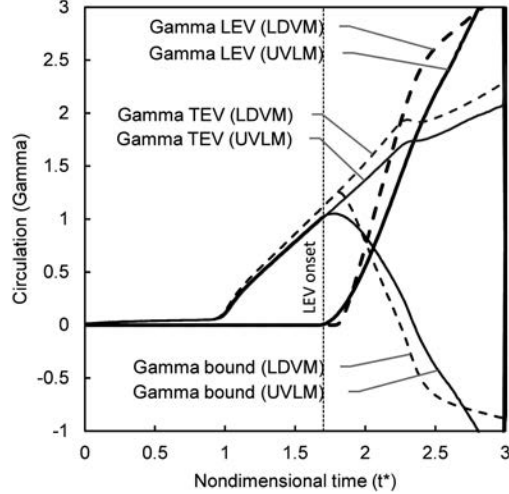


Figure 9.9: Comparison of circulation strength for case Ex 1.

The result of comparison of UVLM for a pseudo-infinite wing and LDVM is presented in figure 9.9. Following the onset of LEV formation, both UVLM and LDVM show that the wing bound circulation decreases while the strength of LEV increases. On the other hand, LEV formation does not clearly influence the increase rate of TEV. UVLM shows the same trend in these three circulations but the strengths of LEV and TEV are weaker than that of LDVM data. The difference of development of circulation must affect the distribution of LEV sheet in UVLM. In detail, the stronger LEV sheet must roll up faster and be slower to convect downstream. Consequently, the sheet distribution must be more dense around the leading edge. Therefore, the dense LEV sheet interacts with stronger circulation on the lifting surface. The concentrated LEV structure developed by fast LEV growth would mitigate the deficiency of wing bound circulation by LEV formation. For this reason, the weak strength of LEV in UVLM prediction would cause the discrepancy in C_L .

These three probable causes do not completely explain all the symptoms. They also relate each other. To conclude, it should be thought that the further improvement of accuracy of prediction of aerodynamic loads requires that these factors be addressed.

9.3 Computation time

Table 9.1: Computation time for baseline case.

| Code | Computation time |
|---------------------|------------------|
| UVLM with LEV model | ~ 25 minutes |
| REACTMB | ~ 1 day |

Result of benchmark test of computation time is summarized in table 9.1. UVLM is a representative low-order method based on theoretical model and NCSU's REACTMB is taken as a referential cutting-edge CFD method based on incompressible Navier-Stokes solver. The benchmark for both the codes is measured by the same computer environment (NC State HPC as of 2015 - 2016). The

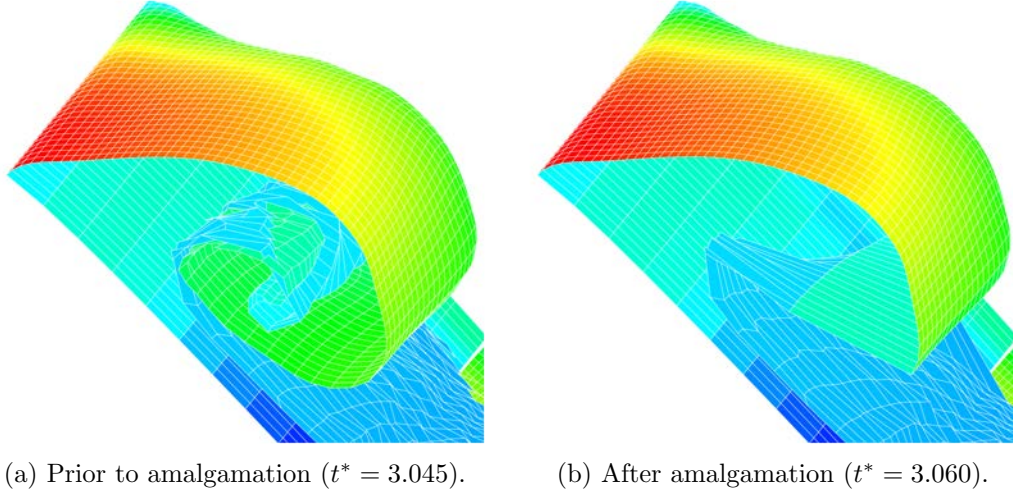


Figure 9.10: Snapshots of three-dimensional amalgamation method

benchmark test shows that current UVLM run about 50 times as faster as REACTMB.

Table 9.2: Contribution of LEV model and vortex roll up to computation time.

| Test No. | Combination | LEV model | Roll up | cpu time |
|----------|----------------------|-----------|---------|----------|
| 1 | UVLM without roll up | off | off | 24 sec |
| 2 | Conventional UVLM | off | on | 93 sec |
| 3 | UVLM with LEV model | on | on | 168 sec |

Conventional UVLM is neither postulated to be used for simulating quick motion kinematics nor in high angle of attack condition.⁷⁶ Conventional UVLM, of course, does not simulate LEV. Therefore, the influence of including LEV model to the total computation time is of interest. The table 9.2 shows a summary of problem analysis for reduction of computation time, which compares the computation time (cpu time) for a few combinations of LEV model and vortex roll up. This benchmark was run the same condition of case 1 using low resolution discretization ($N \sim O(10)$).

The most important information for present work is the increase of computation time by addition of the LEV model. Comparing the combination test 2 to 3, it is known that the new LEV model increases +80.6% of computation time. However, this is not mainly caused by LEV model itself but by vortex roll up. Taking combination test 1 and 2 in table 9.2 as an example, it is shown that vortex roll up occupies 74% ($93-24=69$ sec) of conventional UVLM run (93sec). This is because vortex roll up needs to estimate influence coefficients for all vortex rings in every time-step. The computational time of vortex roll up is proportional to the square of total number of vortex rings and the LEV model eventually adds LEV rings in computation. Thus, an engineering item to reduce the number of vortex elements would be required to save the computation time. As pointed out by Suresh Babu *et al.*,¹⁰⁶ the most promising avenue for reducing the number of LEV grids is an amalgamation of shed vortex elements.

9.4 Demonstration of three-dimensional amalgamation method

As mentioned in previous section, main objection of amalgamation in vortex method is to reduce the computation time and to prevent impingement of the vortex sheets. Current UVLM has an amalgamation model for LEV sheet and the test result is presented in figure 9.10. The present amalgamation method simply amalgamates the inner turn of primary LEV by merging the spanwise row of LEV sheets when the external angle of LEV surface projected on XZ plane ($y = 0$) θ exceeds the threshold $\theta_a = 180$ deg. (For convenience of presentation, the amalgamation condition is turned “off” for a while, to allow some build up of the LEV, and then turned “on” to merge the accumulated inner turns.) As be seen, an inner turn structure of primary LEV shown in figure 9.10a is amalgamated into a single line in figure 9.10b and the outer half circular surface of LEV sheet is left because $\theta_a = 180$. The present action of amalgamation has collapsed 28 rows of LEV sheet in the primary LEV and eventually 1680 LEV panels has been eliminated between the time-step. As a result, correct operation of amalgamation was confirmed in the test and it can be said the basic idea of amalgamation method for vortex ring discretization works well. Unfortunately clear contribution to reduction of computation time was not shown in this test condition because the amalgamation was always activated toward end of the simulation sequence. However a large saving would be expected in general situation. On the other hand, current amalgamation method indicates a side effect and it is discussed in following section.

9.5 Known problems

While current UVLM has demonstrated adequate prediction of LEV formation, a few numeric problems have also been found.

9.5.1 Geometric restrictions

UVLM deals with a hyperplane problem, and three-dimensional flow field is determined by lumped vortex sheets which form a curvilinear surface. Therefore, UVLM is governed by not only fluid dynamics but also geometry. The problem is that the vortex structure which determines the flow field is not always available from vortex sheet distribution. UVLM may not be acceptable in particular situations which violate geometric restrictions.

First problem of geometric restriction in UVLM is the shape of vortex panel element. Vortex method commonly defines a unit vortex element as quadrilateral form. Quadrilateral has four corners and can bend in one axis including two of four corners. This geometric character of quadrilateral vortex panel does not allow bends in two direction if it is in a cross point of two rolled structures. For example, UVLM cannot correctly calculate the vortex structure at the region where conical LEV turns and trailing tip vortex, as be seen in case 10. Quadrilateral vortex element is not always suitable for describing a complicated flow structure.

Second problem of geometric restriction is about resolution. To form a curvilinear surface by two or less points is impossible. Similarly, the vortical structure requires to have sufficient number of vortex sheets to be described correctly. However, the number of vortex sheets depends on the flow field and numeric condition such as time-step and panel size. Furthermore, LEV and tip vortices is known to have a multiple vortex structure but the limit of resolution cannot always depict them. The formation of secondary and subsequent vortices often causes an unreal distortion and

impingement in vortex sheet. Thus, regionally low resolution is often seen, resulting in difficulty in simulating correct vortex flow structure, and causes a numeric error in UVLM.³¹

Third problem of geometric restriction is provided by singularity of vortex element itself. It is known that shed vortex grids gradually congest and form a vortical structure.¹⁰⁵ Accordingly, they automatically approach to their singularity zone. As mentioned before, application of cutoff radius can mitigate an individual input error but cannot prevent from the tendency of congestion which would increase the input error. Singularity is also problematic in a situation which does not have enough space to build a vortex structure by discretized vortex elements. For one example, a sharp leading edge wing generates LEV in low incidence angle but this low incidence situation does not give a sufficient space of recirculation region behind LEV to develop. For another example, a case which is very low $LESP_{crit}$ and slow K motion tends to be unstable because LEV sheds in a narrow space between bulk flow and the wing surface and easily enter the singularity zone. Thus, time-step and cutoff radius also restrict the case.

Essentially, these geometric restrictions are mathematically fundamental problem of conventional vortex roll up. Process of vortex roll up is a continuous mapping from last time-step to present. The problem is that the ordinary mapping function in vortex method must include singularities of vortex filaments. This is one of difficulties of all vortex methods. Consider a sphere covered by a number of quadrilateral elements as an example. In an ordinary mapping, it is possible to fit each quadrilateral element for the curvature and the quadrilaterals at the poles must be deformed to almost triangle shape. Singularity restriction in vortex method could not allow this mapping. Several experimental observation shows that LEV shed from a finite leading edge gradually transforms to be a curvilinear shape. However, current LEV model in UVLM does not always provide sufficient degree of freedom to form an arbitrary vortex structure because of these geometric restrictions as already seen. Furthermore, the actual vortex structure does not always satisfy the mathematical consistency. For example, if the problem requires to simulate a long-term wake distribution, UVLM must be able to model vortex dissipation, separation and reconnection, as introduced in the reference.¹²⁸ Vortex reconnection is an intriguing topic because it is a violation of topological fluid dynamics. This phenomenon is thought to be caused by viscous interaction and turbulent transition but UVLM tends to maintain the topological consistency and preserve the helicity in the system because it is based on potential flow theory.

One of solution of geometric difficulty is an amalgamation method as shown in previous section. However, it is also noticed that the amalgamation method is fundamentally nonlinear operation and violation of topology, while amalgamation method has to be identified to resulting velocity field. To prevent the topological violation and ensure the identification of velocity field, UVLM must have sufficient degree of freedom but it is disturbed by aforementioned geometric restrictions. Amalgamation model in current UVLM does not have clear solution to cover all these problems and becomes unstable after the operation of amalgamation. To sum up, further improvement of LEV model will be required to simulate more advanced conditions and the solution must be a technique to satisfy or avoid these geometric difficulties.

9.5.2 Management of numeric instability

Generally, control of the UVLM numeric instability is difficult to manage due to nonlinearity of modelling. Thus, the solution of instability in UVLM has tended to be ad hoc. Current UVLM and LEV model does not equip any control method against the instability and there are no ways to mitigate the amplification of numeric error.

The formulation of velocity field of UVLM is not suitable for a common stability analysis. Procedure of the common stability analysis consists of to give a perturbation (in most cases, the perturbation is defined as e^{at+ikx} where a is an amplifier, i is imaginary unit, k is a wave number), to reduce the original equation to an eigenfunction by linealization, to evaluate the distribution of the eigenvalues (amplifier). One example of instability analysis in vortex method was reported by Crow.¹²⁸ Crow modelled the two trailing vortices from wing tip as a couple of parallel vortex filaments and implemented an eigen-mode analysis. In his instability analysis, the two tip vortices were assumed to locate in sufficient distance from each other and both tip vortex can be linearized as a cylindrical velocity field formulated by Bessel function. However, the nonlinearity of UVLM system does not allow implementation of linealization because the relative distance of discrete vortices varies in broad range.

There were a number of instability analysis for UVLM from a different perspective. Subvortex technique proposed by Maskew¹²⁹ was an example of uncommon instability analysis for UVLM. In subvortex technique, the numeric instability was simply evaluated by a function of the distance of vortex filaments. This function shows an optimal vortex panel size and the unstable vortex panels were temporally split by a few subvortices to avoid the numeric error. Subvortex technique equips the method of instability analysis in relative location but the derivation of the optimal subvortex size is cumbersome and not suitable for three-dimensional UVLM.

To sum up, the tendency of the instability is not clearly determined in UVLM. With a new idea of stability analysis method, some numeric errors in UVLM would potentially be predicted and appropriately inhibited in future.

Chapter 10

Conclusions and Future Work

The major focus of the current work was to extend the LESP concept, which provides a measure of leading-edge suction in two-dimensional geometries, to handle low-order prediction of LEV initiation and formation on three-dimensional finite-wing systems. Earlier work on airfoils in 2D unsteady flow showed that when the instantaneous LESP exceeds a critical value, LEV shedding occurs. One of the major insights from that research effort was that the critical LESP is dependent only on the airfoil and Reynolds number, and is largely independent of motion kinematics so long as the LEV formation is not preceded by significant trailing-edge separation. Thus, for this class of motions, the critical LESP for a given airfoil and Reynolds number can be determined from CFD or experiment for one prototypical motion, and can then be used for *any* other high-rate motion, including arbitrary combinations of pitch, plunge, and surge.

The current work started with the hypothesis that the flow physics governing LEV initiation on airfoil and finite-wing geometries are the same, provided that the induced-flow effects due to finite-wing effects are taken into consideration. The implication is that the value of critical *LESP* for a given airfoil and Reynolds number will also be applicable to a finite wing which uses that airfoil geometry. To test this hypothesis about LEV *initiation* on finite wings, a standard unsteady vortex lattice method (UVLM) was adapted to calculate the spanwise distribution of instantaneous *LESP* along the wing at every time instant in the motion. LEV initiation, from low-order prediction, is assumed to occur at the time instant and spanwise location when the local value of *LESP* equals the two-dimensional value of critical *LESP*. Low-order predictions for LEV initiation for several wing planforms (13 cases with variations in planform geometry, pivot location, pitch rate, twist angle, aspect ratio, and cross-section shape) were compared with RANS CFD predictions.

It was seen that, for any given airfoil shape and Reynolds number, the low-order predictions of angle of attack and spanwise location of LEV initiation were acceptably close to the corresponding CFD predictions. Specifically, the angle of attack for LEV initiation between the two approaches were within ± 2 -degree accuracy against a 40-degree spread in angle of attack for all the cases considered. The current results confirm that initiation of LEV formation on finite wings is governed by the same critical value of the LESP that is applicable in 2D flow. The major implication is that the critical value of LESP obtained from a two-dimensional study for one “high-rate” motion can be used for prediction of LEV initiation on any finite-wing geometry undergoing any other “high-rate” motion. A further implication is that the LESP concept opens up avenues for LEV flow control by tailoring either the instantaneous or critical *LESP* at different portions of the wing span.

The second part of the research focused on modifying the UVLM to handle LEV *formation*. In this

modified UVLM, a vortex sheet from the leading edge is modeled, and its geometry is calculated in each time step by assuming that the corner points of the panels forming the sheet convect with the local velocity. An important element of this effort is the development of a new idea—pseudo vortex ring—for vortex lattice method to enable calculation of LEV formation in spite of problems with vortex-ring discretization at the leading edge. The modified UVLM was successfully in achieving good prediction of time-dependent development of LEV structure. For the calculation of aerodynamic loads, an approximately 15% of underestimation of circulation strength of LEV was observed in current low-order LEV formation model. On the other hand, the low-order computations are 50 times faster than the RANS CFD computations, which makes the current method suitable for engineering and design tasks.

While the low-order prediction of LEV formation shows promise, significant challenges remain in modeling of the sheet roll up and its intersection with the wing geometry. Discrete-vortex amalgamation techniques, studied in the current effort for 2D flows, shows some promise for reducing the number of vortex lattices in LEV sheets from finite wings. It is likely that some adaption of vortex amalgamation applied to vortex sheets from leading edges will allow for robust modeling of LEV shedding on finite wings. Improved modeling of the rolled-up tip vortex structures is also necessary if prediction accuracy for low aspect-ratio-wings is to be improved.

Suggested future work includes (i) augmentation of the current UVLM formulation to include better modeling of tip-vortex shedding, (ii) development of a hybrid vortex-sheet / vortex-filament model for LEV shedding from finite wings, and (iii) extensions to the UVLM to handle LEV formation, growth, and detachment, allowing for modeling of intermittent LEV shedding.

Bibliography

- ¹ Ramesh, K., Gopalarathnam, A., Edwards, J. R., Ol, M. V., and Granlund, K., “An Unsteady Airfoil Theory Applied to Pitching Motions Validated Against Experiment and Computation,” *Theoretical and Computational Fluid Dynamics*, Vol. 27, No. 6, 2013, pp. 843–864.
- ² Ramesh, K., Gopalarathnam, A., Granlund, K., Ol, M. V., and Edwards, J. R., “Discrete-vortex method with novel shedding criterion for unsteady airfoil flows with intermittent leading-edge vortex shedding,” *Journal of Fluid Mechanics*, Vol. 751, 2014, pp. 500–538.
- ³ Ramesh, K., Murua, J., and Gopalarathnam, A., “Limit-cycle oscillations in unsteady flows dominated by intermittent leading-edge vortex shedding,” *Journal of Fluids and Structures*, Vol. 55, 2015, pp. 84–105.
- ⁴ Leishman, J. G., *Principles of Helicopter Aerodynamics*, Cambridge Aerospace Series, 2002.
- ⁵ Wagner, H., “Über die Entstehung des dynamischen Auftriebes von Tragflügeln,” *ZaMM*, Vol. 5, No. 1, 1925, pp. 17–35.
- ⁶ Theodorsen, T., “General Theory of Aerodynamic Instability and the Mechanism of Flutter,” NACA Rept. 496, 1935.
- ⁷ McGowan, G. Z., Granlund, K., Ol, M. V., Gopalarathnam, A., and Edwards, J. R., “Investigations of lift-based pitch-plunge equivalence for airfoils at low Reynolds numbers,” *AIAA Journal*, Vol. 49, No. 7, 2011, pp. 1511–1524.
- ⁸ Ol, M. V., Bernal, L., Kang, C. K., and Shyy, W., “Shallow and deep dynamic stall for flapping low Reynolds number airfoils,” *Experiments in Fluids*, Vol. 46, No. 5, 2009, pp. 883–901.
- ⁹ Garmann, D. J. and Visbal, M. R., “Numerical investigation of transitional flow over a rapidly pitching plate,” *Physics of Fluids*, Vol. 23, 2011, pp. 094106.
- ¹⁰ Granlund, K. O., Ol, M. V., and Bernal, L. P., “Unsteady Pitching Flat Plates,” *Journal of Fluid Mechanics*, Vol. 733, 2013.
- ¹¹ Ford, C. W. P. and Babinsky, H., “Lift and the leading-edge vortex,” *Journal of Fluid Mechanics*, Vol. 720, 2013, pp. 280–313.
- ¹² Baik, Y. S., Bernal, L. P., Granlund, K., and Ol, M. V., “Unsteady force generation and vortex dynamics of pitching and plunging aerofoils,” *Journal of Fluid Mechanics*, Vol. 709, No. 1, 10 2012, pp. 37–68.

- 13 Rival, D. E., Kriegseis, J., Schaub, P., Widmann, A., and Tropea, C., “Characteristic length scales for vortex detachment on plunging profiles with varying leading-edge geometry,” *Experiments in Fluids*, Vol. 55, No. 1, January 2014, pp. 18, DOI: 10.1007/s00348-013-1660-x.
- 14 Clements, R. R. and Maull, D. J., “The representation of sheets of vorticity by discrete vortices,” *Progress in Aerospace Sciences*, Vol. 16, No. 2, 1975, pp. 129–146.
- 15 Saffman, P. G. and Baker, G. R., “Vortex interactions,” *Annual Review of Fluid Mechanics*, Vol. 11, No. 1, 1979, pp. 95–121.
- 16 Leonard, A., “Vortex methods for flow simulation,” *Journal of Computational Physics*, Vol. 37, No. 3, 1980, pp. 289–335.
- 17 Sarpkaya, T., “An inviscid model of two-dimensional vortex shedding for transient and asymptotically steady separated flow over an inclined plate,” *Journal of Fluid Mechanics*, Vol. 68, No. 1, 1975, pp. 109–128.
- 18 Clements, R. R., “An inviscid model of two-dimensional vortex shedding,” *Journal of Fluid Mechanics*, Vol. 57, No. 2, 1973, pp. 321–336.
- 19 Kiya, M. and Arie, M., “A contribution to an inviscid vortex-shedding model for an inclined flat plate in uniform flow,” *Journal of Fluid Mechanics*, Vol. 82, No. 2, 1977, pp. 241–253.
- 20 Katz, J., “Discrete vortex method for the non-steady separated flow over an airfoil,” *Journal of Fluid Mechanics*, Vol. 102, No. 1, 1981, pp. 315–328.
- 21 Ansari, S. A., Żbikowski, R., and Knowles, K., “Non-linear unsteady aerodynamic model for insect-like flapping wings in the hover. Part 1: methodology and analysis,” *Proceedings of the Institution of Mechanical Engineers, Part G: Journal of Aerospace Engineering*, Vol. 220, No. 2, 2006, pp. 61–83.
- 22 Wang, C. and Eldredge, J. D., “Low-order phenomenological modeling of leading-edge vortex formation,” *Theoretical and Computational Fluid Dynamics*, Vol. 27, No. 5, 2013, pp. 577–598.
- 23 Brown, C. E. and W. H. Michael, J., “Effect of Leading-Edge Separation on the Lift of a Delta Wing,” *Journal of the Aeronautical Sciences*, Vol. 21, 1954, pp. 690–694, 706.
- 24 Howe, M. S., “Emendation of the Brown Michael equation, with application to sound generation by vortex motion near a half-plane,” *Journal of Fluid Mechanics*, Vol. 329, 1996, pp. 89–101.
- 25 Cortelezzi, L. and Leonard, A., “Point vortex model of the unsteady separated flow past a semi-infinite plate with transverse motion,” *Fluid Dynamics Research*, Vol. 11, 1993, pp. 263–295.
- 26 Darakananda, D., Eldredge, J. D., Colonius, T., and Williams, D. R., “A vortex sheet/point vortex dynamical model for unsteady separated flows,” AIAA Paper 2016–2072, Jan. 2016.
- 27 Milano, M. and Gharib, M., “Uncovering the physics of flapping plates with artificial evolution,” *Journal of Fluid Mechanics*, Vol. 534, 2005, pp. 403–409.
- 28 Rival, D., Prangemeier, T., and Tropea, C., “The influence of airfoil kinematics on the formation of leading-edge vortices in bio-inspired flight,” *Experiments in Fluids*, Vol. 46, 2009, pp. 823–833.

- 29 Antonini, E. G. A., Bedon, G., Betta, S. D., Michelini, L., Castelli, M. R., and Benini, E., “Innovative Discrete-Vortex Model for Dynamic Stall Simulations,” *AIAA Journal*, Vol. 53, 2015, pp. 479–485.
- 30 Cortelezzi, L., *A theoretical and computational study on active wake control*, Ph.D. thesis, California Institute of Technology, 1992.
- 31 Moore, D. W., “A Numerical Study of the Roll-up of a Finite Vortex Sheet,” *Journal of Fluid Mechanics*, Vol. 63, No. 2, 1974, pp. 225–235.
- 32 Nair, A. G. and Taira, K., “Network-theoretic approach to sparsified discrete vortex dynamics,” *Journal of Fluid Mechanics*, Vol. 768, 2015, pp. 549–571.
- 33 Ellington, C. P., van den Berg, C., Willmott, A. P., and Thomas, A. L. R., “Leading-edge vortices in insect flight,” *Nature*, Vol. 384, 1996, pp. 626–630.
- 34 Muijres, F. T., Johansson, L. C., Barfield, R., Wolf, M., Spedding, G. R., and Hedenström, A., “Leading-Edge Vortex Improves Lift in Slow-Flying Bats,” *Science*, Vol. 319, No. 5867, 2008, pp. 1250–1253.
- 35 Taylor, G. K., Nudds, R. L., and Thomas, A. L., “Flying and swimming animals cruise at a Strouhal number tuned for high power efficiency,” *Nature*, Vol. 425, No. 6959, 2003, pp. 707–711.
- 36 Lentink, D., Dickson, W. B., Van Leeuwen, J. L., and Dickinson, M. H., “Leading-edge vortices elevate lift of autorotating plant seeds,” *Science*, Vol. 324, No. 5933, 2009, pp. 1438–1440.
- 37 McCullough, G. B. and Gault, D. E., “Examples of Three Representative Types of Airfoil-Section Stall at Low Speed,” Tech. Rep. NACA TN 2502, NACA, 1951.
- 38 Schreck, S. and Robinson, M., “Blade Three-Dimensional Dynamic Stall Response to Wind Turbine Operating Condition,” *Journal of Solar Energy Engineering*, Vol. 127, No. 4, 2005, pp. 488–495.
- 39 Maltby, R. L., “The Development of the Slender Delta Concept,” *Aircraft Engineering and Aerospace Technology*, Vol. 40, No. 3, 1968, pp. 12–17.
- 40 HITZEL, M. and Schmidt, W., “Slender wings with leading-edge vortex separation-A challenge for panel methods and Euler solvers,” *Journal of aircraft*, Vol. 21, No. 10, 1984, pp. 751–759.
- 41 Ellington, C. P., “The novel aerodynamics of insect flight: applications to micro-air vehicles,” *Journal of Experimental Biology*, Vol. 202, No. 23, 1999, pp. 3439–3448.
- 42 Bryant, M. and Garcia, E., “Modeling and testing of a novel aeroelastic flutter energy harvester,” *Journal of Vibration and Acoustics*, Vol. 133, No. 1, 2011.
- 43 Bryant, M., Gomez, J. C., and Garcia, E., “Reduced-order aerodynamic modeling of flapping wing energy harvesting at low Reynolds number,” *AIAA Journal*, Vol. 51, No. 12, 2013, pp. 2771–2782.
- 44 Gault, D. E., “A Correlation of Low-Speed, Airfoil-Section Stalling Characteristics with Reynolds Number and Airfoil Geometry,” Tech. Rep. NACA TN 3963, NACA, 1957.

- 45 Ham, N. D. and Garelick, M. S., “Dynamic Stall Considerations in Helicopter Rotors,” *Journal of the American Helicopter Society*, Vol. 13, 1968, pp. 49–55.
- 46 Visbal, M. R. and Shang, J. S., “Investigation of the Flow Structure around a Rapidly Pitching Airfoil,” *AIAA Journal*, Vol. 27, No. 8, 1989, pp. 1044–1051.
- 47 Choudhuri, P. G. and Knight, D. D., “Effects of compressibility, pitch rate, and Reynolds number on unsteady incipient leading-edge boundary layer separation over a pitching airfoil,” *Journal of Fluid Mechanics*, Vol. 308, 1996, pp. 195–217.
- 48 Choudhuri, P. G., Knight, D. D., and Visbal, M. R., “Two-Dimensional Unsteady Leading-Edge Separation on a Pitching Airfoil,” *AIAA Journal*, Vol. 32, No. 4, 1994, pp. 673–681.
- 49 Ol, M. V., “The High-Frequency, High-Amplitude Pitch Problem: Airfoils, Plates and Wings,” *AIAA 2009-3686*, 39th AIAA Fluid Dynamics Conference, 2009.
- 50 Ansari, S. A., Żbikowski, R., and Knowles, K., “A Nonlinear Unsteady Aerodynamic Model for Insect-like Flapping Wings in the Hover: Part I. Methodology and Analysis,” *Proceedings of the Institution of Mechanical Engineers, Part G: Journal of Aerospace Engineering*, Vol. 220, No. 2, 2006, pp. 61–83.
- 51 Ansari, S. A., Żbikowski, R., and Knowles, K., “A Nonlinear Unsteady Aerodynamic Model for Insect-like Flapping Wings in the Hover: Part 2. Implementation and Validation,” *Proceedings of the Institution of Mechanical Engineers, Part G: Journal of Aerospace Engineering*, Vol. 220, 2006, pp. 169–186.
- 52 Maxworthy, T., “Experiments on the Weis-Fogh mechanism of Lift Generation by Insects in Hovering Flight. Part 1. Dynamics of the ‘Fling’,” *Journal of Fluid Mechanics*, Vol. 93, 1979, pp. 47–63.
- 53 Dickinson, M. H. and Gotz, K. G., “Unsteady Aerodynamic Performance of Model Wings at Low Reynolds Numbers,” *Journal of Experimental Biology*, Vol. 174, 1993, pp. 45–64.
- 54 Rao, D. M. and Campbell, J. F., “Vortical flow management techniques,” *Progress in Aerospace Sciences*, Vol. 24, No. 3, 1987, pp. 173 – 224.
- 55 Polhamus, E. C., “A Concept of the Vortex Lift of Sharp-Edge Delta Wings Based on a Leading-Edge-Suction Analogy,” Tech. Rep. NASA TN D-3767, NASA, 1966.
- 56 Polhamus, E. C., “Prediction of Vortex-Lift Characteristics by a Leading-Edge Suction Analogy,” *Journal of Aircraft*, Vol. 8, No. 4, 1971, pp. 193–199.
- 57 Freymuth, P., “Three-Dimensional Vortex Systems of Finite Wings,” *Journal of Aircraft*, Vol. 25, No. 10, 1988, pp. 971–972.
- 58 Schreck, S. J. and Helin, H. E., “Unsteady Vortex Dynamics and Surface Pressure Topologies on a Finite Pitching Wing,” *Journal of Aircraft*, Vol. 31, No. 4, 1994, pp. 899–907.
- 59 Yilmaz, T. O. and Rockwell, D., “Flow structure on finite-span wings due to pitch-up motion,” *Journal of Fluid Mechanics*, Vol. 691, 2012, pp. 518–545.
- 60 Jones, A. R. and Babinsky, H., “Reynolds number effects on leading edge vortex development,” *Experiments in Fluids*, Vol. 51, No. 1, 2011, pp. 197–210.

- ⁶¹ Cassidy, D. A., Edwards, J. R., and Tian, M., “An Investigation of Interface-Sharpener Schemes for Multiphase Mixture Flows,” *Journal of Computational Physics*, Vol. 228, No. 16, 2009, pp. 5628–5649.
- ⁶² Spalart, P. R. and Allmaras, S. R., “A one-equation turbulence model for aerodynamic flows,” *La recherche aérospatiale*, Vol. 1, No. 1, 1994, pp. 5–21.
- ⁶³ Edwards, J. R. and Chandra, S., “Comparison of Eddy Viscosity - Transport Turbulence Models for Three-Dimensional, Shock-Separated Flowfields,” *AIAA Journal*, Vol. 34, No. 4, 1996, pp. 756–763.
- ⁶⁴ Colella, P. and Woodward, P. R., “The Piecewise Parabolic Method (PPM) for Gas-dynamic Simulations,” *Journal of Computational Physics*, Vol. 54, 1984, pp. 174–201.
- ⁶⁵ Lenormand, E., Sagaut, P., Ta Phuoc, L., and Comte, P., “Subgrid-Scale Models for Large-Eddy Simulations of Compressible Wall Bounded Flows,” *AIAA journal*, Vol. 38, No. 8, 2000, pp. 1340–1350.
- ⁶⁶ Giesecking, D., Choi, J. I., Edwards, J. R., and Hassan, H. A., “Compressible-Flow Simulations Using a New Large-Eddy Simulation/Reynolds-Averaged Navier-Stokes Model,” *AIAA journal*, Vol. 49, No. 10, 2011, pp. 2194–2209.
- ⁶⁷ Giesecking, D. A. and Edwards, J. R., “Simulation of a Mach 3 Compression-Ramp Interaction Using LES/RANS Models,” *AIAA Paper*, Vol. 726, 2011.
- ⁶⁸ Choi, J. I., Edwards, J. R., and Baurle, R. A., “Compressible Boundary-Layer Predictions at High Reynolds Number Using Hybrid LES/RANS Methods,” *AIAA journal*, Vol. 47, No. 9, 2009, pp. 2179–2193.
- ⁶⁹ Langtry, R. B. and Menter, F. R., “Correlation-Based Transition Modeling for Unstructured Parallelized Computational Fluid Dynamics Codes,” *AIAA journal*, Vol. 47, No. 12, 2009, pp. 2894–2906.
- ⁷⁰ Gleyzes, C., “Opération Décrochage—Résultats des Essais à la Soufflerie F2,” *RT-DERAT*, Vol. 55, 1988, pp. 4004.
- ⁷¹ Mary, I. and Sagaut, P., “Large Eddy Simulation of Flow Around an Airfoil Near Stall,” *AIAA journal*, Vol. 40, No. 6, 2002, pp. 1139–1145.
- ⁷² Alam, M. and Sandham, N. D., “Direct Numerical Simulation of Short Laminar Separation Bubbles with Turbulent Reattachment,” *Journal of Fluid Mechanics*, Vol. 410, No. 1, 2000, pp. 1–28.
- ⁷³ Kawai, S. and Asada, K., “Wall-Modeled Large-Eddy Simulation of High Reynolds Number Flow Around an Airfoil Near Stall Condition,” *Computers & Fluids*, 2012.
- ⁷⁴ Granlund, K., Ol, M. V., and Bernal, L., “Experiments on pitching plates : force and flowfield measurements at low Reynolds numbers,” *AIAA Paper* 2011–0872, 2011.
- ⁷⁵ Ol, M., McAuliffe, B., Hanff, E., Scholz, U., and Kähler, C., “Comparison of Laminar Separation Bubble Measurements on a Low Reynolds Number Airfoil in Three Facilities,” *AIAA Paper* 2005–5149, June 2005.

- ⁷⁶ Katz, J. and Plotkin, A., *Low-Speed Aerodynamics*, Cambridge university press, 2nd ed., 2001.
- ⁷⁷ Garrick, I. E., “Propulsion of a Flapping and Oscillating Airfoil,” Tech. Rep. NACA TR 567, NACA, 1937.
- ⁷⁸ Kármán, T. v. and Burgers, J. M., *General Aerodynamic Theory - Perfect Fluids*, Vol. 2 of Aerodynamic theory: a general review of progress, Durand, W. F. , Dover Publications, 1963.
- ⁷⁹ Theodorsen, T., “On the Theory of Wing Sections with Particular Reference to the Lift Distribution,” NASA TR 383, 1931.
- ⁸⁰ Abbott, I. H. and von Doenhoff, A. E., *Theory of Wing Sections*, Dover, New York, 1959.
- ⁸¹ McAvoy, C. W. and Gopalarathnam, A., “Automated Cruise Flap for Airfoil Drag Reduction Over a Large Lift Range,” *Journal of Aircraft*, Vol. 39, No. 6, November–December 2002, pp. 981–988.
- ⁸² Morris, W. J. and Rusak, Z., “Stall onset on aerofoils a low to moderately high Reynolds number flows,” *Journal of Fluid Mechanics*, Vol. 733, No. 1, 2013, pp. 439–472.
- ⁸³ Fage, A. and Johansen, F. C., “On the flow of air behind an inclined flat plate of infinite span,” *Proceedings of the Royal Society of London. Series A, Containing Papers of a Mathematical and Physical Character*, Vol. 116, No. 773, 1927, pp. 170–197.
- ⁸⁴ Koochesfahani, M. M. and Smiljanovski, V., “Initial acceleration effects on flow evolution around airfoils pitching to high angles of attack,” *AIAA journal*, Vol. 31, No. 8, 1993, pp. 1529–1531.
- ⁸⁵ Vatistas, G. H., Kozel, V., and Mih, W. C., “A Simpler Model for Concentrated Vortices,” *Experiments in Fluids*, Vol. 11, No. 1, 1991, pp. 73–76.
- ⁸⁶ Eldredge, J. D., Wang, C. J., and Ol, M. V., “A Computational Study of a Canonical Pitch-up, Pitch-down Wing Maneuver,” *AIAA Paper 2009-3687*, 2009.
- ⁸⁷ Aggarwal, S., *An Inviscid Numerical Method for Unsteady Flows over Airfoils and Wings to Predict the Onset of Leading Edge Vortex Formation*, Master’s thesis, North Carolina State University, 2013.
- ⁸⁸ Levin, D. and Katz, J., “Vortex-Lattice Method for the Calculation of the nonsteady Separated Flow over Delta Wings,” *Journal of Aircraft*, Vol. 18, No. 12, 1980, pp. 1032–1037.
- ⁸⁹ Kandil, O. A., Mook, D. T., and Nayfeh, A. H., “Nonlinear Prediction of Aerodynamic Loads on Lifting Surfaces,” *Journal of Aircraft*, Vol. 13, No. 1, 1976, pp. 22–28.
- ⁹⁰ Katz, J., “Large-Scale Vortex-Lattice Model for the Locally Separated Flow over Wings,” *AIAA Journal*, Vol. 20, No. 12, 1982, pp. 1640–1646.
- ⁹¹ Smith, J. H. B., “Theoretical modelling of three-dimensional vortex flows in aerodynamics,” *The Aeronautical Journal*, Vol. 88, No. 874, 1984, pp. 101–116.
- ⁹² Wu, J.-Z., Ma, H.-Y., and Zhou, M.-D., *Vorticity and Vortex Dynamics*, Springer, 2006.
- ⁹³ Crighton, D. G., “The Kutta Condition In Unsteady Flow,” *Annual Review of Fluid Mechanics*, Vol. 17, 1985, pp. 411–445.

- ⁹⁴ Pinkerton, R. M., “The Variation with Reynolds Number of Pressure Distribution over an Airfoil Section,” Tech. Rep. NACA-TR-613, NACA, 1937.
- ⁹⁵ Dovgiĭ, S. A. and Shekhovtsov, A. V., “Dynamic Stall Experiments on Oscillating Airfoils,” *Journal of Mathematical Sciences*, Vol. 104, No. 6, 2001, pp. 1615–1627.
- ⁹⁶ Paul, R., Murua, J., and Gopalarathnam, A., “Unsteady and Post-Stall Aerodynamic Modeling for Flight Dynamics Simulation,” *AIAA 2014-0729*, AIAA SciTech 2014, Atmospheric Flight Mechanics Conference, 2014.
- ⁹⁷ Sarpkaya, T., “Computational Methods with Vortices - The 1988 Freeman Scholar Lecture,” *Journal of Fluids Engineering*, Vol. 111, No. 1, 1989.
- ⁹⁸ Kuwahara, K. and Takami, H., “Numerical Studies of Two-Dimensional Vortex Motion by a System of Point Vortices,” *Journal of the Physical Society of Japan*, Vol. 34, No. 1, 1973, pp. 247–253.
- ⁹⁹ Gennaretti, M. and Bernardini, G., “Novel Boundary Integral Formulation for Blade-Vortex Interaction Aerodynamics of Helicopter Rotors,” *AIAA Journal*, Vol. 45, No. 6, 2007, pp. 1169–1176.
- ¹⁰⁰ Summa, J. M., “A Numerical Method for the Exact Calculation of Airloads associated with Impulsively Started Wings,” *AIAA paper 77-2*, Aerospace Sciences Meeting; 15th, 1977.
- ¹⁰¹ Rosenhead, L., “The Formation of Vortices from a Surface of Discontinuity,” *Proceedings of the Royal Society of London. Series A*, Vol. 134, No. 823, 1931, pp. 170–192.
- ¹⁰² Wie, S. Y., Lee, S., and Lee, D. J., “Potential Panel and Time-Marching Free-Wake Coupling Analysis for Helicopter Rotor,” *Journal of Aircraft*, Vol. 46, No. 3, 2009.
- ¹⁰³ Ham, N. D., “Aerodynamic Loading on a Two-Dimensional Airfoil during Dynamic Stall,” *AIAA Journal*, Vol. 6, No. 10, 1968, pp. 1927–1934.
- ¹⁰⁴ Spalart, P. R., “Vortex Methods for Separated Flows,” Tech. Rep. NASA-TM-1000068, NASA, 1988.
- ¹⁰⁵ Lamarre, F. and Paraschivoiu, I., “Efficient Panel Method for Vortex Sheet Roll-Up,” *Journal of Aircraft*, Vol. 29, No. 1, 1992, pp. 28–33.
- ¹⁰⁶ Babu, A. V. S., Ramesh, K., and Gopalarathnam, A., “Model Reduction in Discrete Vortex Methods for 2D Unsteady Aerodynamic Flows,” *AIAA-2016-4163*, 34th AIAA Applied Aerodynamics Conference, 2016.
- ¹⁰⁷ Selig, M. S., Donovan, J. F., and Fraser, D. B., *Airfoils at Low Speeds*, Soartech 8, SoarTech Publications, Virginia Beach, Virginia, 1989.
- ¹⁰⁸ Lorber, P. F., Carta, F. O., and Alfred F. Covinno, J., “An Oscillating Three-Dimensional Wing Experiment: Compressibility, Sweep, Rate, Waveform, and Geometry Effects on Unsteady Separation and Dynamic Stall,” Tech. Rep. R92-958325-6, UTRC, 1992.
- ¹⁰⁹ Spentzos, A., Barakos, G., Badcock, K., Richards, B., Wernert, P., Schreck, S., and Raffel, M., “Investigation of Three-Dimensional Dynamic Stall Using Computational Fluid Dynamics,” *AIAA Journal*, Vol. 43, No. 5, 2005, pp. 1023–1033.

- ¹¹⁰ Spentzos, A., Barakos, G. N., Badcock, K. J., Richards, B. E., Coton, F. N., and Galbraith, R. A. M., “Computational Fluid Dynamics Study of Three-Dimensional Symmetric Stall of Various Planform Shapes,” *Journal of Aircraft*, Vol. 44, No. 4, 2007, pp. 1118–1128.
- ¹¹¹ Granlund, K., Ol, M., and Bernal, L., “Experiment on Pitching Plates: Force and Flowfield Measurements at Low Reynolds Numbers,” *AIAA 2011-872*, 49th AIAA Aerospace Sciences Meeting including the New Horizons Forum and Aerospace Exposition, 2011.
- ¹¹² Visbal, M., Yilmaz, T. O., and Rockwell, D., “Three-dimensional vortex formation on a heaving low-aspect-ratio wing: Computations and experiments,” *Journal of Fluids and Structures*, Vol. 38, 2013, pp. 58–76.
- ¹¹³ Gordnier, R. E. and Demasi, L., “Implicit LES Simulations of a Flapping Wing in Forward Flight,” *FEDSM 2013-16540*, ASME 2013 Fluids Engineering Division Summer Meeting, 2013.
- ¹¹⁴ Visbal, M. R. and Gordnier, R. E., “Pitch Rate and Pitch-Axis Location Effects on Vortex Breakdown Onset,” *Journal of Aircraft*, Vol. 32, No. 5, 1995, pp. 929–935.
- ¹¹⁵ Ericsson, L. E., “Moving wall effects in Unsteady Flow,” *Journal of Aircraft*, Vol. 25, No. 11, 1988, pp. 977–990.
- ¹¹⁶ Johnson, W. and Ham, N. D., “On the Mechanism of Dynamic Stall,” *Journal of the American Helicopter Society*, Vol. 17, 1972, pp. 36–45.
- ¹¹⁷ McCroskey, W. J., Carr, L. W., and McAlister, K. W., “Dynamic Stall Experiments on Oscillating Airfoils,” *AIAA Journal*, Vol. 14, No. 1, 1976, pp. 57–63.
- ¹¹⁸ McCroskey, W. J., McAlister, K., Carr, L. W., Pucci, S. L., Lambert, O., and Indergrand, L. R. F., “Dynamic Stall on Advanced Airfoil Sections,” *Journal of the American Helicopter Society*, Vol. 26, 1981, pp. 40–50.
- ¹¹⁹ McCroskey, W. J. and Picci, S. L., “Viscous-Inviscid Interaction on Oscillating Airfoils in Subsonic Flow,” *AIAA Journal*, Vol. 20, No. 2, 1982, pp. 167–174.
- ¹²⁰ Walker, J. M., Helin, H. E., and Strickland, J. H., “An Experimental Investigation of an Airfoil Undergoing Large-Amplitude Pitching Motions,” *AIAA Journal*, Vol. 23, No. 8, 1985, pp. 1141–1142.
- ¹²¹ Carr, L. W., “Progress in Analysis and Prediction of Dynamic Stall,” *Journal of Aircraft*, Vol. 25, No. 1, 1988, pp. 6–17.
- ¹²² Acharya, M. and Metwally, M. H., “Unsteady Pressure Field and Vorticity Production over a Pitching Airfoil,” *AIAA Journal*, Vol. 30, No. 2, 1992, pp. 403–411.
- ¹²³ Lian, Y., “Parametric Study of a Pitching Flat Plate at Low Reynolds Numbers,” *AIAA-2009-3688*, 39th AIAA Fluid Dynamics Conference, 2009.
- ¹²⁴ Jantzen, R., Taira, K., Granlund, K., and Ol, M. V., “On the Influence of Pitching and Acceleration on Vortex Dynamics Around Low-Aspect-Ratio Rectangular Wing,” *AIAA 2013-833*, 51st AIAA Aerospace Sciences Meeting including the New Horizons Forum and Aerospace Exposition, 2013.

- ¹²⁵ Lorber, P. F., Jr., A. F. C., and Carta, F. O., “Dynamic Stall Experiments on a Swept Three-Dimensional Wing in Compressible Flow,” *AIAA-91-1795-CP*, 22nd Fluid Dynamics, Plasma Dynamics and Lasers Conference, 1991, pp. 84–99.
- ¹²⁶ Narsipur, S., Hosangadi, P., Gopalarathnam, A., and Edwards, J. R., “Variation of Leading-Edge Suction at Stall for Steady and Unsteady Airfoil Motions,” *AIAA 2016-1354*, 54th AIAA Aerospace Sciences Meeting, AIAA SciTech, 2016.
- ¹²⁷ Simpson, R. J. S., Palacios, R., and Murua, J., “Induced Drag Calculations in the Unsteady Vortex Lattice Method,” *AIAA Journal*, Vol. 51, No. 7, 2013, pp. 1775–1779.
- ¹²⁸ Crow, S. C., “Stability Theory for a Pair of Trailing Vortices,” *AIAA Journal*, Vol. 8, No. 12, 1970, pp. 2172–2179.
- ¹²⁹ Maskew, B., “Subvortex Technique for the Close Approach to a Discretized Vortex Sheet,” *Journal of Aircraft*, Vol. 14, No. 2, 1975, pp. 188–193.

AFOSR Deliverables Submission Survey

Response ID:6673 Data

1.

1. Report Type

Final Report

Primary Contact E-mail

Contact email if there is a problem with the report.

agopalar@ncsu.edu

Primary Contact Phone Number

Contact phone number if there is a problem with the report

919-515-5669

Organization / Institution name

North Carolina State University

Grant/Contract Title

The full title of the funded effort.

Theory, Computation, and Experiment on Criticality and Stability of Vortices Separating from Edges

Grant/Contract Number

AFOSR assigned control number. It must begin with "FA9550" or "F49620" or "FA2386".

FA9550-13-1-0179

Principal Investigator Name

The full name of the principal investigator on the grant or contract.

Ashok Gopalarathnam

Program Manager

The AFOSR Program Manager currently assigned to the award

Dr. Douglas R. Smith

Reporting Period Start Date

04/15/2013

Reporting Period End Date

04/15/2016

Abstract

The aim of this research effort was to extend earlier work on two-dimensional airfoils undergoing high-intensity unsteady motions dominated by leading-edge vortex (LEV) shedding to finite-wing geometries. In the earlier work (supported by AFOSR grant FA9550-10-1-0120, PIs: Gopalarathnam, Edwards, and OI, PM: Dr. Douglas Smith), an integrated theoretical, computational, and experimental research effort was used, in which experiments and higher-order computations were used to develop a low-order method for unsteady aerodynamic analysis of airfoils and plates undergoing large-amplitude, high-rate motions. Owing to the fact that such flows are dominated by LEV shedding and flow separation, they are well outside the validity of classical theoretical methods.

The major contribution from the earlier research effort was in identifying the importance of leading-edge suction in governing the initiation, formation, and termination of vortex shedding from rounded leading edges of unsteady airfoils in two-dimensional flow. It was shown that the value of this leading-edge suction at any time instant in unsteady flow could be tracked in an unsteady thin airfoil theory using an inviscid parameter which was named the Leading-Edge Suction Parameter, or LESP. When the instantaneous

DISTRIBUTION A: Distribution approved for public release.

LESP exceeds a critical value, LEV shedding occurs. One of the major insights from that research effort was that the critical LESP is dependent only on the airfoil and Reynolds number, and is largely independent of motion kinematics so long as the LEV formation is not preceded by significant trailing-edge separation. Typically, LEV formation without accompanying trailing-edge separation occurs in high-rate and high-reduced-frequency motions. Thus, for this class of motions, the critical LESP for a given airfoil and Reynolds number can be determined from CFD or experiment for one prototypical motion, and can then be used for any other high-rate motion, including arbitrary combinations of pitch, plunge, and surge. This insight was used to augment an inviscid unsteady thin airfoil theory (Ramesh et al., *Theor. Comput. Fluid Dyn.*, January 2013, DOI 10.1007/s00162-012-0292-8) with the addition of a discrete-vortex method to handle intermittent LEV shedding. The resulting method, named the LESP-modulated discrete vortex method, or LDVM, is described in detail in Ramesh et al. (*Journal of Fluid Mechanics*, Volume 751, July 2014, pp 500-538. DOI: <http://dx.doi.org/10.1017/jfm.2014.297>). The results from LDVM show remarkably good agreement in forces and flow fields with computational fluid dynamics (CFD) and experiments. The advantage of the rapid computational capability offered by a low-order method like the LDVM was illustrated in the prediction of non-linear aeroelastic behavior of airfoils having LEV shedding. As described in Ramesh et al. (*Journal of Fluids and Structures*, Vol. 55, May 2015, pp. 84-105. <http://dx.doi.org/10.1016/j.jfluidstructs.2015.02.005>), such aeroelastic analysis requires computation for at least 1,000~convective times to establish the long-time aeroelastic behavior, which would be prohibitive with any high-order CFD-like method.

Motivated by the success of the two-dimensional-flow work, the research in the current effort was aimed at extending a three-dimensional inviscid analysis method to handle vortex shedding from rounded leading edges of finite wings. Systematic studies of finite wings with LEV shedding were analyzed using an incompressible Reynolds-Averaged Navier Stokes (RANS) CFD method, the results of which were used for the development of the low-order method. At the foundation of the low-order finite-wing analysis method is a traditional unsteady vortex lattice method (UVLM). In the first part of the current work, the objective was to assess the applicability of the LESP concept to prediction of the time instant and spanwise location of LEV initiation on a finite wing undergoing unsteady motion. The UVLM was used to calculate the spanwise variation of LESP at every time step. LEV initiation, from low-order prediction, is assumed to occur at the time instant and spanwise location when the local value of LESP equals the two-dimensional value of critical LESP. Comparison of the low-order prediction of LEV initiation for a large number of wing planforms with CFD predictions is excellent, confirming that the flow physics governing LEV initiation in finite wings is the same as that for airfoils. Further, the critical value of LESP obtained for two-dimensional airfoil flow for one "high-rate" motion can be used for prediction of LEV initiation on any finite-wing geometry undergoing any other "high-rate" motion. Discrepancies between the low- and high-order prediction of LEV initiation were seen in very low-aspect-ratio wing ($AR = 2$), for which the rolled-up shed vorticity from the wing tip has a significant influence on the wing flow. Since the UVLM does not model the tip-vortex roll up, there is a noticeable discrepancy for the $AR = 2$ geometry.

The second part of the research focused on modifying the UVLM to handle LEV formation. In this modified UVLM, a vortex sheet from the leading edge is modeled, and its geometry is calculated in each time step by assuming that the corner points of the panels forming the sheet convect with the local velocity. The resulting self-induced roll up of the sheet is simulated, with the geometry agreeing reasonably well with CFD results. While the low-order prediction of LEV formation shows promise, significant challenges remain in the modeling of the sheet roll up and its intersection with the wing geometry. Discrete-vortex amalgamation techniques, studied as part of the current effort for 2D flows, shows some promise for reducing the number of vortex lattices in LEV sheets from finite wings. It is likely that some adaption of vortex amalgamation applied to vortex sheets from leading edges will allow for robust modeling for LEV shedding on finite wings.

Suggested future work includes (i) augmentation of the current UVLM formulation to include better modeling of tip-vortex shedding, (ii) development of a hybrid vortex-sheet / vortex-filament model for LEV shedding from finite wings, and (iii) extensions to the UVLM to handle LEV formation, growth, and

detachment, allowing for modeling of intermittent LEV shedding.

Distribution Statement

This is block 12 on the SF298 form.

Distribution A - Approved for Public Release

Explanation for Distribution Statement

If this is not approved for public release, please provide a short explanation. E.g., contains proprietary information.

SF298 Form

Please attach your SF298 form. A blank SF298 can be found [here](#). Please do not password protect or secure the PDF. The maximum file size for an SF298 is 50MB.

[SF298.pdf](#)

Upload the Report Document. File must be a PDF. Please do not password protect or secure the PDF. The maximum file size for the Report Document is 50MB.

[final-report_reduced_file_size.pdf](#)

Upload a Report Document, if any. The maximum file size for the Report Document is 50MB.

Archival Publications (published) during reporting period:

Journal articles:

(1)

Kiran Ramesh, Ashok Gopalarathnam, Kenneth Granlund, Michael V. Ol and Jack R. Edwards, "Discrete-vortex method with novel shedding criterion for unsteady aerofoil flows with intermittent leading-edge vortex shedding," Journal of Fluid Mechanics, Volume 751, July 2014, pp 500-538.

DOI: <http://dx.doi.org/10.1017/jfm.2014.297>

(2)

Ramesh, K., Murua, J., and Gopalarathnam, A., "Limit-Cycle Oscillations in Unsteady Flows Dominated by Intermittent Leading-Edge Vortex Shedding," Journal of Fluids and Structures, Vol. 55, May 2015, pp. 84-105.

<http://dx.doi.org/10.1016/j.jfluidstructs.2015.02.005>

Conference publications:

(1)

Yoshikazu Hirato, Minao Shen, Sachin Aggarwal, Ashok Gopalarathnam, and Jack R. Edwards. "Initiation of Leading-Edge-Vortex Formation on Finite Wings in Unsteady Flow", 53rd AIAA Aerospace Sciences Meeting, AIAA SciTech, (AIAA 2015-0546). <http://dx.doi.org/10.2514/6.2015-0546>

(2)

Arun Vishnu Suresh Babu, Kiran Kumar Ramesh, and Ashok Gopalarathnam. "Model Reduction in Discrete Vortex Methods for 2D Unsteady Aerodynamic Flows", 34th AIAA Applied Aerodynamics Conference, AIAA Aviation, (AIAA 2016-4163). <http://dx.doi.org/10.2514/6.2016-4163>

2. New discoveries, inventions, or patent disclosures:

Do you have any discoveries, inventions, or patent disclosures to report for this period?

No

Please describe and include any notable dates

Do you plan to pursue a claim for personal or organizational intellectual property?

Changes in research objectives (if any):

None

Change in AFOSR Program Manager, if any:

None

Extensions granted or milestones slipped, if any:

We apologize for the one-month delay in submitting this final report.

AFOSR LRIR Number

LRIR Title

Reporting Period

Laboratory Task Manager

Program Officer

Research Objectives

Technical Summary

Funding Summary by Cost Category (by FY, \$K)

| | Starting FY | FY+1 | FY+2 |
|----------------------|-------------|------|------|
| Salary | | | |
| Equipment/Facilities | | | |
| Supplies | | | |
| Total | | | |

Report Document

Report Document - Text Analysis

Report Document - Text Analysis

Appendix Documents

2. Thank You

E-mail user

Aug 15, 2016 17:04:57 Success: Email Sent to: agopalar@ncsu.edu